

An Investigation of Terahertz Near-Field Imaging

by

Hungyen Lin

B.E. (Computer Systems, First Class Honours),
The University of Adelaide, Australia, 2003
M.Eng. (Manufacturing Engineering, Masters by Research),
University of South Australia, Australia, 2006

Thesis submitted for the degree of

Doctor of Philosophy

in

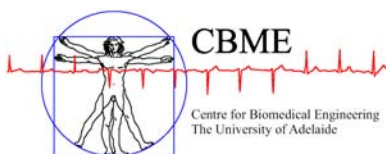
School of Electrical & Electronic Engineering
Faculty of Engineering, Computer & Mathematical Sciences
The University of Adelaide, Australia

12 December, 2011

Supervisor: Prof Derek Abbott

Co-supervisor: Associate Prof Christophe Fumeaux

Co-supervisor: Dr Bernd Michael Fischer



© 2011
Hungyen Lin
All Rights Reserved



Contents

Contents	iii
Abstract	ix
Statement of Originality	xi
Acknowledgments	xiii
Conventions	xvii
Publications	xix
List of Figures	xxi
List of Tables	xxvii
Chapter 1. Introduction and Motivation	1
1.1 Introduction	3
1.1.1 Terahertz radiation	3
1.1.2 Major THz radiation sources	3
1.1.3 THz radiation characteristics & applications	6
1.2 Motivation	7
1.3 Significance of microscopy	7
1.4 Thesis overview	8
1.5 Original contributions	10
Chapter 2. Pulsed THz Radiation Generation & Detection	13
2.1 Pulsed THz radiation sources	15
2.1.1 Optical rectification	15
2.1.2 Photoconductive antenna	21
2.2 Pulsed THz radiation detectors	23

2.2.1	Electro-optical sampling	23
2.2.2	Photoconductive sampling	25
2.3	THz systems	28
2.3.1	PCA emission PCA detection	28
2.3.2	PCA emission electro-optical detection	29
2.3.3	Electro-optical emission PCA detection	31
2.4	Chapter summary	31
Chapter 3. Terahertz Near-Field Imaging Techniques: Review		35
3.1	Introduction	37
3.2	Principles of near-field microscopy	38
3.3	Review of THz near-field imaging	39
3.3.1	Aperture based techniques	39
3.3.2	Tip based techniques	42
3.3.3	Highly focused beam techniques	47
3.4	Chapter summary	53
Chapter 4. Far-Field Modelling of Focused THz Radiation Generation		55
4.1	Introduction	57
4.2	Experiment	60
4.2.1	Pinhole	60
4.2.2	Knife-edge profile	61
4.3	Numerical simulation	67
4.3.1	High frequency structural simulator	67
4.3.2	Beam modelling as radiation from a Gaussian aperture	68
4.3.3	Equivalent crossed-dipole model	68
4.3.4	Far-field pattern	71
4.4	Results and discussion	72
4.4.1	Experimental results	72
4.4.2	Model validation	72
4.5	Ramifications to THz	74
4.6	Crystal heating effects	75
4.7	Chapter summary	77

Chapter 5. Modelling of Terahertz Microscope	87
5.1 Introduction	89
5.2 Enhancement replication	90
5.2.1 Experiment	90
5.2.2 Results	91
5.3 Terahertz microscope modelling	94
5.3.1 Experimental near-field beam characterization	95
5.3.2 Modeling of the THz knife-edge experiment	96
5.3.3 Results and discussion	103
5.4 Terahertz microscopy application	109
5.5 Chapter summary	111
Chapter 6. Thesis Summary	113
6.1 Thesis conclusions	115
6.1.1 Review of THz near-field imaging	115
6.1.2 Far-field modelling of focused THz radiation generation	115
6.1.3 Terahertz microscope modelling	116
6.1.4 Summary	116
6.2 Future work	116
6.2.1 Far-field modelling of focused THz radiation generation	116
6.2.2 Terahertz microscope modelling	117
6.3 Summary of original contributions	117
Appendix A. Terahertz Time Domain Spectroscopy Setup	119
A.1 Optical alignment	121
A.1.1 Practical safety advice	121
A.1.2 Practical alignment tips	121
A.2 Hardware specification	123
A.2.1 IR beam path	123
A.2.2 THz radiation emitters & detectors	125
A.2.3 THz radiation path	127
A.2.4 Mechanical components	128
A.3 Sample	129

Appendix B. Material Characterisation in THz PCA Manufacture	131
B.1 Introduction	133
B.2 Ultrafast semiconductor dynamics	136
B.3 Radiation damaged silicon-on-sapphire	137
B.3.1 Ion implantation	137
B.4 Semi-insulating gallium arsenide	139
B.5 Carrier lifetime measurement	141
B.5.1 Drude model	141
B.5.2 Experimental setup	142
B.6 Material characterisation	146
B.6.1 Low-temperature gallium arsenide	146
B.6.2 Semi-insulating gallium arsenide	148
B.6.3 Silicon-on-sapphire	148
B.7 Chapter summary	149
Appendix C. Terahertz Near-Field Material Detection	155
C.1 System setup	157
C.2 Enhancement structure	158
C.2.1 Structure design	158
C.2.2 Structure simulation	159
C.2.3 Structure fabrication	159
C.2.4 Experimental result	160
C.3 Substrate structure	161
C.3.1 Structure design	161
C.3.2 Structure fabrication	161
Appendix D. Gas Recognition with Terahertz Time Domain Spectroscopy	173
D.1 Introduction	175
D.1.1 Gas sensing technologies	175
D.1.2 Fundamental considerations	176
D.1.3 Real-time gas recognition	177

D.2	Feature extraction	177
D.2.1	Spectroscopic catalog features	178
D.2.2	Sample spectral features	179
D.2.3	Reference-free spectral features	181
D.2.4	Feature encoding	181
D.3	Feature selection	181
D.4	Euclidean distance classifier	182
Appendix E. Software Implementation		191
E.1	Data acquisition	193
E.1.1	THz-TDS algorithm	193
E.1.2	Knife-edge algorithm	193
E.1.3	Imaging algorithm	193
E.2	Data processing	193
E.2.1	Code listings	197
Bibliography		213
Glossary		229
Acronyms		231
Index		233
Biography		237

Abstract

The spatial resolution of conventional terahertz (THz) images is limited by the wavelength of THz radiation (0.3 mm for 1 THz) and is therefore in the submillimetre range. The general motivation behind an increased spatial resolution is to distinguish objects separated by sub-wavelength distances and to cater for a smaller sample size. Owing to the infancy of the technology, much work has to be carried out to improve the system resolution. The focus of this Thesis is not to further improve the resolution, but rather, take a step back to elucidate further understanding THz near-field approach. This thesis, in the scope of engineering, investigates the focused beam near-field technique through experimentation and modelling with an aim to provide a better understanding in the far-field and near-field regime. The work aims to assist with the future implementation of THz near-field imaging systems. This body of work performs far-field studies of a sub-wavelength THz source (Chapter 5) and a near-field investigation for potential microscopic application (Chapter 6). In particular, this can be outlined into two categories:

Far-field studies of a sub-wavelength THz source focus on modelling the source as a radiating Gaussian aperture and illustrate the breakdown of the paraxial approximation at low THz frequencies. The findings show that the shape of the radiation pattern causes a reduction in detectable THz radiation and hence contribute significantly to low signal-to-noise ratio in THz radiation generation. The investigation can apply without a loss of generality to other types of sub-wavelength sources for THz generation, such as, in photoconduction and plasma generation. Simulation of the laser heating effects from prolonged intense exposure of a highly confined optical beam on the THz emitter is also conducted.

The near-field investigation of a sub-wavelength THz source in a THz emitter also models the source as a radiating Gaussian aperture. Based on realistic parameter values, the model allows for THz beam characterisation in the near-field region for potential microscopy applications. The proposed validated numerical model therefore aids in the quantitative understanding of the performance parameters. The work can

be applied to other focused beam THz techniques such as photoconductive antennas without a loss of generality. Thin THz emitters have been reported to generate THz radiation power enhancement. Empirical investigation of a reported unexpected thin crystal power enhancement is also conducted.

In addition to these parts of the original contributions, the Thesis offers an introductory background to THz-TDS and THz near-field imaging. Three side investigations are described in the appendices: (i) THz photoconductive antenna material characterisation, (ii) THz near-field material detection, and (iii) Gas recognition with THz-TDS.

Statement of Originality

This work contains no material which has been accepted for the award of any other degree or diploma in any university or other tertiary institution to Hungyen Lin and, to the best of my knowledge and belief, contains no material previously published or written by another person, except where due reference has been made in the text.

I give consent to this copy of my thesis when deposited in the University Library, being made available for loan and photocopying, subject to the provisions of the Copyright Act 1968. The author acknowledges that copyright of published works contained within this thesis resides with the copyright holder(s) of those works.

I also give permission for the digital version of my thesis to be made available on the web, via the Universitys digital research repository, the Library catalogue, the Australasian Digital Theses Program (ADTP) and also through web search engines, unless permission has been granted by the University to restrict access for a period of time.

December 12, 2011

Signed

Date

Acknowledgments

I gratify this opportunity and glorify this Thesis to the Lord and His precious son Jesus Christ. He is truly the amazing rock in my life no matter what happens and the source of everything. I praise Him!

The fruition of this Thesis has come about because of many people and a few lines here are not sufficient to express my uttermost gratitude and appreciation.

I would like to express my gratitude to my principal supervisor Prof Derek Abbott for accepting me as a PhD candidate in 2006 and introducing to me the glorious world of THz near-field imaging. His unwavering optimism, linguistic finesse, ever-so encouraging attitude, generous travel financial assistance has been helpful in propelling my research forward. I have had the pleasure to work alongside two further great scientists, my co-supervisors, Dr Bernd M. Fischer and A/Prof Christophe Fumeaux. Seeing and experiencing how internationally renowned scientists conduct fundamental research is the very reason why I pursued a PhD following a Masters by research degree. Together, they have defined the word quality for the research. Dr Bernd M. Fischer's long experience with THz radiation has been of great importance to my research. His practical experience in THz-TDS systems underpins the many setups that we house in the Australian National T-ray Facility today. His knowledge of the field and international links is the inspiration behind THz photoconductive antenna development in Appendix D. I am also deeply grateful to Bernd, Birgitte, and family for their warm hospitality during my research visit to Freiburg THz Physics Group, Germany and Institute of Saint Louis, France in February 2011. Another person that I am strongly indebted to is A/Prof Christophe Fumeaux. His theoretical understanding of the electromagnetic regime spanning from optics to microwaves, complemented with proficiency in numerical simulation, has consolidated with my THz near-field experiments. Christophe has always welcomed scientific discussions and has given me critical technical feedback. I have thoroughly enjoyed our collaboration and I am thankful for his understanding and patience. I also thank Prof Masayoshi Tonouchi for hosting my short-term stay at Osaka University, A/Prof Hironaru Murakami for warm hospitality and Dr Iwao Kawayama for technical discussions.

Acknowledgments

I also like to express my appreciation to the staff of The School of Electrical & Electronic Engineering at The University of Adelaide. To the technical staff, Mr Ian Linke, Mr Alban O'Brien and Mr Pavel Simcik for their practical suggestions and fabrication of samples in the midst of tight time frames. Mr Danny Di Giacomo for his friendliness and logistical supply of parts. The administrative staff, Mrs Rose-Marie Descalzi, Mrs Ivana Rebellato and Ms Philomena Jensen-Schmidt for their kindness and assistance. To the supervisors of the courses that I tutored: A/Prof Mike Liebelt, Prof Lang White and Dr Benham Jamali; it was great to work with you all.

While a PhD is a solitary experience by nature, I have had the privilege to interact with all the people at the Adelaide T-ray Group, the School and Osaka University. I would specially like to acknowledge and thank Mr Benjamin Ung and Dr Withawat Withayachumnankul, for being supportive colleagues and friends. Much of the work on THz systems setup and uncertainty analysis resulted from our collaboration. I would also like to thank Mr Henry Ho, Mr Shaoming Zhu, and Mr Andrew Li for interesting friendship and being great gym buddies, and Ms Shaghik Atakaramians, Dr Gretel M. Png and Mr Mayank Kaushik for fruitful discussions and encouragement. Other people include Dr Jegathisvaran Balakrishnan and Inke Jones. Special mention to Dr Samuel P. Mickan, who has provided his optical component drawings that are vastly used throughout this Thesis.

I have had the privilege to serve alongside many postgraduate students in the executive committee of Electrical and Electronic Engineering Society of Adelaide University (EESAU). Special thanks to the executive members Prof Bevan Bates, Dr Brian Ng, Mr Luke Balzan, Mr Simon Knight, Mr Daniel Kelly, Dr Muammar Kabir, Mr Robert Moric, Mr Adam Burdeniuk, Mr James Kitchener, Ms Hui Min Tan and Mr Barry Yang. It was a pleasure to work with you all for the greater good of the school. Despite hectic schedules, I have enjoyed weekly Christian bible study and fellowship with Dr Wen Soong, Mr Greg Pullman, Mr David Bowler, Mr Matthew Trinkle in the school and Mr Geoff Lin at Evangelical Society at the university. I appreciate the sacrifice and commitment that you all put in reminding us of God's Word in our lives. Other postgraduates in the school that I have become well acquainted with include Mr Omid Kavehi, Mr Mostafa Rahimi, Ms Taraneh Aria, Mr Ruiting Yang, Mr Danny Wong, and Mr Arash Mehdizadeh. Experiences in Japan was paramount to my spiritual growth. I treasure the time with Ms Tatiane Teru Takahashi and I look forward in a journey together. I would like to thank the following people that I met whilst in Osaka University; Mr

Kazunori Serita, Mr Yuki Sano, Ms Gong Qian, Mr Andreas Glossner, Mr Weiming Xu, Mr Shinya Kikuta, Mr Yuki Maekawa, Ms Mayo Iwami, Ms Azusa Ebisuya and Ms Makie Tachikawa, I thank you all for the warm friendship and the precious moments together.

Outside research, I would like to express my deepest gratitude to my family especially my parents and sister for their abundance in love, advice, words of wisdom and unwavering support that I know I can always count on no matter what. I would also like to thank my fellow brothers and sisters at Hope Christian Fellowship, Holy Trinity Church and Osaka International Church for their patience, love and encouragement towards Christ.

Finally, I gratefully acknowledge the many funding agencies whose generous grants facilitated this research. This was enabled by Australian Postgraduate Award, Australian Research Council (ARC) Grant-Funded Scholarship, IEEE Photonics Society Graduate Student Fellowship, DR Stranks Postgraduate Travelling Fellowship, The University of Adelaide Research Abroad Scholarship, IEEE South Australia Section Travel Assistance Fund and Barbara Crase Bursary from the Australian Federation of University Women (AFUW). This work is mainly funded by the ARC project number DP09888673. Special thanks are due to Department of Education, Employment and Workplace Relations and the Endeavour Awards Management Team for the funding and an opportunity of a lifetime in the form of a one year educational exchange to Institute of Laser Engineering at Osaka University in Japan.

Conventions

Typesetting : This Thesis is typeset using the L^AT_EX₂e software. Processed plots and images were generated using Matlab 7.6 (Mathworks Inc.), Ansoft HFSS 11.0 (Ansoft Corporation), CorelDRAW 11 (Corel Corporation), and Adobe Illustrator CS3 (Adobe Systems Incorporated) was used to produce schematic diagrams and other drawings.

Spelling : Australian English spelling has been adopted throughout, as defined by the Macquarie English Dictionary (Delbridge 2001). Where more than one spelling variant is permitted such as biassing or biasing and infra-red or infrared the option with the fewest characters has been chosen.

System of units : The units comply with the international system of units recommended in an Australian Standard: AS ISO 1000—1998 (Standards Australia committee ME/71, Quantities, Units, and Conversion 1998).

Physical constants : The physical constants comply with a recommendation by the Committee on Data for Science and Technology: CODATA (Mohr and Taylor 2005).

Frequency band definition : The terahertz spectrum from 0.1 to 10 THz is referred to as terahertz radiation as opposed to 'T-rays' in Abbott and Zhang (2007). This is because of the growing popularity of terms such as 'terahertz time-domain spectroscopy—THz-TDS' and 'terahertz gap' in the community.

Referencing : The Harvard style is used for referencing and citation in this Thesis.

Publications

Journal publications

- UNG-B. S. Y., FUMEAUX-C., **LIN-H.**, FISCHER-B. M., NG-B.-W.-H., AND ABBOTT-D. (2012). A low-cost ultra-thin polymer broadband terahertz beam-splitter, *Opt. Express*, **20**(5), pp. 4968–4978.
- WITHAYACHUMNANKUL-W., **LIN-H.**, SERITA-K., SHAH-C. M., SRIRAM-S., BHASKARAN-M., TONOUCHI-M., FUMEAUX-C., AND ABBOTT-D. (2012). Sub-diffraction thin-film sensing with planar terahertz metamaterials, *Opt. Express*, **20**(3), pp. 3345–3352.
- KHODASEVYCH-I. E., SHAH-C. M., SRIRAM-S., BHASKARAN-M., WITHAYACHUMNANKUL-W., UNG-B. S. Y., **LIN-H.**, ROWE-W. S. T, ABBOTT-D, AND MITCHELL-A. (2011). Elastomeric silicone substrates for terahertz fishnet metamaterials, *Appl. Phys. Lett.*, doi: 10.1063/1.3665180.
- LIN-H.**, FUMEAUX-C., UNG-B. S. Y., AND ABBOTT-D. (2011). Comprehensive modeling of THz microscope with a sub-wavelength source, *Opt. Express*, **19**(6), pp. 5327–5338.
- LIN-H.**, FUMEAUX-C., FISCHER-B. M., AND ABBOTT-D. (2010b). Modelling of sub-wavelength THz sources as gaussian apertures, *Opt. Express*, **18**(17), pp. 17672–17683.
- WITHAYACHUMNANKUL-W., FISCHER-B. M., **LIN-H.**, AND ABBOTT-D. (2008). Uncertainty in terahertz time-domain spectroscopy measurement, *Journal of the Optical Society of America B: Optical Physics*, **25**(6), pp. 1059–1072.
- WITHAYACHUMNANKUL-W., PNG-G., YIN-X., ATAKARAMIANS-S., JONES-I., **LIN-H.**, UNG-B.-S. Y., BALAKRISHNAN-J., NG-B.-W.-H., FERGUSON-B., MICKAN-S., FISCHER-B., AND ABBOTT-D. (2007b). T-ray sensing and imaging, *Proceedings of the IEEE*, **95**(8), pp. 1528–1558.

Conference publications

- LIN-H.**, FUMEAUX-C., FISCHER-B. M., AND ABBOTT-D. (2011). Sub-wavelength THz source modelling, *International Symposium on Terahertz Nanoscience (TeraNano 2011) & Workshop of International Terahertz Research Network (GDR-I)*, Osaka, Japan, p. 255.
- LIN-H.**, FUMEAUX-C., FISCHER-B. M., AND ABBOTT-D. (2011). Near-field & far-field modelling of a sub-wavelength THz source, *36th International Conference on Infrared, Millimeter, and Terahertz*

Waves, Houston, USA, doi: 10.1109/IRMMW-THz.2011.6104774.

SHAH-C. M., SRIRAM-S., BHASKARAN-M., KHODASEVYCH-I., WITHAYACHUMNANKUL-W, UNG-B, LIN-H., ABBOTT-D., AND MITCHELL-A. (2011). Microfabrication of flexible large-area Terahertz fishnet metamaterials, *International Conference on Materials for Advanced Technologies*, Singapore (Accepted on 1 March 2011).

LIN-H., FISCHER-B. M., AND ABBOTT-D. (2010). Comparative simulation study of ZnTe heating effects in focused THz radiation generation, *35th International Conference on Infrared, Millimeter, and Terahertz Waves*, Rome, Italy, doi:10.1109/ICIMW.2010.561272.

LIN-H., UNG-B. S. Y., FISCHER-B. M., MICKAN-S. P., AND ABBOTT-D. (2009). Effect of crystal thickness in localized terahertz generation via optical rectification in ZnTe — preliminary investigation, *34th International Conference on Infrared and Millimeter Waves and Terahertz Waves*, Busan, Korea, doi: 10.1109/ICIMW.2009.5325560.

LIN-H., WITHAYACHUMNANKUL-W., FISCHER-B., AND ABBOTT-D. (2008). Gas recognition with terahertz time-domain spectroscopy and reference-free spectrum: a preliminary study, *33rd International Conference on Infrared and Millimeter Waves and Terahertz Waves*, Pasadena, USA, doi: 10.1109/ICIMW.2008.4665829.

LIN-H., WITHAYACHUMNANKUL-W., FISCHER-B., MICKAN-S., AND ABBOTT-D. (2007). Gas recognition with terahertz time-domain spectroscopy and spectral catalog: a preliminary study, *Proceedings of SPIE Photonics Asia*, 6840, Beijing, China, art. no. 68400X.

LIN-H., WITHAYACHUMNANKUL-W., FISCHER-B., MICKAN-S., AND ABBOTT-D. (2007). THz time-domain spectroscopy uncertainties *Joint 32nd International Conference on Infrared and Millimeter Waves and 15th International Conference on Terahertz Electronics*, Cardiff, UK, pp. 222-223.

WITHAYACHUMNANKUL-W., LIN-H., MICKAN-S. P., FISCHER-B. M., AND ABBOTT-D. (2007). Analysis of measurement uncertainty in THz-TDS *Proceedings SPIE Photonic Materials, Devices, and Applications II*, 6593 Gran Canaria, Spain, art. no. 659326L.

LIN-H., FISCHER-B., MICKAN-S., AND ABBOTT-D. (2006). Review of THz near-field methods *Proceedings SPIE Smart Structures, Devices, and Systems III* 6414, Adelaide, Australia, art. no. 64140L.

LIN-H., FISCHER-B. M., MICKAN-S. P., AND ABBOTT-D. (2006). THz near-field microscopy — a review *Joint 31st International Conference on Infrared and Millimeter Waves and 14th International Conference on Terahertz Electronics*, Shanghai, China, p. 441.

List of Figures

1.1	THz band	4
1.2	Thesis framework	9
<hr/>		
2.1	Optical rectification for generating THz radiation	16
2.2	Photoconductive antenna for generating THz radiation	23
2.3	Electro-optical sampling for detecting THz radiation	26
2.4	Photoconductive dipole antenna for detecting THz radiation	27
2.5	PCA emission PCA detection THz system schematic	28
2.6	Pulse from PCA emission PCA detection THz system	29
2.7	Spectrum from PCA emission PCA detection THz system	30
2.8	PCA emission electro-optical detection THz system schematic	30
2.9	Pulse from PCA emission electro-optical detection THz system	31
2.10	Spectrum from PCA emission electro-optical detection THz system	32
2.11	Electro-optical emission PCA detection THz system schematic	32
2.12	Pulse from electro-optical emission PCA detection THz system	33
2.13	Spectrum from electro-optical emission PCA detection THz system	34
<hr/>		
3.1	Collection mode probe	41
3.2	Confocal microscopy inspired setup	41
3.3	On-chip THz near-field detector	42
3.4	Tip with electro-optic detection	43
3.5	A tip based method by Chen <i>et al.</i> (2003)	44
3.6	Atomic force microscopic tip	45
3.7	Scattering-SNOM inspired setup	45
3.8	Tapered PCA probe	46
3.9	Low-loss dielectric waveguide	46

List of Figures

3.10	Laser terahertz emission microscope	48
3.11	Improved laser terahertz emission microscope	49
3.12	Dynamic Aperture	49
3.13	Peak electric field with different crystal thickness	50
3.14	Electro-optic THz microscope schematics	51
3.15	Electro-optic experimental setup in Lecaque <i>et al.</i> (2006)	51
3.16	Integrated GaP crystal	52
3.17	Metallic metal microstructures with SOS PCA detector	53
3.18	Terahertz chemical microscope setup in Kiwa <i>et al.</i> (2010)	53
<hr/>		
4.1	True Gaussian beam	58
4.2	Gaussian beam depth of focus	59
4.3	Pinhole experiment for observing obliquity factor and paraxial theory .	61
4.4	Knife-edge experiment for observing obliquity factor and paraxial theory	62
4.5	Bird's eye view of the knife crystal system with a CCD camera	64
4.6	Parabolic mirrors placement	66
4.7	Effect of crystal parabolic distance on image formation	66
4.8	Experimental setup	67
4.9	High Frequency Structural Simulator model	68
4.10	Far-field distribution of a plane wave through the aperture	69
4.11	Gaussian aperture modeling methodology	70
4.12	Power spectrum at certain knife locations	73
4.13	Knife-edge profile of selected frequencies	74
4.14	Model validation at 0.375 THz	75
4.15	Model validation at 0.712 THz	76
4.16	Model validation at 1.35 THz	77
4.17	Model validation at 1.5 THz	78
4.18	Model validation at 1.91 THz	78
4.19	Model validation at 2.14 THz	79
4.20	Model validation at 2.51 THz	79

4.21	Illustration of goodness of fit	80
4.22	Detectable THz power percentage	81
4.23	ZnTe temperature increase for the high and low pump power density . .	82
4.24	ZnTe temperature increase for the high and low pump power density . .	83
4.25	Contour plot of penetration depth for high power density	84
4.26	Contour plot of penetration depth for low power density	85

5.1	Varying the excitation size	91
5.2	Thin crystal enhancement experimental setup	92
5.3	Varying excitation size	93
5.4	Pulse from thin electro-optical crystal and PCA detection	93
5.5	Spectrum from thin electro-optical crystal and PCA detection	94
5.6	Measured peak THz electric field for the thick crystal	95
5.7	Measured peak THz electric field for the thin crystal	96
5.8	Experimental setup	97
5.9	Two knife system	97
5.10	Bird's eye view CCD images of x -axis knife-edge	98
5.11	Bird's eye view CCD images of y -axis knife-edge	98
5.12	Dual-axis experimental knife-edge	99
5.13	Schematic of the numerical FVTD model	100
5.14	THz amplitude distribution at 0.8 THz	102
5.15	THz amplitude distribution at 2.4 THz	102
5.16	Normalized THz amplitude radiation pattern	103
5.17	Power spectrum at certain x -axis knife locations	104
5.18	X -axis knife-edge profile of selected frequencies	105
5.19	Power spectrum at certain y -axis knife locations	106
5.20	Y -axis knife-edge profile of selected frequencies	107
5.21	Model validation at 0.35 THz	107
5.22	Model validation at 0.615 THz	108
5.23	Model validation at 1.04 THz	108

List of Figures

5.24	Model validation at 1.46 THz	108
5.25	Model validation at 2.1 THz	109
5.26	Model validation at 2.5 THz	109
5.27	Contour plot along the x and y -axis of the THz beam profile at $50 \mu\text{m}$. .	110
5.28	THz microscopy application	111
<hr/>		
A.1	Use of IR viewer card	122
A.2	Beam horizontal alignment	123
A.3	Femtosecond laser source	124
A.4	Beam splitters	125
A.5	Parabolic mirror	128
A.6	Near-field sample design	130
<hr/>		
B.1	Low-temperature GaAs PCA	135
B.2	Silicon-on-sapphire PCA	135
B.3	SOS Wafers	137
B.4	Ion implantation on a test wafer	138
B.5	Uniform ion implantation with depth of sample	140
B.6	Optical pump probe schematic	142
B.7	Optimised optical pump probe schematic	145
B.8	Probe zero delay	146
B.9	Freiburg LT-GaAs test sample	147
B.10	Transient reflectivity measurements of LT-GaAs	147
B.11	Transient reflectivity measurements of SI-GaAs	148
B.12	Transient reflectivity measurements of unimplanted SOS	150
B.13	Transient reflectivity measurements of radiation damaged SOS with oxygen ions	151
B.14	Transient reflectivity measurements of the radiation damaged SOS with silicon ions	152
B.15	Carrier lifetime of radiation damaged SOS with oxygen and silicon ions	153

C.1	Scanning THz near-field imaging system	162
C.2	Mask structures	163
C.3	Mask design	164
C.4	Bow-tie near-field simulation in free-space	165
C.5	Simulated bow-tie near-field frequency response	166
C.6	Simulated bow-tie far-field transmission spectra	166
C.7	Photomask development	167
C.8	Device fabrication	168
C.9	Fabricated devices	168
C.10	Optical and THz image of bow-tie structure	169
C.11	Experimental bow-tie far-field transmission spectra	169
C.12	Square structures	170
C.13	Square aperture transmission spectra	170
C.14	Experimental design	171
C.15	Mask design	171
C.16	GaAs etching rate	172

D.1	The flow chart for the proposed gas recognition system	184
D.2	Spectra for reference, recovered reference, and water vapour	185
D.3	Absorption coefficient and extracted features	185
D.4	Water vapour absorption coefficient and reference-free spectrum	186
D.5	Absorption coefficient and extracted features for ammonia gas	187
D.6	Ammonia gas absorption coefficient with dynamic range	188
D.7	Data encoding for the catalog and sample spectral features	188
D.8	Column plot of the Euclidean distance measures	189

E.1	THz-TDS LabVIEW algorithm	194
E.2	LabVIEW algorithm for single axis sample scanning	195
E.3	LabVIEW algorithm for two axis sample scanning	196

List of Tables

4.1	Lens selection	63
4.2	ZnTe physical parameters	77
4.3	Initial experimental parameters	78
B.1	Photoconductive material properties	134
B.2	Oxygen ions implants	139
B.3	Silicon ion implants	140
B.4	Measured oxygen ion implanted silicon-on-sapphire carrier lifetimes . .	150
B.5	Measured silicon ion implanted siliconon sapphire carrier lifetimes . . .	153

Introduction and Motivation

TERAHERTZ (THz) radiation or T-ray radiation is a relatively under developed region of the electromagnetic spectrum neighbouring the well established microwave and infrared regions. The THz frequency band spans the frequency range from 0.1 to 10 THz. The frequencies in this range are higher than microwaves but lower than mid-infrared. Techniques have been developed to the point where the frequencies can be generated, detected and manipulated effectively with tabletop equipment. Terahertz near-field imaging or microscopy endeavors to bring the many advantages intrinsic to THz radiation, down to sub-wavelength dimensions. This introductory Chapter offers a brief background to THz radiation, its characteristics and THz Time-Domain Spectroscopy (TDS), along with the thesis outline.

1.1 Introduction

This Chapter introduces THz radiation and the motivation for the work towards THz near-field imaging or microscopy. The roadmap for the Thesis and a summary of the novel contributions are presented here.

1.1.1 Terahertz radiation

Terahertz (THz) radiation, also known as T-rays, is situated on the electromagnetic spectrum between 0.1 and 10 THz (Abbott and Zhang 2007), where 1 THz corresponds to 10^{12} cycles/second, 1 ps, 33.3 cm^{-1} , 0.3 mm and 4.1 meV as illustrated in Figure 1.1. This frequency band overlaps with neighbouring microwave and far-infrared (FIR) regimes. These frequency bands can also be distinguished by their respective technologies. As an example, at low frequencies such as Radio Frequency (RF) and below, radiation is measured by the coherent, polarised electric and magnetic fields induced by photons in an antenna as voltages. The low energy nature of the photons at low frequencies means that they are characterised by waves. Analogously, at frequencies higher than infrared, the electric and magnetic fields oscillate too fast for conventional measurement technologies. Therefore, photons with sufficient energy can be measured individually. Examples include photovoltaic devices, or photoreceptor molecules in our eyes. Since the measurement of individual photons is possible, particle terminology is often used to describe this type of radiation. Neighbouring millimetre wave radiation is traditionally generated by solid-state devices that exploit microwave technologies while, FIR emitters and detectors rely on optical and thermal devices. The THz region has traditionally been dubbed as the “THz gap” due to its resistance to the techniques commonly employed in the well-established, neighbouring frequency bands and high atmospheric absorption (Siegel 2004).

1.1.2 Major THz radiation sources

Since the 1980s, advances in optics and electronics research have provided new avenues for higher power THz radiation sources in an effort to make the “THz gap” evermore accessible. The sections below briefly describe the generation technologies for continuous-wave (single frequency) and pulsed THz radiation (broadband) respectively. Terahertz Time-Domain Spectroscopy (THz-TDS), central to studies in this Thesis, is also introduced.

1.1 Introduction

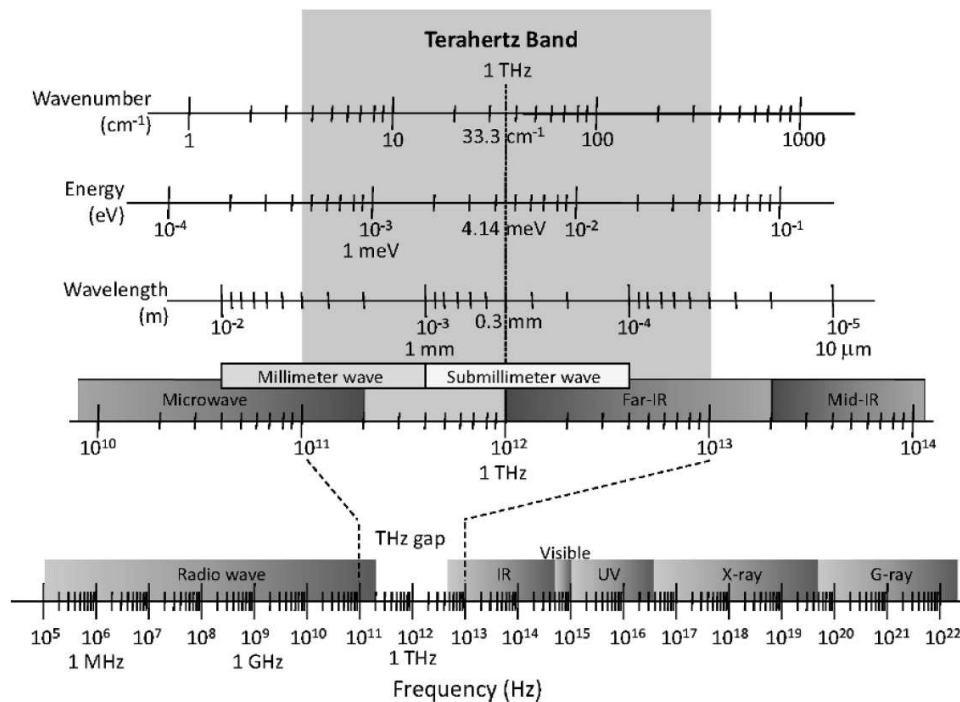


Figure 1.1. THz band. The T-ray or THz band and its neighbouring designations. The THz band is loosely defined to be between 0.1 and 10 THz, the lower part and upper part of which overlap with the conventional designations of EHF microwave (millimetre wave) and far infrared, respectively. After Lee (2008).

Continuous-wave THz radiation

Continuous-Wave (CW) THz radiation can be generated by the nonlinearity of a crystal with two monochromatic optical beams through a process known as Difference Frequency Generation (DFG). This is known as photomixing. An alternative material to a nonlinear crystal is a photoconductor such as Low Temperature grown Gallium Arsenide (LT-GaAs) (Stone *et al.* 2005). In such a configuration, two CW pump lasers of different frequencies overlap on the photoconductor surface, designed such that the difference frequency is in the THz range. The generated photocarriers at the overlap will oscillate at the difference frequency. Under the presence of a DC bias to accelerate the photocarriers, THz radiation is generated at the difference frequency. Further discussion on the topic of photomixers is available in book chapters Duffy *et al.* (2004) and Matsuura and Ito (2005). Accelerating electrons are also a means for producing CW THz radiation. Backward-Wave Oscillators (BWOs) and Free-Electron Lasers (FEL) generate an electron beam that interacts with a slow-wave periodic structure such as a metal grating in a BWO and a magnet array in an FEL. The periodic acceleration of electrons produces CW THz radiation. Further reading is available in Lee

(2008). Heterostructure semiconductor lasers such as Quantum Cascade Lasers (QCL) can be engineered to lase at mid- to far-infrared frequencies. Such a laser consists of periodically alternating layers of dissimilar semiconductors. Exploiting the electron transitions between energy sub-bands, coherent THz radiation is emitted. An extensive coverage can be found in Williams (2007).

Pulsed THz radiation

Bearing a close similarity to CW THz radiation generation schemes, pulsed THz radiation can also be generated with a nonlinear medium and photoconductors. However, in such techniques, the use of femtosecond mode-locked laser pulses is essential. With a nonlinear medium, THz radiation is generated by optical rectification i.e. the generation process of difference frequency components between the many frequencies in the femtosecond pulse. In the photoconductive approach, THz radiation is generated by the acceleration of the induced photocarriers upon femtosecond laser pulse excitation. Details on the principle of operation can be found in Chapter 2. Another mechanism for pulsed THz radiation generation is by means of a surge current on a semiconductor surface with a depleted field. Upon impinging a femtosecond optical pulse on the semiconductor surface, photons are absorbed leading to the creation of electron-hole pairs. The Schottky-barrier potential field accelerates the the carriers in opposing directions leading to the generation of photocurrent or also known as the surge current that emits pulsed THz radiation. Further reading on THz radiation generation by surge current can be found in Gu *et al.* (2002). Other techniques for pulsed THz radiation generation includes the use of semiconductor quantum well structures (Roskos *et al.* 1992), coherent longitudinal optical phonons (Leitenstorfer *et al.* 2000) and high temperature superconductors (Sakai 2005).

Pulsed THz radiation time domain spectroscopy

A combined setup comprising of a pulsed THz radiation emitter and detector that measures pulsed THz radiation coherently, is a technique known as THz Time Domain Spectroscopy (TDS). The system provides information to determine the sample absorption and refractive index as a function of frequency simultaneously. As a result, THz-TDS has received much attention from researchers. Experimental demonstration of THz-TDS can be found in Chapter 2.

1.1.3 THz radiation characteristics & applications

Historically, THz radiation has been employed in spectral characterisation of simple molecules in chemistry and astronomy. In general, nonpolar, dry, and non-metallic materials are transparent to THz radiation. This transparency motivates the use of THz radiation in quality control and security applications (Ferguson *et al.* 2003, Coward and Appleby 2003, Zandonella 2003, Liu *et al.* 2007b). As an example, weapons concealed beneath clothing or products contained in plastic packages can be sensed by THz radiation. Nondestructive detection of hidden explosives or illicit drugs via THz radiation is also possible (Kawase *et al.* 2003, Watanabe *et al.* 2003, Yamamoto *et al.* 2004, Liu *et al.* 2006). The strong absorption of THz energy by water molecules, which complicates measurements in an open-air setting, is beneficial in biology, where THz radiation can perform functional spectroscopy. Terahertz radiation is highly sensitive to the hydration level in biological tissue (Hadjiloucas *et al.* 1999, Han *et al.* 2000a, Pickwell *et al.* 2004, Markelz 2008) and is non-ionizing leading to harmless application to dental (Pickwell and Wallace 2006) and human biological tissues (Liu *et al.* 2007a). Examples include the assistance to skin cancer (Woodward *et al.* 2002, Woodward *et al.* 2003a, Woodward *et al.* 2003b, Wallace *et al.* 2006) and breast cancer diagnoses (Ashworth *et al.* 2009). Terahertz radiation is also of great importance to material spectroscopy (Naftaly and Miles 2007). From the perspective of fundamental science, essentially most polar molecules, either in the solid or liquid phase, absorb unique THz energies for their intermolecular vibrational transitions (Braly *et al.* 2000, Fischer *et al.* 2002, Walther *et al.* 2003). Meanwhile, polar molecules in the gas phase have their rotational transition energies spanning the microwave and THz frequencies (Harde *et al.* 1997, Mittleman *et al.* 1998). The absorption spectrum across this range, therefore, allows material characterization, classification or recognition by means of THz spectroscopy (Jacobsen *et al.* 1996, Strachan *et al.* 2004, Taday 2004, Fischer *et al.* 2005, Strachan *et al.* 2005). Moreover, moderately doped semiconductors also have plasma frequencies and damping rates in the THz frequency region, i.e. between 0.1 and 2.0 THz (van Exter and Grischkowsky 1990b, Jeon and Grischkowsky 1998). The plasma frequency and the damping rate are proportional to the carrier density and mobility of semiconductors, respectively (Cole *et al.* 2001). Thus, THz spectroscopy is ideal for the study of carrier dynamics in semiconductors. Terahertz radiation is also used to stimulate Rabi oscillations in two-level impurity states in semiconductors, which enables the manipulation of physical qubits (Brandi *et al.* 2003).

1.2 Motivation

Terahertz images measure the spectral response of samples in the THz frequency band, thus the resulting images are two-dimensional arrays of spectral information. The images are acquired by raster scanning the sample in x and y dimensions in a THz-TDS. Imaging with THz radiation offers many attractive advantages over existing modalities, especially in its ability to obtain spectroscopic information from the samples of interest. In particular, THz spectra are extremely sensitive to small changes of the molecular structure and different isomeric and intermolecular configurations like in the hydrogen bridge network of organic biomolecules. Moreover, THz radiation is non-destructive and non-invasive, which makes it a suitable candidate for biological investigations. Terahertz imaging are used in a wide range of applications, such as medical diagnostics (Fitzgerald *et al.* 2003, Knobloch *et al.* 2002) and semiconductor characterisation (Mittleman *et al.* 1997, Herrmann *et al.* 2002). However, with a comparatively longer wavelength (0.3 mm at 1 THz), THz images suffer from the problem of low spatial resolution, as determined by Rayleigh's criterion and this proves to be a major limitation (Boyd 2003). The general aim of increased resolution is to distinguish objects sub-wavelengths apart and to cater for a smaller sample size. Zhang (2002) envisioned an endoscopic THz imaging probe for *in vivo* molecular imaging where the probe is capable of near-field micrometre resolution and spectroscopic analysis. With various materials having their unique rotational, vibrational and other low energy responses in this frequency range, the potential use of such a technology allows the exploration and identification of chemical composition in biological and organic materials. At a cellular level, this technology has the potential to cater for the "earlier detection and characterization of disease, understanding of biology and evaluation of treatment" (Zhang 2002). Other specific areas of application include receptor binding and DNA hybridizations and atmospheric sensing (Siegel 2004). As a whole, by bringing non-invasive chemical recognition down to cellular dimensions, THz near-field imaging will open up novel applications and new lines of enquiry.

1.3 Significance of microscopy

The idea of seeing objects on a finer dimension than what is observable through human eyes has always been intriguing, and its realisation has always opened up new lines

1.4 Thesis overview

of fundamental scientific enquiry. Typical human cell sizes range from a few to hundreds of microns, depending on the type (Vander *et al.* 1990), while bacterial spores like bacillus anthracis (anthrax) are in the order of a few microns. The significance of new forms of microscopic analysis is heightened as humankind seeks to probe the nano-bio regime. In 1953, Frits Zernike won the Nobel Prize for optical phase-contrast microscopy and, in 1986, Gerd Binnig and Heinrich Rohrer won it for Scanning Tunneling Microscopy (STM) and Ernst Ruska for electron microscopy—these techniques all provided new ways to probe materials and opened up new fundamental science.

1.4 Thesis overview

Having inherited a brand new THz laboratory and drawing from the research motivation behind existing microscopy, this Thesis explores pulsed THz near-field imaging for the first time in Australia at our National T-ray Facility at The University of Adelaide. Some preliminary work on real-time gas recognition is also presented at the latter section of the Thesis. As a result of the breadth and scope of this Thesis, this research encompasses several disparate disciplines; from quasi-optical system design and implementation, to THz photoconductor fabrication, to signal processing with gas recognition. The outline for this Thesis is presented in Figure 1.2.

The present Chapter initiates the introduction, background and motivation for our investigations. The key contributions are also presented. Chapter 2 introduces pulsed THz radiation generation and detection techniques while at the same time, technically highlights the many THz-TDS systems designed and implemented in-house from scratch. The systems are constructed in conjunction with fellow PhD candidate Mr Benjamin Seam Yu Ung, under the close guidance of Dr Bernd Michael Fischer. The many systems discussed form the necessary research backbone for subsequent research detailed in later Chapters. These THz-TDS systems include a photoconductive antenna emission photoconductive antenna detection system, a photoconductive antenna emission electro-optical detection system and an electro-optical emission photoconductive antenna detection system.

Chapter 3 extensively reviews the current state of the art in THz near-field imaging systems and identifies potential areas of investigation. These techniques are classified in accordance with the electromagnetic energy confinement method for achieving

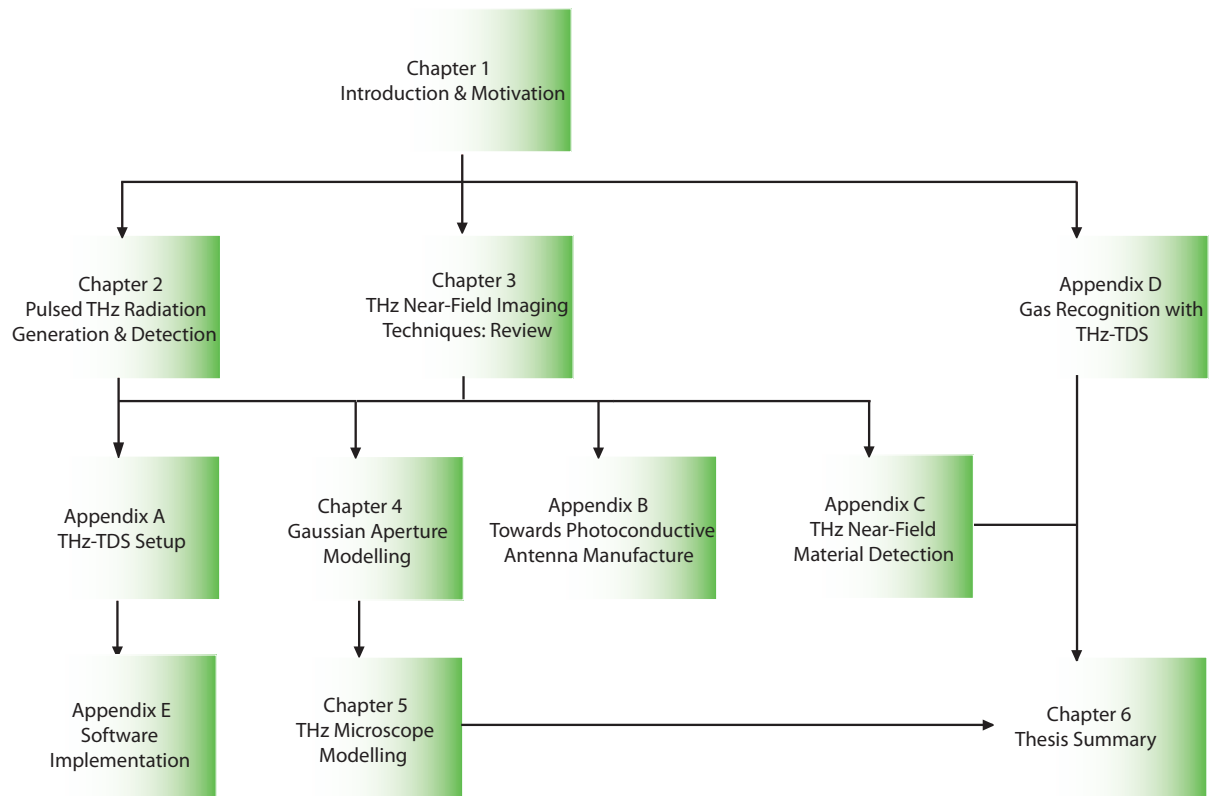


Figure 1.2. Thesis framework. This flow chart shows how the Chapters in this Thesis are connected together. Original contributions to THz technology are found in the Chapters 5 & 6.

sub-wavelength resolution, namely, aperture, tip, and focused beam approaches. The principle of operation of each of the respective techniques are described.

Chapter 4 provides an in-depth examination on the far-field THz radiation pattern from an electro-optical emission photoconductive antenna detection system described in Chapter 2. The Chapter demonstrates that the shape of the radiation pattern causes a reduction in detectable THz radiation and hence contributes significantly to low Signal-to-Noise ratio (SNR) in focused pump beam THz radiation generation in optical rectification. The work also investigates crystal heating effects with a reduced power density through prolonged exposure through simulations.

Following the investigation, Chapter 5 comprehensively studies the electro-optical emission photoconductive antenna detection system in the near-field regime with a focused optical beam. The THz radiation beam spot is numerically simulated that is confirmed experimentally. The numerical model endeavors to assist the designers of this form of THz microscopy in understanding the many performance parameter trade-offs in such a setup. This Chapter also attempts to experimentally replicate the

1.5 Original contributions

unexpected power enhancement associated with tight optical focusing in a thin electro-optical crystal that was described in Yuan *et al.* (2002).

Finally, the work in this Thesis is summarised in the conclusion along with the possible future research directions. Appendix A outlines the equipment used in a THz-TDS setup and offers practical advices gained. Appendix B studies THz photoconductive antenna fabrication for potential THz radiation source and detector application in a THz near-field system. In particular, a carrier lifetime system is designed and implemented for the first time at the National T-ray Facility to measure the transient reflectivity of photoconductors such as Gallium Arsenide (GaAs). Silicon-On-sapphire (SOS) substrates are radiation damaged by means of oxygen and silicon ion implantation conducted at the Department of Electronic Materials Engineering at Australian National University. The lifetimes of which are measured, by our collaborator Dr Raphael Clady, at the Laser Spectroscopy Group of the School of Chemistry, University of Sydney. Appendix C carries out preliminary experimental investigation into THz near-field detection of liquid at Tonouchi Laboratory, Institute of Laser Engineering, Osaka University. Appendix D conducts exploration into real-time gas recognition with THz-TDS. Some of the algorithms and software implementation used in this Thesis are listed in Appendix E.

1.5 Original contributions

In addition to designing and realising many THz-TDS systems for the first time in Australia and an optical pump probe setup in the National T-ray Facility, this Thesis has also made some original and ancillary contributions to the field of THz technology, as highlighted in this section.

A higher-order nonlinear process such as two photon absorption is often attributed as the cause behind a reduction in THz radiation throughput in localised THz radiation generation. In close collaboration with Associate Professor Christophe Fumeaux, this contribution considers localised THz radiation emission from a radiating aperture theory perspective, and demonstrates the changing of the radiation pattern as another plausible cause. In particular, it is shown that at lower THz frequencies, the THz radiation pattern is no longer confined to the direction of propagation but rather diffracted widely and dispersed around the crystal leading to a reduction in measurable THz power in a standard THz-TDS setup (Lin *et al.* 2010b). We have also applied a recently

published water heating model to model the prolonged heating effects of an optical beam on a ZnTe crystal during THz radiation generation. The simulation result quantitatively compares the worst case scenario average temperature rise for high pump power density and low power density (Lin *et al.* 2010a). The study brings an awareness to the THz community the effect of localised THz radiation generation.

Following the far-field studies in localised THz radiation generation, THz near-field effects are studied experimentally and numerically for the first time also in close collaboration with Dr Christophe Fumeaux. The work has ramifications to the field of focused beam THz near-field technique (Lin *et al.* 2011). This contribution enable designers of this form of THz microscopy to predict qualitatively the achievable spatial resolution, while at the same time, better understand the many performance trade-offs in this form of setup. This contribution has also experimentally demonstrated the absence of a power enhancement associated with the use of thin electro-optical crystal in THz radiation generation (Lin *et al.* 2009).

Ancillary contributions in this Thesis are addressed in the Appendix. These include:

1. Silicon-on-sapphire material characterisation through systematic radiation damage and carrier lifetime measurement. The work is conducted in conjunction with Dr Raphael Clady, at the Laser Spectroscopy Group of the School of Chemistry, University of Sydney. The work is in close agreement with the findings in the literature (Doany *et al.* 1987) and empirically demonstrates silicon ion implantation as an alternative promising means to reduce the carrier lifetime for further improvement in the THz bandwidth.
2. In collaboration with Prof Masayoshi Tonouchi at Tonouchi Laboratory, Institute of Laser Engineering, Osaka University, investigation on the application of THz near-field system for material detection is conducted. In particular, the preliminary experimental work focuses on studying structures for sample deposition with near-field illumination and far-field detection. Such an approach has not been attempted and therefore underpins the future development of THz near-field technology.
3. Finally, some brief contribution is made in the preliminary demonstration of THz-TDS to real-time gas recognition. The work outlines the framework for such a system and applies two different type of features; reference free spectrum (Lin *et al.* 2008) and spectrally from reference pulse estimation (Lin *et al.*

1.5 Original contributions

2007). Classification is performed by means of the minimum Euclidean distance classifier and the Submillimeter, Millimeter, and Microwave Spectral Line Catalog.

As a whole, these contributions serve to advance subdisciplines of THz radiation generation, THz near-field microscopy modelling and THz signals processing.



Pulsed THz Radiation Generation & Detection

PULSED THz radiation systems are a recent addition to the wide array of available spectroscopic measurement approaches. This Chapter reviews the common THz radiation generation and detection techniques and details the principle of operation. This knowledge is then applied into realising THz time domain spectrometers in the Adelaide T-ray laboratory for subsequent research investigations as detailed in later Chapters.

Extensive reviews on techniques for generating and detecting broadband THz radiation have been covered in the literature (Sakai 2005, Dexheimer 2007, Lee 2008). This Chapter describes the two main approaches in pulsed THz radiation generation and detection, namely, photoconduction and optical rectification that are conducted experimentally as the research backbone for this Thesis.

2.1 Pulsed THz radiation sources

Photoconduction and Optical Rectification (OR) are two of the most common approaches in generating broadband THz radiation. When comparing the two approaches in modern THz applications, OR generally is less power efficient but has the advantage of a higher bandwidth (Bonvalet *et al.* 1995). Photoconduction only requires a few milliwatts of laser power for THz radiation generation as opposed to a minimum of 100 mW laser power for OR. Photoconduction is therefore an ideal choice for spectroscopic applications. In order to obtain high performance THz PCAs, they have to be specially custom fabricated. On the other hand, good crystals for OR can be commercially obtained with relative ease.

2.1.1 Optical rectification

Optical rectification is a nonlinear effect first observed by Bass *et al.* (1962) that is conventionally referred to as the generation of DC polarisation by an optical beam in a nonlinear crystal (Saleh and Teich 1991). Spectrally, OR is the low frequency response of a nonlinear material to the envelope of a fast, intense laser pulse. For THz radiation generation, OR refers to the creation of beat polarisations in a nonlinear medium with an ultrafast laser pulse. In the early days, Difference Frequency Generation (DFG), analogous to second harmonic generation, was used to generate THz radiation. The process, however, was limited by low conversion efficiencies and phase matching requirements (Shen 1976). Optical rectification is analogous to DFG in nonlinear crystals, with THz radiation being generated as the difference frequencies between Fourier components of the femtosecond laser pulses. Such a generation scheme is capable of producing an electric field with frequencies ranging from DC (Ward 1966) to mid-infrared (Bonvalet *et al.* 1995). In pulsed THz radiation generation, an ultrashort optical

2.1 Pulsed THz radiation sources

pulse is focused onto a nonlinear crystal and the electric field of the pulse induces polarisation transients in the electro-optical crystal, which according to Maxwell's equations, radiates a new electromagnetic field at the THz frequency range. This is illustrated in Figure 2.1.

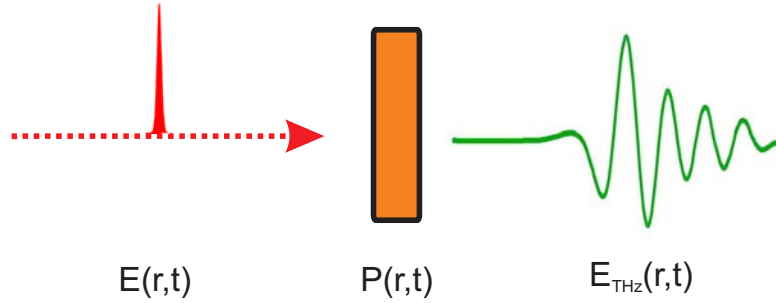


Figure 2.1. Optical rectification for generating THz radiation. Optical rectification is a technique for THz radiation generation. The transient nature of the femtosecond optical pulse induces polarisations in the second order nonlinear crystal at the difference frequencies of optical pulse Fourier components. The transient polarisations in the nonlinear medium in turn generates the THz pulse.

The electric field of the THz pulse is dependent on the second-order time derivatives of the polarisation transients ($E_{\text{THz}} \propto d^2\mathbf{P}(\mathbf{r},t)/dt^2$) and the polarisation $\mathbf{P}(\mathbf{r},t)$ is given by the optical pulse electric field $\mathbf{E}(\mathbf{r},t)$ and the second order nonlinearity (Shen 1984).

Typical values of the second order nonlinearity term materials such as semiconductors, dielectric and organic crystals range from 10^{-24} to 10^{-21} A-s/V² (Saleh and Teich 1991). Low frequency induced polarisations computed for parallel and geometrical optical polarisations are presented in Zhang *et al.* (1992), while Rice *et al.* (1994) generalise the calculation to include frequencies up to the bandwidth of the optical beam. The bandwidth of the THz pulse depends on duration of the polarisation transients, which in turn depends on the the duration of the pump pulse. With durations down to 15 fs, THz pulses have been reported with a bandwidth of above 40 THz (Bonvalet *et al.* 1995).

$$\mathbf{P}(\mathbf{r},t) = \epsilon_0 \left(\chi^{(1)}\mathbf{E}(\mathbf{r},t) + \chi^{(2)}\mathbf{E}(\mathbf{r},t)^2 + \chi^{(3)}\mathbf{E}(\mathbf{r},t)^3 \right) \quad (2.1)$$

where $\chi^{(n)}(\mathbf{r},t)$ is the n th order nonlinear susceptibility tensor of the medium determined from taking the n th derivatives of $\mathbf{P}(\mathbf{r},t)$ with respect to $\mathbf{E}(\mathbf{r},t) = 0$. For small $\mathbf{E}(\mathbf{r},t)$, $\mathbf{P}(\mathbf{r},t)$ is approximately linear, deviating only slightly as $\mathbf{E}(\mathbf{r},t)$ increases. In

OR, only the second order term comes to play and the higher orders of nonlinearity are assumed to be negligible. Assuming the incident light is a plane wave i.e.

$$\mathbf{E}(t) = \int_0^{+\infty} E(\omega) \exp(-i\omega t) d\omega \quad (2.2)$$

then the polarisation leading to OR is given by

$$\mathbf{P}(\omega) = 2\chi^{(2)} \int_0^{\infty} \int_0^{\infty} \mathbf{E}(\omega + \Omega) \mathbf{E}(\omega) \exp(-i\Omega t) d\Omega d\omega \quad (2.3)$$

where Ω is the frequency difference. The propagation of THz radiation is then governed by Maxwell's wave equation in a nonlinear medium i.e.

$$\left(\nabla^2 - \frac{\epsilon(\omega)}{c^2} \frac{\partial^2}{\partial t^2}\right) \mathbf{E}_{\text{THz}}(\mathbf{r}, t) = \frac{4\pi}{c^2} \frac{\partial^2 \mathbf{P}(\mathbf{r}, t)}{\partial t^2}. \quad (2.4)$$

The THz wave equation is then solved with the first Born approximation assuming the depleted incident light is negligible. Measurement of the radiated THz radiation as a function of the azimuthal angle is presented for various materials with a zinc blende crystal structure such as GaAs, CdTe and InP (Rice *et al.* 1994, Bonvalet *et al.* 1995). In the context of generation, the azimuthal angle is the angle between the crystallographic axis (001) and pump beam polarisation. Optimal generation occurs at four angles (starting at 55°) that give rise to maximum absolute value of polarisation, which in turn is proportional to the radiated THz field (Chen and Zhang 1999). Rice *et al.* (1994) present a detailed study for GaAs and CdTe. Practically, the crystal needs to be rotated to find the best polarisation.

Phase matching

The power and bandwidth of the THz radiation generated by OR is determined by the driving optical pulse (optical fluence and orientation), nonlinear electro-optical coefficient of the crystal, crystal damage threshold, output coupling constraints and phase matching (Rice *et al.* 1994). In particular, the conversion efficiency of OR and electro-optical sampling is dictated by the interference of the electromagnetic waves generated over the length of the crystal. This is described as phase matching between the optical pulse to the generated THz radiation. The phase matching constraint given by Shen (1976) for OR is expressed in Nahata *et al.* (1996) as:

$$\Delta \vec{k} = \vec{k}(w_{\text{opt}+\text{THz}}) - \vec{k}(w_{\text{opt}}) - \vec{k}(w_{\text{THz}}) = 0 \quad (2.5)$$

2.1 Pulsed THz radiation sources

where \vec{k} is the wave vector of the respective optical frequencies; $\omega_{\text{opt+THz}}$ and ω_{opt} , and THz frequencies ω_{THz} . The phase matching condition is the consequence of the the energy and momentum conservation laws for photons in nonlinear optics (Saleh and Teich 1991). An equivalent equation from the electro-optical sampling perspective, also by Nahata *et al.* (1996), is the coherence length that is expressed as

$$l_c = \frac{\pi c_0}{\omega_{\text{THz}} |n_{\text{opt}} - n_{\text{THz}}|} \quad (2.6)$$

where c_0 is the speed of light, n_{opt} and n_{THz} are the refractive indexes for optical and THz frequencies respectively. The expression assumes the negligible effect of dispersion and birefringence. By considering the effect of dispersion at optical frequencies, the phase matching condition is achieved when the THz wave phase velocity is the same as the optical group velocity (Nahata *et al.* 1996) i.e.

$$\frac{k(\omega_{\text{THz}})}{\omega_{\text{THz}}} \approx \left(\frac{dk}{d\omega} \right)_{\text{opt}}. \quad (2.7)$$

This fact is indirectly verified empirically by van der Valk *et al.* (2005), where crystals of various thickness were used to generate THz radiation. The work explained that because of velocity mismatching, the THz radiation generated from different parts of the crystal will not constructively interfere, thereby leading to a reduced efficiency in thicker crystals. By adopting thin crystals (Huber *et al.* 2000, Liu *et al.* 2004), the resulting phase difference due to velocity mismatch is smaller because of a shorter path length, and this diminishes the extent of destructive interference. This hence provides a possible explanation into the unexpected high THz signal generated from thin ZnTe crystals using a tightly focused beam (Yuan *et al.* 2002, Micken 2002). However, this effect is mooted as it has not been subsequently reproduced by other groups.

Materials

To achieve velocity matching yet maintain a feasible electro-optical crystal thickness, a greater understanding into the existing methods in overcoming velocity mismatching is necessary. This section will base the discussion around the suitable OR materials

along with the velocity matching methods. To generate the wide bandwidth THz radiation from ultrafast laser pulses, materials with non zero second-order nonlinear susceptibility χ^2 and an instantaneous optical response are useful (Nahata *et al.* 1996). The materials can be broadly classified as inorganic, organic and polymers. The following discusses each of the respective materials and how they achieve velocity matching.

Inorganic

Inorganic electro-optical crystals can be loosely grouped as either ionic or covalent bonded. The ionic crystals described in Wu and Zhang (1996b) such as LiNbO₃, LiTaO₃, KDP and BaTiO₃ have high electro-optical coefficients — however, due to the high static dielectric constants, non collinear velocity matching is applied. In contrast, covalent bonded crystals such as GaAs, ZnS, InP, GaP and ZnTe have moderate electro-optical coefficients, lower dielectric constants and zero intrinsic birefringence. Due to similarity in refractive indices in the optical and THz frequency regime, collinear velocity matching is possible. We now briefly describe three electro-optical materials.

1. Gallium selenide

Gallium selenide (GaSe) is a negative uniaxial crystal with type-I phase matching that has a relatively high electro-optical coefficient (54 pm/V), high damage threshold and a low absorption coefficient (Dmitriev *et al.* 1999). Terahertz radiation generation with a GaSe emitter is demonstrated as difference frequency generation in Kaindl *et al.* (1998) and optical rectification (Huber *et al.* 2000, Kubler *et al.* 2005) where the natural birefringence of the crystal is exploited to achieve phase matching via angle tuning. More specifically, the crystal is tilted by some phase matching angle. Kubler *et al.* (2005) concluded that by using thin emitter crystals (tens of microns), the transparency range is enhanced while the dispersion is minimized suitable for the generation of femtosecond IR pulses. The use of thin crystals also lessens the significance of the phase matching condition.

2. Zinc telluride

Zinc Telluride (ZnTe) is a commonly used electro-optical material used in the THz community, possessing a zinc blende crystal structure. Zinc blende electro-optical materials are described in Wu and Zhang (1996a). Zinc telluride in the

THz field is first reported in Nahata *et al.* (1996) and proves to be the most popular because of a reasonable electro-optical coefficient and good phase matching properties (Stepanov and Hebling 2005). Using optical dispersion, velocity matching between optical and phase velocities is found to be possible at specific optical frequencies (Nahata *et al.* 1996, Wu and Zhang 1996a). In particular, velocity matching is achieved within the tuning range of the Ti:sapphire femtosecond lasers i.e. 822 nm (Wu and Zhang 1996a). Zinc telluride, however, suffers from two-photon absorption which reduces the intensity of the propagating laser pulse, leading to a reduction in THz radiation generation efficiency (Xu and Zhang 2002).

3. Lithium niobate

Lithium Niobate (LiNbO_3) have high electro-optical coefficients and noncollinear velocity matching, which involves determining the propagation direction of the optical and THz beam and is used to achieve velocity matching (Wu and Zhang 1996a). The different geometries described in Stepanov and Hebling (2005) include the point source, line source, and tilted pulse front. A point source is achieved by tightly focusing the optical beam which leads to a Cherenkov cone with an angle given by Stepanov and Hebling (2005). A line source is demonstrated with some success in Stepanov and Hebling (2005) using stoichiometric LiNbO_3 . The tilted pulse front, which is first attempted in Xu *et al.* (1992), is achieved by slightly focusing the optical beam (Hebling *et al.* 2004, Stepanov and Hebling 2005). Periodically poled LiNbO_3 has also been shown to achieve quasi-phase matching condition in Lee *et al.* (2000).

Polymers

Electro-optical polymers offer the intuitive advantage of flexibility in mechanical properties and in terms of fabrication. They have been demonstrated to be more efficient emitters than LiNbO_3 and ZnTe , respectively, for given thickness, but suffer from the problem of decay and photodegradation (Nahata *et al.* 1995, Sinyukov and Hayden 2002). For this reason we do not consider polymer options any further in this Thesis.

Organic crystals

The patented organic ionic salt crystal dimethylamino-N-methylstilbazolium tosylate (DAST), has been investigated (Carrig *et al.* 1995, Han *et al.* 2000b, Schneider *et al.* 2006). The material is designed to have a very high nonlinear electro-optical coefficient and low dielectric constant at THz frequencies. The high coefficient value can theoretically lead to a greater THz radiation amplitude several times greater than ZnTe (Han *et al.* 2000b), assuming the birefringence due to the imperfections are accounted for. The work of Han *et al.* (2000b) demonstrated a sixfold increase in THz radiation amplitude compared with ZnTe of thickness equivalent to the coherence length. The low dielectric constant of DAST caters for fast electro-optical modulation and detection while the high Pockels coefficient makes it an attractive choice for far and mid IR sensors (Han *et al.* 2000b). However, DAST has a very strong intrinsic birefringence leading to a large phase mismatch that cannot be easily compensated for, which limits its popularity compared with isotropic or weak anisotropic materials such as ZnTe and LiTaO₃. In addition, the emitted THz radiation power scales sublinearly with increasing optical fluence compared with the inorganic crystals leading to more efficient sources (Sinyukov and Hayden 2002). However, DAST, is hygroscopic, therefore making it impractical for real applications, though usable for research purposes.

2.1.2 Photoconductive antenna

An alternative mechanism for generation and detection of THz radiation is by means of photoconduction. The photoconductive approach essentially exploits the ultrafast carrier response time of photoconductive materials as transient current sources for radiating antennas (Mourou *et al.* 1981, Fattinger and Grischkowsky 1988). Table B.1 presents an in-depth comparison of photoconductive materials in the literature for THz radiation generation. A THz photoconductive antenna is comprised of a strip line antenna structure and a photoconductive substrate. During the generation process, photocarriers are generated in the photoconductive substrate through irradiation with an ultrafast laser pulse of photon energy greater than the substrate bandgap. Applying a static DC bias through the strip lines will then create a high field region near the anode (Jepsen *et al.* 1996) and accelerates the photocarriers. This will in turn create a transient current in the substrate between the strip lines, generating a time dependent dipole moment $p(t)$, leading to a time dependent current flow $I(t)$, which according

2.1 Pulsed THz radiation sources

to Maxwell's law will give rise to an emission of electromagnetic radiation with a time-dependence of the electric field, $E_{\text{THz}}(\mathbf{r}, t)$, as follows:

$$\mathbf{I}(t) = \frac{\partial \mathbf{p}(t)}{\partial t} \quad (2.8)$$

$$\mathbf{E}_{\text{THz}}(\mathbf{r}, t) = \frac{1}{4\pi\epsilon_0 c^2 r^3} \times \left(\mathbf{r} \times \frac{\partial^2 \mathbf{p}}{\partial t^2} \right). \quad (2.9)$$

With the photocurrent having a subpicosecond rise time, this gives rise to subpicosecond THz pulse emitted in a cone shape normal to the substrate surface. The flat surface of a crystalline silicon lens is physically attached to the substrate side of the PCA so that the lens and the substrate may form a hyperhemispherical lens collecting and collimating the generated THz radiation (Rudd and Mittleman 2002). This is illustrated in Figure 2.2. The hyperhemispherical lens is typically made of high-resistivity silicon that is non-absorptive and non-dispersive at THz frequencies. Photoconductive emitters are capable of relatively large average THz powers in excess of $40 \mu\text{W}$ (Zhao *et al.* 2002) and bandwidths as high as 20 THz (Shen *et al.* 2003). The generated THz pulse is dependent on the laser pulsewidth, substrate material properties, and electrodes transmission line properties. For high THz bandwidth applications, substrates with fast photocurrent rise and decay times are necessary. These materials include Low Temperature grown (LT)-GaAs and radiation damaged Silicon-On-Sapphire (SOS). It is noted in particular that the radiation generated is mainly dependent on the photocurrent rise with the decay only making a small contribution (Tani *et al.* 1997). Common antenna structures include the dipole, bow-tie and coplanar strip lines (van Exter and Grischkowsky 1990a, Harde and Grischkowsky 1991, Warren *et al.* 1991, Katzenellenbogen and Grischkowsky 1991). For the dipole antenna, generally the smaller the electrodes separation distance, the greater is the achievable bandwidth up to a reported 4.5 THz. In contrast, higher separation distance allows for higher operational DC bias voltage leading to almost double the THz pulse strength (Walther 2003). Selection of the separation distance therefore depends on the bandwidth and intensity requirement of application. It is found that bow-tie antennas yield a stronger THz signal at lower frequencies and more THz radiated power under the same pump power and DC bias conditions (Tani *et al.* 1997).

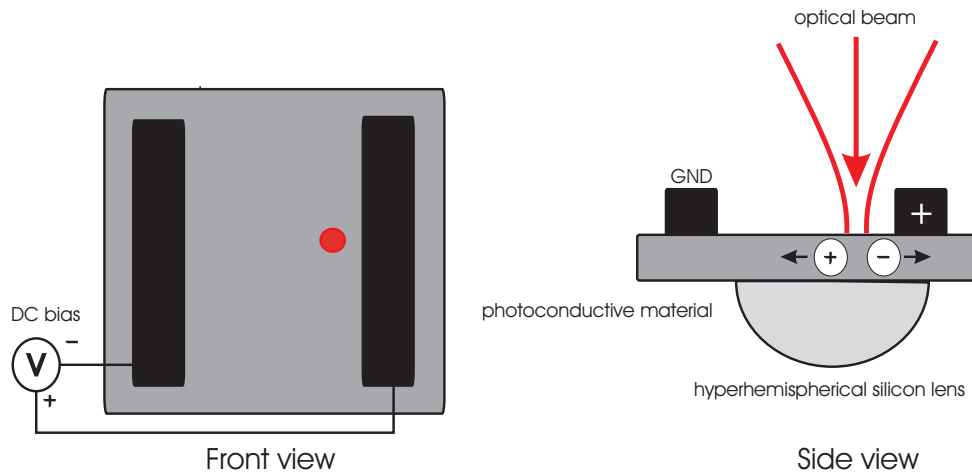


Figure 2.2. Photoconductive antenna for generating THz radiation. Photoconduction is also a common means for THz radiation generation. A THz photoconductive antenna comprises a strip line antenna structure with a typical separation distance of 30 to 100 μm embedded in a photoconductive substrate. Photocarriers are generated in the substrate through irradiation with an ultrafast laser pulse near the anode that are subsequently accelerated by the applied DC bias field. The induced transient photocurrent gives rise to the emission of THz pulses that are coupled by the hyperhemispherical lens.

2.2 Pulsed THz radiation detectors

Analogous to broadband THz radiation sources, photoconduction and electro-optical sampling are also used for detecting broadband THz radiation. Photoconduction detection has the added simplicity in terms of practical setup over electro-optical sampling, but the latter offers the possibility of extremely high detection bandwidths, especially with thin detectors, as demonstrated by Brodschelm *et al.* (2000).

2.2.1 Electro-optical sampling

Coherent detection of the generated THz pulse beam is achieved with electro-optical sampling that produces an electrical signal proportional to the THz electric field. In electro-optical sampling, as illustrated in Figure 2.3, a pellicle beam splitter combines the incident THz pulse and a linearly polarised probe beam so both can co-propagate in the electro-optical crystal. The electric field of the THz pulse modifies the birefringence of an electro-optical crystal through the Pockels effect, which in turn, alters the polarisation of the synchronised probe pulse. The Pockels effect is an electro-optical effect where the refractive index is linearly dependent on the electric field. Equations

2.2 Pulsed THz radiation detectors

2.10 and 2.11 describe the Pockels effect as follows,

$$P = \epsilon_0 \left[\chi^{(1)}E + \chi^{(2)}E^2 + \chi^{(3)}E^3 + \dots \right] \quad (2.10)$$

$$n = \sqrt{1 + \chi^{(1)} + \chi^{(2)}E + \chi^{(3)}E^2 + \dots} \quad (2.11)$$

The optical properties of the crystal such as the refractive index can be described by an index ellipsoid in Equation 2.12 for determining the polarisation and propagation direction of near-IR wave. The index ellipsoid of a wave travelling in an arbitrary direction to the principal axis of the crystal as follows,

$$\sum_{ij} \eta_{ij} x_i x_j = 1 \quad (2.12)$$

where $i, j = 1, 2, 3$ and $x = 1, y = 2$ and $z = 3$. In the presence of an applied electric field and the Pockels effect, the impermeability tensor is modified to become

$$\eta_{ij}(E) = \eta_{ij}(0) + \sum_k r_{ijk} E_k \quad (2.13)$$

where $\eta_{ij}(0)$ is a diagonal matrix containing the inverse principal refractive index squared and r_{ijk} is the Pockels coefficient. Note that η is the electric impermeability tensor that equates to $\epsilon_0 \epsilon^{-1}$ or n^{-1} (Saleh and Teich 1991). For isotropic crystals, diagonal elements of $\eta_{ij}(0)$ become $1/n^2$. Equation 2.14 shows the Pockels coefficients for cubic $\bar{4}3m$ electro-optical crystals such as ZnTe and GaAs. Notice only r_{41} , r_{52} and r_{63} are non zero elements and equates to the value of r_{41} ,

$$r_{ij} = \begin{pmatrix} 0 & 0 & 0 \\ 0 & 0 & 0 \\ 0 & 0 & 0 \\ r_{41} & 0 & 0 \\ 0 & r_{41} & 0 \\ 0 & 0 & r_{41} \end{pmatrix}. \quad (2.14)$$

Given the propagation of light, the index ellipsoid in Eqn. 2.12 is used in conjunction with Equations 2.13 and 2.14 to determine the refractive indices. With the same procedure, the index ellipsoid for isotropic crystals becomes,

$$\frac{x^2 + y^2 + z^2}{n^2} + 2r_{41} E_{THz} xy = 1 \quad (2.15)$$

assuming that E_{THz} is linearly polarised along the crystal axis (001), which is along the z axis (Saleh and Teich 1991). This is assumed for the sake of mathematical simplicity, as generalising the orientation will involve complicated coordinate transformations. This area is generalised by Planken *et al.* (2001). The new principal axes are rotated 45° about the z axis with the refractive indices of new principle axes x' and y' becoming

$$n_{x'} = n + \frac{1}{2}n_0^3 r_{41} E_{\text{THz}} \quad (2.16)$$

$$n_{y'} = n - \frac{1}{2}n_0^3 r_{41} E_{\text{THz}} \quad (2.17)$$

$$n_z = n. \quad (2.18)$$

The wave vector along the y' axis can be decomposed into components along the x' and z axis with the difference giving rise to a phase retardation expressed as

$$\Delta\phi = \Delta kd = \frac{\omega}{c} (n_{x'} - n_{z'}) d = \frac{\omega}{2c} dn^3 r_{41} E_{\text{THz}}. \quad (2.19)$$

As the probe beam propagates out from the electro-optical crystal, an optical bias is provided by means of a quarter-wave plate for the electro-optical crystal without intrinsic birefringence (De Lucia 2003). A Wollaston prism is then used to split the circular polarisation into horizontal and vertical components for subsequent difference voltage measurement via a balanced photodetector. This voltage is proportional to the the induced phase retardation that is in turn proportional to the THz electric field vector. Electro-optical sampling is limited by the finite pulse duration of optical probe, dispersion of nonlinear susceptibility, and mismatch between optical group and THz phase velocity. The detection sensitivity increases linearly as the crystal thickness increases but at the expense of the detection bandwidth because of the velocity mismatch (Gallot *et al.* 1999).

2.2.2 Photoconductive sampling

The detection principle of a PCA is the inverse process of generation. In THz radiation generation, photocarriers are created by the optical pulses and are accelerated by the bias electric field between the antenna electrodes. The acceleration of carriers generates THz pulses. Conversely, for detection, an optical probe pulse is used to generate photocarriers in the substrate that are subsequently accelerated by the incident THz electric field. The acceleration of the photocarriers is physically measured as a current by an ammeter at a maximum of several μA . This is illustrated in Figure 2.4.

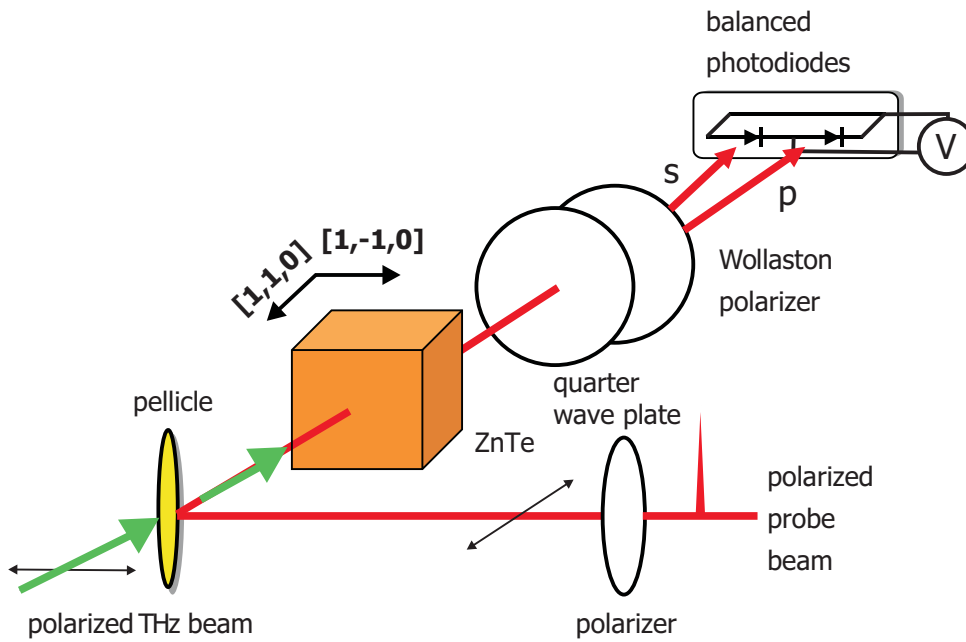


Figure 2.3. Electro-optical sampling for detecting THz radiation. A pellicle beam splitter combines the incident THz pulse and a linearly polarised probe beam so both can co-propagate in the electro-optical crystal. The electric field of the THz pulse modifies the birefringence of an electro-optical crystal through the Pockels effect, which in turn, rotates the polarisation of the synchronised probe pulse. An optical bias is provided by means of a quarter-wave plate for electro-optical crystal (De Lucia 2003) and a Wollaston prism is then used to split the circular polarisations into horizontal and vertical components for subsequent difference voltage measurement via a balanced photodetector. This voltage is proportional to the induced phase retardation that is in turn proportional to the THz electric field vector. The parallel and perpendicular components are annotated as p and s respectively. After (Lu *et al.* 1997).

The measured current is proportional to the product of the incident THz field and the photocarriers. The optical probe pulse has femtosecond duration as opposed to the picosecond time duration of the THz pulse, therefore the THz waveform can be sampled in time by the delay between consecutive pulses. Time resolution of the measured THz waveform is therefore dictated by the delay line resolution. The photocurrent by the incident radiation $E_{\text{THz}}(t)$ at a time delay τ is described by the following equation

$$j(\tau) = e\mu \int_{-\infty}^{\infty} E_{\text{THz}}(t)N(t - \tau)dt \quad (2.20)$$

where $N(t)$, e and μ are the photoconductivity, elementary electric charge, and mobility respectively (Park *et al.* 1998). The finite lifetime of the photocarriers leads to a time dependent photoconductivity. Substrates with low carrier lifetimes such as

LT-GaAs or radiation damaged SOS are therefore used. Investigation on carrier lifetime is conducted in Chapter 4. The antenna structure is also a factor in determining the measured THz waveform. In general smaller antennas have larger bandwidths and are approximated as an ideal Hertzian dipole, where the antenna dimensions are much less than the radiated wavelength. The dipole antenna structure takes form of an 'H' shape shown in Figure 2.4 to increase the THz radiation sensitivity and bandwidth (van Exter *et al.* 1989). The redesign in antenna structure allows for a direct flow of photocurrent through the antenna arms for measurement as opposed to transversal through the more separated the coplanar transmission lines. Further discussions on photoconductive sampling can be found in Jepsen *et al.* (1996).

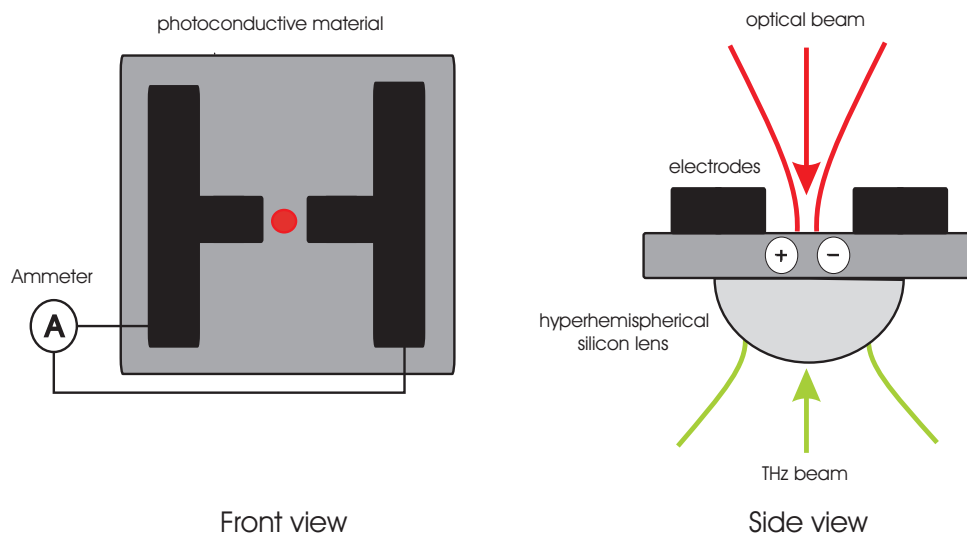


Figure 2.4. Photoconductive dipole antenna for detecting THz radiation. Photoconduction is also used for THz radiation detection. A THz photoconductive antenna comprises of a strip line antenna structure with a typical separation distance of several microns embedded in a photoconductive substrate. Photocarriers are generated in the substrate through irradiation with an ultrafast laser pulse that are accelerated by the THz electric field coupled by an hyperhemispherical lens. The induced photocurrent flow is proportional to the applied THz electric field and is measured by an ammeter. The design of the 'H' shaped antenna structure allows for a direct flow of photocurrent through the antenna arms for measurement as opposed to transversal through the more separated the coplanar transmission lines. This offers advantage in terms of improved THz bandwidth and sensitivity.

2.3 THz systems

Several THz systems are designed and realised in the Adelaide T-ray laboratory utilising the sources and detectors with the principle of operations described in earlier sections. The systems are designed and built with an intent for subsequent research investigations conducted in latter Chapters. A list of optical components used is elaborated in Appendix A in conjunction with practical tips on optical alignment gained from experiment.

2.3.1 PCA emission PCA detection

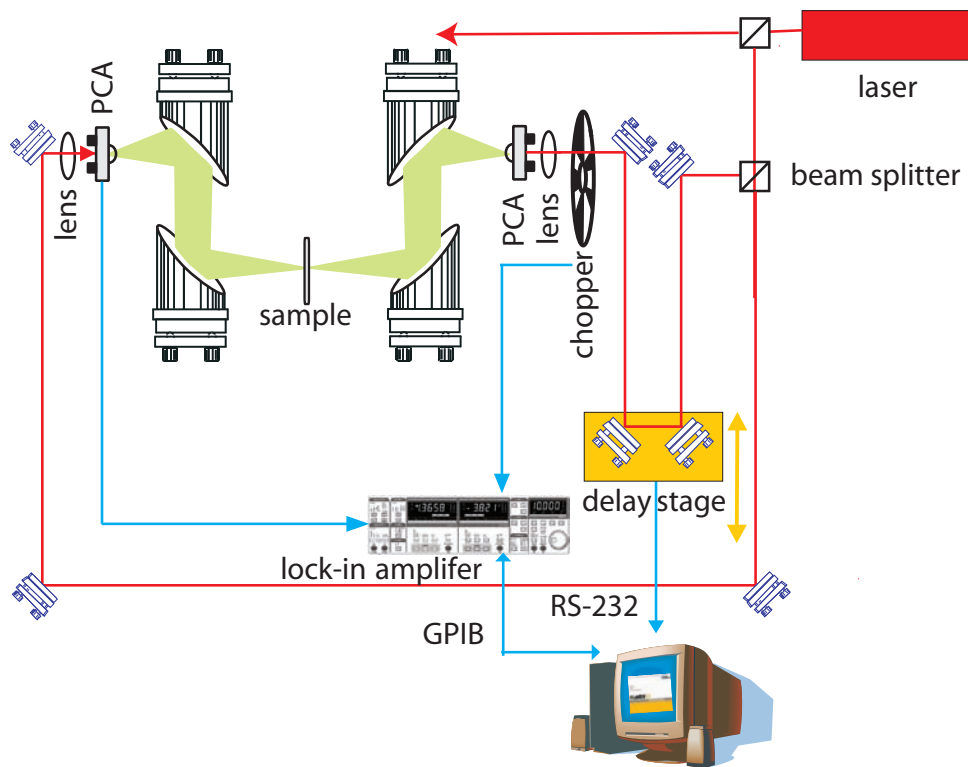


Figure 2.5. PCA emission PCA detection THz system schematic. A THz system employing PCA emitters and PCA detectors is first built due to the simplicity of optical alignment. The PCAs can then be swapped out later for electro-optical emitters and/or detectors.

A standard THz-TDS system comprising a PCA emitter and PCA detector is built. Such a system is perhaps the simplest in terms of construction, alignment and pulse finding. Figure 2.5 illustrates the schematic for our setup. Because of the simplicity involved, this configuration is commonly used as the stepping stone for more advanced

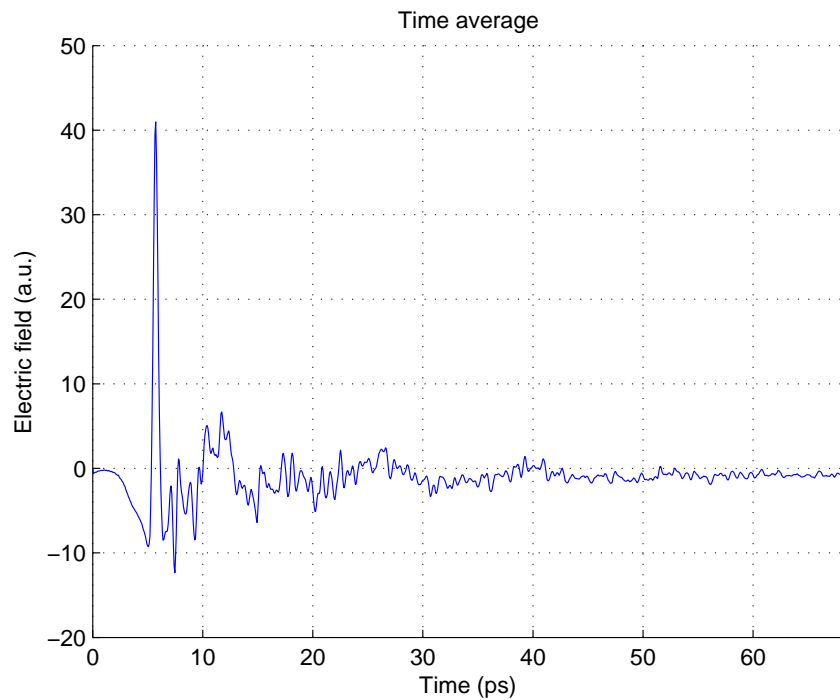


Figure 2.6. Pulse from PCA emission PCA detection THz system. The THz electric field waveform generated with a PCA emission PCA detection setup achieved a SNR of 50 dB and a bandwidth up to 3.7 THz, for the setup in Figure 2.5.

THz-TDS setups. The photoconductive antenna for emission is a pair of strip lines antenna on a LT-GaAs substrate fabricated at Freiburg University, Germany. Similarly, the detector is an 'H' structure also on a LT-GaAs substrate. Such a system is able to generate THz pulses with a bandwidth up to 3.7 THz and a SNR of 50 dB as shown in Figures 2.6 and 2.7 respectively.

2.3.2 PCA emission electro-optical detection

In order to test the fabricated Semi-Insulating (SI) GaAs and SOS PCAs, a theoretically non-bandwidth limited THz system is designed and implemented i.e. PCA emission and electro-optical detection. The setup can also be expanded to an electro-optical detection THz near-field setup. The emitter is a Freiburg manufactured pair of strip lines on a LT-GaAs substrate, while the detector is a Zomega $\langle 110 \rangle$ 1 mm thick ZnTe crystal. Figure 2.8 illustrates the schematic for our setup. Such a setup is able to generate THz pulses up to 3.5 THz bandwidth with a SNR of 50 dB as shown in Figure 2.9 and 2.10 respectively.

2.3 THz systems

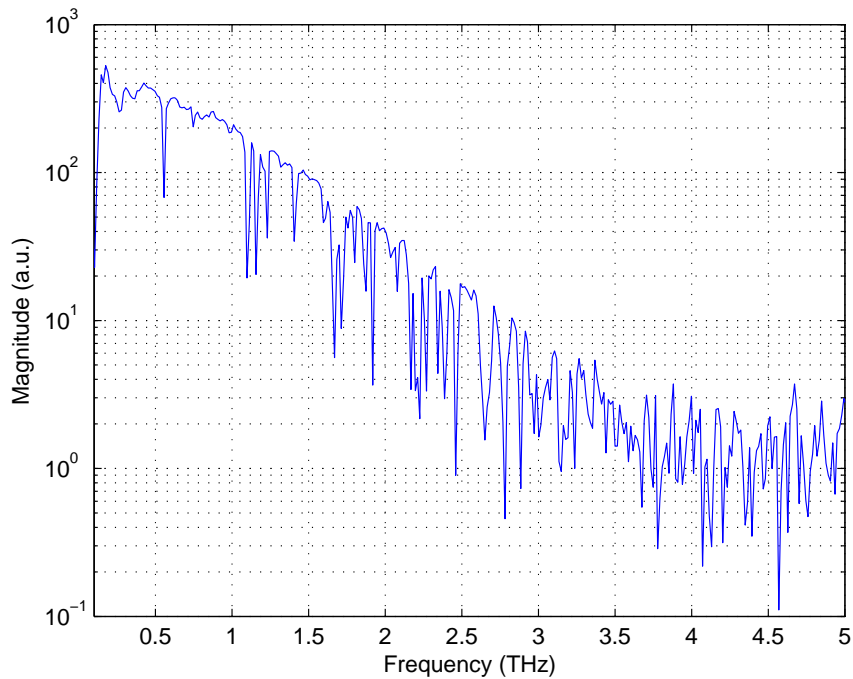


Figure 2.7. Spectrum from PCA emission PCA detection THz system. The THz spectrum generated with a PCA emission PCA detection setup obtained with a SNR of 50 dB and a bandwidth up to 3.7 THz, for the setup in Figure 2.5. As nitrogen is not used, in this example, the water vapour absorption lines can be clearly seen in the spectrum.

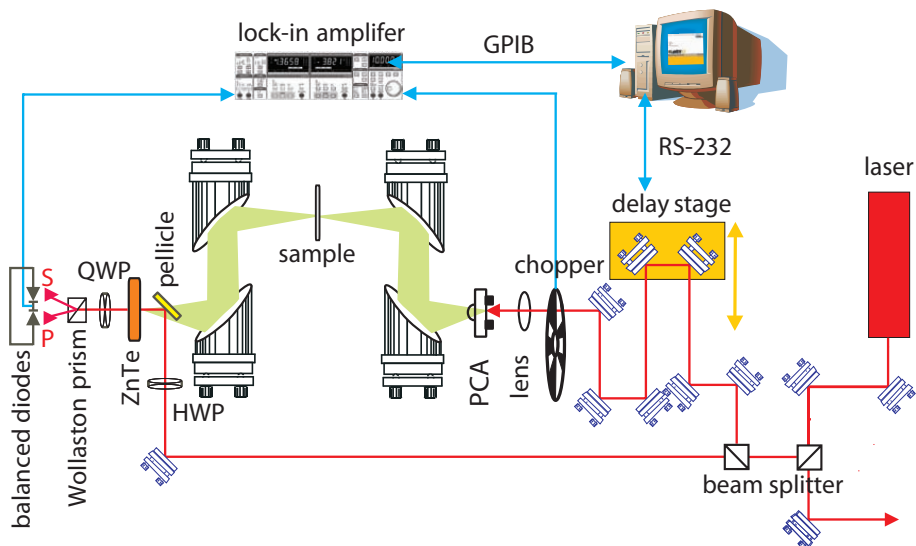


Figure 2.8. PCA emission electro-optical detection THz system schematic. A THz system employing PCA emitters and electro-optical detectors. It is built because it is later used for testing fabricated GaAs and SOS PCAs. It can be expanded to an electro-optical detection THz near-field system analogous to a system operating in the emission mode. For description on electro-optical sampling, please refer to Figure 2.3.

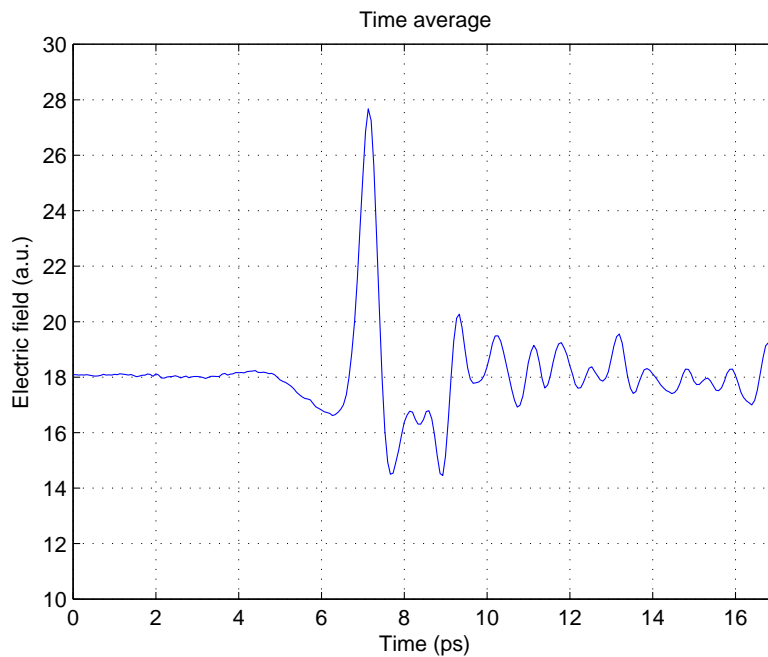


Figure 2.9. Pulse from PCA emission electro-optical detection THz system. The THz electric field waveform generated with a PCA emission electro-optical detection setup achieved a SNR of 40 dB and a bandwidth up to 3 THz, for the setup in Figure 2.8.

2.3.3 Electro-optical emission PCA detection

To setup an electro-optical emission THz near-field system, a THz system with electro-optical emission is necessary. For simplicity, a PCA is used in the detection path. A pump power of 200 mW is used for THz radiation generation with a 1 mm thick $\langle 110 \rangle$ Zomega ZnTe crystal. The detector is a Freiburg manufactured H structure on a LT-GaAs substrate. Figures 2.12 and 2.13 show the THz waveform and spectrum respectively. Figure 2.11 illustrates the schematic for our setup. A SNR of 40 dB and a bandwidth of 3 THz is achieved.

2.4 Chapter summary

This Chapter has reviewed and described pulsed THz radiation generation and detection techniques. These principles have been put into practice by realising three types of THz-TDS systems in the Adelaide T-ray laboratory, namely PCA emission PCA detection, PCA emission electro-optical detection and electro-optical emission PCA detection. With this foundation on THz-TDS system design and implementation, we are

2.4 Chapter summary

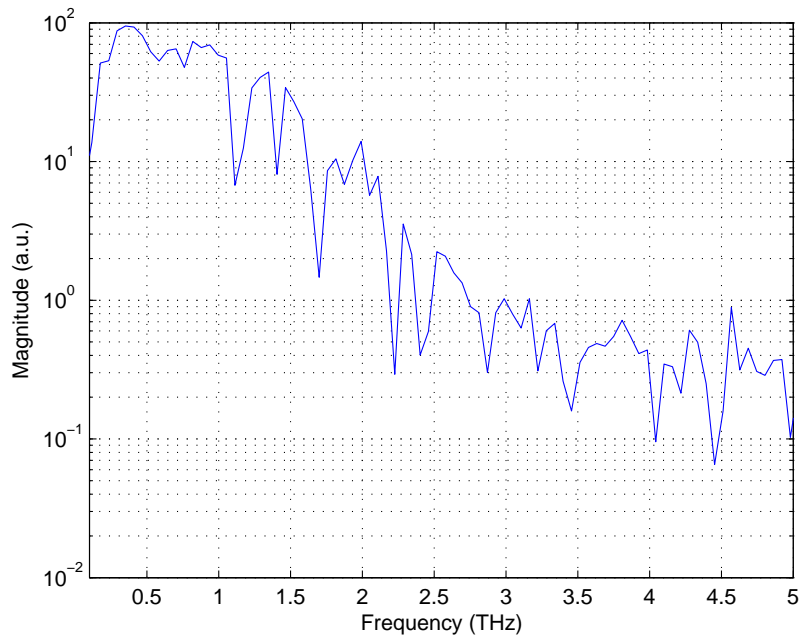


Figure 2.10. Spectrum from PCA emission electro-optical detection THz system. The THz spectrum generated with a PCA emission electro-optical detection setup achieved a SNR of 40 dB and a bandwidth up to 3 THz, for the setup in Figure 2.8. As nitrogen is not used, in this example, the water vapor absorption lines can be clearly seen in the spectrum. The spectrum has a limited frequency resolution compared to the spectrum in Figure 2.7 due to a reduced number of data points.

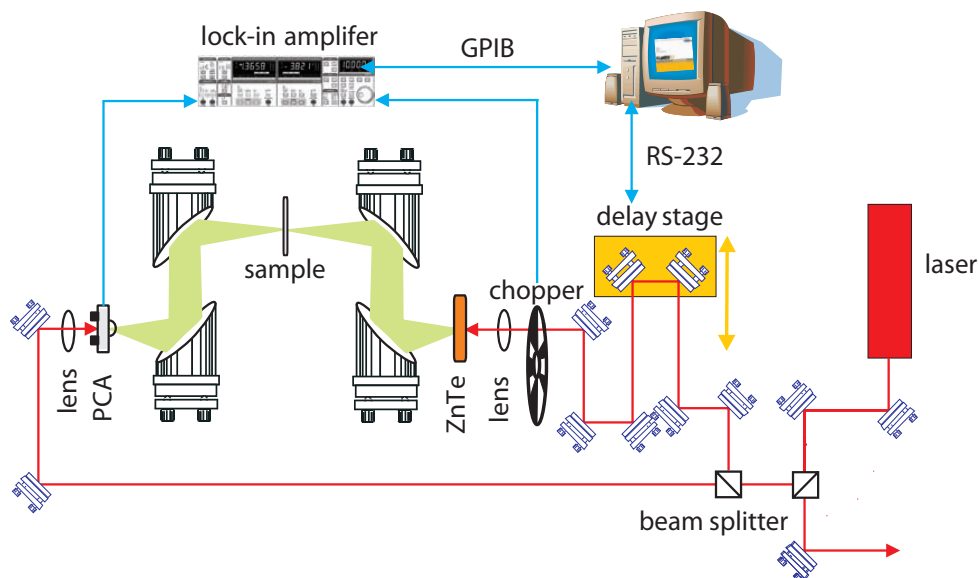


Figure 2.11. Electro-optical emission PCA detection THz system schematic. A THz system employing electro-optical emitters and PCA detectors. It is built for the sake of an electro-optical emission THz near-field system.

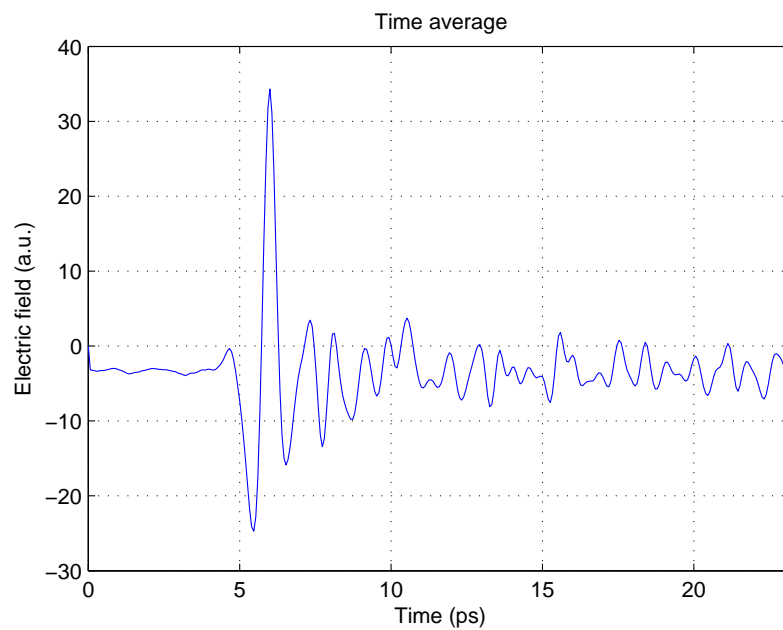


Figure 2.12. Pulse from electro-optical emission PCA detection THz system. The THz electric field waveform generated with an electro-optical emission PCA detection. Such a setup achieved a SNR of 40 dB and a bandwidth of up to 3 THz, for the setup in Figure 2.11

now in a position to apply it to THz near-field imaging techniques that are comprehensively reviewed in the next Chapter.

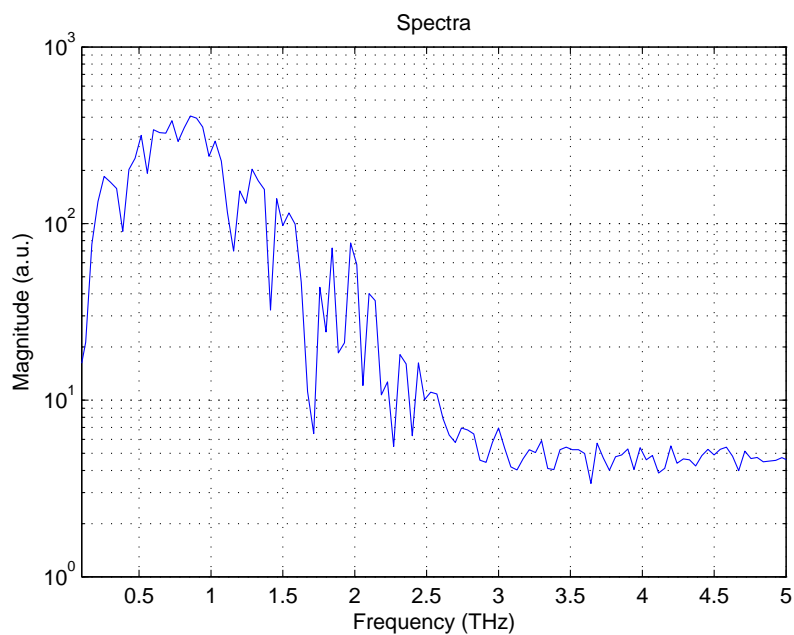


Figure 2.13. Spectrum from electro-optical emission PCA detection THz system. Such a setup achieved a SNR of 40 dB and a bandwidth up to 3 THz, for the setup in Figure 2.11. As nitrogen is not used, in this example, the water vapor absorption lines can be clearly seen in the spectrum. The spectrum has a limited frequency resolution compared to spectrum in Figure 2.7 due to a reduced number of data points.



Terahertz Near-Field Imaging Techniques: Review

TERAHERTZ imaging offers many attractive advantages over existing modalities in its ability to obtain spectroscopic information. However, one of the major limitations of THz imaging is low spatial resolution, as determined by Rayleigh's criterion with a comparatively longer wavelength ($300\ \mu\text{m}$ at 1 THz). As a result, various techniques have been proposed in the literature with the aim of breaking the diffraction limit. Many of the existing techniques draw inspiration from near-field scanning optical microscopy, with the near-field methods being used in conjunction with THz Time-Domain Spectroscopy (TDS). This Chapter presents a review on the existing THz near-field methods in the literature and introduces possible research directions.

3.1 Introduction

Terahertz imaging offers many attractive advantages over existing modalities in its ability to obtain spectroscopic information for chemical recognition. The spatial resolution of conventional THz images is limited by the wavelength of the THz radiation (300 μm at 1 THz) and is therefore in the submillimetre range. Such a spatial resolution is clearly too low for imaging samples such as biological cells (micron to sub-micron range) and micro-structures in semiconductor structures (sub-micron to nanometer range). The general motivation of increased resolution is to distinguish objects sub-wavelengths apart and to cater for a smaller sample size. The resolution of THz far-field imaging is in the sub-millimeter range.

Various well-known attempts have been made in the field of optical microscopy in an effort to improve the resolution. Examples of these include reducing the wavelength of the illuminating light, adopting a high refractive index material that is the principle behind immersion microscopy, and increasing the aperture angle of the microscope (Courjon and Bainier 1994). All of these, however, lead only to minor improvements. Near-field methods that involve the detection of the evanescent waves, also known as non-radiating fields, have been demonstrated widely in optical microscopy to break the diffraction barrier (Girard *et al.* 2000, De Serio *et al.* 2003).

In a similar fashion, various techniques have been proposed in the literature with the aim of breaking the diffraction limit for THz imaging. Methods for confining electromagnetic energy to sub-wavelength dimensions have been studied extensively in near-field microscopy and adapted to the THz regime. In particular, near-field probes such as tapered waveguide apertures and metallic tips have been used in conjunction with THz-TDS. Other approaches to electromagnetic energy confinement tightly focuses optical beams into THz radiation emitters to reduce the size of the THz source element. As evanescent waves are limited to sample surfaces, energy confinement is required to take place at near-field regions of sample surfaces. Pulsed THz near-field imaging is a rapid growing area and a review on the topic is presented in Yuan *et al.* (2004) and Withayachumnankul *et al.* (2007b). This Chapter extends the review with updates on emerging trends in this rapid area of THz research. The Chapter is organized as follows: Section 3.2 describes the principles behind microscopy and lays the

3.2 Principles of near-field microscopy

foundations for application to the THz regime. Section 3.3 presents a review on existing THz near-field methods, followed by an objective outlook of potential topics for investigation in this Thesis.

3.2 Principles of near-field microscopy

Evanescent waves are critical to near-field microscopy systems. Systems that capture the information contained in evanescent waves can overcome the diffraction limit and hence improve the resolution. The word evanescent comes from the Latin word *evanescere* that means “to vanish”. Evanescent waves can be described by the superposition of plane waves and are characterized by at least one imaginary component of the wave vector k leading to no propagation in that direction but rather an exponential decay. Evanescent waves do not occur in a homogeneous medium but are inevitably connected to the interaction of light with inhomogeneities (Wolf and Nieto-Vesperinas 1985). The simplest case of an inhomogeneity is a plane interface. According to the angular spectrum representation of optical fields (Novotny and Hecht 2006), evanescent waves oscillate with the high spatial frequencies in the plane transverse to the direction of propagation. The higher the spatial frequencies of an evanescent wave, the faster the field decay along the z -axis. The loss of these spatial frequencies leads to the diffraction limit and hence constrains the spatial resolution.

The central idea of near-field microscopy is therefore to retain the spatial frequencies associated with evanescent waves, thereby increasing the bandwidth of spatial frequencies. In principle, arbitrary resolution can be achieved provided that the bandwidth is infinite. As the evanescent waves are bound to sample surfaces, there is the necessity to transport the evanescent waves for far-field detection. Examples of the transportation methods include a sub-wavelength pinhole on a metal screen, tapered fibre or a metallic tip probe. The trade-off of having an evanescent wave transporting object close to the sample complicates the data analysis significantly, because the transporting object becomes part of the sample system. In addition, since the object cannot be moved into the sample, near-field imaging is bound to the sample surface. Derivations on transporting of information from near-field to far-field can be found in Novotny and Hecht (2006). Two major configurations exist for microscopy: near-field excitation and near-field detection. The former excites the sample with the generated evanescent waves for detection in the far-field. In contrast, the latter excites the

sample with far-field illumination and measures the scattered evanescent wave in the near-field region. The techniques in the subsequent section reviews and describes the application of these microscopy techniques with pulsed THz radiation.

3.3 Review of THz near-field imaging

In 2004, Yuan *et al.* (2004) published a review of near-field imaging techniques that encompasses the principle of operation of each method and the developments with the achieved spatial resolution are briefly discussed. The major challenges for each of the respective methods are also highlighted. Here we present a review on the techniques in the literature that can be broadly classified by means of electromagnetic energy confinement. These three groups are: aperture, tip and highly focused beam methods.

3.3.1 Aperture based techniques

One class of near-field imaging technique uses an aperture probe to achieve high spatial resolution. Ideally, a sub-wavelength hole is realized on an infinitely thin, metallic film (Levine and Schwinger 1948). The method is used in near-field optical microscopy, which historically is implemented as a small pierced hole in a sufficiently thin opaque screen. The hole, however, is required to be smaller than the wavelength of illuminating light. In addition, such an approach can not easily be fabricated and also increases the risk of contact with the object due to the large flat screen. An alternative solution proposed was a tapered probe with an aperture as small as 100 nm. The main drawback of such an approach is the low transmission of the light through the aperture (Courjon and Bainier 1994). In the illumination mode, the light scattered from the sample is measured through the sub-wavelength aperture placed in the near-field. Early work in THz near-field imaging adapted this approach to block out a small fraction of the THz radiation (Hunsche *et al.* 1998).

An early investigation to study the local properties of a semiconductor structure used tapered metallic waveguides as apertures using continuous wave THz radiation from a CO₂ laser (Keilmann 1995). The first demonstration of pulsed THz near-field imaging is presented in Hunsche *et al.* (1998), where an elliptical sub-wavelength aperture at the end of a tapered metal tip is used to achieve a spatial resolution approximately 50 μm at 1.36 THz or $\lambda/4$ in illumination mode. The 50 by 80 μm aperture is placed at the focal

3.3 Review of THz near-field imaging

point of the THz beam with the sample being placed in the aperture near-field. A PCA source is used to achieve a similar resolution by placing the sample in the near-field of the source (Brener *et al.* 1998). The PCA is also used in the operation of a collection or illumination mode probe, on a transparent substrate, with a metallic aperture to confine the generated THz radiation (Mitrofanov *et al.* 2000b), where a resolution of $60\ \mu\text{m}$ was achieved for 0.8 THz. With a higher refractive indexed material ($n_{\text{GaAs}} = 3.6$) protruding through the aperture in a pyramidal shape, the probe effectively shortens the wavelength. The probe in collector mode is demonstrated with a spatial resolution of approximately $40\ \mu\text{m}$ at 0.5 THz ($\lambda/15$) (Mitrofanov *et al.* 2000a) for a comparatively smaller spectrum and a resolution of $7\ \mu\text{m}$ with 0.5 THz pulses (Mitrofanov *et al.* 2001a) as shown in Figure 3.1. In this near-field method, the spatial resolution is no longer determined by the wavelength but by the aperture size. The major limitation to this method is the low throughput resulting from the sub-wavelength aperture. Much of the radiation is reflected at the aperture plane, thereby leading to a significant deterioration in the signal-to-noise ratio. For an elliptical aperture of 50 by $80\ \mu\text{m}$, a signal reduction factor of 130 is reported in Hunsche *et al.* (1998). Mitrofanov *et al.* (2001b) attempted to overcome this limitation by placing the detecting element in the near-field zone of the probe aperture. This however, is limited by the device technology. Small apertures are also affected by the metallic film thickness, which needs to be sufficiently thick to reduce the incident THz radiation from penetration that would otherwise lead to significant background transmission. Temporal and spectral content alteration of the transmitted THz pulses pose another limitation (Mitrofanov *et al.* 2001b), while the finite thickness of the aperture exhibits waveguide effects that strongly attenuate long wavelength components and makes their detection difficult. Such a method is also costly to realize in practice as it heavily relies on micro-fabrication. A confocal microscopy inspired technique utilises physical aperture in the form of small pinholes (diameter down to $1\ \mu\text{m}$) on thin copper foils (1 to $10\ \mu\text{m}$) as near-field probes (Mair *et al.* 2004), where highly monochromatic THz radiation is employed and continuously tuned to achieve bandwidth up to 1.5 THz with high spectral resolution as shown in Figure 3.2.

In an effort to address the problem of concentrating the incident THz wave into the sub-wavelength aperture and detecting weak THz evanescent field generated, Kawano and Ishibashi (2008) successfully demonstrated the integration of an aperture in an on-chip THz near-field detector in Figure 3.3 to achieve several microns resolution comparable to aperture size.

NOTE:
This figure is included on page 41 of the print copy of the thesis held in the University of Adelaide Library.

Figure 3.1. Collection mode probe. An example of the aperture-based technique is the collection mode probe presented by Mitrofanov *et al.* (2001a). The aperture is $5\ \mu\text{m}$ with a sample separation distance of approximately $2\ \mu\text{m}$. The probe achieved a resolution of $7\ \mu\text{m}$ with 0.5 THz pulses in the knife edge test. After Mitrofanov *et al.* (2001a).

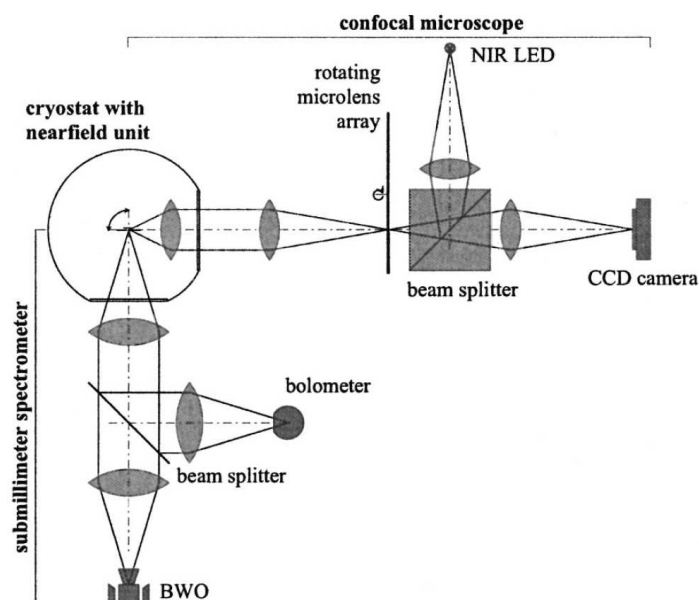


Figure 3.2. Confocal microscopy inspired setup. A confocal microscope inspired setup that uses physical small pinholes of diameter down to $1\ \mu\text{m}$ on 1 to $10\ \mu\text{m}$ thick copper foils as near-field probes. The setup generates continuous wave THz radiation by means of backward-wave oscillators (BWO) and scanned across the spectrum up to 1.5 THz with high spectral resolution. After Mair *et al.* (2004).

NOTE:
This figure is included on page 42 of the print copy of
the thesis held in the University of Adelaide Library.

Figure 3.3. On-chip THz near-field detector. The THz radiation detector is integrated with a sub-wavelength aperture in an on-chip setup to demonstrate several microns resolution and high sensitivity. After Kawano and Ishibashi (2008).

3.3.2 Tip based techniques

The tip based method draws inspiration from the work conducted using infrared radiation (Knoll and Keilmann 1999, Hillenbrand *et al.* 2002) and Scanning Near-field Optical Microscopy (SNOM) (Zenhausern *et al.* 1995). In this setup, a very sharp solid metallic tip at the end of a metallic probe is placed near the sample surface illuminated by a far-field THz beam and is mechanically dithered. The metallic tip interacts and scatters the evanescent THz field in the near-field region of the sample surface for remote detection. A lock-in amplifier is then used to measure the THz field at the probe oscillation frequency. The area of interaction is determined by the size of the tip, which hence determines the spatial resolution.

The first THz tip based method was demonstrated by van der Valk and Planken (2002) with a resolution of approximately $18 \mu\text{m}$ at 0.15 THz or $\lambda/110$ as shown in Figure 3.4. In the setup, THz pulses are focused onto a sharpened copper tip placed a few microns away from a GaP detection crystal. Through the electro-optic effect, the polarization (linear to elliptical) of the synchronised probe pulse, which is focused oppositely onto the crystal, is changed by the THz electric field from the tip. The amount of ellipticity in the probe polarization is proportional to the instantaneous THz electric field, which is measured by a differential detector. In contrast to the conventional usage of a $\langle 110 \rangle$ oriented crystal for electro-optic detection, a $\langle 100 \rangle$ oriented crystal is used instead to

account for the perpendicular THz electric field from the tip. The probe polarization is hence modulated by the electric field that is perpendicular to the crystal surface instead of the parallel incident THz polarization.

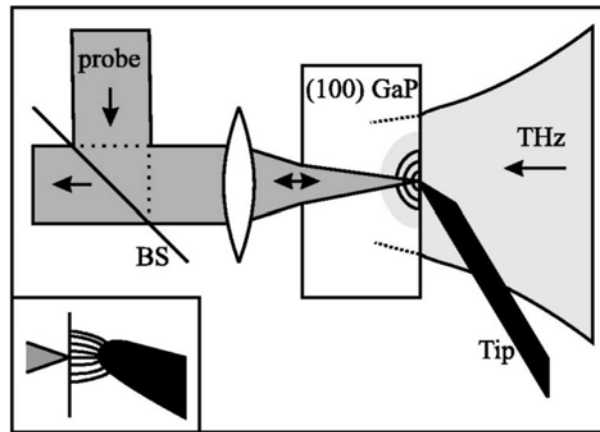


Figure 3.4. Tip with electro-optic detection. A tip based method with electro-optic detection achieved a resolution of $18 \mu\text{m}$ (van der Valk and Planken 2002). This technique places the sample in close proximity to the detector (electro-optic or semi conducting medium). A synchronized probe pulse is focused into the crystal and the polarization is changed by the electro-optic effect at the tip, and reflects back for detection. After van der Valk and Planken (2002).

Another THz tip based method similar to a SNOM setup is presented in Wang *et al.* (2003). The setup uses a vibrating copper tip (head diameter $5 \mu\text{m}$) placed in the near-field of the sample surface that is illuminated by a THz beam from PCA source. The scattered THz radiation is detected near the sample surface using a photoconductive dipole antenna (Wang *et al.* 2003, Yuan *et al.* 2004). A similar adaptation of the SNOM setup is presented in Chen *et al.* (2003) as shown in Figure 3.5, where a resolution of 150 nm for 2 THz pulses or $\lambda/1000$ is achieved. A THz beam is focused to a $500 \mu\text{m}$ spot size on a semi-insulating silicon substrate surface lined with $10 \mu\text{m}$ wide metallic stripes. A sharpened tungsten tip is placed about 200 nm above the sample surface with a radius of 100 nm . The transmitted radiation is measured by electro-optic sampling. A similar setup that implements atomic force microscopy in conjunction with THz-TDS is presented in Hillenbrand and Keilmann (2002) where a resolution of 10 nm is reported. Recent reports on probing the edge between GaAs and Au achieved a lateral resolution of 80 nm (Park *et al.* 2006). Instead of illuminating the sample with the generated THz radiation, Yuan *et al.* (2005) achieved a sub 100 nm spatial resolution

3.3 Review of THz near-field imaging

by modulating a metal tip in close contact (<100 nm) or in contact with a semiconductor surface in a weakly focused pump light spot. The purpose of the tip is to modulate the emitted THz pulses for subsequent electro-optical sampling in the far-field. The method, however, works only for a semiconductor sample to generate THz radiation.

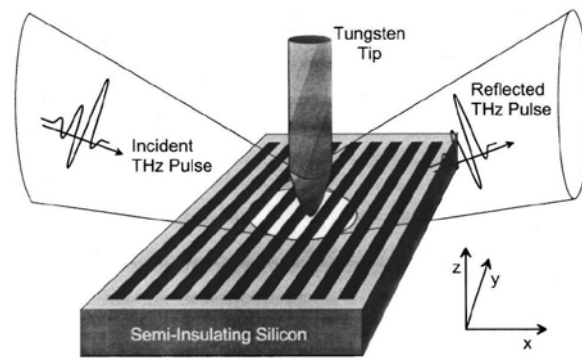


Figure 3.5. A tip based method by Chen *et al.* (2003). Chen *et al.* (2003) achieved a resolution of $10\ \mu\text{m}$. The tip has a radius of $100\ \text{nm}$ placed $200\ \text{nm}$ above the sample surface and the transmitted THz radiation is detected by electro-optical sampling or a bolometer. After Chen *et al.* (2003).

A nanoscale resolution of $40\ \text{nm}$ is demonstrated in Huber *et al.* (2008) along with the simultaneous recognition of materials and mobile carriers in a nanodevice. The setup in Figure 3.6 employs a continuous wave THz laser at $2.54\ \text{THz}$ to illuminate a cantilevered atomic force microscopic tip for backscatter THz radiation detection. Also using a cantilevered tip, von Ribbeck *et al.* (2008) also demonstrated a similar setup in Figure 3.7 illumination mode with asynchronous optical sampling to optimise the direct scattering spectrum. A complete description of the tip approach for semiconductor characterisation is presented in Kersting *et al.* (2008). The recent development of integrated tapered tip with a PCA detector (Wächter *et al.* 2009) has provided a means for commercial of the shelf THz near-field detectors. A resolution of $10\ \mu\text{m}$ is achieved and a bandwidth of $2\ \text{THz}$.

The development of a low-loss dielectric material waveguide with a partial metalized sharpened pyramidal tip has been proposed to demonstrate a resolution of about $20\ \mu\text{m}$ at $80\ \text{GHz}$ or $\lambda/200$ (Klein *et al.* 2005). This alternative arrangement, which does not illuminate the tip with THz radiation, operates in close contact with the sample in both illumination and collection modes and does not involve evanescent waves shown in Figure 3.9. The micron-sized plane facet at the end of the pyramidal tip confines the

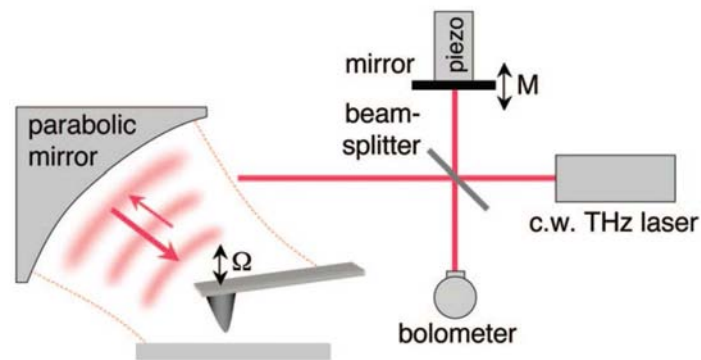


Figure 3.6. Atomic force microscopic tip. A cantilevered atomic force microscopic tip is used as the local element source in imaging a nanodevice. The tip is illuminated by a continuous wave THz laser at 2.54 THz and weak backscatter radiation is detected by means of a bolometer. The setup achieved a resolution of 40 nm. After Huber *et al.* (2008).

NOTE:

This figure is included on page 45 of the print copy of the thesis held in the University of Adelaide Library.

Figure 3.7. Scattering-SNOM inspired setup. Terahertz radiation is generated from a GaAs emitter. A cantilevered tip is used in the a THz setup operating in illumination mode with asynchronous optical sampling for optimising scattered spectrum. The paraboloidal mirror m is used for focusing the THz beam as well as collimating the side-scattered THz radiation. After von Ribbeck *et al.* (2008).

THz wave onto a sub-wavelength spot and the reflected signal is detected by electro-optic sampling at the other end. The work has been applied for the spectroscopy of dielectric materials (Berta *et al.* 2006).

The tip based near-field approach shows a great promise in high-resolution surface topographic and THz spectral imaging. However, it is complicated with the introduction of a near-field tip and low output power in the presence of large background signal. Furthermore, some of the presented techniques are only valid for semiconductor samples. The work presented in Chen *et al.* (2003) demonstrate the need to further refine the existing spherical scatter model for the imaging tip (Knoll and Keilmann 1999)

3.3 Review of THz near-field imaging

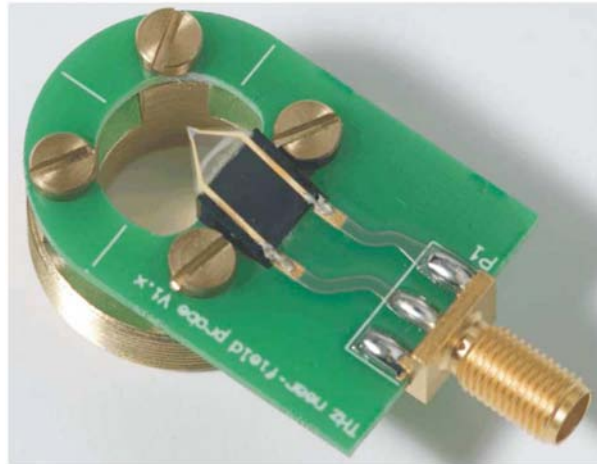


Figure 3.8. Tapered PCA probe. The probe is based on a $1.3 \mu\text{m}$ thick triangular shaped patch of LT-GaAs substrate with a pair of tapered metallic wires on top. A resolution of $10 \mu\text{m}$ is achieved and a bandwidth of 2 THz. After Wächter *et al.* (2009).

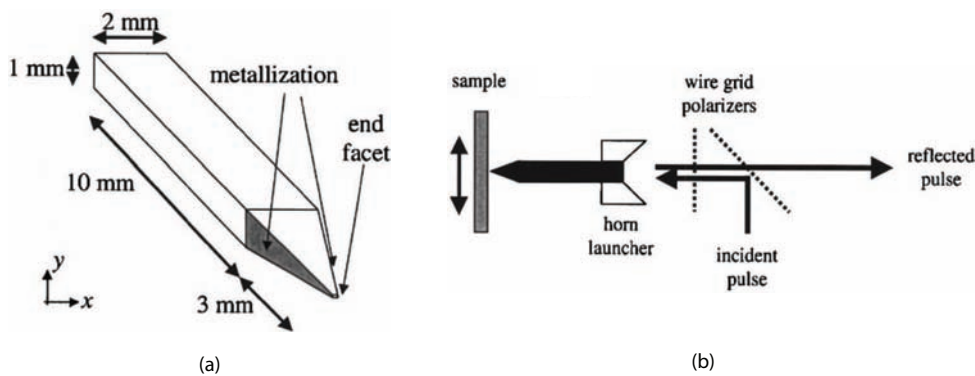


Figure 3.9. Low-loss dielectric waveguide. (a) The low-loss dielectric waveguide with a pyramidal tip achieved a promising resolution of $20 \mu\text{m}$ at 80 GHz (Klein *et al.* 2005). (b) The waveguide operates in contact with the sample. Terahertz pulses are coupled onto the waveguide by the horn launcher and the reflected pulses are detected using electro-optic sampling. After Klein *et al.* (2005).

and the inclusion of antenna properties for the probe (Wang *et al.* 2004a, Wang *et al.* 2004b). An investigation on THz wave guiding on metal wires can be found in Wang and Mittleman (2004). Finite Integration Technique (FIT) simulators such as Computer Simulation Technology (CST) Microwave Studio that operates in time domain and Finite Element Method (FEM) software such as Ansoft Inc. High Frequency Structural Simulator (HFSS) have been used to simulate the tip-sample interaction (Lee *et al.* 2006,

Lee *et al.* 2007) where the tip is modeled as a spherical particle. Scattering of electromagnetic radiation by a sub-wavelength object with irregular shape can be solved by Mie's scattering solution.

3.3.3 Highly focused beam techniques

An alternative near-field imaging technique achieves sub-wavelength resolution by exploiting a sub-wavelength THz emission or detection point induced from high optical focusing. Pulsed THz radiation is generated by exciting either a semiconductor or nonlinear crystal with ultrafast laser beams at near-IR range. With the near-IR radiation having shorter wavelength than THz radiation, it becomes possible to have an excitation spot size much smaller than the generated THz wavelengths. An example of this approach, on semiconductor samples, is the laser THz emission microscope (LTEM) (Kiwa *et al.* 2003) that achieves a resolution below $3\ \mu\text{m}$ (Yamashita *et al.* 2004, Yamashita *et al.* 2005) for inspecting electrical faults in integrated circuits and studying ferroelectric and superconductors (Murakami and Tonouchi 2008). Instead of the tip, a laser pulse is focused to a spot size of about $2.5\ \mu\text{m}$ (Yamashita *et al.* 2004), with the backscattered THz radiation collimated and focused for detection by a bow-tie antenna. The resolution is further improved to less than $1.5\ \mu\text{m}$ by combining the objective lens with a hemispherical solid immersion lens (Kim *et al.* 2008) as shown in Figure 3.10. The recent addition of a galvano mirror to reduce the image acquisition time through raster scanning and the ability to obtain the sample laser image is a significant step toward industry application (Tonouchi *et al.* 2011) in Figure 3.11.

In an inverse fashion, a dynamic aperture is used as shown in Figure 3.12. The technique is motivated by the work in Palanker *et al.* (1998) in the mid-IR frequency range. An optical beam that is synchronised with the pump and probe beams, is focused at the centre of the THz beam spot, which is focused on a semiconductor wafer. The optical beam is used to generate photo-carriers on the wafer, which blocks out a sub- μm cross section of the THz beam, thus creating a dynamic inverse aperture (Chen *et al.* 2000). Modulating the optical beam, by means of an optical chopper, modulates the transmitted THz beam through the dynamic aperture, which is then picked up by a lock-in amplifier. The spatial resolution of this method is determined by the spot size of the

NOTE:
This figure is included on page 48 of the print copy of
the thesis held in the University of Adelaide Library.

Figure 3.10. This diagram shows the schematic of the LTEM system operating in the transmission mode. As shown in the inset, a solid immersion lens on the sample surface to further improve optical confinement. After (Kim *et al.* 2008).

optical beam and a resolution of approximately $50 \mu\text{m}$ at 0.9 THz has been demonstrated (Chen and Zhang 2001). The drawback of this method is low throughput and the need for preparation of samples with semiconductors (Yuan *et al.* 2004).

Another example is the generation of THz radiation via optical rectification on non-linear crystals. In this approach, the THz source is dependent on the optical spot size in the electro-optical crystal. Compared to the aperture and tip method, which suffers from a power reduction of r^6/λ^4 with decreasing source dimension and hence an increasing spatial resolution (Bethe 1944), the electro-optical method has higher efficiency with the THz power decreasing proportionally to the second power of the source dimension (Xu and Zhang 2002). This effect leads to a greater power throughput and resolution. This approach bears similarity to the work presented for the infrared (IR) region (Palanker *et al.* 1998), where a point source of IR radiation is generated through the sample by focusing visible light pulses on a semiconductor with an IR beam. In the THz regime, sub-wavelength resolution is realized by placing the sample close to the emitter, so that the radiation does not diffract prior to interaction with the sample. Wynne and Jaroszynski (1999) tightly focused an optical beam to a small spot in an optical rectification crystal (ZnTe) for the generation of a sub-wavelength diameter THz beam in the near-field region. The achievable resolution would be $\lambda/4.3$ at 0.3 THz, provided the sample is placed on the crystal (Wynne and Jaroszynski 1999).

Yuan *et al.* (2002) focused a near-IR ultra-fast laser into a small spot with the aim of

NOTE:
This figure is included on page 49 of the print copy of
the thesis held in the University of Adelaide Library.

Figure 3.11. This diagram shows the schematic of the LTEM system operating with a galvano mirror to reduce raster scanning time. The reflected optical beam from the sample is acquired to obtain a sample laser image. After (Tonouchi *et al.* 2011).

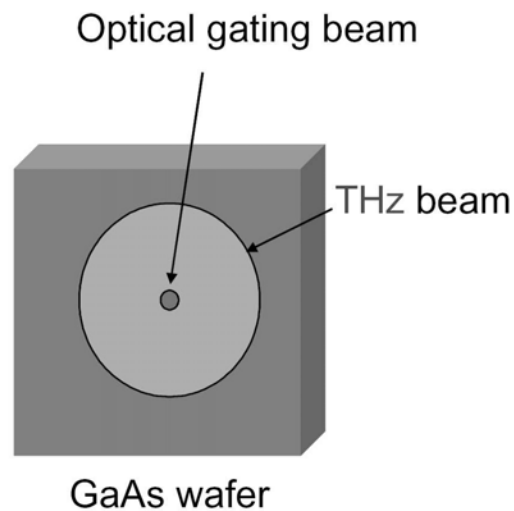


Figure 3.12. Dynamic Aperture. This diagram shows the optical gating beam and the THz beam. The optical beam blocks out a sub- μm cross section of the THz beam thus creating a dynamic inverse aperture (Chen *et al.* 2000). After Yuan *et al.* (2004).

3.3 Review of THz near-field imaging

generating THz signals of a spatial resolution close to the focus spot size. It is demonstrated in Yuan *et al.* (2002) that the generated THz signal at the focus point in a very thin crystal (16 μm) differs to the thicker counterpart (250 μm) as shown in Figure 3.13. Thin crystals generate a strong peak THz signal at the focal point as opposed to the thick crystal, which reduces the THz signal. The strong peak for the thin crystal is unexpected and is shown to be linearly dependent on the pump power, provided it is less than 15 mW. The intensity of the pump beam, however, is limited by the two photon damage threshold of the electro-optical crystal. A thickness in the order of tens of μm is essential to achieve a high resolution. This thickness in turn imposes physical constraints on experimentation and possible future application as thin crystals are thermally and mechanically fragile. A spatial resolution of 20 μm is reported in Yuan *et al.* (2004).

NOTE:

This figure is included on page 50 of the print copy of the thesis held in the University of Adelaide Library.

Figure 3.13. Peak electric field with different crystal thickness. Experimental result from Yuan *et al.* (2002). A thin crystal lead to an unexpected enhancement in the emitted THz power compared to the thick crystal at the focal point of the objective lens. Outside the focal point however, the emitted THz signal of both crystals appear to be constant with the thick crystal being greater than the thin crystal. After Yuan *et al.* (2002).

Similar work is presented in Lecaque *et al.* (2006) and Lecaque *et al.* (2008) shown in Figure 3.15), where a 500 μm thick crystal is used for demonstrating a resolution of approximately 75 μm and 30 μm respectively at 1 THz on imaging a sharpened tungsten wire. The resolution is reported to be equal to the pump beam focused size.

Recent investigation of the focused beam technique has also seen an integration into the detector chip directly. In the work by Adam *et al.* (2008), the detector consists of a GaP electro-optical crystal deposited with a 200 nm thick gold film used to investigate physical sub-wavelength apertures. The resolution achieved is 10 μm . The measured

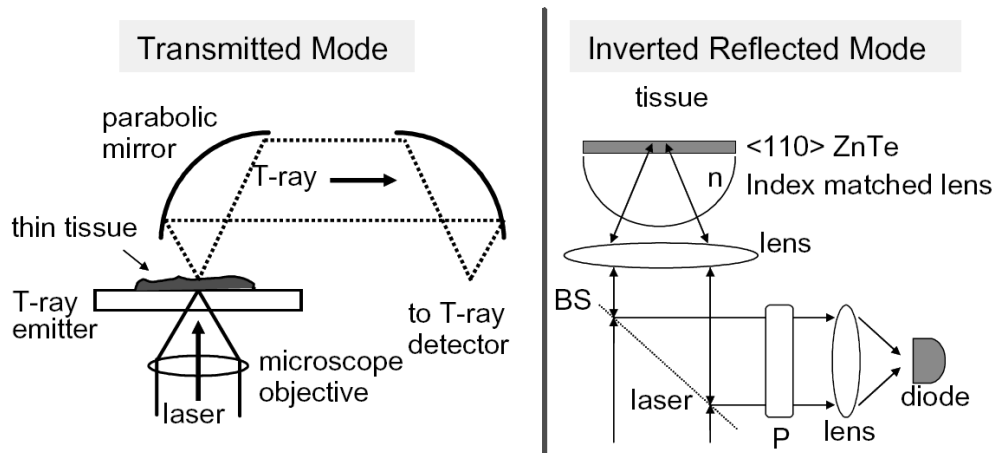


Figure 3.14. Electro-optic THz microscope schematics. This diagram shows the schematics of the electro-optic THz microscope in transmission and reflection mode respectively. After Yuan *et al.* (2004).

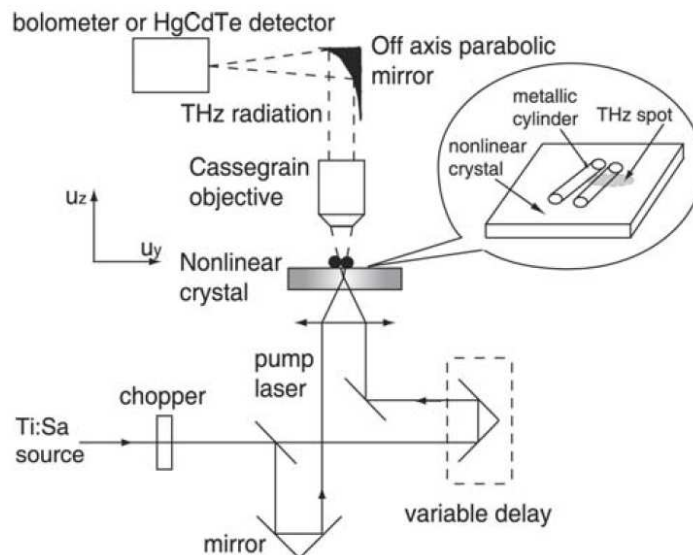


Figure 3.15. Electro-optic experimental setup in Lecaque *et al.* (2006). The electro-optic experimental setup that achieved $75\ \mu\text{m}$ resolution with a $500\ \mu\text{m}$ thick ZnTe. After Lecaque *et al.* (2006).

3.3 Review of THz near-field imaging

spatial distribution is compared with the analytical Bouwkamp model (Bouwkamp 1950b, Bouwkamp 1950a) and Finite-Difference Time-Domain (FDTD) calculations. Using the same GaP detection crystal, the work is extended to study rectangular apertures in Park *et al.* (2009) and aperture arrays for THz vectorial near-field vectorial imaging (Knab *et al.* 2009). The THz transmission properties through a single slit in a thin metallic film is studied in Lee *et al.* (2009). Similarly, Bitzer and Walther (2008) investigated metallic microstructures placed on a SOS PCA detector chip (Bitzer *et al.* 2010) that bears similarity to the work in Brener *et al.* (1998). In this work, the detector chip is translated together with the probe laser for gating in x , y , z direction relative to the stationary sample, with the probe spot size dictating the system resolution of $20\ \mu\text{m}$.

NOTE:

This figure is included on page 52 of the print copy of the thesis held in the University of Adelaide Library.

Figure 3.16. Integrated GaP crystal. Terahertz electric near-field measurements of sub-wavelength metallic apertures are investigated to compare with the well-known Bouwkamp model (Bouwkamp 1950b, Bouwkamp 1950a). In the figure, the electric field of a THz pulse is incident on the aperture with the local electrical field measured using a synchronised probe laser. The use of a highly reflective combination of a Germanium and a SiO_2 layer prevents probe reflection of the gold layer. A resolution of $10\ \mu\text{m}$ is achieved with a highly focused probe beam. After Adam *et al.* (2008).

A recent development of a THz chemical microscope has unveiled the potential for label-free detection of a protein complex. In this approach, THz radiation is generated from Si thin film and is reflected of the biotin-avidin complex in contact with the SiO_2 as shown in Figure 3.18.

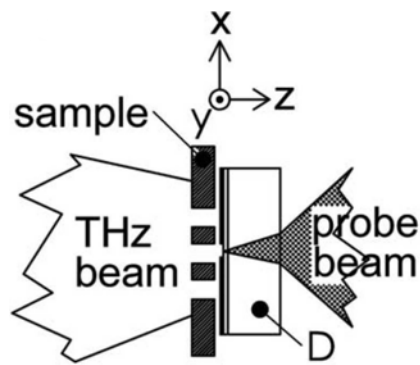


Figure 3.17. Metallic metal microstructures with SOS PCA detector. A SOS PCA detector is used to study metallic sub-wavelength apertures of various arrangements. The detector chip along with the probe laser beam is translated for imaging in reference to the stationary sample. The $20\ \mu\text{m}$ achieved resolution depends on the probe beam spot size and the PCA gap. After Bitzer and Walther (2008).

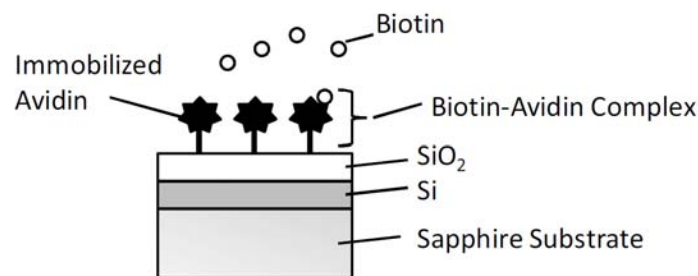


Figure 3.18. Terahertz chemical microscope setup in Kiwa et al. (2010). The THz chemical microscope that demonstrated the detection of biotin-avidin protein complex. Terahertz radiation is generated with an ultrafast optical beam through the sapphire substrate in the 150 nm Si film. With the protein complex mounted on the 275 nm thick SiO₂, the reflected THz radiation is measured by means of a bow-tie type PCA. The spatial resolution of this approach is dependent on the optical spot size. After Kiwa *et al.* (2010).

3.4 Chapter summary

This Chapter has reviewed pulsed THz near-field techniques in the literature, and categorised them into three main classes namely aperture, tip and focused beam based techniques. Even though the tip based method achieves the highest spatial resolution to date, the radiation throughput suffers from a reduction of r^6/λ^4 with a decreasing source dimension. This therefore places a limitation on its practical applicability. In addition, the tip complicates the identification of the near-field components from the incident background THz radiation. Contrary to the aperture and tip based methods,

3.4 Chapter summary

the electro-optical approach with the highly focused beam technique is the more efficient alternative that has received less attention but becoming increasingly attractive lately. The electro-optical method also offers the additional advantage of waveform dependency on the sample topography (Yuan *et al.* 2004, Lecaque *et al.* 2006, Lecaque *et al.* 2008). With a noticeable difference between the achievable resolutions between tip and focused beam techniques, the tip approach promises to find applications particularly with semiconductor and nanodevice imaging (Huber *et al.* 2008). More research on the other hand, are necessary for the the electro-optical approach with the highly focused beam technique. In particular, the unexpected power enhancement from thin crystals needs to be replicated and understood. Other potential areas of research revolve around the development of dielectric antennas (Klein *et al.* 2005) within the research group for spectroscopic purposes. Motivated by the focused beam approach and the THz chemical microscope (Kiwa *et al.* 2010) where the sample is attached to the emitter, the possibility of attaching the sample to PCAs (Brener *et al.* 1998, Bitzer *et al.* 2010) also looms as potential areas of exploration. This body of investigation with SOS PCAs is conducted in Appendix B. Building upon the understanding of state-of-art THz near-field imaging systems and principles of operation, we now investigate the focused beam approach in the far-field in the next Chapter.



Far-Field Modelling of Focused THz Radiation Generation

THE THz emission point on a nonlinear electro-optical crystal for generating broadband THz radiation is modeled as a radiating Gaussian aperture. With the wavelengths of the infrared pump beam being much smaller than the wavelength components of the generated THz pulse, a THz sub-wavelength radiating aperture with Gaussian profile is effectively created. This Chapter investigates Gaussian apertures in focused THz radiation generation in electro-optical crystals and illustrates the breakdown of the paraxial approximation at low THz frequencies. The findings show that the shape of the radiation pattern causes a reduction in detectable THz radiation and hence contributes significantly to low signal-to-noise ratio in THz radiation generation. Whilst we have demonstrated the findings on optical rectification in this work, the model may apply without a loss of generality to other types of apertures sources in THz radiation generation. With prolonged intense exposure of an optical beam on the ZnTe crystal, the problem of crystal photodamage becomes increasingly relevant. This work also investigates the heating effects with a reduced power density through simulations.

4.1 Introduction

A sub-wavelength THz source is employed in the focused beam near-field imaging technique to obtain sub-wavelength spatial resolution. Investigations in the near-field regime is, however, complex with a sub-wavelength operating distance and the presence of evanescent waves. Prior to understanding the comparatively complicated near-field region, it is therefore essential to develop a critical insight into the far-field first. This Chapter conducts far-field investigations of a sub-wavelength source using aperture modelling methodology, commonly applied at microwave frequencies.

Photoconduction (Mourou *et al.* 1981, Fattinger and Grischkowsky 1988) and optical rectification are two of the most common approaches for generating broadband, pulsed THz radiation. Details of the generation mechanisms can be found in Chapter 2. Practical advice in THz radiation generation by means of optical rectification with electro-optical crystal can be found in Rice *et al.* (1994) and Chen and Zhang (1999). In our setup, the primary IR pump beam has a beam waist of approximately 1 mm, therefore some degree of optical focusing is necessary for achieving a smaller spot size and a higher generated THz Signal-to-Noise Ratio (SNR). Focusing is also especially required in the case of electro-optical based THz near-field imaging where a small point source with a radial dimension of only a few microns is desired as detailed in Chapter 3.

The Gaussian beam is a solution to the paraxial wave equation and is characterised by Gaussian intensity distribution in any plane transverse to the direction of propagation (Saleh and Teich 1991). This is illustrated in Figure 4.1. The minimum beam waist w_0 for focusing a Gaussian beam of wavelength λ , lens effective focal length f , and beam waist w can be found as

$$w_0 = \frac{\lambda f}{\pi w}. \quad (4.1)$$

The depth of focus of the Gaussian beam in Figure 4.2 shows that the beam has minimum beam waist or radius w_0 , from which the beam gradually grows out of focus in either direction. The Rayleigh range z_R is the distance along the z -axis from minimum beam waist to $\sqrt{2}w_0$ and is expressed as

4.1 Introduction

$$z_R = \frac{\pi w_0^2}{\lambda}. \quad (4.2)$$

In general, the dependence of the beam radius on z is determined by

$$w(z) = w_0 \sqrt{1 + \left(\frac{z}{z_R}\right)^2}. \quad (4.3)$$

For $z \gg z_R$, a linear relation can be summarised as

$$w(z) \approx \frac{w_0}{z_R} z = \theta z. \quad (4.4)$$

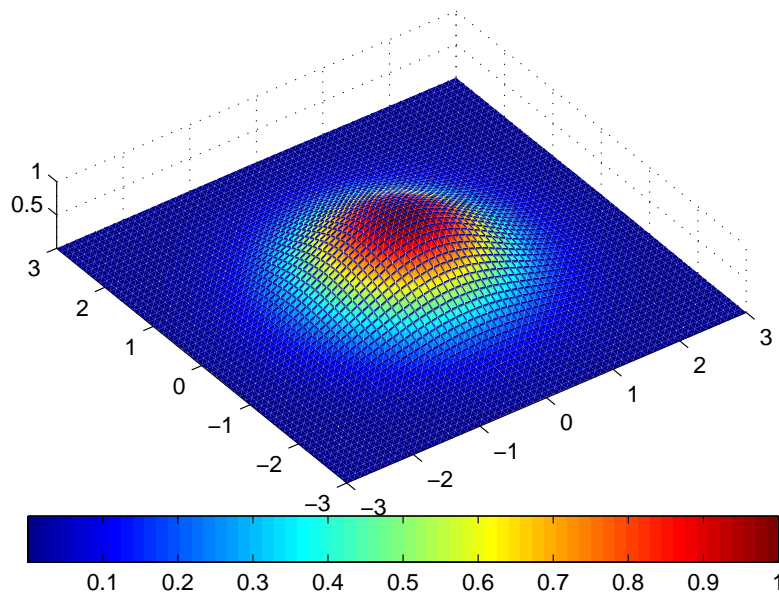


Figure 4.1. True Gaussian beam. A computer simulation showing the theoretical transverse field distribution of a true Gaussian beam that is characterised by a Gaussian intensity distribution in any plane transverse to the direction of propagation. The axes are in arbitrary units, with the relative magnitude shown by the colour contours.

The paraxial approximation is valid for a beam waist w_0 larger than 0.91λ a divergence angle $\theta_0 < 20^\circ$. As extreme illustration on how the paraxial approximation breaks

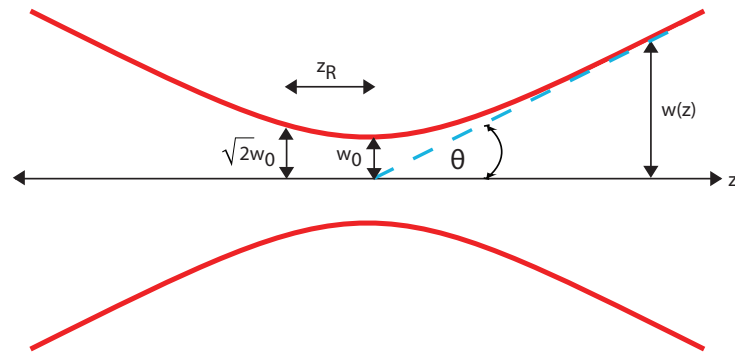


Figure 4.2. Gaussian beam depth of focus. The depth of focus of a Gaussian beam with the minimum beam waist w_0 , Rayleigh range z_R , beam divergence angle θ and beam waist $w(z)$ are annotated.

down, the following case can be considered. For $w_0 < \lambda/5$, the divergence angle becomes unphysical $\theta_0 \rightarrow 90^\circ$, the radiation pattern, obtained from transforming the planar distribution into spherical angular distribution, converges to the well-known obliquity factor pattern (Orfanidis 2008),

$$A_{\text{obl}}(\theta) = \frac{(1 + \cos \theta)}{2}. \quad (4.5)$$

A computational illustration of the transition from paraxial approximation to the obliquity factor with decreasing beam waist can be found in Fumeaux *et al.* (2009). With the THz wavelengths (100 μm to 3 mm) being orders of magnitude longer than wavelengths in the optical regime (centered around 800 nm), the breakdown of paraxial theory for THz beams generated from electro-optical crystals pumped by an optical beam becomes increasingly relevant. The dependence of THz radiation on optical excitation size was first studied in a GaAs emitter (500 μm thick) (Xu and Zhang 2002) where a dependence of the total THz radiation power on the square of the excitation size was observed. This has been further investigated in Dakovski *et al.* (2005) and it was concluded that for excitation waists smaller than the THz wavelength, THz emission is largely excitation size independent. This last work has been extended for lower pump power in Xing *et al.* (2006). A higher-order nonlinear process such as two photon absorption is often attributed as the cause behind a reduction in THz radiation throughput in localised THz radiation generation. This Chapter will consider the problem from a radiating aperture theory perspective, as commonly applied at microwave frequencies. As we will see from the developed numerical model, which has been validated by experimental data, another possible cause in the reduction of power in the lower THz frequency range is that the radiation pattern from the generation crystal

4.2 Experiment

is no longer confined to the direction of propagation but rather diffracted widely and dispersed around the crystal leading to a reduction in measurable THz power. The computational model can easily be generalised to work for any optical excitation sizes, distance, and acceptance angle.

4.2 Experiment

The hybrid EO PCA THz setup, as shown in Figure 2.3.3, is used in our experiment. Average pump power of 30 mW is used for THz radiation generation with a 1 mm thick $\langle 110 \rangle$ ZnTe crystal from Zomega Terahertz Corporation. The detector is a custom H structure on a LT-GaAs substrate manufactured at the University of Freiburg, Germany. The existing LabVIEW code is adapted to automate one axis (x -axis) scanning. Appendix A.1.2 shows the flowchart for the improved LabVIEW algorithm. A 3-axis linear translation stage fitted with linear and μm resolution actuators is installed in the vicinity of the crystal surface. This is effectively used for conducting a knife-edge experiment. Details on the equipment used is elaborated in Appendix A.

4.2.1 Pinhole

In order to demonstrate the failing of the paraxial theory in the THz regime, a pinhole experiment is firstly conducted. The aim of the experiment is to map out the THz intensity distribution of varying wavelength against the pinhole position. Even though on the screen of observation, the projections will appear as nearly Gaussian for all wavelength, for the lower frequency hence longer wavelength, the Gaussian should be broader along the x -axis than for the higher frequency hence shorter wavelength as illustrated in Figure 4.3. A pinhole with a diameter of $220 \mu\text{m}$ is used in the experiment. The IR beam waist initially investigated with a 20 mm EFL lens gives rise to a minimum beam waist of $5 \mu\text{m}$ and a Rayleigh range of 0.1 mm for the 1 mm thick crystal. With the crystal thickness significantly larger than the Rayleigh range, precise estimation of the beam waist through computation is very inaccurate. The pinhole crystal distance is computed from Equation 4.6 to be 2mm with the worst scenario situation of smallest wavelength (highest frequency) and biggest IR beam waist.

Early results from the pinhole experiment show the expected Gaussian shape. However, due to the sub-wavelength nature of the pinhole, much of the THz transmitted

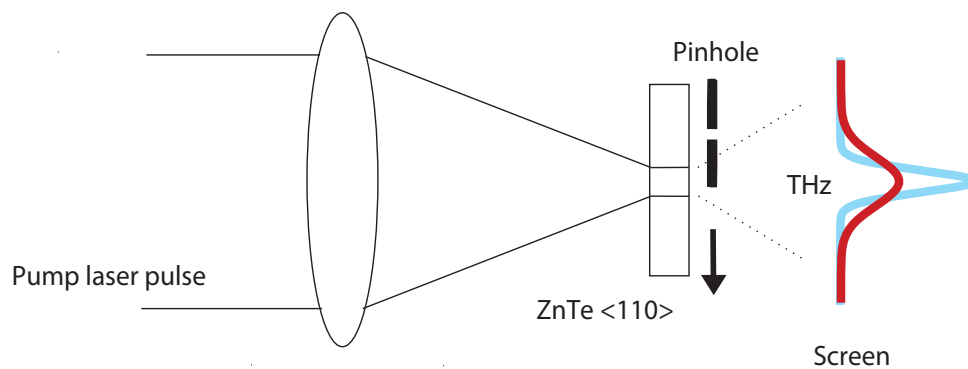


Figure 4.3. Pinhole experiment for observing obliquity factor and paraxial theory. A pump beam is focused into the crystal by means of a lens. The emitted THz radiation is divergent in nature due to a change in refractive index. By translating a small pinhole in the far field region of the crystal surface, we will be able to map out the THz response versus the position on the screen. It is anticipated that the blue curve will represent the projection of the obliquity factor while the red curve for the paraxial Gaussian beam.

signal is reflected leading to a low SNR. The pinhole experiment is thus discarded. It is also observed in this preliminary investigation that prolonged exposure of highly intensive IR on the crystal leads to a reduction in THz generated and hence THz radiation SNR. This is the subject of investigation in later sections.

4.2.2 Knife-edge profile

The knife-edge experiment is an alternative to the pinhole experiment that does not limit the transmitted THz radiation. The experiment is essentially identical to the pinhole setup except with the pinhole sample is replaced by a sharp knife blade. Compared to the pinhole experiment, the knife-edge is an integrated approach from $-\infty$ to ∞ on the y -axis. In essence, the knife-edge profile gives the THz spot size or beam diameter at the chopping position. A knife-edge profile measurement similar to Hattori *et al.* (2001) is conducted on the THz beam generated from the electro-optical crystal with the knife-edge cutting into the x -axis. A Sheffield steel razor blade is used as the knife-edge.

IR beam waist

To demonstrate the transition of the emitted THz radiation from the obliquity factor diffraction pattern at low frequencies (less than 300 GHz) to a paraxial Gaussian beam

4.2 Experiment

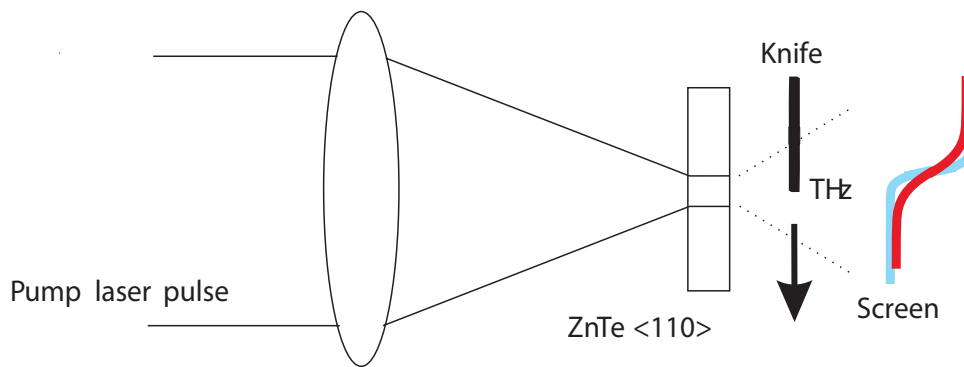


Figure 4.4. Knife-edge experiment for observing obliquity factor and paraxial theory. Like the pinhole experiment, a pump beam is focused into the crystal by means of a lens. The emitted THz radiation is sliced by translating a small sharp blade in the far field region of the crystal surface. By doing so, we will be able to map out the THz knife-edge profile.

at high frequencies (2.5 THz), careful selection of the IR pump laser beam waist is critical as it clearly defines the effective THz aperture size. An IR beam waist that is too small, is unlikely to show a difference between obliquity factor and paraxial theory. Furthermore, prolonged exposure leads to photodamage and hence a reduction in SNR. On the other hand, a pump beam with a large waist will result in a paraxial THz beam for all frequencies. An IR pump beam waist of more than $100\ \mu\text{m}$ is a good trade-off, as $100\ \mu\text{m}$ represents approximately 1.25λ at 2.5 THz, while being $\lambda/5$ at 0.4 THz. With a crystal thickness of 1 mm, we determine the IR beam waist through the crystal through computing the minimum beam waist via Equation 4.1, i.e. Gaussian beam approximation with the selected optical components. An alternative to computation is to conduct a knife-edge profile of the IR beam waist. With computation, however, the Rayleigh range should also be taken into consideration as we need to maintain approximately the same beam waist throughout the crystal. A further requirement for the optical lens is therefore that the Rayleigh range needs to be greater than the crystal thickness to ensure nearly constant beam waist through the crystal. Table 4.1 shows the two different optical lens used for this experiment. The coherence length of the IR pump beam and THz radiation generated can be found in Nahata *et al.* (1996). A longer focal length lens certainly eases optical alignment as there is a longer Rayleigh range. The focal length of the lens is, however, constrained by the physical path length of the setup. A comparatively bigger beam waist, would lessen the likelihood of photodamage. The heating effects of high and low power density is studied in Section 4.6.

Table 4.1. Lens selection. The lens parameters (Effective focal length f , IR beam waist w_0 and Rayleigh range z_R) along with their respective values are used in order to observe the effects in a knife-edge profile.

f (nm)	w_0 (μmm)	z_R (mm)
200	50.9	10
400	102	40.7

A 400 mm focal length optical lens is therefore used resulting in a theoretical IR pump beam waist of 102 μm and Rayleigh range of 41 mm. Taking consideration of beam divergence in crystal, the effective IR pump beam waist is expected to be slightly larger than the theoretical value.

Crystal to knife-edge distance

In the experiment, the knife-edge is placed in the far-field region from the crystal back surface. As the THz radiation generated is broadband, a worst-case scenario is used in determining the required Fraunhofer distance

$$d = \frac{2D^2}{\lambda}, \quad (4.6)$$

i.e. considering shortest THz wavelength. Here, D corresponds to the largest diameter of the radiator. For 2.7 THz, the required sample to crystal surface distance is computed to be 0.75 mm. In the actual experiment, this distance is measured with a Charge Coupled Device (CCD) camera placed with a bird's eye view of the system. Figure 4.5 shows before and after the knife obstructs the beam, respectively, in reference to the crystal surface.

Crystal parabolic distance

The THz radiation generated with electro-optical emission is divergent by nature. It is anticipated that when the paraxial theory fails and THz radiation pattern exhibits a diffraction pattern that approaches the obliquity factor, only a small angular distribution of THz radiation can be detected by the subsequent parabolic mirror. To increase the acceptance angle, the crystal is displaced closer to the parabolic mirror within the limitation of physical spacing constraint. By doing so, however, the crystal is no longer

4.2 Experiment

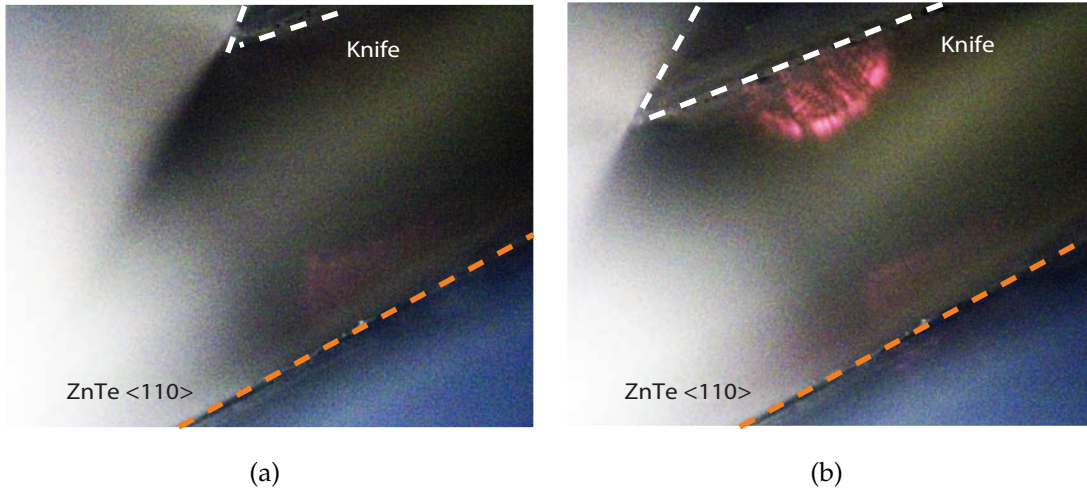


Figure 4.5. Bird's eye view of the knife crystal system with a CCD camera. (a) Knife-edge at the distance of 0.75 mm from the crystal surface that has not obstructed the THz beam. (b) Knife-edge has fully obstructed the THz beam. Reflection of the residual IR beam through the crystal is also obstructed by the knife.

in the focal length of the parabolic mirror, thereby leading to possible detection issues. Even though experimentally there is no significant difference after optimisation with the detector silicon lens, this is analytically investigated with paraxial theory. As shown in Figure 4.6, f_1 , f_2 , f_3 , f_4 and f_5 represent the distance between PCA detector and parabolic mirror M_4 , M_4 and M_3 , M_3 and M_2 , M_2 and M_1 , and M_1 and ZnTe emitter respectively. The ray transfer matrix for free-space propagation and parabolic mirror is shown as

$$M = \begin{bmatrix} 1 & d \\ 0 & 1 \end{bmatrix} \quad (4.7)$$

and

$$M = \begin{bmatrix} 1 & 0 \\ -\frac{1}{f} & 1 \end{bmatrix} \quad (4.8)$$

respectively, where d is the ray traversing distance and f is the focal length. For a cascade of optical components whose ray-transfer matrices are M_1 , M_2 , ..., M_N , it is equivalent to a single optical component with ray matrix in

$$M = M_N \dots M_2 M_1. \quad (4.9)$$

Applying Equation 4.7, 4.8 and 4.9, we obtain 4.10,

$$M = \begin{bmatrix} 1 & f_1 \\ 0 & 1 \end{bmatrix} \begin{bmatrix} 1 & 0 \\ -\frac{1}{f} & 1 \end{bmatrix} \begin{bmatrix} 1 & f_2 \\ 0 & 1 \end{bmatrix} \begin{bmatrix} 1 & 0 \\ -\frac{1}{f} & 1 \end{bmatrix} \begin{bmatrix} 1 & f_3 \\ 0 & 1 \end{bmatrix} \\ \begin{bmatrix} 1 & 0 \\ -\frac{1}{f} & 1 \end{bmatrix} \begin{bmatrix} 1 & f_4 \\ 0 & 1 \end{bmatrix} \begin{bmatrix} 1 & 0 \\ -\frac{1}{f} & 1 \end{bmatrix} \begin{bmatrix} 1 & f_5 \\ 0 & 1 \end{bmatrix} \quad (4.10)$$

with $f_3 = f_2 = 2f$ and $f_1 = f$, the effect of f_5 (i.e. the crystal parabolic mirror distance away from the focal length f) can be analysed. Equation 4.11 shows the equivalent single optical component ray matrix after algebraic simplification,

$$M = \begin{bmatrix} 1 & f_5 - f \\ 0 & 1 \end{bmatrix}. \quad (4.11)$$

The effect on the image at the output plane (y_2 and θ_2) can be determined by considering an arbitrary input beam at input position y_1 and angle θ_1 in Equation 4.12,

$$\begin{bmatrix} y_2 \\ \theta_2 \end{bmatrix} = \begin{bmatrix} 1 & f_5 - f \\ 0 & 1 \end{bmatrix} \begin{bmatrix} y_1 \\ \theta_1 \end{bmatrix} = \begin{bmatrix} y_1 + \theta_1 (f_5 - f) \\ \theta_1 \end{bmatrix}. \quad (4.12)$$

Note that the scaling factor θ_1 is used assuming paraxial approximation so that $\tan(\theta_1) \approx \theta_1$. Intuitively, this makes sense because when $f_5 = f$ i.e. the crystal is placed in the focal plane of the parabolic mirror, the image is identical to the source. With $f_5 \leq f$, the image position y_2 would be less than the source y_1 . Therefore to detect the image with the same position, the detector is required to move backwards under the same angle of propagation. The distance of translation is simply the distance that the crystal is moved away from the focal length as shown in Figure 4.7.

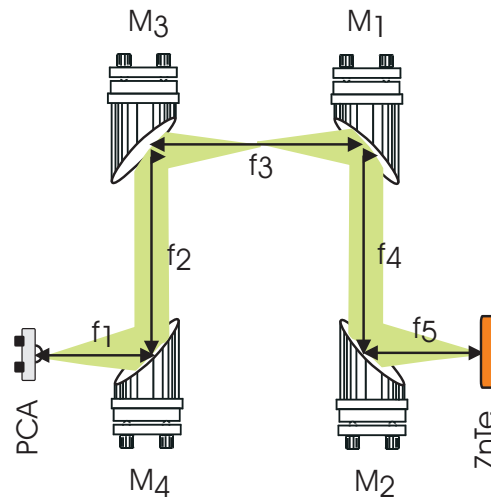


Figure 4.6. Parabolic mirrors placement. This diagram is shown to annotate the respective focal lengths of each parabolic mirror for understanding the varying the crystal parabolic distance. f_1 , f_2 , f_3 , f_4 and f_5 represent the distance between PCA detector and parabolic mirror M_4 , M_4 and M_3 , M_3 and M_2 , M_2 and M_1 , and M_1 and ZnTe emitter respectively.

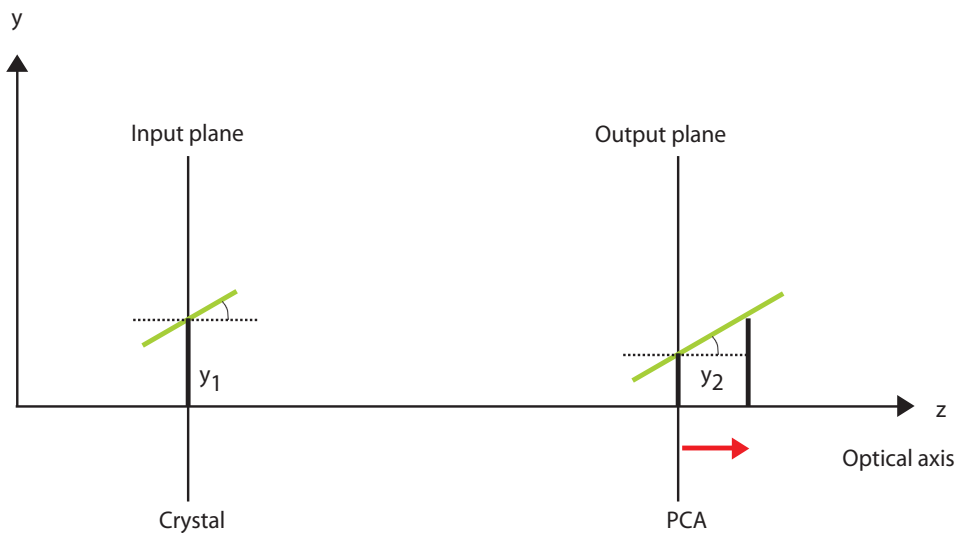


Figure 4.7. Effect of crystal parabolic distance on image formation. From ray optics, the diagram illustrates that if the crystal is at some distance away from the focus of the parabolic mirror, to achieve the same image height at the source y_1 as the at the output plane y_2 , the detector would need to be shifted back by the same distance.

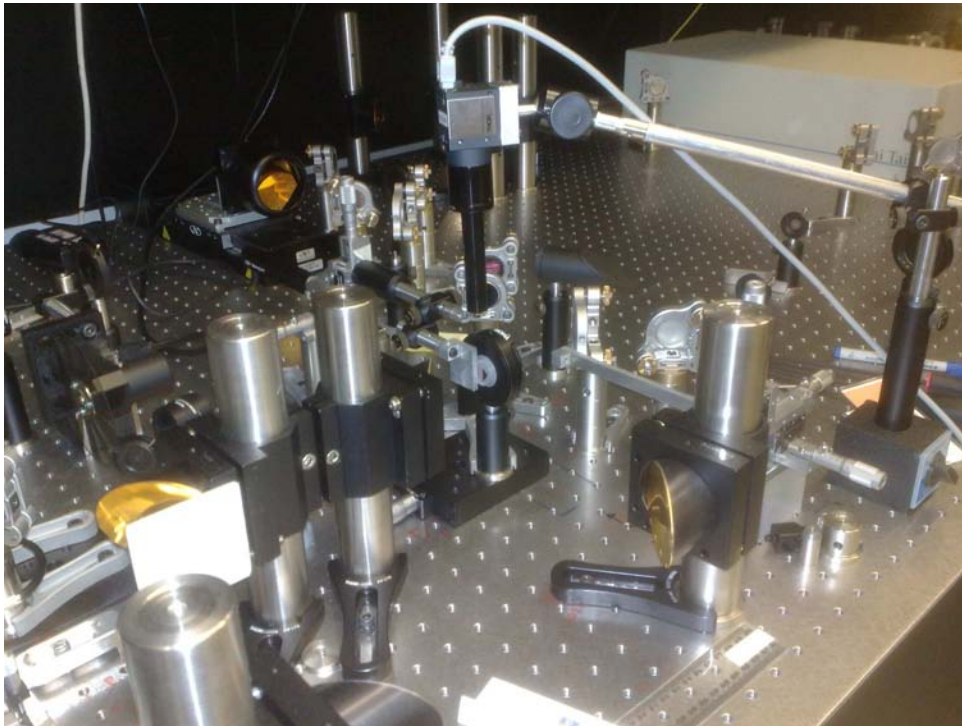


Figure 4.8. Experimental setup. Photograph of the experimental setup in this work. The overhanging CCD camera is able to measure the knife crystal distance at the bird's eye view as shown in Figure 4.5. A knife-edge is placed at a Fraunhofer distance away from the ZnTe crystal.

4.3 Numerical simulation

4.3.1 High frequency structural simulator

To gain a preliminary understanding of the far-field distribution of the radiation through an aperture, High Frequency Structural Simulator (HFSS) is used for 3-D visualisation. A model is developed in Figure 4.9 and simulated with varying frequency of radiation impinging on the aperture. The evolution of the far-field radiation distribution with increasing frequency of the incident radiation is shown in Figure 4.10. As can be observed, paraxial theory fails at low frequencies with the radiation dispersed in all direction around the aperture and the radiation pattern resembles to half doughnut shapes.

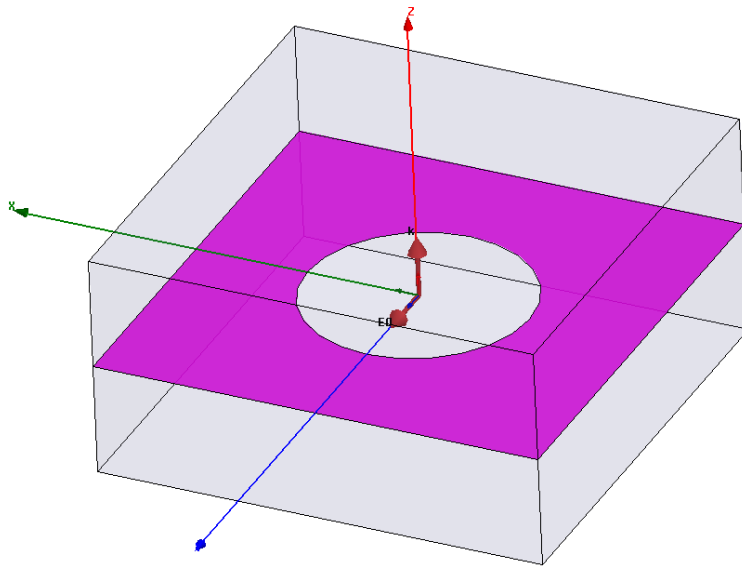


Figure 4.9. High Frequency Structural Simulator model. A perfect electric conductor with an aperture is encapsulated inside a radiation airbox. A plane wave shown by red arrows propagates along the positive z -axis with electric field oscillating along the y -axis. This model is developed to simulate qualitatively the far-field electric field distribution with a fixed aperture and varying incident radiation wavelength.

4.3.2 Beam modelling as radiation from a Gaussian aperture

The electro-optic THz beam generation in the ZnTe crystal is modeled as radiation from an aperture with a Gaussian intensity distribution corresponding to the waist of the IR pump beam. This is justified as THz radiation is coherently generated along the crystal with an IR pump beam with nearly constant beam waist. Figure 4.11 presents the framework for modelling. The model initiates with defining a circular area for computation that encloses the Gaussian aperture, but is sufficiently large as to not introduce numerical truncation effects during computation. The computation time, however, scales up quadratically with increasing radius.

4.3.3 Equivalent crossed-dipole model

The Gaussian aperture with the intensity distribution of the IR pump beam is applied to a circular THz source surface with normal vector $\hat{n}_s \equiv \hat{z}$ for computational implementation. This can be expressed as phasors for the incident electric and magnetic fields as follows,

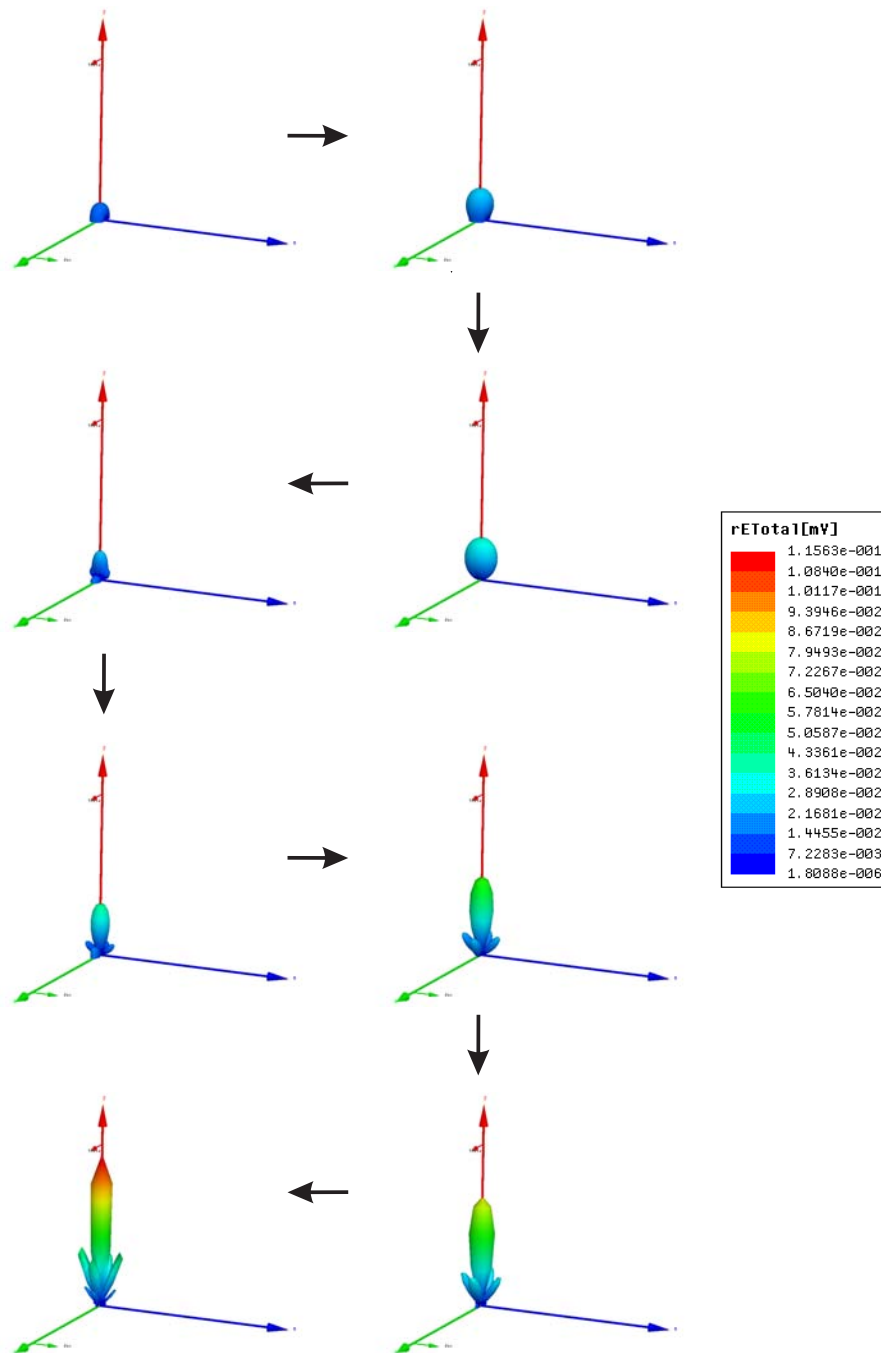


Figure 4.10. Far-field distribution of a plane wave through the aperture. The animation sequence starts from top left and finishes at bottom left, in the direction of the arrows, with varying frequency of the incident plane wave. A plane wave propagating along the z -axis with an oscillating electric field along the y -axis of 1 V/m. A 3-D polar plot of the electric field reveals that the far-field distribution evolves from a doughnut shaped pattern when aperture is very much smaller than the wavelength, and gradually becomes a paraxial Gaussian beam with increasing size. The colours indicate the transmitted electric field strength (rE) in mV.

4.3 Numerical simulation

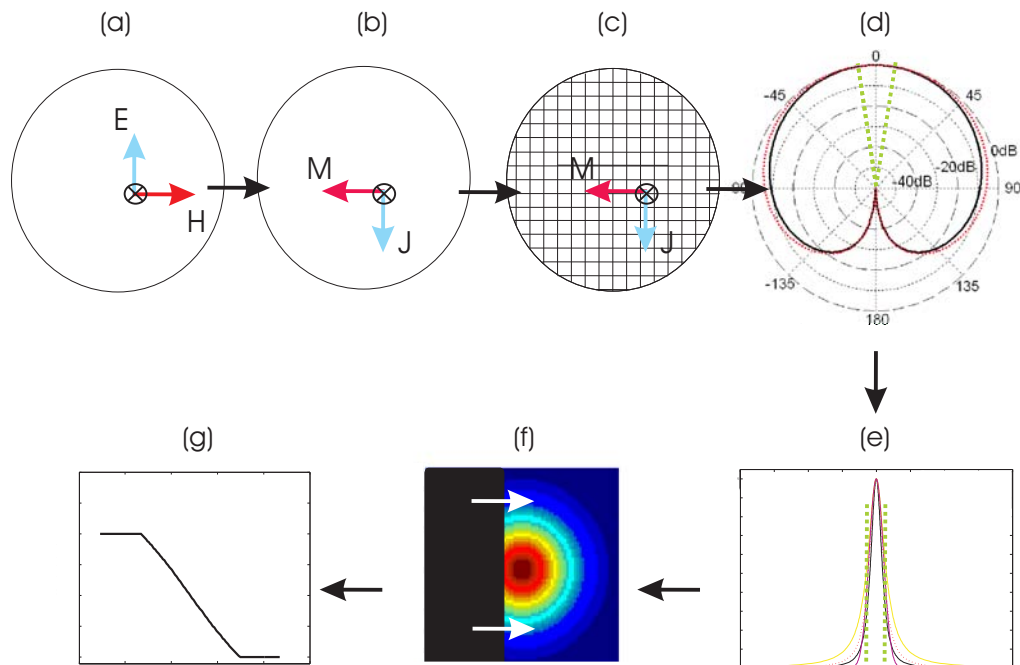


Figure 4.11. Gaussian aperture modeling methodology. Main steps to modelling are summarised, clockwise, as follows: (a) Model the THz radiation generation as an aperture with Gaussian intensity distribution and a beam waist identical to that of the IR pump beam. (b) Using the equivalence principle, introduce equivalent electric and magnetic sources in the source aperture. (c) Discretization of the aperture area in a grid. (d) Perform a near-field to far-field transformation, computing the radiation integrals on the basis of the discretized source distribution. (e) Project the far-field intensity distribution on a screen, taking into account the decay of intensity as a function of distance. Truncate the projection at the acceptance angle θ_{win} of the parabolic mirrors. This is highlighted by the green dashed lines. (f) Perform a numerical knife-edge measurement on the field intensity projected on the screen. (g) The resulting curve corresponds to the measured knife-edge intensity profile. It is noted that the sharp truncation of the acceptance angle neglects diffraction effects.

$$\begin{aligned}
E_{i,y} &= E_0 e^{-\frac{r^2}{w_0^2}} \\
H_{i,x} &= -\frac{E_{i,y}}{\eta_0},
\end{aligned} \tag{4.13}$$

where E_0 defines the pulse electric field amplitude, w_0 is the smallest pump beam waist (radius), r is the distance from the z -axis on the aperture and η_0 is free space impedance. The direction of propagation in this context is $+z$ leading to the negative sign for the magnetic field. With the field equivalence principle, the incident \vec{E}_i and \vec{H}_i field can be replaced with an equivalent problem comprising magnetic and electric current source densities, as classically defined in Balanis (1997), as follows,

$$\begin{aligned}
\vec{M}_S &= -\hat{n}_s \times \vec{E}_i \\
\vec{J}_S &= \hat{n}_s \times \vec{H}_i.
\end{aligned} \tag{4.14}$$

The elementary source element from the excitation aperture is therefore the superposition of two perpendicular infinitesimal magnetic and electric dipoles, both of which, are excited with the same power (Fumeaux *et al.* 2009).

4.3.4 Far-field pattern

The source area, i.e. the Gaussian aperture, is subsequently discretized on a grid in order to compute the radiation integrals (Balanis 1997) as the sum of the contributions from electric and magnetic current sources. The methodology and discrete implementation are described in detail as a frequency-domain near-to-far-field transformation in Taflove and Hagness (2005). The resulting radiation pattern is then projected on a far-field screen, which coincides with the plane where the knife-edge scan is performed. To take into account the path loss from the Gaussian aperture to the location on the screen, the projected pattern needs to be weighted by a $1/r^2$ pattern, which reflects the decay of intensity of a spherical wave with distance. Notice however, due to the nature of a THz-TDS detection setup, we are unable to map out the entire radiation pattern, i.e. $-90^\circ \leq \theta \leq 90^\circ$. Therefore the green dashed lines in Figure 4.11(d) indicate the measurable acceptance angle that translates into the screen indicated by dashed lines in Figure 4.11(e). In order to obtain the integrated power that is observed in the

4.4 Results and discussion

knife-edge experiment, a transformation from a Cartesian to a polar coordinate system is performed as the electric field and magnetic field of the source are rotationally symmetric. With the resulting 2D intensity distribution, it is cumulatively integrated across the columns. To mimic the knife-edge experiment, the model considers a sharp truncation of the measured intensity on the screen because of the limited acceptance angles. This neglects diffraction effects and explains the unphysical discontinuity of the modeled knife-edge curve. Adding a knife-edge diffraction model to the present model would solve this issue, but complicates the present considerations considerably. Our present aim is to gain physical insight via the simplified model, and this can then form the basis of future work for adding further sophistication.

4.4 Results and discussion

4.4.1 Experimental results

Fourier transforms of the acquired THz time-domain waveforms are computed and the amplitude at each extracted frequency is plotted against the position of the knife-edge. For the sake of simplicity, only the power spectrum at a certain knife-edge location and the knife-edge of selected frequency components in this study are shown in Figure 4.12 and Figure 4.13 respectively. As experiment is conducted in dry atmosphere, the frequency components are selected to avoid water vapour absorption and achieve high SNR. A running average over only one point has been used to preserve data integrity.

4.4.2 Model validation

To validate the developed computational beam model from a Gaussian aperture, the model is operated with estimated and measured experimental parameter values such as the (i) IR pump beam waist, (ii) acceptance angle as determined from the crystal-parabolic distance, (iii) distance of projection and (iv) the THz frequency of interest. The exact IR pump beam waist inside the crystal is estimated to be greater than $100\ \mu\text{m}$ on the basis of optical alignment. With a relatively thick crystal of 1 mm and the fact that the ZnTe permittivity at IR and THz frequencies are close, we conclude that THz radiation generation is distributed along the bulk crystal thickness. In the model, this distributed generation is approximated as an aperture located at an effective distance within the crystal. Measuring the distance from crystal surface to the knife-edge gives

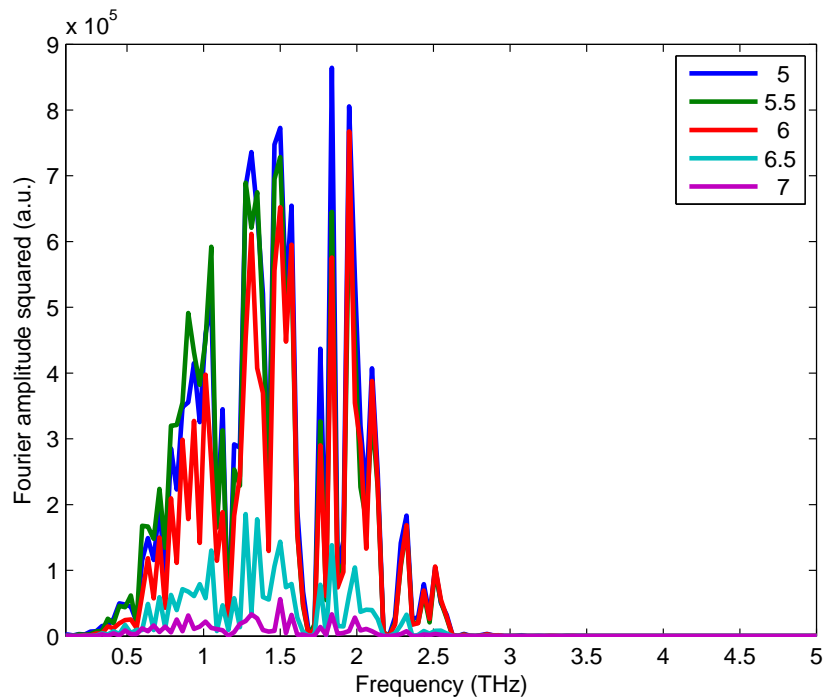


Figure 4.12. Power spectrum at certain knife locations. The power spectrum of the THz waveforms acquired with a knife-edge scanned at a distance of 0.75 mm from the crystal. With each movement of the knife, the THz field becomes weaker until when the THz radiation is totally blocked by the knife. This can be seen at when $x = 5$ mm, where the knife has not obstructed the THz beam, as opposed to $x = 7$ mm, where THz radiation is almost entirely blocked.

us the range of possible distances for adjusting the effective location and fits the model to the empirical integrated knife-edge function. The criterion for curve fitting is that the free-parameters (beam waist and effective location of the source) are within a realistic range of values, and the resulting knife-edge curves must apply simultaneously to all the selected frequency components. Figures 4.14 to 4.20 show the computed normalized radiation patterns and the curve-fitted data for selected frequencies, with an IR beam waist in the crystal of $150 \mu\text{m}$. To illustrate the goodness of the fit, Figure 4.21 shows the knife-edge profile at 2.51 THz fitted with the numerical model of 2.51 THz and 0.375 THz respectively. The computed knife-edge function matches closely all the experimental results in terms of the integral function shape and slope. The effect of diffraction is evident in the measured results. The diffraction effect mostly removes the discontinuity in the model and explains the oscillations observed. With the beam waist or aperture size held constant, it is noteworthy to observe the changes in the radiation pattern as the frequency increases. At low frequencies (0.375 THz), the emitted THz

4.5 Ramifications to THz

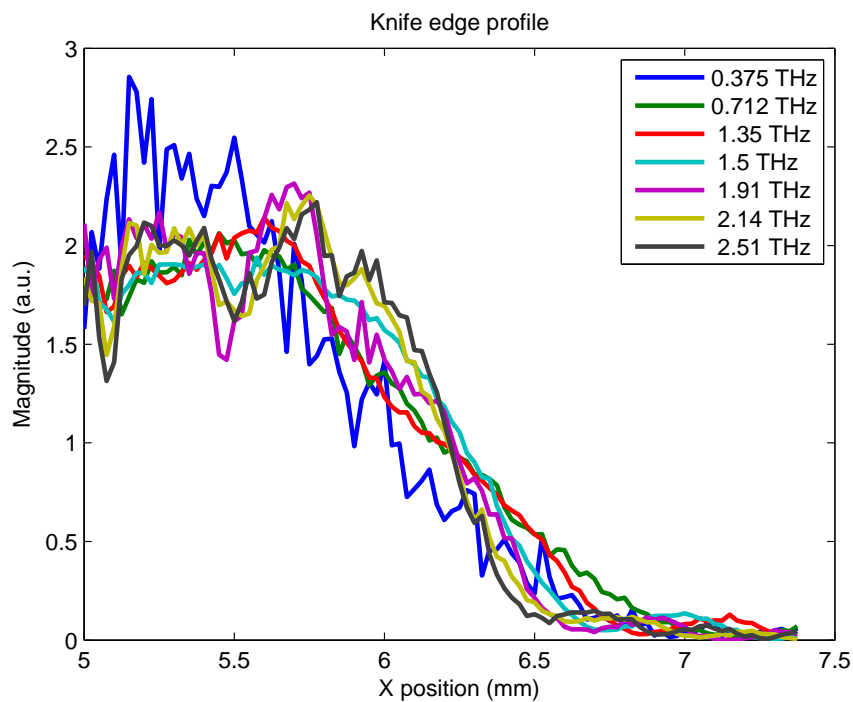


Figure 4.13. Knife-edge profile of selected frequencies. Selected frequency component is shown at intervals of knife movement. The knife-edge profile is also shown to illustrate the integrated spatial distribution of THz pulse at selected frequencies that are unaffected by water vapour absorption and noise that occur at high THz frequencies.

pattern resembles the obliquity factor in Equation 4.5. At frequencies 0.712 and 1.35 THz, the THz beam width begins to approach the paraxial Gaussian beam width. A significant back radiation is also observed in the computational model of the Gaussian aperture. Above those frequencies, the pattern of the THz beam becomes very close to the the paraxial Gaussian pattern, as expected.

4.5 Ramifications to THz

As we can see from the model, as the IR pump beam waist is very much smaller than the generated longer wavelength components of our THz pulse (e.g. 375 GHz), the THz radiation pattern becomes nearly independent of the frequency. The THz beam pattern conforms to the obliquity factor and is hence diffracted in all directions around the crystal. Practically this translates into low SNR THz being detected. The result is consistent with the observations reported in Dakovski *et al.* (2005). We also can infer from those results that as the IR pump beam waist is increased, the pattern approaches

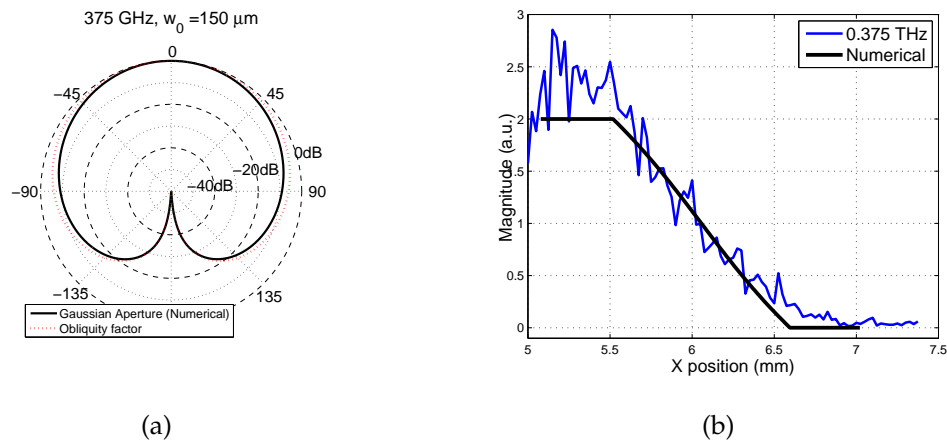


Figure 4.14. Model validation at 0.375 THz. (a) The radiation pattern of the Gaussian aperture and (b) the knife-edge profile at 0.375 THz. The beam waist w_0 is approximately $\lambda/5$ leading to a pattern resembling the obliquity factor.

and becomes a paraxial Gaussian beam. With a greater directivity, the SNR of the detected THz increases. The percentage of the detectable power over the total generated power is plotted in Figure 4.22 against the normalized beam waist w_0/λ for three acceptance angles (10, 20 and 30 degree cones). As expected, at small normalized beam waist, i.e. for IR pump beam waists much smaller than THz wavelengths, the THz radiation is diffracted in all directions leading to little detectable power. As the normalized beam waist increases above one THz, the THz radiation pattern quickly converges to a paraxial Gaussian beam leading progressively to a more directive beam and hence a monotonic increase in detectable power. The curves saturate toward 100% as the divergence angle of the beam decreases below the acceptance angle of detection. Obviously the acceptance angle has an effect on the detectable power and this is governed by the parabolic mirror following the crystal. With a greater acceptance angle, a higher THz power percentage is detectable.

4.6 Crystal heating effects

With prolonged intense exposure of the optical beam on the ZnTe crystal, the problem of crystal photodamage becomes increasingly relevant. Yuan *et al.* (2002) quoted the damage threshold as $100 \text{ GW}/\text{cm}^2$ but this appears to be inconsistent with our experiments as the crystal is subjected to a lower power density that nevertheless resulted in photodamage. Photodamage on the crystal is observable as a black mark

4.6 Crystal heating effects

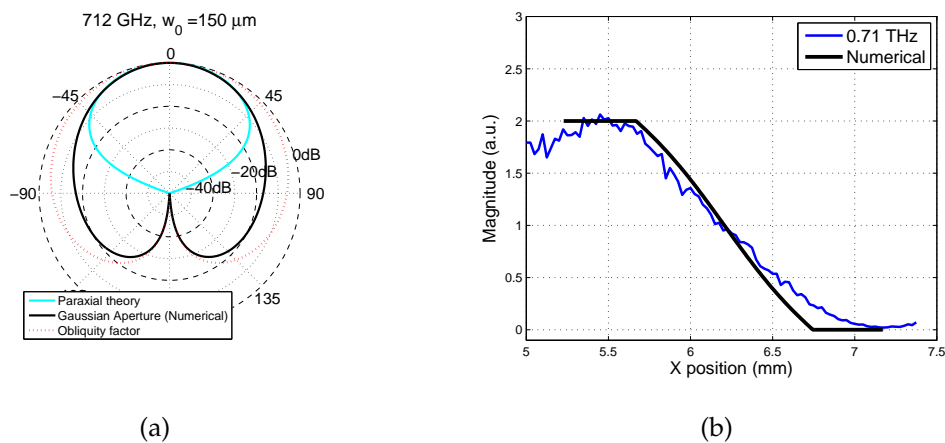


Figure 4.15. Model validation at 0.712 THz. (a) The radiation pattern of the Gaussian aperture and (b) the knife-edge profile at 0.712 THz. The beam waist w_0 is approximately $\lambda/3$ leading to a pattern starting to approach paraxial Gaussian beam towards the front.

on the surface or otherwise as a drop in the generated THz magnitude. In reducing the possibility of photodamage, practically this has meant a decrease in optical power density i.e. increase spot size and decrease pump power. This decrease can be explained by the heating effects to the crystal investigated using a THz water heating model (Kristensen *et al.* 2010). The model applies Kirchhoff's heat equation to model the influence of a THz beam on a sample of water. It is a generalised model and can be easily applied to any dielectric materials by changing the thermal conductivity and optical constants (absorption coefficient and refractive index). Here we apply the model to quantitatively distinguish the temperature difference from high and low pump power density on a ZnTe crystal with the physical parameters in Table 4.2 and experimental values in Table 4.3. The model estimates the worst case scenario temperature rise, which occurs at long time duration when equilibrium is reached. This therefore is applicable to our context as typical knife-edge measurement spans ≥ 12 hours. High power density is conducted with 200 mW chopped IR power, and focused with a 20 mm focal length lens to give a beam waist of $5 \mu\text{m}$. This gives rise to a power density of $2.55 \text{ mW}/\mu\text{m}^2$. Low power density on the other hand is conducted with 25 mW chopped IR power and focused with tens times longer focal length to give an approximately 10 times larger beam waist of $50 \mu\text{m}$. The resulting power density is thus 800 times smaller than the former. The calculated temperature increase on the surface of the crystal at the center of the beam for the high power density is 67°C as opposed to 3°C for the low power density as shown in Fig. 4.23. This is an approximately 20 times

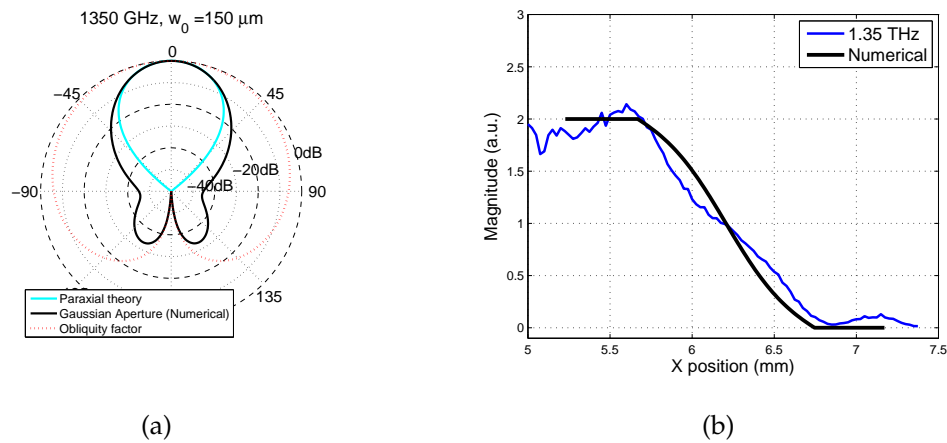


Figure 4.16. Model validation at 1.35 THz. (a) The radiation pattern of the Gaussian aperture and (b) the knife-edge profile at 1.35 THz. The beam waist w_0 is approximately 0.7λ leading to a pattern approaching paraxial Gaussian. Angle of divergence is 27° .

Table 4.2. ZnTe optical constants and thermal conductivity extracted from the following sources required for the simulation.

Description	Value	Source
Absorption coefficient α (cm^{-1})	12500	Palik (1998)
Thermal conductivity k_0 ($\text{Wm}^{-1}\text{K}^{-1}$)	20	Wang and Chu (2009)
Refractive index η	2.853	Palik (1998)

difference. Figure 4.24 shows the distribution of the temperature increase through the crystal thickness and quantifies the maximum heating on the crystal surface. This may aid in explaining the burning of the crystal surface especially considering the actual peak power is higher, thus leading to a reduction in THz generation efficiency for prolonged highly focused IR exposure. Figures 4.25 and 4.26 compare the contour plots for a high and low power density respectively. As can be seen, the heating is large for small beam waist while the penetration depth is comparatively lower, this is consistent with water heating in Kristensen *et al.* (2010).

4.7 Chapter summary

In this Chapter, we have modelled localised THz radiation generation in an ZnTe electro-optical crystal as radiating aperture with Gaussian intensity distribution. We

4.7 Chapter summary

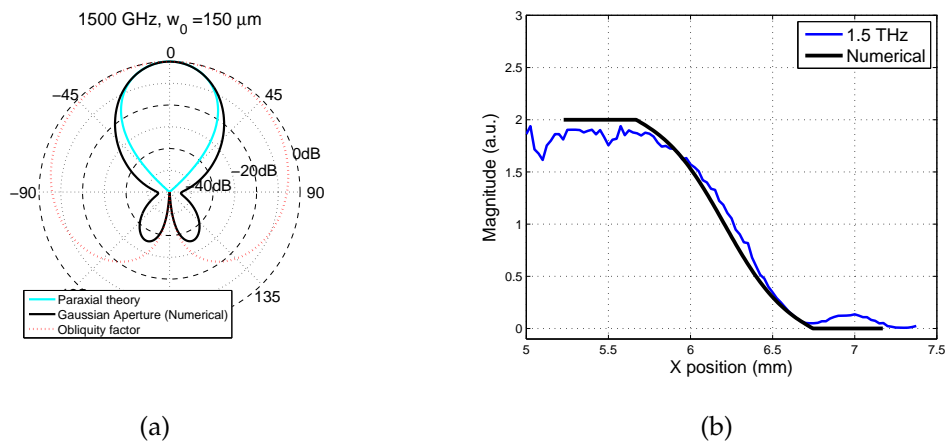


Figure 4.17. Model validation at 1.5 THz. (a) The radiation pattern of the Gaussian aperture and (b) the knife-edge profile at 1.5 THz. The beam waist w_0 is exactly 0.75λ leading to a pattern approaching paraxial Gaussian. Angle of divergence is 24° .

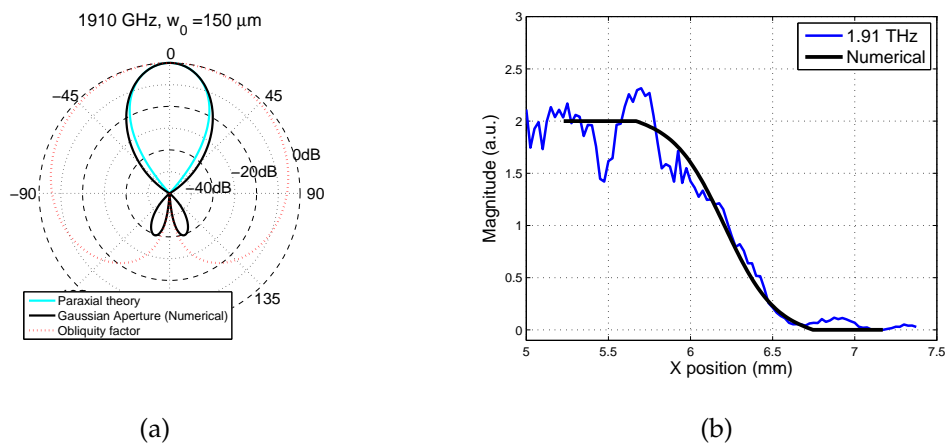


Figure 4.18. Model validation at 1.91 THz. (a) The radiation pattern of the Gaussian aperture and (b) the knife-edge profile at 1.91 THz. The beam waist w_0 is approximately λ leading to a pattern approaching paraxial Gaussian, with the back lobes slightly greater than -40 dB. Angle of divergence is 19° .

Table 4.3. The experimental parameters along with their respective values are applied to the model to quantitatively estimate the temperature increase at equilibrium.

Description	Value
Wavelength (nm)	800
Sample radius (mm)	5
Sample thickness (mm)	1

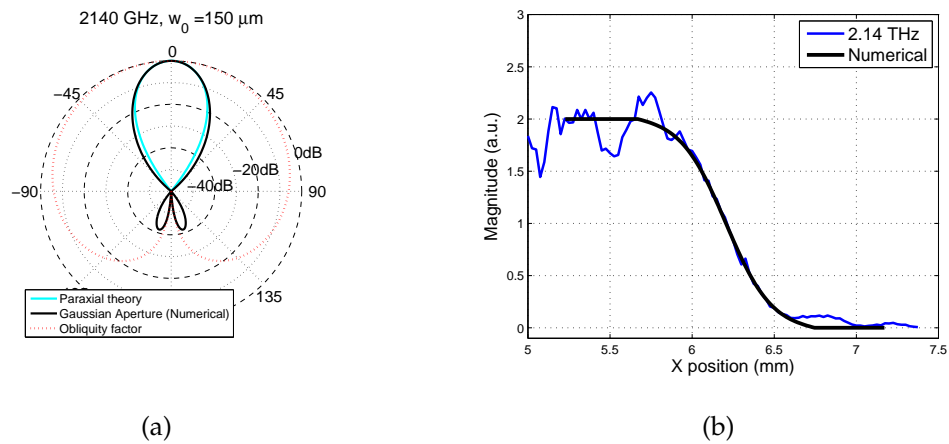


Figure 4.19. Model validation at 2.14 THz. (a) The radiation pattern of the Gaussian aperture and (b) the knife-edge profile at 2.14 THz. The beam waist w_0 is approximately 1.1λ leading to a pattern closely resembling the paraxial Gaussian, except for the back lobes less than -40 dB. Angle of divergence is 17° .

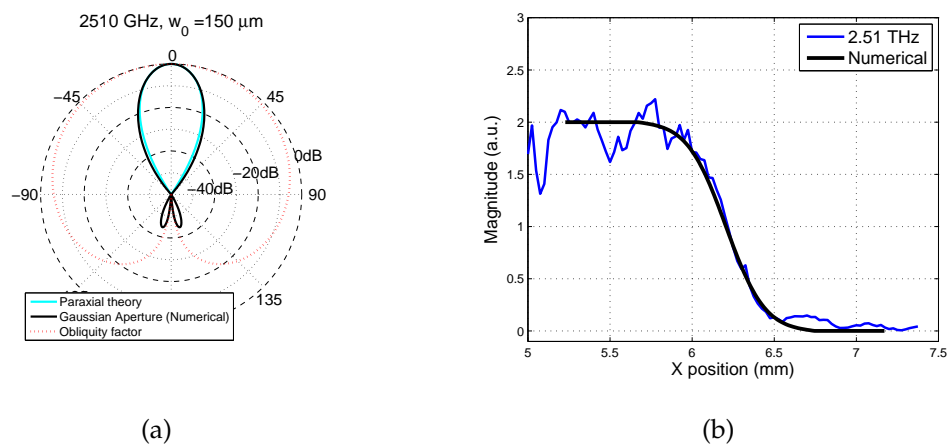


Figure 4.20. Model validation at 2.51 THz. (a) The radiation pattern of the Gaussian aperture and (b) the knife-edge profile at 2.51 THz. The beam waist w_0 is approximately 1.25λ leading to a pattern closely resembling the paraxial Gaussian, except for the back lobes less than -40 dB. Angle of divergence is 14° .

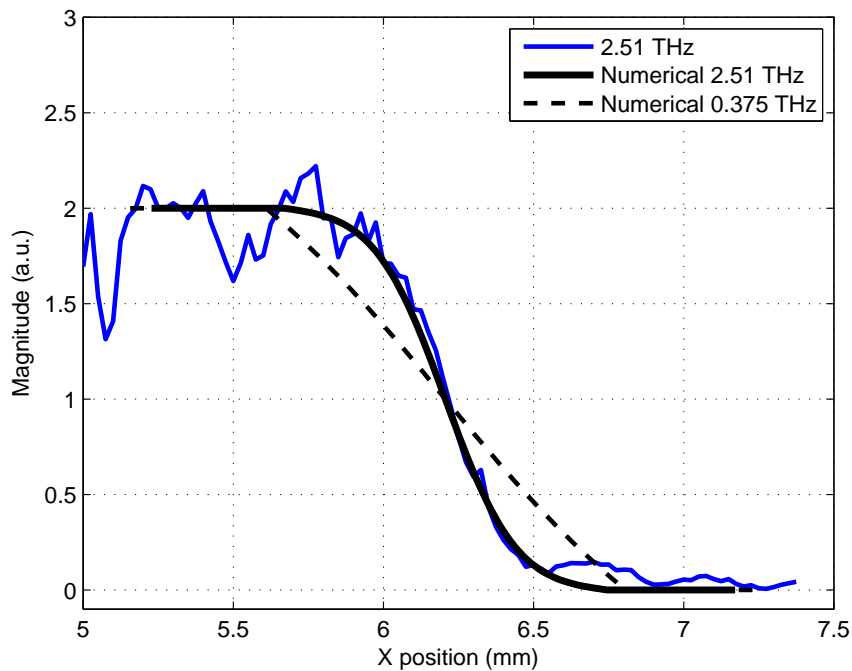


Figure 4.21. Illustration of goodness of fit. The goodness of the fit is demonstrated by fitting the knife-edge profile at 2.51 THz with the numerical model of 2.51 THz and 0.375 THz respectively. The latter is chosen to show a distinctive difference between the fits and the validity of the fitting criterion. For curve fitting, the free-parameters (beam waist and effective location of the source) are within a realistic range of values, and the resulting knife-edge curves must apply simultaneously to all the selected frequency components.

validate the model of Gaussian aperture generation by conducting a knife-edge measurement, taking into account the limitation of the THz radiation detection setup. We find that when the IR pump beam waist is very much smaller than the generated THz wavelength, the THz radiation pattern becomes nearly independent of the frequency, conforms to the obliquity factor and is hence diffracted in all directions from the crystal. Practically, this translates into a decreased SNR for the THz radiation reaching the detector. We also demonstrate that as the IR pump beam waist is increased, the pattern approaches and becomes the paraxial Gaussian beam. With a greater directivity, the detected THz SNR increases. As localised THz radiation generation is not only limited to electro-optical crystals, but also holds for photoconductive antennas and plasma generation (Xie *et al.* 2007), this work aims at bringing an awareness to the THz community of the effect of sub-wavelength aperture-like sources in THz radiation generation. We have also applied a recently published water heating model to model

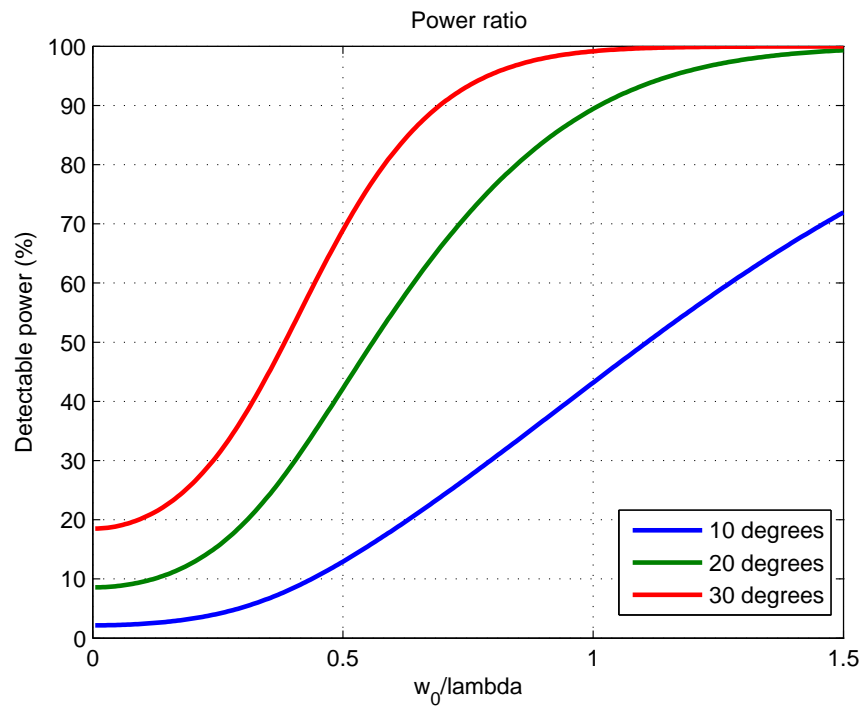


Figure 4.22. Detectable THz power percentage. The detectable THz power percentage over the total generated THz power, with the normalized IR beam waist, w_0/λ , on the x -axis for 3 different angular window $\theta_{win} = 10^\circ$, $\theta_{win} = 20^\circ$ and $\theta_{win} = 30^\circ$.

the prolonged heating effects of an optical beam on a ZnTe crystal for THz radiation generation. The simulation result quantifies the worst case scenario average temperature rise of 67°C for high pump power density as opposed to 3°C for the low power density. Maximum heating is observed to occur on the crystal surface and the heating is large for a small beam waist with a comparative lower penetration depth than lower power density.

As a whole, this Chapter has conducted far-field investigations of a sub-wavelength source employed in the focused beam THz near-field approach. Such a study is essential to understand the evolution of the THz radiation pattern with frequency, while validates the Gaussian aperture modelling methodology. Consequently, in the next Chapter, we build upon this work in the near-field regime. This is an important step toward the understanding of the many trade-offs in this type of THz near-field imaging system design.

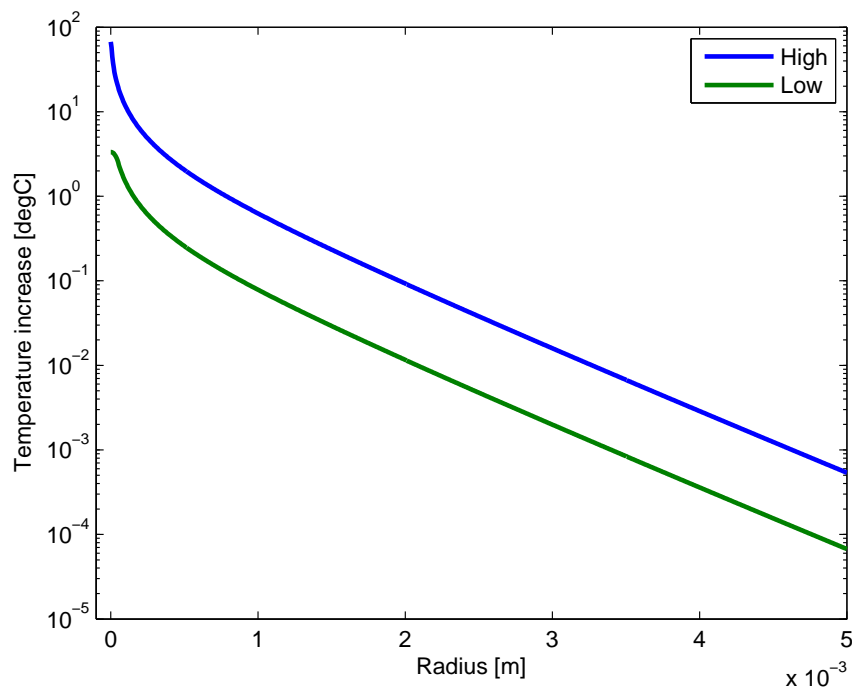


Figure 4.23. ZnTe temperature increase for the high and low pump power density. On the surface of the crystal, the temperature changes as a function of the radial distance from the centre of the beam. A worst case scenario of a 20 times temperature rise is estimated for high pump power density (blue curve) over the lower counterpart (green curve).

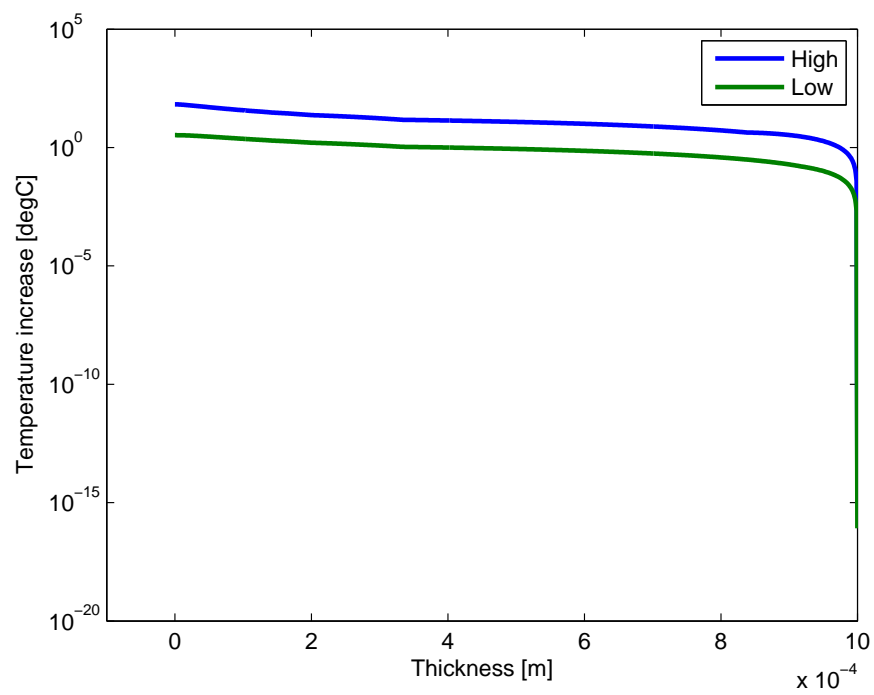


Figure 4.24. ZnTe temperature increase for the high and low pump power density. At the centre of the beam, the temperature change as a function of crystal thickness. It can be observed that maximal heating occurs on the crystal surface.

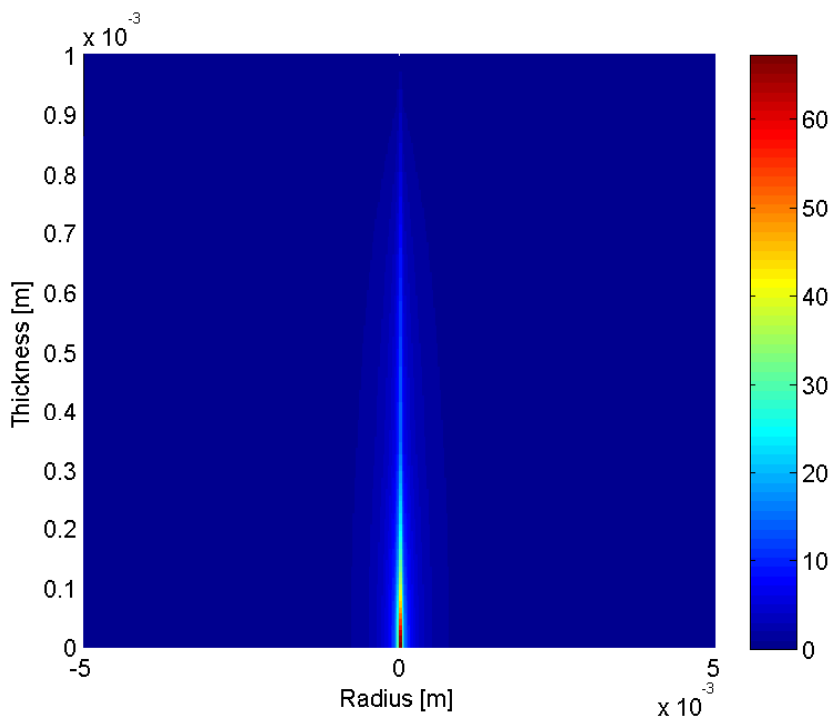


Figure 4.25. Contour plot of penetration depth for high power density. The x -axis is along the laser spot radius and the y -axis is the thickness of the material penetrated by the laser beam. The heating is localised on the crystal surface and is large. The colours indicate the temperature change in degrees Celsius per milliwatt of average pump power.

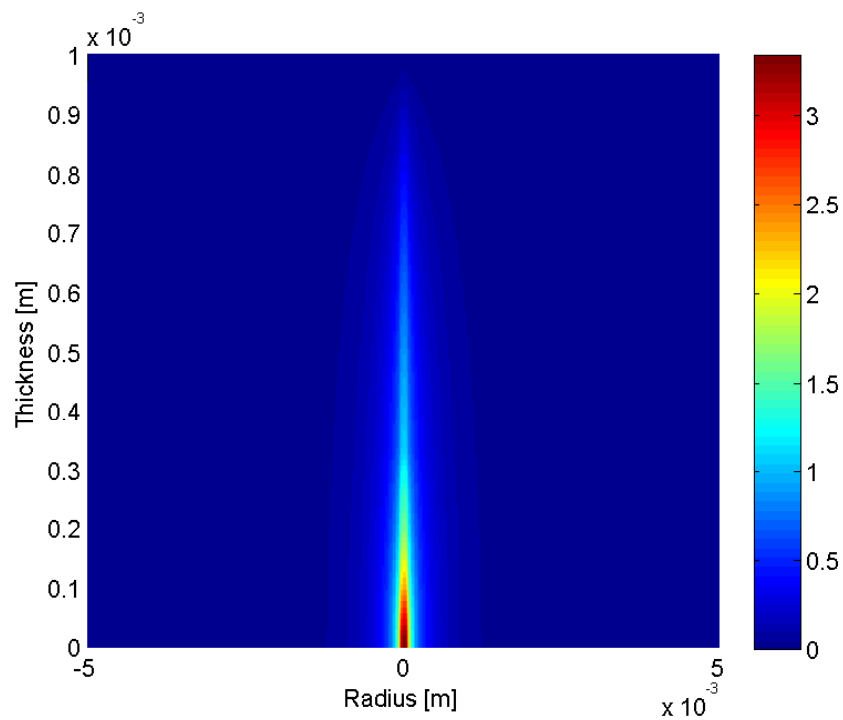


Figure 4.26. Contour plot of penetration depth for low power density. The x -axis is along the laser spot radius and the y -axis is the thickness of the material penetrated by the laser beam. The heating is smaller with greater penetration depth. The colours indicate the temperature change in degrees Celsius per milliwatt of average pump power.



Modelling of Terahertz Microscope

THE thin crystal in focused beam technique has been reported to generate THz radiation power enhancement. This, however, is counter-intuitive as thicker crystals provide a greater volume for optical rectification. This Chapter therefore investigates THz optical rectification with a thin crystal experimentally. The sub-wavelength THz emission point on the nonlinear electro-optical crystal, used in broadband THz near-field emission microscopy, is computationally modelled as a radiating aperture of Gaussian intensity profile. This Chapter also comprehensively studies the Gaussian aperture model in the THz near-field regime. Based on realistic parameter values, the model allows for THz beam characterisation in the near-field region for potential microscopy applications. An application example is demonstrated by scanning over a cyclic-olefin copolymer sample containing grooves placed sub-wavelengths apart. The nature of THz microscopy in the near-field is highly complex and studies have traditionally been empirical. The proposed validated numerical model therefore aids in the quantitative understanding of the performance parameters. Whilst we demonstrate the model on broadband electro-optical THz near-field emission microscopy, the model may apply without a loss of generality to other types of THz near-field focused beam techniques.

5.1 Introduction

Terahertz imaging offers many attractive advantages over existing imaging modalities especially in its ability to obtain spectroscopic information (Siegel 2004, Tonouchi 2007). However, one of the major limitations of THz imaging is low spatial resolution, as determined by Rayleigh's criterion with a wavelength ($300 \mu\text{m}$ at 1 THz). The general motivation behind an increased resolution is to distinguish objects in close proximity and to cater for a smaller sample size. The resolution of THz far-field imaging is in the sub-millimeter range and therefore insufficient for potential future imaging applications such as biological cells (micron to sub-micron range) and micro-structures in semiconductor structures (sub-micron to nanometer range).

Extensive reviews on pulsed THz near-field imaging have been published (Yuan *et al.* 2004, Withayachumnankul *et al.* 2007b). The techniques in general can be categorised as aperture, tip, and highly focused-beam approaches as explored in Chapter 3. Aperture based approaches (Hunsche *et al.* 1998, Mitrofanov *et al.* 2000a, Mitrofanov *et al.* 2000b, Mair *et al.* 2004, Kawano and Ishibashi 2008) require physical sub-wavelength apertures where the spatial resolution is dependent on the aperture size, but no longer on the wavelength. However, the sub-wavelength nature of the aperture places a limitation on the radiation throughput leading to a deterioration in the SNR. The finite thickness of the aperture also exhibits waveguide effects that attenuates evanescent low-frequency components and makes detection difficult. Metallic tip based approaches (van der Valk and Planken 2002, Wang *et al.* 2003, Chen *et al.* 2003, Yuan *et al.* 2005, Huber *et al.* 2008, Kersting *et al.* 2008, von Ribbeck *et al.* 2008, Wächter *et al.* 2009) have to date demonstrated the highest resolution down to the nanometer range. The approach, however, is complicated with the introduction of a near-field tip, and suffers from low output power. Furthermore, some of the presented techniques are only valid for semiconductor samples.

Focused-beam techniques exploit the micron sized far-infrared pump or probe beam spot for generating or detecting THz radiation respectively to achieve sub-wavelength resolution (Wynne and Jaroszynski 1999, Chen *et al.* 2000, Yuan *et al.* 2002, Kiwa *et al.* 2003, Adam *et al.* 2008, Bitzer and Walther 2008, Lecaque *et al.* 2008, Kiwa *et al.* 2010). The approach is comparatively simpler and does not heavily rely on micro-fabrication

5.2 Enhancement replication

technologies. Furthermore, a very thin electro-optical crystal (16 μm) has been observed to generate higher powered THz radiation pulses at the focal point than the thicker counterpart (250 μm) (Yuan *et al.* 2002). The spot size was measured to be 1.7 μm . The unexpected enhancement from the thin crystal is counter-intuitive as thicker crystals provide a greater volume for optical rectification. The initial part of this Chapter will therefore investigate THz optical rectification with thin ZnTe (25 μm) experimentally. Motivated by an increasing interest in the focused-beam THz near-field microscopy technique and drawing from the Gaussian aperture modelling in Chapter 4, the latter section of this Chapter will provide a numerical model to accurately characterize electro-optically generated THz radiation in the near-field regime. The numerical results based on a radiating Gaussian aperture source are validated experimentally, and a practical application of the model to extrapolate the THz beam spot to infer system resolution is also demonstrated.

5.2 Enhancement replication

Xu and Zhang (2002) first studied the dependence of THz radiation on optical excitation size in a GaAs emitter (500 μm thick). The pump beam radii studied were either much larger or much smaller than the THz radiation wavelength. They observed a dependence of the total THz radiation power on the square of the excitation diameter. Dakovski *et al.* (2005) investigated THz radiation as a function of optical excitation size showing that THz radiation emission under fixed optical excitation power is largely excitation size-independent, provided the size is smaller than the THz wavelength. Their work is extended for lower pump power in Xing *et al.* (2006).

5.2.1 Experiment

A standard THz-TDS setup employing an electro-optical crystal as the THz source is used in our investigation. The laser source is a Ti:sapphire pulsed laser producing 800 nm pulses at a maximum of 2 W output power with a 80 MHz pulse repetition rate and 100 fs pulsewidth. The laser is used to pump a $\langle 110 \rangle$ ZnTe emission crystal and probe a $\langle 110 \rangle$ 1 mm thick ZnTe in the detection path. The detection setup is fixed in this investigation and only the emission crystal is varied. The emission crystal comprises a 1 mm thick ZnTe (Zomega Terahertz Corporation) that is annotated as the thick crystal. In contrast, the thin crystal is a 25 μm ZnTe (MaTeck GmbH) adhered to a

$\langle 100 \rangle$ 500 μm thick ZnTe using epoxy resin in order to overcome fragility, as reported in Yuan *et al.* (2002). The epoxy has a thickness of 10 μm so therefore we can assume good index matching between the substrates. Such a setup follows the configuration in Dakovski *et al.* (2005). A 10 mm focal length objective lens is mounted on a linear translation stage to ensure the pump beam is well focused onto the emitter. The excitation size with the Gaussian beam is thus expected to have a radius of 2.5 μm , comparable to 1.7 μm in Yuan *et al.* (2002). In order to confirm THz radiation generation from the thin crystal, a pump power of 200 mW is initially used to generate THz pulses for both crystals. Chapter 2 provides further information on the THz optical rectification process. The excitation size is varied by varying the lens-crystal distance for focusing the optical beam onto the crystal. This is achieved by translating the 10 mm optical lens on the z -axis, and monitoring the peak output THz electric field signal. A sketch of the experiment is found in Figure 5.1. A photograph of the experimental setup is shown in Figure 5.2.

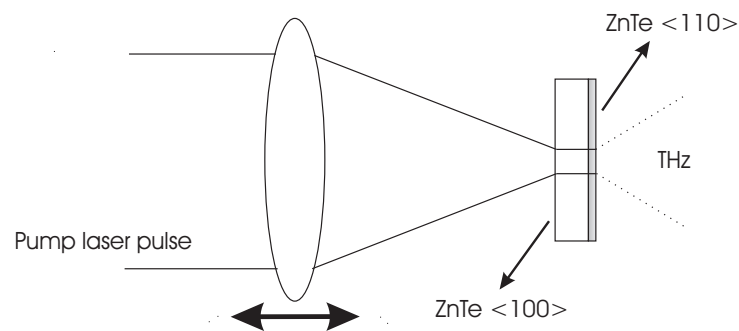


Figure 5.1. Varying the excitation size. The excitation size is varied by varying the lens-crystal distance for focusing the optical beam onto the thin crystal. The thin crystal is a 25 μm ZnTe (MaTeck GmbH) adhered via a 10 μm layer of epoxy to a $\langle 100 \rangle$ 500 μm thick ZnTe in order to overcome fragility, as reported in Yuan *et al.* (2002)

5.2.2 Results

Experimental results for 200 mW pump power are presented to confirm correct experimental setup. The waveform and spectra for THz radiation generation via the thick crystal is shown in Chapter 2. A bandwidth of approximately 3 THz is achieved with a SNR of 40 dB. It is found that as the excitation size is decreased, the effect of two photon absorption becomes prevalent with the generation of bright piercing white light. Depending on the exposure duration and the pump power, this can quickly burn away the ZnTe crystal thus limiting the generated THz radiation power. The optimal pulse

5.2 Enhancement replication

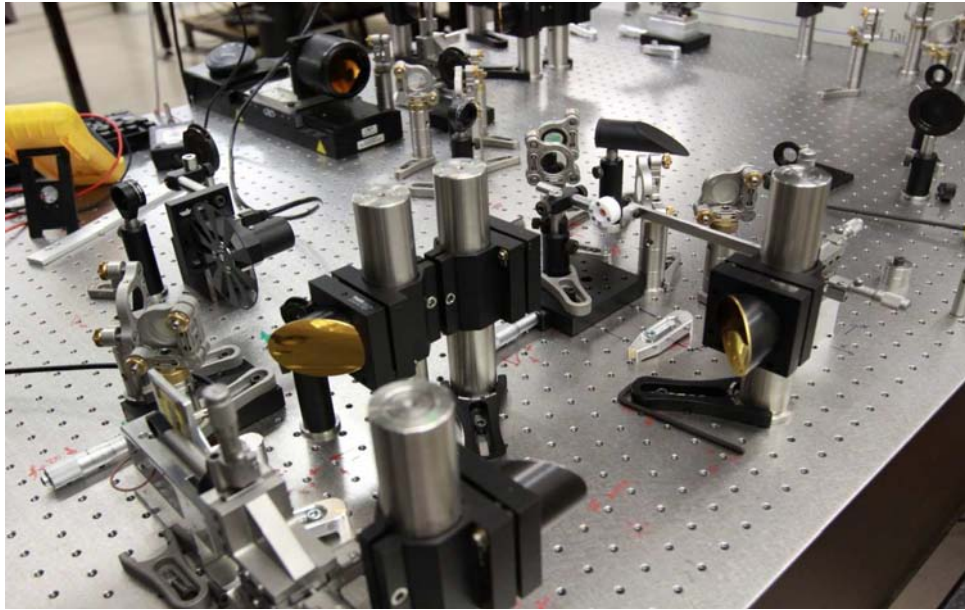


Figure 5.2. Thin crystal enhancement experimental setup. The photograph depicts the experimental setup for generating THz radiation from a thin ZnTe crystal in an effort to critically investigate the reported power enhancement.

generated is with the optical beam out of focus. The waveform and spectra for the thin crystal is shown in Figure 5.4 and 5.5 respectively. A bandwidth of up to 2 THz with a SNR of 9.5 dB is achieved.

The obtained THz waveform and spectra from pumping 200 mW onto the thin crystal has confirmed the crystal installation and the experimental setup. The dependence of the peak THz electric field on the excitation size and hence the lens-crystal distance is subsequently investigated with a lower pump power of 10 mW similar to Yuan *et al.* (2002). The data points with the thick crystal in Figure 5.6 indicate a dip at the optical focal point hence smallest excitation spot. This result is consistent with the experimental findings detailed in Yuan *et al.* (2002) and Xing *et al.* (2006). The dips arise to nonlinear absorption in the ZnTe crystal such as two-photon absorption. Results for the thin crystal in Figure 5.7 does not show power enhancement at the focal point but instead, it dips similar to that of the thick crystal. As such, we were unable to replicate the unexpected power enhancement with thin crystals as described in Yuan *et al.* (2002). As a matter of fact, under such low pump power, it is extremely difficult to detect and hence observe the generated THz radiation embedded in noise.

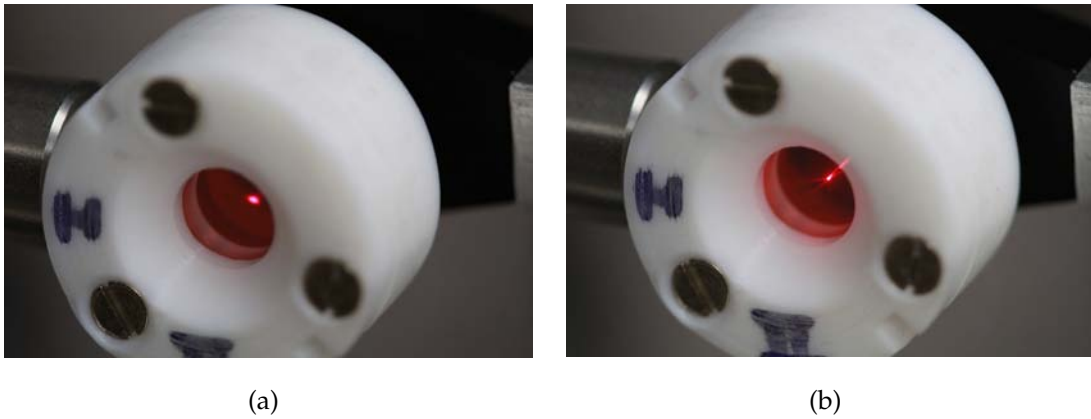


Figure 5.3. Varying excitation size. By varying the lens-crystal distance, the optical excitation size is effectively varied. The photographs show the excitation sizes taken from the crystal back surface when IR beam is (a) loosely focused and (b) tightly focused and hence the generation of white piercing light.

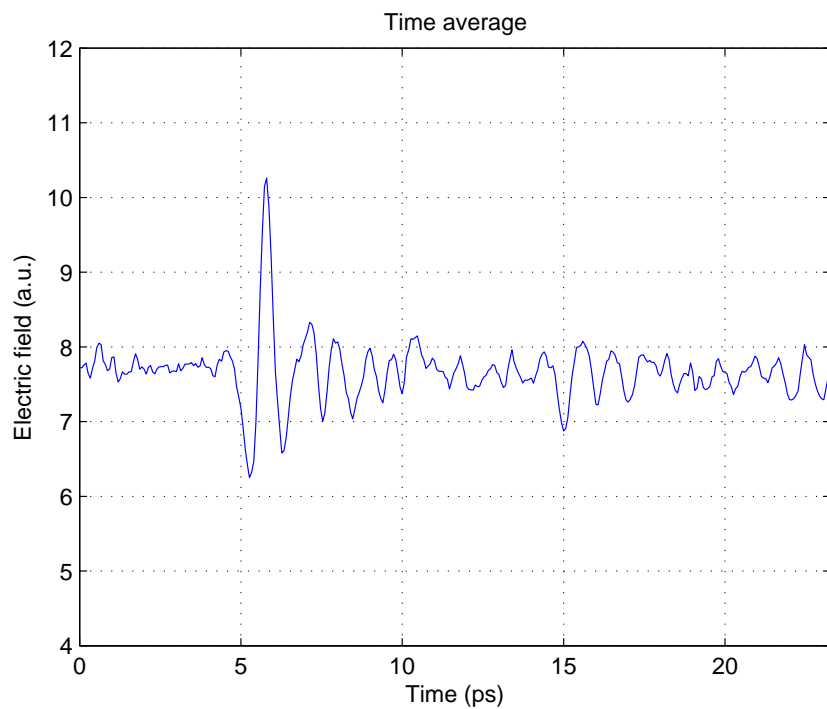


Figure 5.4. Pulse from thin electro-optical crystal and PCA detection. The THz electric field waveform generated with a thin electro-optical crystal ($25 \mu\text{m}$) and detected with a PCA. Such a setup achieved a SNR of 9.5 dB and a bandwidth of up to 2 THz.

5.3 Terahertz microscope modelling

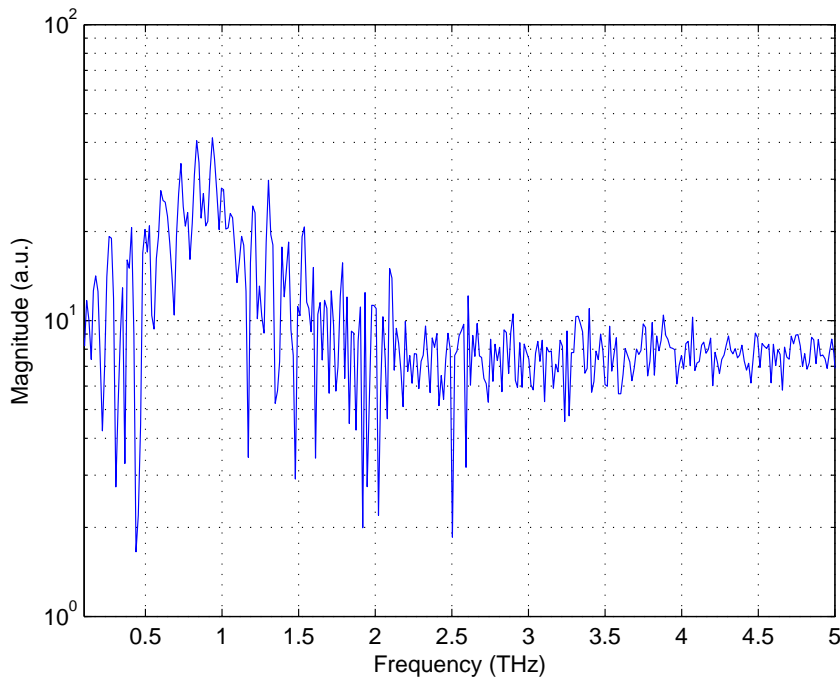


Figure 5.5. Spectrum from thin electro-optical crystal and PCA detection. The THz spectrum generated with a thin electro-optical crystal and detected with a PCA. Such a setup achieved a SNR of 9.5 dB and a bandwidth up to 2 THz. As nitrogen is not used, the water vapour absorption lines can be clearly seen in the spectrum. The spectrum has a limited frequency resolution due to a reduced number of data points.

5.3 Terahertz microscope modelling

Sub-wavelength THz sources have been investigated in the far-field regime as a radiating aperture of Gaussian profile in Chapter 4, using semi-analytical techniques commonly applied at microwave frequencies. The results of that investigation helped in explaining the far-field observations in Xu and Zhang (2002) and Dakovski *et al.* (2005). The techniques presented are however, only applicable for far-field interactions and far-field detection, and therefore, are unsuitable for interpreting the effect in the more complicated near-field regime. Motivated by an increasing interest in the focused-beam THz near-field microscopy technique, the present paper provides a numerical approach to accurately characterize electro-optically generated THz radiation in the near-field. The numerical results based on a radiating Gaussian aperture source are validated experimentally, and a practical application of the model to extrapolate the THz beam spot to infer system resolution is also demonstrated.

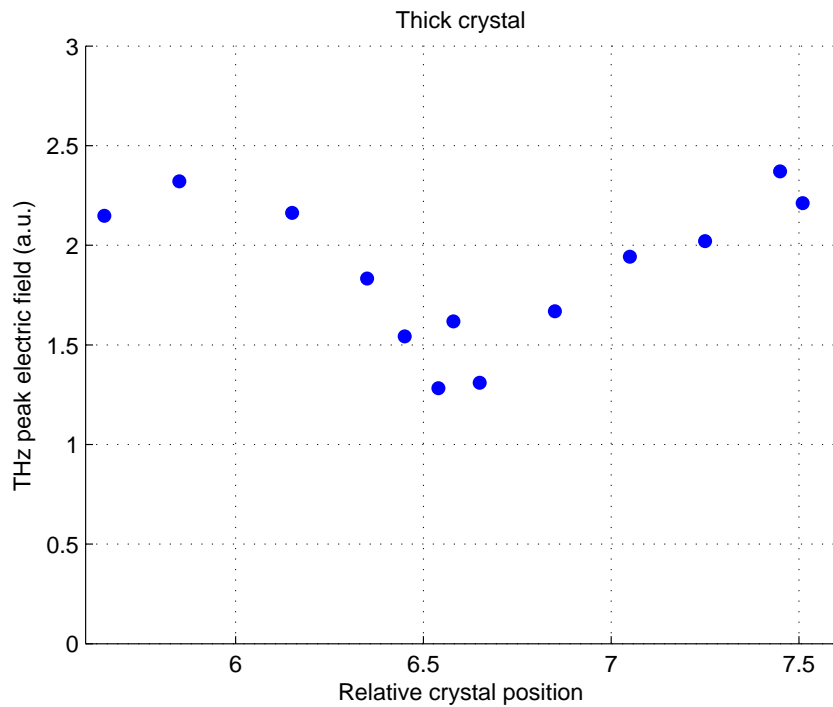


Figure 5.6. Measured peak THz electric field for the thick crystal. A plot of the experimental data collected shows a dip at the pump beam focal point that gives rise to the smallest excitation spot. The finding is consistent with the experimental results detailed in Yuan *et al.* (2002) and Xing *et al.* (2006).

5.3.1 Experimental near-field beam characterization

A THz hybrid setup that generates THz radiation by optical rectification and PCA detection is used in our experiment, as shown in Figure 5.8. An average IR pump power of 30 mW is used for THz radiation generation with a 1 mm thick $\langle 110 \rangle$ ZnTe crystal from Zomega Terahertz Corporation. An IR beam waist of $38 \mu\text{m}$ with a 150 mm focal length lens is initially used. However, this requires the crystal to be placed at a distance outside the parabolic mirror focal length. This therefore places uncertainty on the THz beam propagation within the parabolic mirrors, because the beam is no longer well collimated. To overcome the uncertainty, a longer focal length lens of 200 mm focal length is used to focus down the IR pump beam to a waist of $51 \mu\text{m}$ with a Rayleigh range of 10 mm. Taking into consideration the beam divergence in the crystal, the effective IR pump beam waist is expected to be slightly larger than the theoretical value. An approximate maximal SNR of 40 dB and a bandwidth of more than 2.5 THz is achieved. A dual-axis (i.e. x and y -axis) knife-edge profile measurement is conducted on the generated THz beam at a distance of $150 \mu\text{m}$, as determined from the tip of the knife-edge

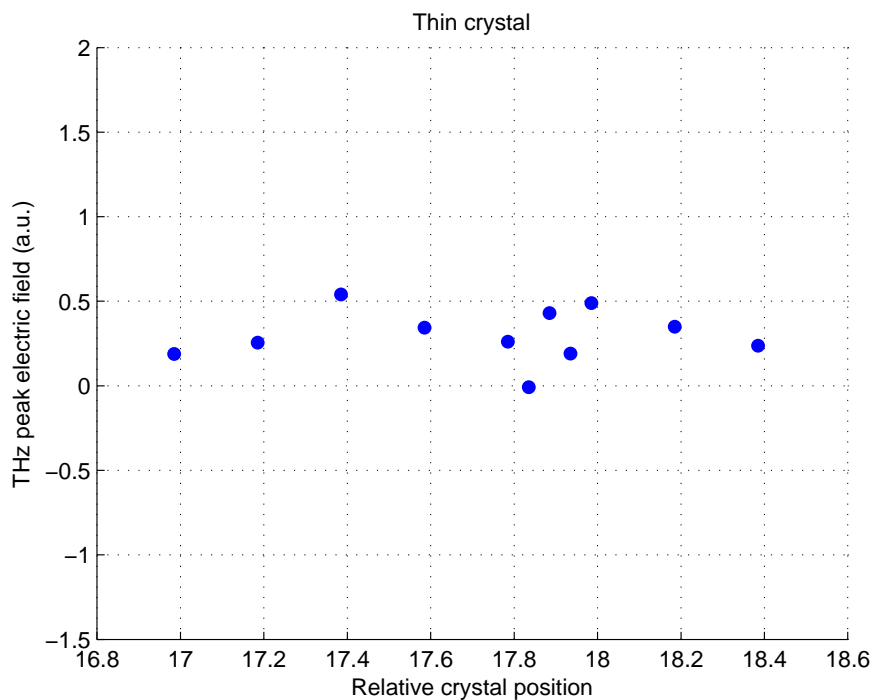


Figure 5.7. Measured peak THz electric field for the thin crystal. A plot of the experimental data collected do not show power enhancement at the pump beam focal point. Like the thick crystal experimental result, a dip is also observed.

to the crystal surface. The minimal possible near-field distance is constrained in this case by the razor blade's thickness. This distance is measured with a CCD camera in the actual experiment. A dual-axis knife-edge profile is necessary for a thorough THz beam characterization in the near-field because the radial symmetry of the polarized THz beam is broken at the air-crystal interface. The poorly focused images obtained with the CCD camera can be found from Figure 5.10 to 5.11. Even though the crystal to knife-edge distance cannot be achieved simultaneously for both axes, a two knife system as shown in Figure 5.9 to minimize experimental uncertainties. Sheffield steel razor blades are used as knife-edges. The inset to Figure 5.8 is realized in the photograph in Figure 5.12.

5.3.2 Modeling of the THz knife-edge experiment

The following sections describe the electromagnetic modelling of the full knife-edge experiment from electro-optical beam generation to detection. The model combines several techniques and requires simplifications to become tractable in terms of complexity and computational effort. Modeling the knife-edge experiment and comparing

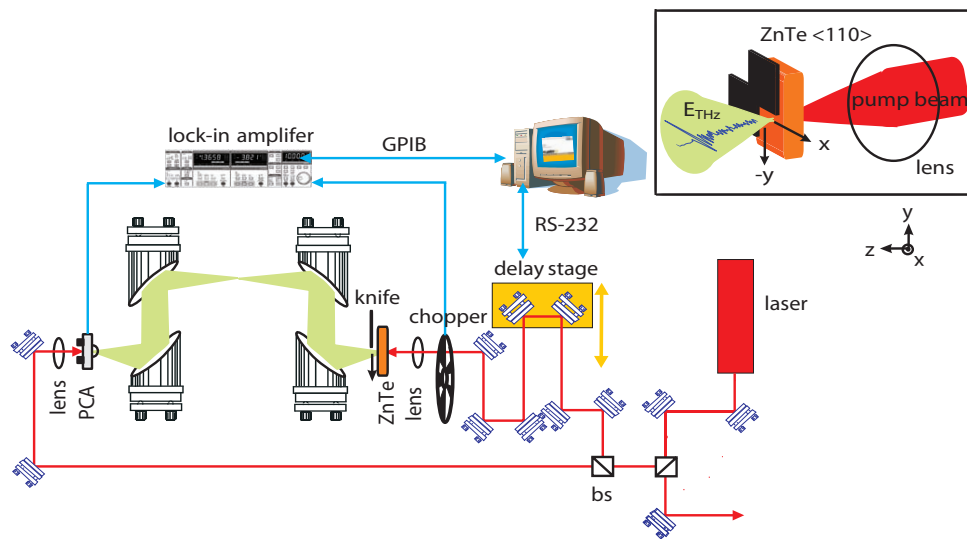


Figure 5.8. Experimental setup. A THz-TDS setup comprising of a Zomega ZnTe $\langle 110 \rangle$ crystal as the emitter and a University of Freiburg, Germany, manufactured PCA as detector. The inset zooms in on the crystal and dual-axis (i.e. x and y -axis) knife-edge setup. The pump laser beam is focused into a 1 mm thick ZnTe crystal by means of an optical lens. The emitted THz radiation polarized parallel to the x -axis is sliced along the x -axis and y -axis respectively by translating two sharp razor blades in the near-field region in parallel to the crystal back surface.

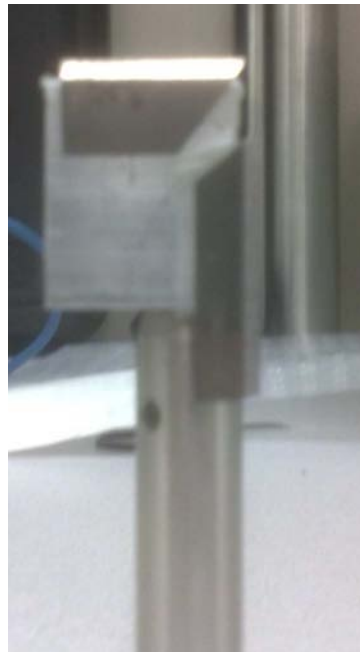


Figure 5.9. Two knife system. The two knife system is installed to minimise experimental uncertainties for maintaining the same crystal to knife-edge distance in both axes. This is essential for performing a dual-axis knife-edge profile.

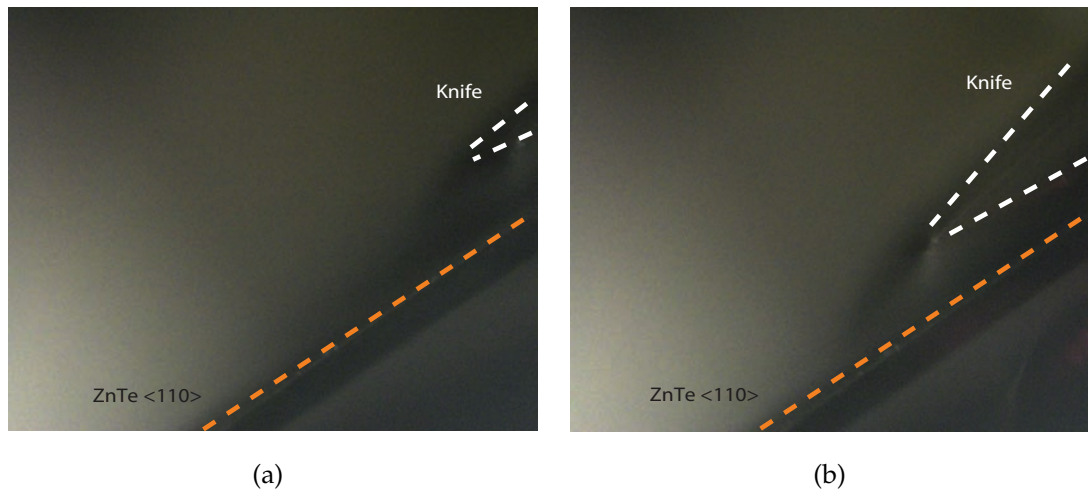


Figure 5.10. Bird's eye view CCD images of x -axis knife-edge. The knife-edge (white dashed lines) moving in a direction parallel to the ZnTe crystal surface (orange dashed lines) when (a) knife-edge does not obstruct the THz beam, as opposed (b), where the THz radiation is totally blocked.

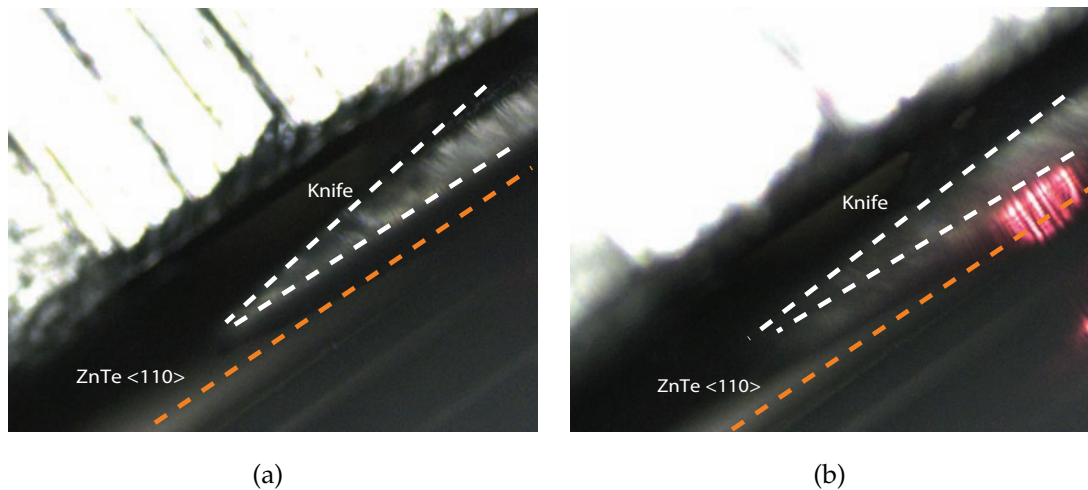


Figure 5.11. Bird's eye view CCD images of y -axis knife-edge. The knife-edge (white dashed lines) moving in a direction perpendicular to the ZnTe crystal surface (orange dashed lines) when (a) knife-edge has not obstructed the THz beam, as opposed (b), where the THz radiation and the leakage optical beam through the crystal is totally blocked.

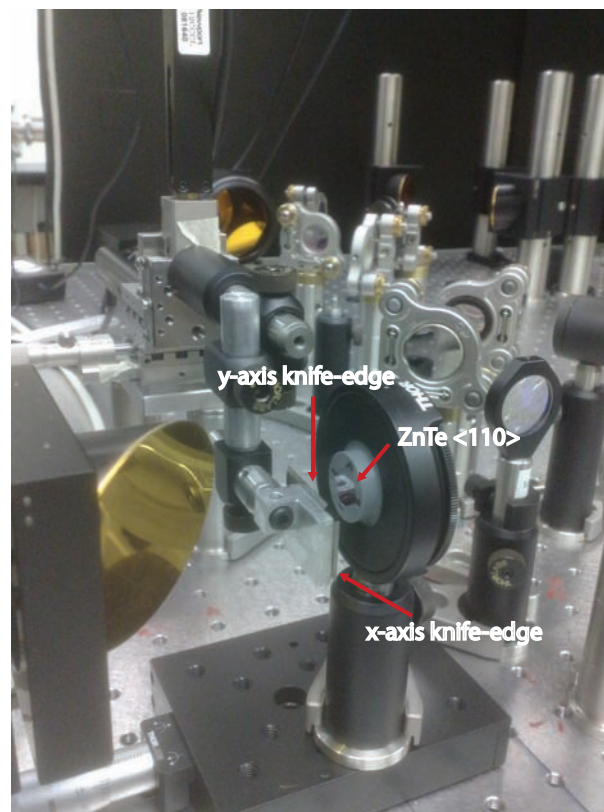


Figure 5.12. Dual-axis experimental knife-edge. The photograph shows the two knife system installed at a near-field distance of $150\ \mu\text{m}$ away from the electro-optical crystal surface. The knife-edges and the crystal back surface are annotated by the arrows.

the results to experimental data provides a validation of the general simulation approach.

Sub-wavelength THz source

The generation of THz radiation with optical rectification in a nonlinear crystal is a square-law process (Lee 2008). The pump beam is typically a Gaussian IR beam, i.e. can be approximated as a solution to the paraxial wave equation characterised by a Gaussian intensity distribution in any plane transverse to the direction of propagation (Saleh and Teich 1991). The coherent generation of THz radiation in the ZnTe electro-optical crystal is then a source with Gaussian profile distributed along the optical beam axis. The square relationship between generated THz electric field to the optical electric field therefore implies a reduction factor of $\sqrt{2}$ in the radius of THz source. This is consistent with the estimation in Xu and Zhang (2002). In the present model, the THz source is approximated as the radiation from an aperture with a Gaussian intensity profile, located inside the crystal. This type of Gaussian aperture is similar

5.3 Terahertz microscope modelling

to the one introduced, in Chapter 4, for investigation of far-field THz radiation. This simplified approach could be in principle refined by using as a source an aperture field distribution based on analytical modelling of the nonlinear effects a presented in Bakunov *et al.* (2007).

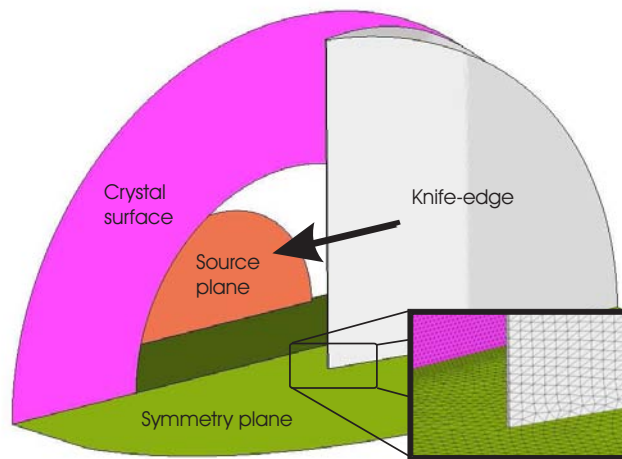


Figure 5.13. Schematic of the numerical FVTD model. The customised simulation tool is based on Finite Volume Time-Domain (FVTD) method. The numerical model opens up the center of the electro-optical crystal surface to reveal the source plane. The direction of the arrow points the direction of knife-edge movement. The inset shows the surface skin triangulation and illustrates the refinement of the mesh near the blade tip and on the crystal surface.

Full-wave near-field electromagnetic simulation

In the present study, the Gaussian aperture source is placed inside the crystal surface and the near-field wave propagation is simulated with a electromagnetic simulation tool based on the Finite-Volume Time-Domain (FVTD) method (Bonnet *et al.* 1999, Baumann *et al.* 2009). The application of in-house developed code is motivated by the possibility of implementing a sub-wavelength Gaussian aperture source as demonstrated in Fumeaux *et al.* (2009). This flexibility in implementation is not readily available in most commercial software, even if other full-wave simulation methods such as the Finite-Difference Time-Domain (FDTD) method (Taflove and Hagness 2005) would in principle be appropriate for simulation. The FVTD model is shown in Figure 5.13. The Gaussian aperture source plane is displaced inside the crystal, 300 μm away from the output surface. A metallic knife-edge is scanned through the beam in a series of

simulations, mimicking the experimental beam characterization. The knife-edge has a thickness of $150\ \mu\text{m}$ and is scanned parallel to the crystal surface at a fixed distance of $150\ \mu\text{m}$ between its tip and the crystal surface. The blade tip is tapered at an approximate angle of 21° as observed from CCD images, and the tip end is flattened to mimic a realistic finite tip sharp width of $4\ \mu\text{m}$. A symmetry plane is introduced to halve the computational domain size. The nature of this symmetry plane depends on the knife-edge slice considered, i.e. scanning along the x or y -axis in the inset of Figure 5.8, which corresponds to the two orthogonal polarizations in the computational model.

For the y -axis scan, the electric field is perpendicular to the symmetry plane leading to a Perfect Electric Conductor (PEC). Analogously, the symmetry plane is a Perfect Magnetic Conductor (PMC) in the x -axis scan. The volume is discretized with an inhomogeneous tetrahedron mesh (Fumeaux *et al.* 2004) to resolve the geometry near the fine tip, and to refine the discretization in the crystal with a relative permittivity of ϵ_r of 9. The computational domain is subsequently truncated with a perfectly matched absorber (Fumeaux *et al.* 2007). The Gaussian sub-wavelength source is excited with a sine-modulated Gaussian pulse, which covers the frequency spectrum from 300 GHz to 2.5 THz.

The computational cost is relatively heavy considering the size of the computational domain in terms of wavelength, and the fact that a simulation has to be performed sequentially for each position of the blade. Also at every blade position, discrete Fourier transformation are performed on the fly during the time iteration of the FVTD simulation to obtain the equivalent frequency representations. Figures 5.14 and 5.15 illustrate the THz electric field amplitude for the x -axis and y -axis knife-edge with the tip positioned at the center of the beam for selected low and high frequencies respectively. The images show a standing-wave pattern inside of the crystal because of the reflection at the output surface. The dielectric interface breaks the radial symmetry of the beam, as the refraction is polarization-dependent. The figures further illustrate the polarization dependent diffraction from the knife-edge tip.

Near-field to far-field transformation

The full-field simulation can only describe wave propagation and material interactions in a very limited volume close to the source. Therefore, a discrete implementation of the frequency-domain near-to-far-field transformation is performed in accordance

5.3 Terahertz microscope modelling

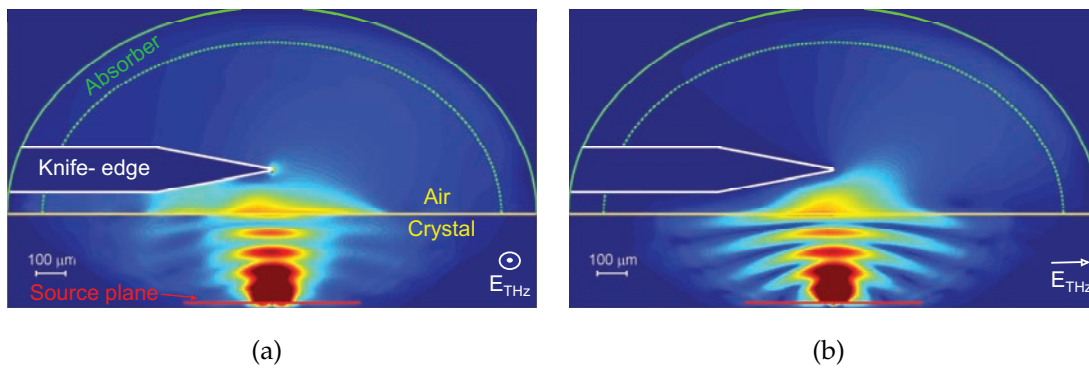


Figure 5.14. THz amplitude distribution at 0.8 THz. The simulated (a) x -axis and (b) y -axis knife-edge with the tip positioned at the center of the beam at a distance of $150 \mu\text{m}$ from the crystal surface.

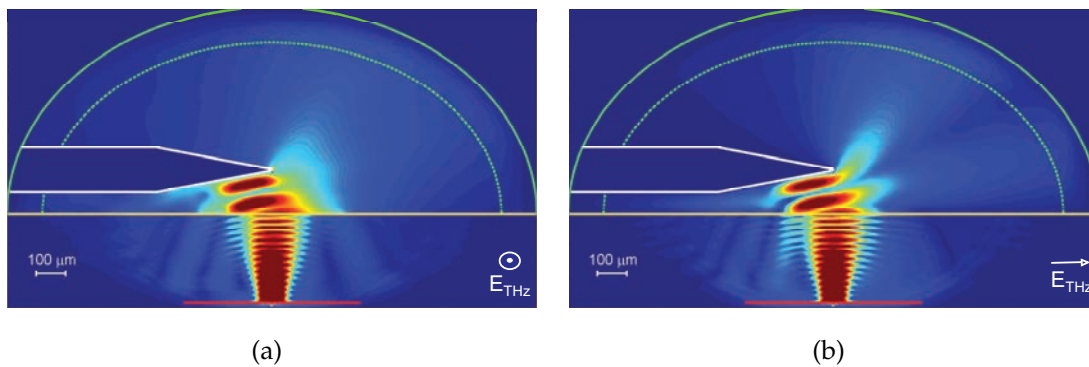


Figure 5.15. THz amplitude distribution at 2.4 THz. The simulated (a) x -axis and (b) y -axis knife-edge with the tip positioned at the center of the beam at a distance of $150 \mu\text{m}$ from the crystal surface.

with (Taflove and Hagness 2005) to simulate the radiation pattern relevant for far-field detection. The surface where the equivalent currents are sampled (Huygens' surface) is chosen as a flat plane located after the knife-edge. Figures 5.16 show the obtained amplitude radiation patterns at 0.8 and 2.4 THz respectively. The nature of the THz-TDS detection setup constrains the angle of acceptance at the first parabolic mirror for the power guided to the detector. The green dashed lines on the radiation patterns therefore delimit this acceptance angle of 28° . Effects of aberration, diffraction and propagation losses through the rest of the optical detection path are assumed to be negligible.

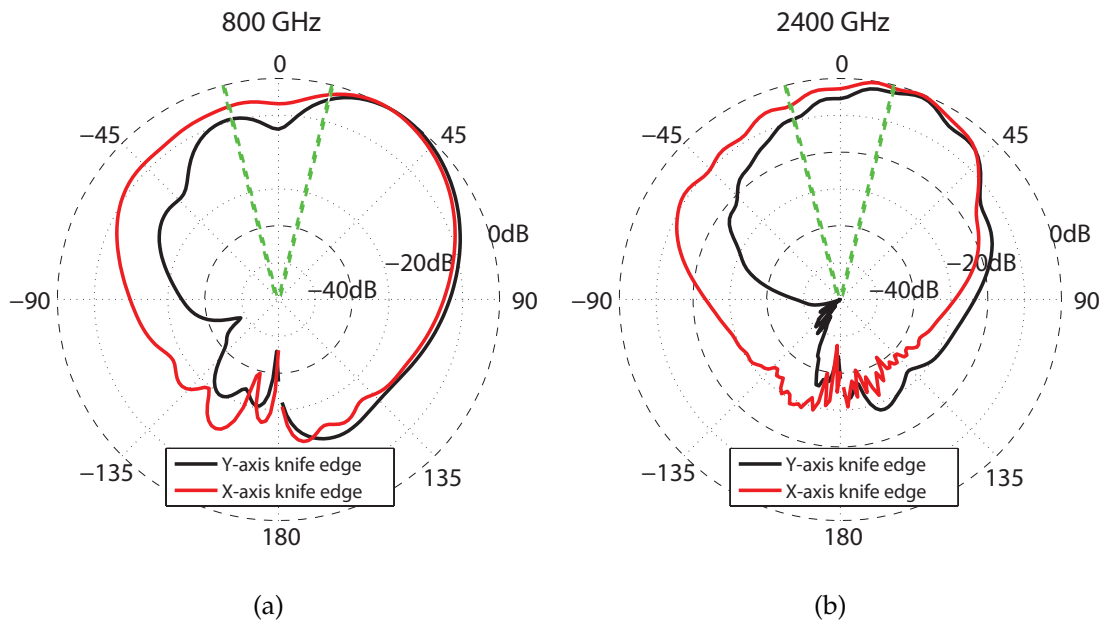


Figure 5.16. Normalized THz amplitude radiation pattern. The normalized THz amplitude radiation pattern obtained with the x -axis and y -axis knife-edge at the centre of the beam for frequencies (a) 0.8 THz and (b) 2.4 THz. The green dashed lines highlight the acceptance angle of 28° from the crystal to the parabolic mirror, within which the THz radiation is measured.

Detection modelling

In our modeled knife-edge experiment, the power available for detection is not the total radiated power that passes the knife-edge, but only the power integrated in the mentioned acceptance angle from the crystal to the parabolic mirror about the axis of optical propagation. To mimic the THz radiation detection by the PCA in a typical THz-TDS setup, the far-field power has to be integrated coherently in the acceptance angle, e.g. taking into account both amplitude and phase patterns.

5.3.3 Results and discussion

Experimental results

Fourier transforms of the experimentally acquired THz time-domain waveforms are computed and the amplitude at each extracted frequency is plotted against the position of the knife-edge for the respective axes. For the sake of simplicity, only the power spectrum at a certain knife-edge location and the knife-edge of selected frequency components in this study are shown in Figures 5.17, 5.19 and Figures 5.18, 5.20 for x and

5.3 Terahertz microscope modelling

y -axis respectively. As the experiment is conducted in low humidity atmosphere, the frequency components selected are unaffected by water vapour absorption and noise that occur at high THz frequencies. A one step running average over two points has been used to preserve data integrity. The y -axis knife-edge profile shows a stronger diffraction over the x -axis as imposed by the boundary conditions from having the knife-edge parallel to the THz electric field.

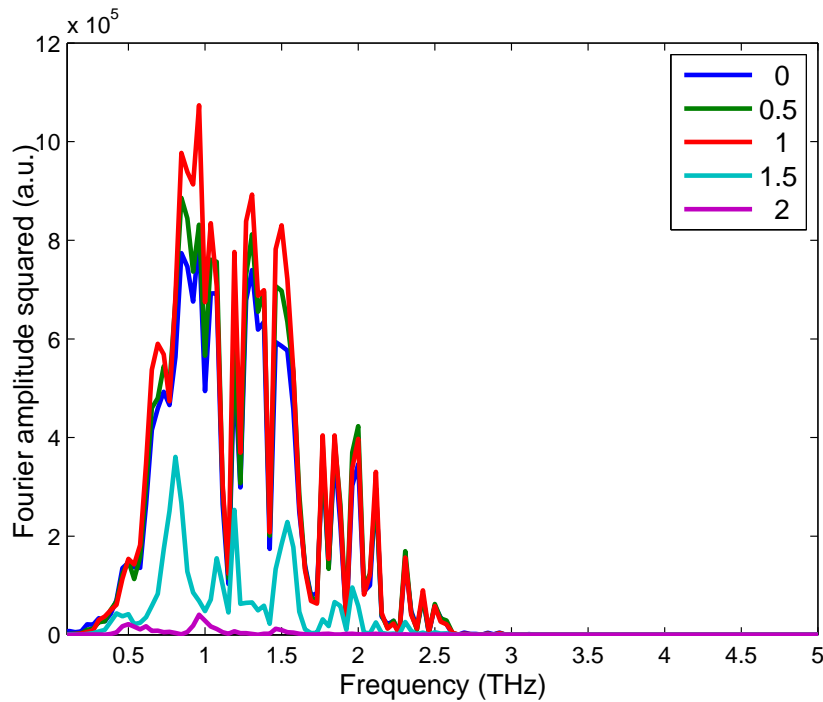


Figure 5.17. Power spectrum at certain x -axis knife locations. The power spectrum of the THz waveforms acquired with a x -axis knife-edge scanned at a distance of $150\ \mu\text{m}$ from the crystal. Colours represent different x -axis positions. At each successive position of the knife, the THz electric field becomes weaker until when the THz radiation is entirely blocked by the knife. This can be seen at $x = 0\ \text{mm}$, where the knife does not obstruct the THz beam, as opposed to $x = 2\ \text{mm}$, where the THz radiation is totally blocked.

Model validation

In order to validate the developed Gaussian aperture numerical model, the experimental setup is simulated with the estimated and measured values for experimental parameters like (i) IR pump beam waist, (ii) acceptance angle as determined from the crystal-parabolic distance at the parabolic mirror focal point, (iii) knife to crystal surface distance and (iv) the THz frequency of interest. The exact IR pump beam waist

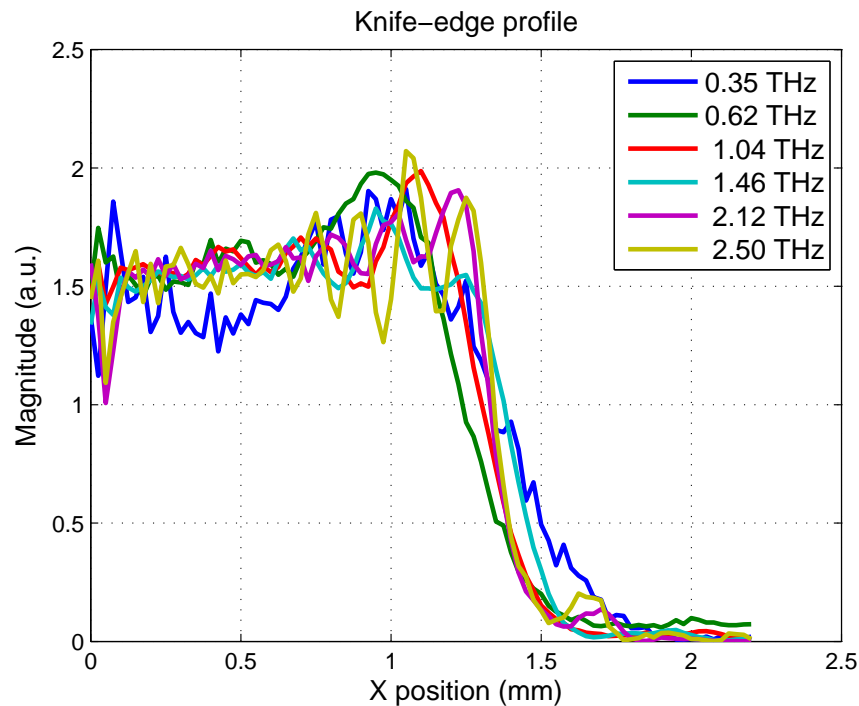


Figure 5.18. X-axis knife-edge profile of selected frequencies. Selected frequency components are shown at intervals of x -axis knife position. This knife-edge profile is also shown to illustrate the integrated spatial distribution of THz pulse at selected frequencies that are unaffected by water vapour absorption and noise that occur at higher THz frequencies.

inside the crystal is estimated to be $51 \mu\text{m}$ from the optical setup. The Gaussian profile of the generated THz beam is proportional to the IR power, i.e. the waist will be reduced by a factor of $\sqrt{2}$ to $36 \mu\text{m}$. In reality, THz radiation generation is distributed along the bulk crystal thickness, but in our model, the distributed THz radiation generation is approximated as an aperture located at an effective distance ($300 \mu\text{m}$) within the crystal. Figures 5.21 to 5.26 show the simulated and experimental x -axis and y -axis knife-edge profiles at selected frequencies. The simulation is normalized with respect to the full power, while the measurement is normalized for best visual fit because measurement does not clearly yield the full power. The sensitivity of the system modelling to this parameter is probed by altering this distance to $100 \mu\text{m}$ and negligible qualitative changes in the final results are observed. The simulated knife-edges matches closely to all the experimental results in terms of the integral function shape and slope. Qualitatively, diffraction effects in the simulated knife-edge profiles appear to coincide well with the measured results. Differences are attributed to the discrepancy between the modeled and physical shape of the blade tip. With the beam

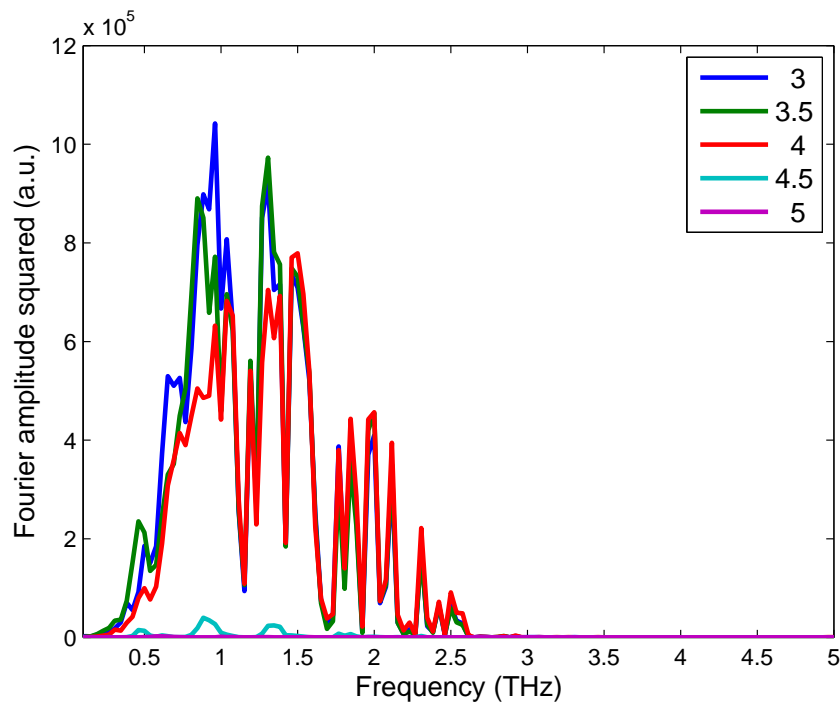


Figure 5.19. Power spectrum at certain y -axis knife locations. The power spectrum of the THz waveforms acquired with a y -axis knife-edge scanned at a distance of $150 \mu\text{m}$ from the crystal. Colours represent different y -axis positions. At each successive position of the knife, the THz field becomes weaker until when the THz radiation is entirely blocked by the knife. This can be seen at $y = 3 \text{ mm}$, where the knife does not obstruct the THz beam, as opposed to $y = 5 \text{ mm}$, where the THz radiation is totally blocked.

waist or aperture size held constant, it is noteworthy to observe the changes in the THz beam waist as the frequency increases. At low frequencies (such as 0.35 THz), the knife-edge profiles have a small slope implying a relatively large THz beam waist. This frequency range corresponds to the regime where the far-field radiation pattern resembles that of an obliquity factor in the far-field (Lin *et al.* 2010b) and Chapter 4. At higher frequencies (0.615 THz and 1.04 THz), the slopes begin to increase consistently with the increase of aperture size relatively to the wavelength. The overall agreement between the modeled and the experimental knife-edge characterization validates the modelling procedure. The decrease in beam waist with increasing frequency is well described quantitatively by the simulations, while the diffraction effects that are strongly dependent on the actual dimensions of the blade are demonstrated qualitatively.

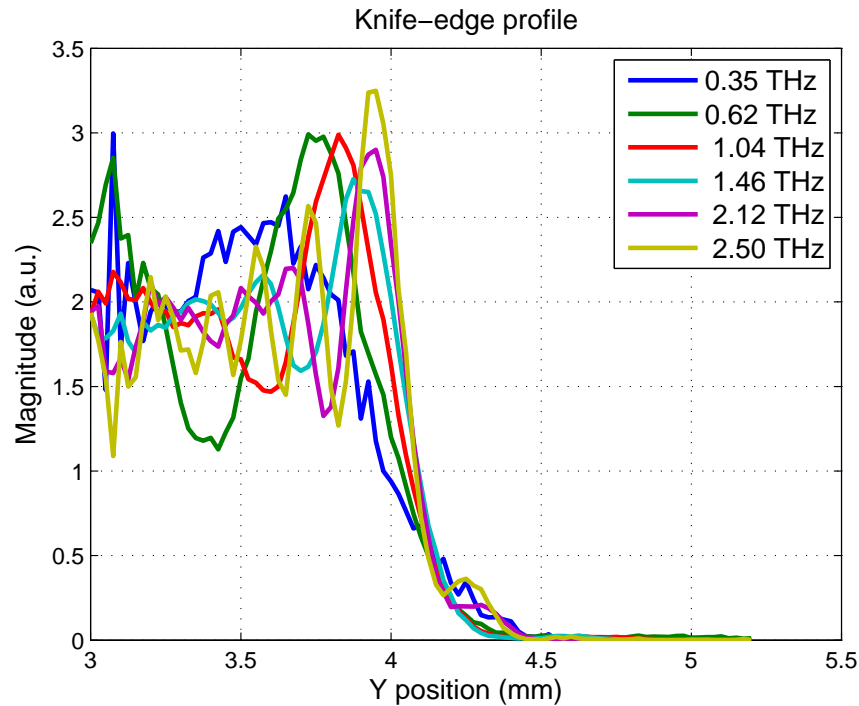


Figure 5.20. *Y*-axis knife-edge profile of selected frequencies. Selected frequency component is shown at intervals of *y*-axis knife position. This knife-edge profile is also shown to illustrate the integrated spatial distribution of THz pulse at selected frequencies that are unaffected by water vapour absorption and noise that occur at higher THz frequencies.

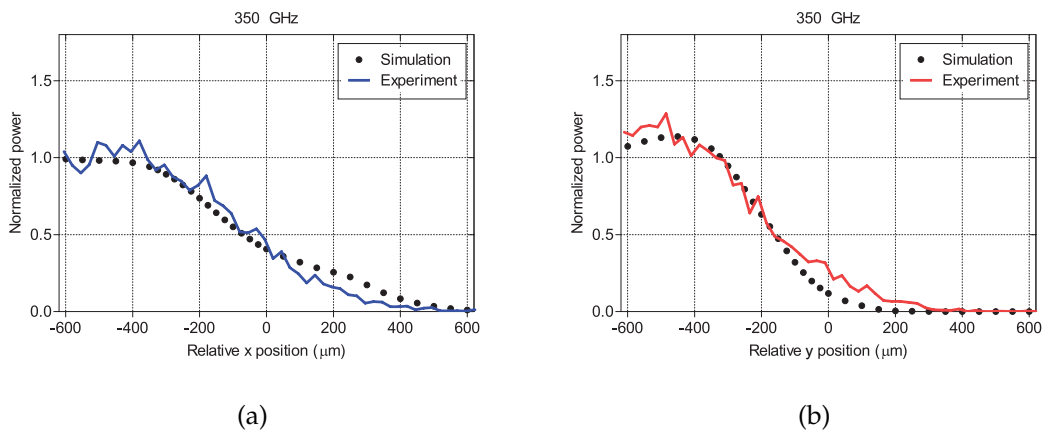


Figure 5.21. Model validation at 0.35 THz. (a) *x*-axis and (b) *y*-axis experimental and simulated knife-edge profile of THz radiation beam at 150 μm from the crystal backside.

5.3 Terahertz microscope modelling

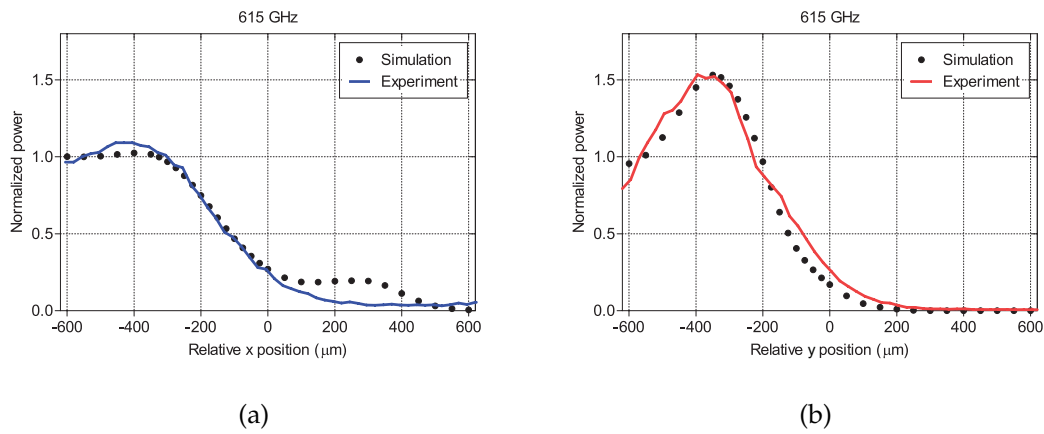


Figure 5.22. Model validation at 0.615 THz. (a) x -axis and (b) y -axis experimental and simulated knife-edge profile of THz radiation beam at $150 \mu\text{m}$ from the crystal backside.

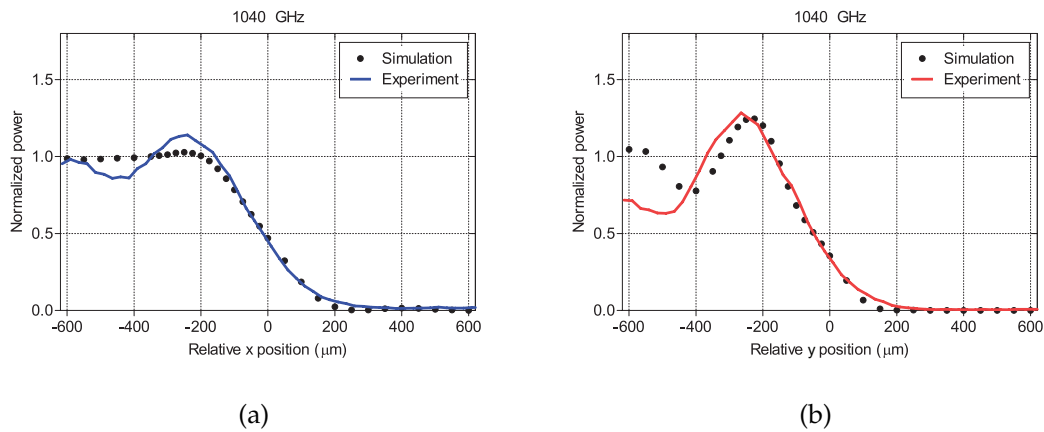


Figure 5.23. Model validation at 1.04 THz. (a) x -axis and (b) y -axis experimental and simulated knife-edge profile of THz radiation beam at $150 \mu\text{m}$ from the crystal backside.

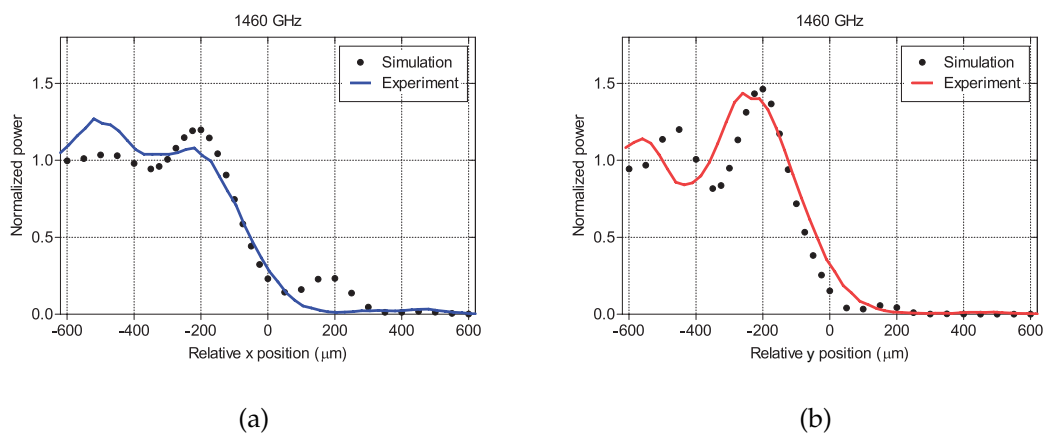


Figure 5.24. Model validation at 1.46 THz. (a) x -axis and (b) y -axis experimental and simulated knife-edge profile of THz radiation beam at $150 \mu\text{m}$ from the crystal backside.

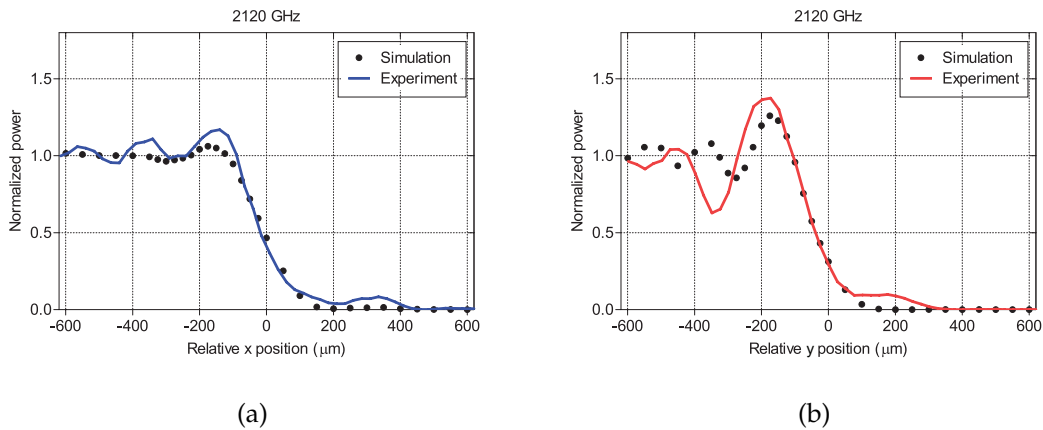


Figure 5.25. Model validation at 2.1 THz. (a) x -axis and (b) y -axis experimental and simulated knife-edge profile of THz radiation beam at $150\ \mu\text{m}$ from the crystal backside.

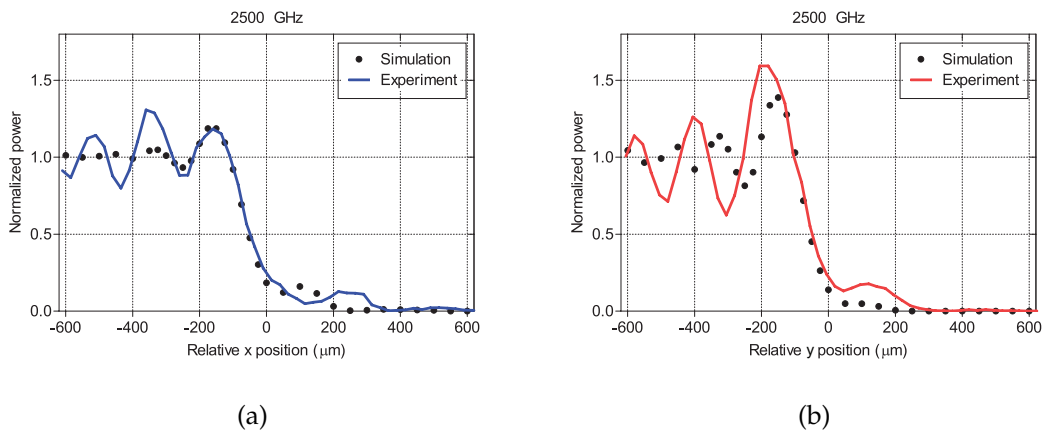


Figure 5.26. Model validation at 2.5 THz. (a) x -axis and (b) y -axis experimental and simulated knife-edge profile of THz radiation beam at $150\ \mu\text{m}$ from the crystal backside

5.4 Terahertz microscopy application

The intent of near-field studies is to resolve small samples that are sub-wavelength distance apart. To demonstrate an application of the computational model, the validated model can be used to predict the THz beam profile of selected frequencies at a near-field distances of $50\ \mu\text{m}$ from the crystal emitting surfaces as shown in Figure 5.27. Vertical structures with decreasing sub-wavelength separation distance are simulated by a groove pattern as illustrated in the left column of Figure 5.28(a). Convolution of the simulated THz beam profile (electric field distribution) with the decreasing groove separation distances in the groove pattern indicates the expected imaging performance. Note, however, convolution does not take diffraction into account that is present in real scans. The system response to convolution predicts the resolving of the

5.4 Terahertz microscopy application

grooves at 1.26 THz and above as can be seen in the left column of Figure 5.28(b)-(d). For experimental verification, a cyclic-olefin copolymer (TOPAS) sample comprising of identical vertical grooves is designed, fabricated, and scanned with the THz near-field microscope at an identical distance of $50\ \mu\text{m}$ from crystal surface. The vertical structure of the grooves ensures that only scans along x -axis is required. This minimizes the typically long scanning time associated with two-dimensional THz pixel-by-pixel imaging. Optical constants of TOPAS in the THz region as a function of frequency as measured by THz-TDS can be found in Fischer (2005). A groove depth of $50\ \mu\text{m}$ ensures it is within the THz source near-field region as considered from the output surface from the crystal, and the groove width effectively dictates the sample size. A photo of the optically transparent sample on a black background is shown in right column of Figure 5.28(a), with the grooves in gray. Figures 5.28(b)-(d) show the grayscale image of the amplitude component of the selected frequencies. Bright regions indicate a high amplitude caused by diffraction as opposed to the dark regions that represent the low amplitudes. Resolving a separation distance of $100\ \mu\text{m}$ with 1.26 THz confirms sub-wavelength resolution of smaller than $\lambda/2.3$. This is in close qualitative agreement with the extrapolated results in the left column.

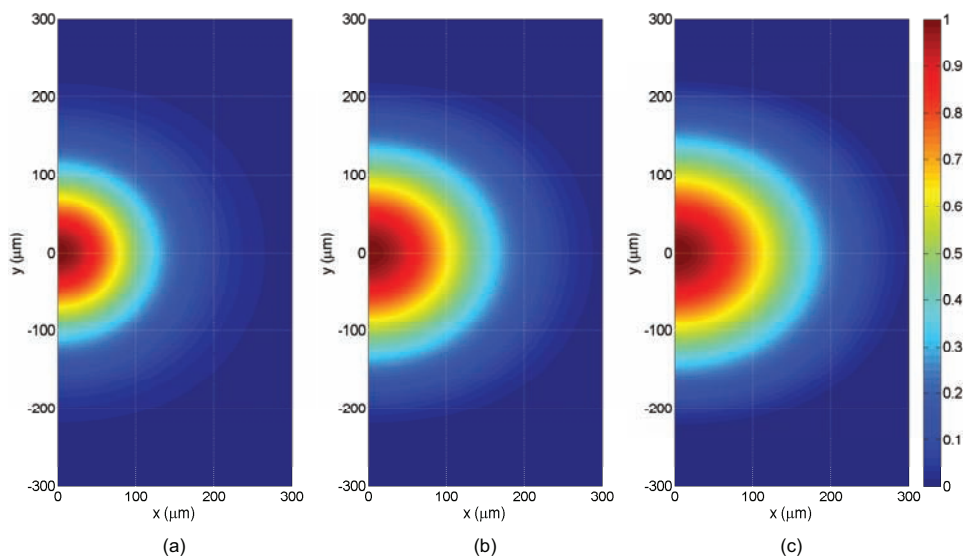


Figure 5.27. Contour plot along the x and y -axis of the THz beam profile at $50\ \mu\text{m}$. THz beam profile at (a) 2 THz (b) 1.26 THz and (c) 1 THz. The normalized z -component of the Poynting vector is represented by colour scale.

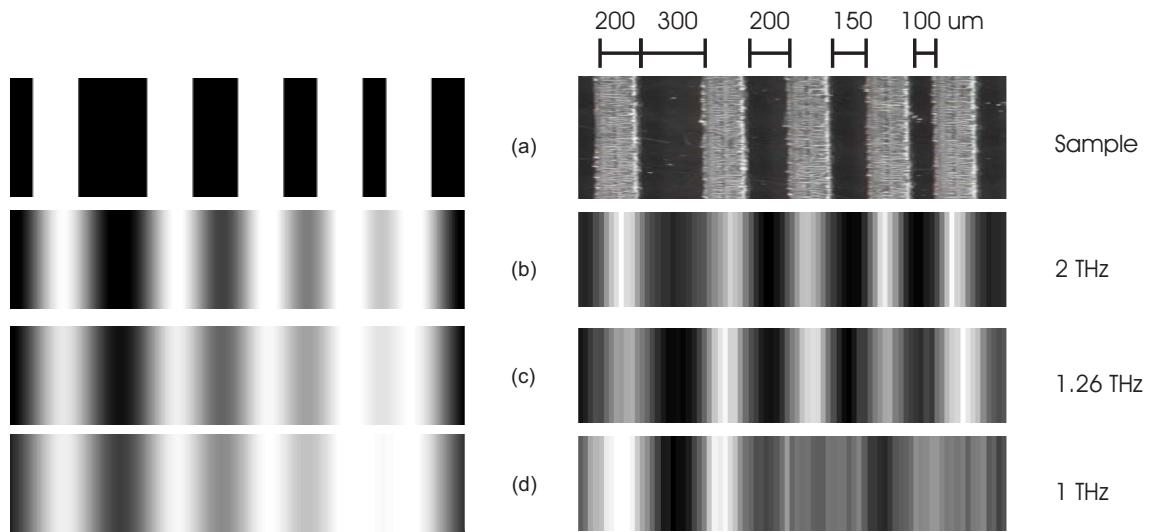


Figure 5.28. THz microscopy application. (a) (Left) Simulated sample structure comprising of grooves separated by decreasing sub-wavelength distances. (Right) The TOPAS sample comprising of vertical grooves (in white) separated by sub-wavelength distances of 300 μm , 200 μm , 150 μm and 100 μm . (b) (Left) Response from convolving THz beam waist at 2 THz with the simulated sample. (Right) Experimental grayscale image of the magnitude at 2 THz, resolves all distances. (c) (Left) Response from convolving THz beam waist at 1.26 THz with the simulated sample. (Right) Experimental grayscale image of the magnitude at 1.26 THz, resolves all distances. (d) (Left) Response from convolving THz beam waist at 1 THz with the simulated sample. (Right) Experimental grayscale image of the magnitude at 1 THz, resolves only the 300 μm distance.

5.5 Chapter summary

In this Chapter, we have attempted to reproduce the reported THz power enhancement from thin ZnTe electro-optical crystal (Yuan *et al.* 2002) and have obtained a null result. In addition to the investigation, we have computationally modeled the sub-wavelength THz emission point on a nonlinear electro-optical crystal, used in broadband THz near-field emission microscopy, as a radiating aperture with Gaussian intensity distribution. We have validated the model of the Gaussian aperture by conducting dual-axis experimental knife-edge experiment in the near-field region while taking into account the limitation of THz radiation detection setup. An application example is demonstrated by scanning over a fabricated cyclic-olefin copolymer sample, embedded with grooves sub-wavelengths apart, and a resolution of smaller than $\lambda/2.3$

5.5 Chapter summary

is achieved in accordance with the model. As a whole, the model aids in the quantitative understanding of the many trade-offs between parameters, such as optical beam waist, crystal sample distance and frequency components, critical to this type of THz near-field microscope design. A micron-sized resolution for biological microscopy is achievable by means of a smaller aperture realized by tighter focusing of the IR pump beam and a shorter detection setup distance. This in turn implies a smaller Rayleigh range and hence requires a crystal tens of microns thick. As the generated THz electric field is proportional to the crystal length and that prolonged exposure leads to heating effects (Lin *et al.* 2010a), future work may incorporate crystal length and hence the generated THz power into the numerical model. The work has introduced and validated numerical techniques for the 3D modelling of a focused beam THz near-field setup with an electro-optical crystal and can be extended without a loss of generality to other focused beam THz techniques. This therefore concludes the investigation into focused beam THz near-field imaging. The next Chapter summaries the research work conducted in this Thesis and discusses future directions.

Thesis Summary

THIS Chapter concludes the work described in this Thesis by drawing together the research described in previous chapters and discussing future directions. Chapters 1 to 3 contains the necessary background review materials to THz near-field imaging. Chapters 4 studies the THz photoconductive antenna material aspect for fabrication purposes toward potential application in a THz near-field system. Chapters 5 and 6 provides an in-depth examination of the generated THz radiation in the far-field and near-field regime respectively. This Chapter also aims at summarising the original contributions thus far.

6.1 Thesis conclusions

This Thesis is aimed at investigating the focused beam near-field technique. This Thesis begins the investigation by introducing THz radiation, sources and detectors and outlines the motivations for near-field imaging in Chapter 1. Mechanisms of common THz radiation generation and detection techniques are described and applied into realising several THz time domain spectrometers for the first time at National T-ray Facility as described in Chapter 2.

6.1.1 Review of THz near-field imaging

Chapter 3 reviews the THz near-field imaging techniques in the literature. Pulsed THz near-field techniques can be categorised into three main approaches based on electromagnetic confinement means, namely aperture, tip and focused beam based techniques. Even though the tip based method achieves the highest spatial resolution to date, the radiation throughput suffers from a reduction of r^6/λ^4 with a decreasing source dimension. This hence places a limitation on its practical applicability. In addition, the tip complicates the identification of the near-field components from the incident background THz radiation. Contrary to the aperture and tip based methods, the electro-optical approach with the highly focused beam technique is the more efficient alternative that has received less attention but is emerging as an important candidate for near-field application.

6.1.2 Far-field modelling of focused THz radiation generation

Chapter 4 models localised THz radiation generation in a ZnTe electro-optical crystal as radiating aperture with Gaussian intensity distribution and validates it experimentally. The work demonstrates that the reduction of THz SNR with increasing confinement is not only due to higher order nonlinear process such as two photon absorption, but also due to the evolution of the THz radiation pattern, leading to measuring less of the generated THz radiation. This work aims at bringing an awareness to the THz community of the effect of sub-wavelength aperture-like sources in THz radiation generation. This Chapter also applies a published water heating model to model the prolonged heating effects of an optical beam on a ZnTe crystal for THz radiation generation. The simulation result quantifies the worst-case scenario average temperature

6.2 Future work

rise for high and low pump power density. Maximum heating is observed to occur on the crystal surface and the heating is large for a small beam waist with a comparative lower penetration depth than lower power density.

6.1.3 Terahertz microscope modelling

Chapter 5 attempts to reproduce the reported THz power enhancement from thin ZnTe electro-optical crystal experimentally with null result. In addition to the investigation, this Chapter computationally models the sub-wavelength THz emission point on a nonlinear electro-optical crystal with as Gaussian intensity distribution and validates it accordingly with dual-axis experimental knife-edges in the near-field regime. An application example is demonstrated by scanning over a fabricated cyclic-olefin copolymer sample, embedded with grooves sub-wavelengths apart, and a resolution of smaller than $\lambda/2.3$ is achieved in accordance with the model.

6.1.4 Summary

As a whole, Chapter 1 and 2 presents the fundamentals of this Thesis. Review of existing THz near-field techniques are discussed in Chapter 3. The investigation of the focused beam near-field approach is carried out in two folds; far-field in Chapter 4 and near-field in Chapter 5. In addition to these parts of the original contributions, the Thesis presents three sided investigations are described in the appendices: (i) THz photoconductive antenna material characterisation (ii) Gas recognition with THz-TDS (iii) THz near-field material detection.

6.2 Future work

6.2.1 Far-field modelling of focused THz radiation generation

The simple model can be extended to include diffraction effects for a better curvefit to the experimental knife-edge measurements for the investigated THz frequencies. To better simulate the heating effects, the peak pump power should be used. Ideally, this can be experimentally verified by measuring the thermal radiation rise remotely, using non-contact thermometers such as an infrared pyrometer. Uncertainties, however, will be introduced due to the measurement distance and instrument noise.

6.2.2 Terahertz microscope modelling

Sub-micron resolution for THz biological microscopy is achievable by means of a tighter electromagnetic confinement realized by smaller focusing of the IR pump beam and a shorter detection setup distance. This in turn implies a smaller Rayleigh range and hence a crystal length of several tens of microns for constant THz source size. As the generated THz electric field is proportional to the crystal length and that prolonged exposure leads to heating effects, future work may experimentally study the trade-offs between crystal thickness, achievable resolution, and photodamage threshold. This can subsequently be incorporated into the numerical model for useful extrapolations.

6.3 Summary of original contributions

The key contributions in this Thesis are summarised as following:

1. Far-field modelling of focused THz radiation generation

It is widely known in the literature that a higher-order nonlinear process such as two photon absorption is the cause behind a reduction in THz radiation throughput in localised THz radiation generation in a typical THz-TDS system. The contribution in this Thesis semi-analytically models the beam confinement as a radiating Gaussian aperture. Validated by experimental results, the model illustrates the breakdown of the paraxial approximation at low THz frequencies. The findings show that the shape of the radiation pattern causes a reduction in detectable THz radiation and hence contributes significantly to low signal-to-noise ratio in THz radiation generation (Lin *et al.* 2010b).

2. Terahertz microscope modelling

This Thesis makes a further contribution via an investigation of high optical confinement in a THz emitter with full-wave numerical Gaussian aperture modelling, in the near-field. Based on realistic parameter values, the model allows for THz beam profile extrapolation, in the near-field regime, for potential THz microscope design and application. The proposed validated numerical model therefore aids in the quantitative understanding of the performance parameters (Lin *et al.* 2011).

Ancillary contributions in this Thesis are addressed in the Appendix. These include:

1. Material characterisation in THz PCA Manufacture

Silicon-on-sapphire material is characterised through systematic radiation damage and carrier lifetime measurement. The work is conducted in conjunction with Dr Raphael Clady, at the Laser Spectroscopy Group of the School of Chemistry, University of Sydney. The work is in close agreement with the findings in the literature (Doany *et al.* 1987) and empirically demonstrates silicon ion implantation as an alternative promising means to reduce the carrier lifetime for further improvement in the THz bandwidth.

2. Terahertz near-field material detection

In collaboration with Prof Masayoshi Tonouchi at Tonouchi Laboratory, Institute of Laser Engineering, Osaka University, investigation on the application of THz near-field system for material detection is conducted. In particular, the preliminary experimental work focuses on studying structures for sample deposition with near-field illumination and far-field detection. Such an approach has not been attempted and therefore underpins the future development of THz near-field technology.

3. Gas recognition with THz-TDS

Finally, a small contribution is made in the preliminary demonstration of THz-TDS to real-time gas recognition. The work outlines the framework for such a system and applies two different type of features; reference free spectrum and frequency features from reference pulse estimation. Classification is performed by means of the minimum Euclidean distance classifier and the Submillimeter, Millimeter, and Microwave Spectral Line Catalog (Lin *et al.* 2007, Lin *et al.* 2008).

Terahertz Time Domain Spectroscopy Setup

SETTING up a THz-TDS from scratch is a highly involved and time consuming exercise. This Chapter lists and briefly describes the components and equipment used in this Thesis as well as summarising the practical lessons gained from the process.

A.1 Optical alignment

Setting up a THz-TDS system from scratch is a highly involved and time consuming exercise. The process of a setup is an evolved one that typically begins with an understanding of an existing setup; the purpose, requirements and limitation of the optical components. This is then followed by drafting up a proposed layout and then implementing it. Due to high power of the pulsed laser, alignment of the optical components with an alignment laser of a relatively low power (e.g. laser pointer, class 2 lasers) is necessary for inexperienced personnel at the beginning stage.

A.1.1 Practical safety advice

The femtosecond laser used in generating THz radiation in our laboratory is centered around 800 nm and is classified as class 4 (high powered) laser, i.e. capable of producing hazardous diffuse reflections, skin burns and fire hazards. Safety is therefore a must with these lasers. Supervised training is received prior to working alone in the laboratory. Precautions include the following:

- Remove any shining object that may reflect/scatter light (e.g. necklace, watch, rings) prior to entering laboratory.
- Wear laser safety goggles marked with the protected wavelength, spectral range and test mark. Goggles are advised for optical alignment or open beam experiments, and during laser service.
- Open communication with other personnels.
- Use an IR viewer card to determine the beam path as shown in Figure A.1.
- Use the “arm stance” in optical alignment to avoid accidentally moving the eye level to beam height.

A.1.2 Practical alignment tips

1. Component height

Make sure the mirrors, stands for optical components, and irises are adjusted to

A.1 Optical alignment

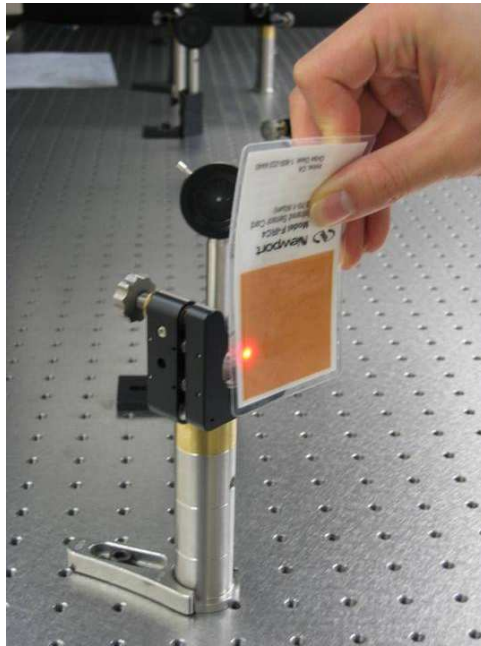


Figure A.1. Use of IR viewer card. The IR viewer card is used to determine the beam path particularly when working with low IR powers or the use of goggles.

the same height as the laser output. For the stands, achieve this by measurement with a ruler and stack on extra brass rings to compensate for the height difference. For the pinhole or iris, fix location on the tabletop, adjust height accordingly to allow alignment beam to pass through.

2. Beam height

Before placing a mirror, ensure the beam is flat, i.e. same height. Achieve this by means of having two pinholes of same height, one close to the source and one at the location of the mirror. The beam should pass through both pinholes.

3. Mirror horizontal translation

Once height of the mirror and beam height is fixed, the mirror is translated in the x - y direction where the beam is at. At the same time, orientate the mirror to enable the alignment beam to pass through both irises. If the beam is displaced further in one direction from the pinhole, the mirror needs to be displaced in the same direction orientated slightly for a straight beam path.

NOTE:
This figure is included on page 123 of the print copy of
the thesis held in the University of Adelaide Library.

Figure A.2. Beam horizontal alignment. The mirror is displaced along the x , y axis and orientated to guide the beam through both irises. (Figure: courtesy of Mr Benjamin Seam Yu Ung).

A.2 Hardware specification

This section highlights the main equipment required for THz-TDS setup using either generation by means of optical rectification or photoconduction, and detection via electro-optical sampling or photoconductive sampling. Photoconductive sampling is comparatively simpler than electro-optics as less optical parts are required.

A.2.1 IR beam path

The optical components are all readily available commercially off the shelf.

Femtosecond laser

The Mai-Tai by Spectra-Physics laser is a class 4 laser that generates near 800 nm pulses of femtosecond duration with an average power greater than 1.5 W. The Mai Tai is composed of a CW diode-pumped laser and a mode-locked Ti:sapphire pulsed laser. In the CW laser, a diode laser is used to pump the Nd:YVO₄ lasing medium to produce 1064 nm output, which, is then frequency doubled to the visible spectrum in a temperature tuned Lithium Triborate (LBO) nonlinear crystal. The output then pumps the Ti:sapphire lasing medium in a folded cavity and uses an acousto-optic modulator for mode-locking and wavelength tuning. The beam waist is reported to be less than 1.2 mm. A full description of its operation can be found in the manufacturer's manual.

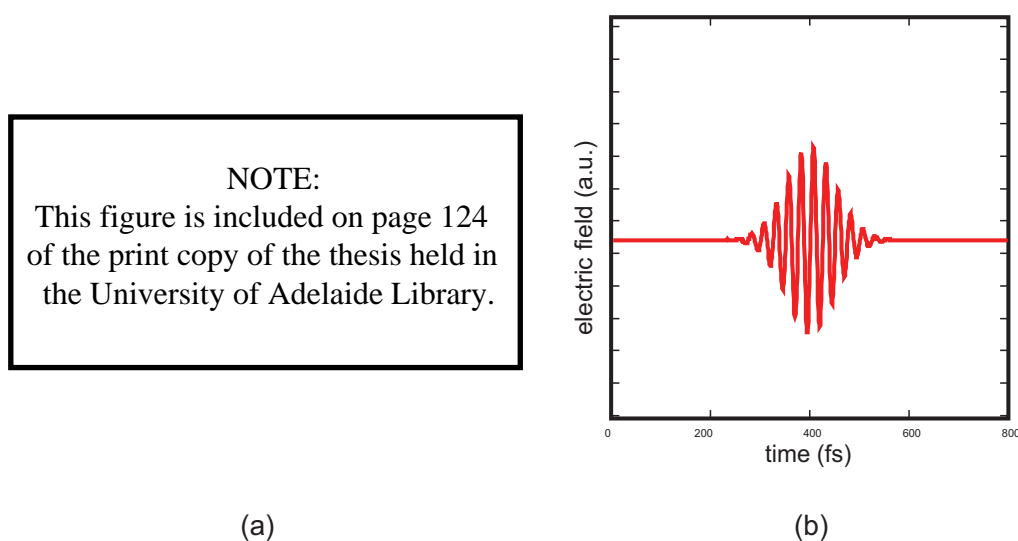


Figure A.3. Femtosecond laser source. (a) Spectra-Physics Mai-Tai that generates near 800 nm pulses with an averaged power greater than 1.5 W. (Photo: courtesy of Spectra-Physics). (b) The electric field oscillations in a femtosecond pulse, where the angular frequency corresponds to the central wavelength of the pulse.

Optical mirrors

The optical mirrors for guiding probe and pump beam paths are adapted for broad-band radiation. They have silver metallic coating for highly reflectivity for the 680-820 nm femtosecond pulses. The mirrors are supplied by Newport.

Beam splitters

Thorlabs Optics beam splitters are polarisation independent therefore no polarisation rotation is necessary for subsequent experimentation. The beam splitters are made from a broadband material: UV Fused Silica and coated for optimal performance at 700 to 1100 nm.

Neutral density filters

New Focus 25.4 mm diameter Neutral Density (ND) filters with attenuation that spans from 10 to 99% are used widely throughout the optical setup to cater for stringent power level requirements of THz emitters and detectors.

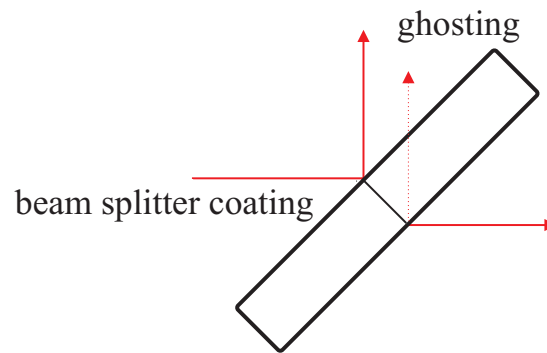


Figure A.4. Beam splitters. The finite thickness of beam splitters and the refractive index change causes deviation in the transmitted beam from the incident beam. A ghosting beam close to parallel to the reflected beam with a reduced power is also induced due to the refractive index change.

Retroreflector

A gold hollow retroreflector with 63.5 mm clear aperture diameter mounted on a linear delay stage is used in the probe beam delay path to reflect the incident light back along the same vector but opposite direction. A retroreflector with longer clear aperture diameter eases optical alignment.

Optical lens

Thorlabs plano-convex BK 7 25.4 mm diameter optical lenses are used for reducing the optical beam waist for THz radiation electro-optical generation and electro-optical sampling. The lenses have anti-reflective coating for optimal operation at 650 to 1050 nm. The minimal optical beam waist or spot size and Rayleigh range is a function of the focal length. Focal lengths spanning from 150 to 400 mm have been used. The same type of lenses with a diameter of 6 mm diameter and 10 mm focal length are used focusing optical beams onto photoconductive antennas.

A.2.2 THz radiation emitters & detectors

Zinc Telluride

The ZnTe electro-optical crystal used are square cut $\langle 110 \rangle$ crystal from Zomega Terahertz Corporation with a thickness of 1 mm and a MaTeck GmbH supplied 25 μm ZnTe adhered by epoxy (1 μm thick) to a $\langle 100 \rangle$ 500 μm thick ZnTe crystal. Note that

A.2 Hardware specification

eV Products is an alternative supplier. For generation, in order to optimise the radiated field, the $\langle 110 \rangle$ crystal needs to be rotated via the mount to an angle between the crystal (001) axis and the pump beam polarisation. A guideline for determining the rotational angle for zinc blend crystals can be found in Rice *et al.* (1994). A starting angle of 55° is recommended and note that 180° will produce no polarisation and hence THz field (Chen and Zhang 1999). The direction of the wave vector is along the (110) crystal axis and a straight cut crystal is preferred over a round cut counterpart, as finding the other crystal axis would then become intuitive. Similarly in detection, to optimise the measured electric field magnitude, the crystal axis (001) needs to be 90° or 270° with respect to the THz electric field, and the field also needs to be either perpendicular or parallel to the probe polarisation (Planken *et al.* 2001).

PCA & silicon lens

The photoconductive antennas for THz radiation emission and detection are Freiburg University, Germany, custom fabricated strip lines and H structure antennas on a LT-GaAs substrate. Specifications of the antennas are detailed in Walther (2003). The high impedance hyper hemi-spherical Tydex silicon lens is used to couple the generated or detected THz radiation into and from air. The lens has a resistance value of $1 \text{ G}\Omega$.

Wave retarders

Newport wave retarders also known as wave plates modifies the polarisation of light and are used in the THz electro-optical sampling setup. In the polarisation plane, the axis is broken down to a fast and slow axis with the wavelength difference between the 2 axis governed by the ratio between the refractive indices n_{fast} and n_{slow} . The phase difference, known as retardation, is commonly expressed in terms of wavelength and therefore a half wave retardation means a phase difference between the fast and slow waves of $\pi/2$. Half wave plates rotate linearly polarised light with an angle θ into linearly polarised light to 2θ in an anti-clockwise direction when y -axis is the fast axis. Similarly, for a clockwise circular polarisation, it rotates it to be anti-clockwise. Quarter wave plates converts linearly polarised light to anti-clockwise circular polarisation and the inverse is true. Circular polarisation only holds when θ is 45° , otherwise it is elliptically polarised.

Pellicle

A Thorlabs 50.4 mm diameter pellicle beam splitter combines the incident THz pulse and a linearly polarised probe beam so both can copropagate in the electro-optical crystal as part of the electro-optical sampling setup. The pellicle beam splitter is coated for an averaged reflection to transmission ratio of 45 to 55 for 700 to 900 nm.

Wollaston prism

Thorlabs Wollaston prism separates the circularly polarised probe beam into two orthogonal components in the electro-optical sampling setup. The angle of separation between the polarised output is 20° .

Balanced photodiodes

New Focus Silicon large-area balanced photodiodes are used in electro-optical sampling to measure the polarised outputs of the probe beam. The maximum power per photodiode is 10 mW/mm^2 . Typical common mode rejection is 40 dB.

A.2.3 THz radiation path

Parabolic mirrors

Edmund Optics gold coated off-axis parabolic mirrors are used to collimate and focus the generated THz radiation. An off-axis angle of 90° is used. In a standard THz-TDS setup, the distance between two parabolic mirrors is twice the focal length even for the collimated beam path. The 25.4 mm diameter parabolic mirror has an effective focal length of 101.6 mm.

Teflon plate

An in-house fabricated Teflon plate is inserted prior to the last parabolic mirror before the detection stage in a THz-TDS setup with optical rectification. This is to ensure the residual optical beam does not interfere with subsequent detection.

A.2 Hardware specification

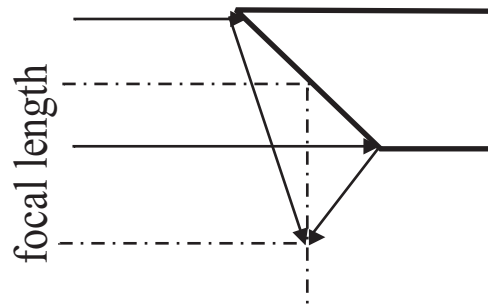


Figure A.5. Parabolic mirror. Parabolic mirrors with an off-axis angle of 90° are used to collimate and focus the generated THz radiation. The annotated focal length here is the effective focal length.

A.2.4 Mechanical components

Motorised linear delay stage

The ILS micro-stepper motor driven linear delay stage by Newport has a step size of $0.5 \mu\text{m}$ over a distance of 100 mm. The delay stage is controlled by a motion controller.

XYZ linear delay stage

Newport XYZ linear delay stages are used for displacing optics where alignment precision is critical. An example includes the optical alignment of a 10 mm focal length lens for the photoconductive antennas. The stages allow for a maximum travel of 12.7 mm along the x , y and z axis and are available in left or right hand configurations.

High resolution micrometer

Newport high resolution micrometers are used as linear actuators for the XYZ linear delay stage. The actuator has a travel of 13 mm, resolution of $0.5 \mu\text{m}$, and is driven manually.

Motorised actuators

Compact Newport motorised actuators with 12.5 mm travel, $0.2 \mu\text{m}$ resolution and closed-loop DC servo drive are installed to the XYZ linear delay stage for experiments such as a knife-edge profile for THz beam characterisation. The actuators are controlled by the motion controller.

Motion controller

Newport ESP 300 and 301 three axis motion controllers are used for controlling the motorised linear delay stage and actuators. The controller interfaces with a computer via a standard RS-232C or an optional GPIB interface.

Optical chopper system

The MC1000A optical chopper system by Thorlabs is used in conjunction with the lock-in amplifier to reduce the effect of the noise. This is achieved by simply amplitude modulating (chopper) the THz radiation pulse to a higher frequency, and demodulating (lock-in) for detection. The chopper system primarily consists of a chopper control box, optical chopper head and a 10-slot chopping blade. The system operates with an internal reference to produce a maximum chopper frequency of 1 kHz. The chopping frequency is used as the reference signal to the lock-in amplifier because it represents the actual measurement of the chopper frequency, which the lock-in amplifier needs to measure for measurement.

Lock-in amplifier

In order to recover the modulated sampled THz electric field, a Stanford Research Systems SRS830 lock-in amplifier is used. The lock-in amplifier measures the amplitude voltage of an AC input that is synchronised with the optical chopper signal, and therefore is able to measure voltages as small as few nano-volts in the presence of noise.

CCD camera

Thorlabs USB CCD camera is used for visually measuring distances of close proximities such as the distance between sample and THz source in a THz near-field setup. The camera is equipped with lens of approximately 40 mm focal length.

A.3 Sample

To demonstrate near-field imaging capability, a cyclic-olefin copolymer (TOPAS) sample comprising identical vertical grooves is designed as shown in Figures A.6. The vertical structure of the grooves ensures that only scans along x -axis is required. This minimizes the typically long scanning time associated with two-dimensional THz pixel-by-pixel imaging.

A.3 Sample

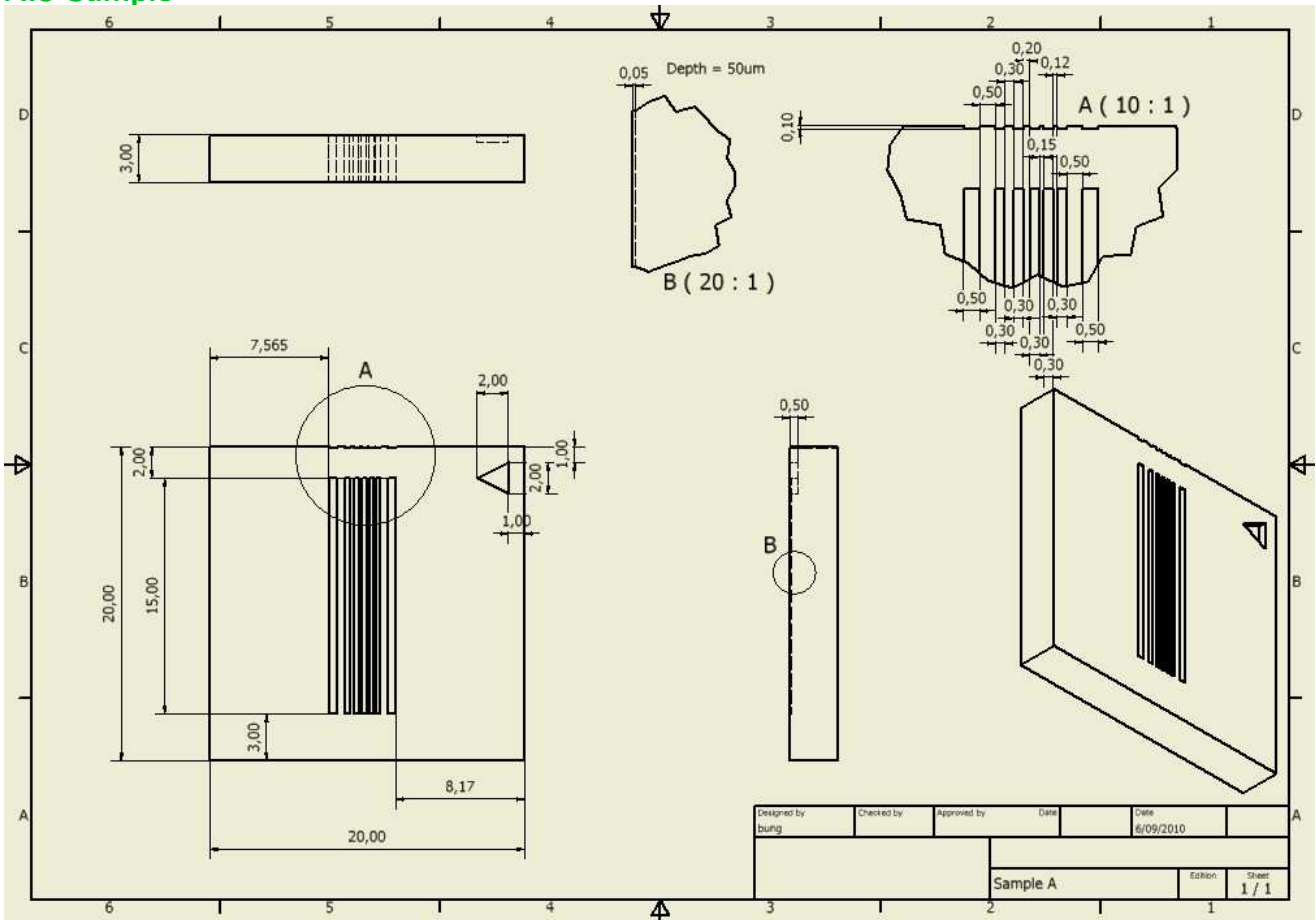



Figure A.6. Near-field sample design. The sample design comprising vertical grooves separated at increasing THz wavelengths used to determine the spatial resolution of the THz near-field imaging system. The design shows the different perspectives of the sample and the dimensions of the groove structures in mm.

Material Characterisation in THz PCA Manufacture



MOTIVATED by the shortage of THz sources and the need to produce antennas suitable for THz near-field imaging, silicon-on-sapphire THz photoconductive antennas are investigated with a geometry inspired by Freiburg's THz Physics Group design. With the optically transparent sapphire layer, silicon-on-sapphire offers the advantage of backside illumination thus allowing the photoconductive layer to be displaced in the sample's near-field region. This Chapter describes the material aspects of the THz photoconductive antenna fabrication process.

B.1 Introduction

Photoconduction is one of the means in generating and detecting THz radiation. The principles of operation are described extensively in Chapter 2. The shape of the THz pulse generated by PCA depends on the laser pulsewidth, substrate material properties, and the electrodes' electrical transmission line properties. The impinging laser pulses usually have a pulse-width shorter than 100 fs, therefore it is negligibly small compared to the generated THz pulse. Circuit reactances may be eliminated by having a small focused beam spot on the antenna. Therefore the critical parameter in antenna design is the selection of substrate materials.

Historically, various photoconductive materials have been used and the key operational parameters are tabulated in Table B.1. Carrier lifetime is an indicator for the achievable THz bandwidth. In general, the shorter the lifetime, the greater is the THz bandwidth. Carrier mobility is a measure for conversion efficiency or system responsivity from the applied DC bias to the peak amplitude of the THz pulse. Resistivity determines the maximum applicable DC bias, above which the system breaks down. The direct bandgap energy parameter dictates the minimum central wavelength of the laser for photoconduction. From the list of materials, radiation damaged SOS and LT-GaAs have been commonly used because of a good trade-off between short carrier lifetime (i.e. 0.6 ps and 0.3 ps) respectively and carrier mobility. Materials such as CdTe fabricated by Ultra-Violet (UV) enhanced organometallic vapor phase epitaxy also exhibit a very short carrier lifetime of 0.5 ps and a high carrier mobility. The epitaxial growth process, however, is non-conventional and can not be easily integrated with exiting semiconductor device technology (Nuss *et al.* 1989).

Photoconductive antennas on SOS substrates are suitable for THz near-field imaging as opposed to LT-GaAs because the optically transparent sapphire layer allows the antenna to be placed in the sample near-field region. A typical LT-GaAs has a substrate thickness of 600 μm (Walther 2003). With the photocarriers being generated on the semiconductor surface, the longest Fraunhofer distance with the maximum achievable 3 THz bandwidth for the smallest IR beam waist i.e. 2.5 μm is 0.5 μm , implying that the photoconductive layer is no longer in the near-field region of the sample and that the THz radiation would need to traverse through the substrate as shown in Figure B.1. In

Table B.1. Photoconductive material properties. Various photoconductive materials have been used for THz generation. The Table is adapted from Sakai (2005) and compares the material characteristics from the perspective of THz antenna fabrication. Carrier lifetime is an indicator for the achievable THz bandwidth. Carrier mobility is a measure for conversion efficiency or system responsivity from the applied DC bias to the peak amplitude of the THz pulse. Resistivity determines the maximum applicable DC bias, above which the system breaks down. The direct bandgap energy parameter dictates the minimum central wavelength of the laser for photoconduction. Radiation damaged SOS and LT-GaAs substrates offer the best trade-off in terms of carrier lifetime and carrier mobility and are hence commonly used as photoconductive materials for THz antennas.

Photoconductive material	Carrier lifetime (ps)	Mobility ($\text{cm}^2/(\text{VS})$)	Resistivity (Ωcm)	Bandgap (eV)
Cr:doped SI-GaAs	50-100	≈ 1000	10^7	1.43
LT-GaAs	0.3	150-200	10^6	1.43
SI-InP	50-100.0	≈ 1000	10^7	1.34
Ion-Implanted InP	2-4.0	200	10^6	1.34
Radiation damaged SOS	0.6	30		1.10
Amorphous Si	0.8-20.0	1	10^7	1.10
MOCVD CdTe	0.5	180		1.49
LT- $\text{In}_{0.52}\text{Al}_{0.48}\text{As}$	0.4	5		1.45
Ion-implanted Ge	0.6	100		0.66

an alternative arrangement, reflecting the PCA on the y -axis will yield the configuration shown in Figure B.1 right-hand side with the photoconductive layer also in the far-field region of the sample constrained by substrate thickness. Furthermore, detection sensitivity will be diminished because the optically induced carriers are not confined to surface region between the electrodes. A SOS PCA shown in Figure B.2 overcomes this dilemma with an optically transparent sapphire substrate well index matched to a thin silicon photoconductive layer that is placed in sample near-field vicinity. An application of a SOS PCA in THz near-field imaging can found in Bitzer *et al.* (2010). Even though SOS PCAs have been readily available in the past, they have seen a large decline commercially due to the various environmental laws in the USA and Europe. In an effort to also realise THz near-field setups with PCAs, this chapter therefore describes the process in fabricating SOS PCA. Semi-insulating GaAs PCA is also briefly described.

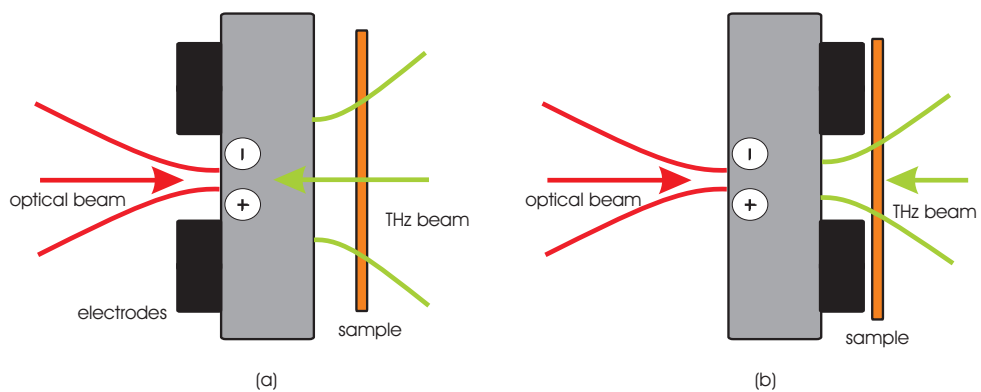


Figure B.1. Low-temperature GaAs PCA. The unsuitability of a LT-GaAs PCA for THz near-field imaging is demonstrated. a) With the photocarriers being generated on the photoconductor surface and a typical thickness of $600\ \mu\text{m}$ (Walther 2003), the photoconductive layer is no longer in the near-field region of the sample. b) Reflecting the PCA on the vertical axis will yield the configuration with the photoconductive layer also in the far-field region of the sample.

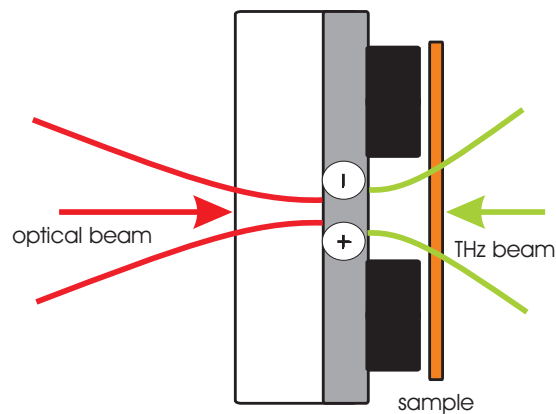


Figure B.2. Silicon-on-sapphire PCA. The suitability of the SOS PCA for THz near-field imaging is demonstrated. In this configuration, the optical beam impinges onto an optically transparent sapphire substrate that is closely index matched to the silicon photoconductive layer so that the thin photoconductive layer can be placed in the sample's near-field vicinity. An application of a SOS PCA in THz near-field imaging can be found in Bitzer *et al.* (2010).

B.2 Ultrafast semiconductor dynamics

To obtain an improved understanding of carrier dynamics in SOS and LT-GaAs photoconductors, we will present a summary of some of the effects occurring after optical excitation with an ultra-short laser pulse. An extensive coverage of ultrashort processes in semiconductors can be found in Othonos (1998). In a semiconductor at equilibrium, the energy of electrons and holes are described by Fermi-Dirac statistics. The energy of the phonons are governed by Bose-Einstein statistics. Thermal equilibrium is established through carrier-carrier and carrier-phonon interactions. At the equilibrium, the average momentum of carriers is zero. In the case of an optical pulse with energy greater than the bandgap energy level E_g , the pulse is absorbed by the semiconductor to generate hot carriers with an energy being the difference between the optical and bandgap energy level. Due to the polarization of the laser pulse, the average momentum initially may not be zero, but the momentum does undergo a very fast randomization in a time less than 100 fs. At this time the electrons and holes can be treated as separate systems. The electrons possess most of the excess kinetic energy because of their smaller mass. The hot carriers lose their kinetic energy by various scattering mechanisms, mostly by optical phonon scattering on a picosecond timescale. The carriers then either recombine sending out a photon or are trapped at a defect like an impurity, crystal defect or at the surface. These trapping mechanisms usually have time constants in the tens to hundred of picoseconds range. The trapping time constant τ_t is usually described by Shockley-Read-Hall statistics to be inversely proportional to the trap density N_t , expressed as

$$\tau_t = \frac{1}{N_t \sigma v_{th}} \quad (\text{B.1})$$

where v_{th} is the average carrier thermal velocity and σ is the capture cross section. In THz applications, we are interested in very fast optical switches to maximise THz bandwidth. Semiconductors with a high level of defects are therefore promising materials. The deep level trappings or recombination centres can be induced by means of radiation damaging materials such as in SOS where a carrier lifetime of 0.6 ps has been reached (Doany *et al.* 1987). Proton bombardment has been used in InP materials while retaining a relatively high electron mobility (Lamprecht *et al.* 1991). Other alternative approaches such as doping with compensating impurities have demonstrated a reduced carrier lifetimes to 60 ps with Cr:doped SI-GaAs (Lee *et al.* 1977). With a large density of defects in the form of grain boundaries, amorphous or polycrystalline

materials such as amorphous silicon (Auston *et al.* 1980) have also been explored. The downside of the amorphous structure is a reduced carrier mobility. As a whole, radiation damaged SOS offers the trade-off between short carrier lifetime and applicability for THz near-field imaging.

B.3 Radiation damaged silicon-on-sapphire

Silicon-on-sapphire consists of a thin layer (typically less than $0.6 \mu\text{m}$) of silicon grown on a sapphire (Al_2O_3) wafer. Silicon-on-sapphire is part of the Silicon-On-Insulator (SOI) family typically used for Complementary Metal-Oxide-Semiconductor (CMOS) technologies with the sapphire being an excellent electrical insulator and is transparent to an optical beam at 800 nm. Our SOS is sourced from Valley Design Corporation with 100 mm diameter (4 inch). The R-plane sapphire is $0.53 \text{ mm} \pm 0.05 \text{ mm}$ thick, while the epitaxial intrinsic $\langle 100 \rangle$ silicon layer has 100 Ohm-cm and $0.6 \mu\text{m} \pm 0.06 \mu\text{m}$ thickness.



Figure B.3. SOS Wafers. The packaged SOS wafers consist of a thin layer ($0.6 \mu\text{m}$) of silicon grown on a sapphire wafer (0.53 mm). The SOS wafers are from Vally Design Corporation with 100 mm diameter.

B.3.1 Ion implantation

In order to give rise to short carrier lifetimes, whilst maintaining the mobility, the SOS substrates are uniformly radiation damaged by means of ion implantation and

B.3 Radiation damaged silicon-on-sapphire

this is an alternative method (Smith *et al.* 1981) to other techniques. Doping with Si ions has also been investigated to reduce the carrier lifetime (Kappert *et al.* 1979) but only leads to a minor improvement. Radiation damage by means of ion implantation intends to introduce a predetermined defect density into the crystalline structure of the material with the defects acting as traps and recombination centres to increase the rate of recombination and hence lowers the carrier lifetime. The trap density and therefore the carrier trapping rate will vary linearly with the ion implantation dosage. Doany *et al.* (1987) investigated carrier lifetime as a function of various implantation dosages and discovered empirically that the lifetime saturates to 600 fs at a dosage level of $3 \times 10^{14} \text{ cm}^{-2}$. Various ions have been used, these include oxygen (Smith *et al.* 1981), argon (Brener *et al.* 1998), and silicon (Sakai 2005).

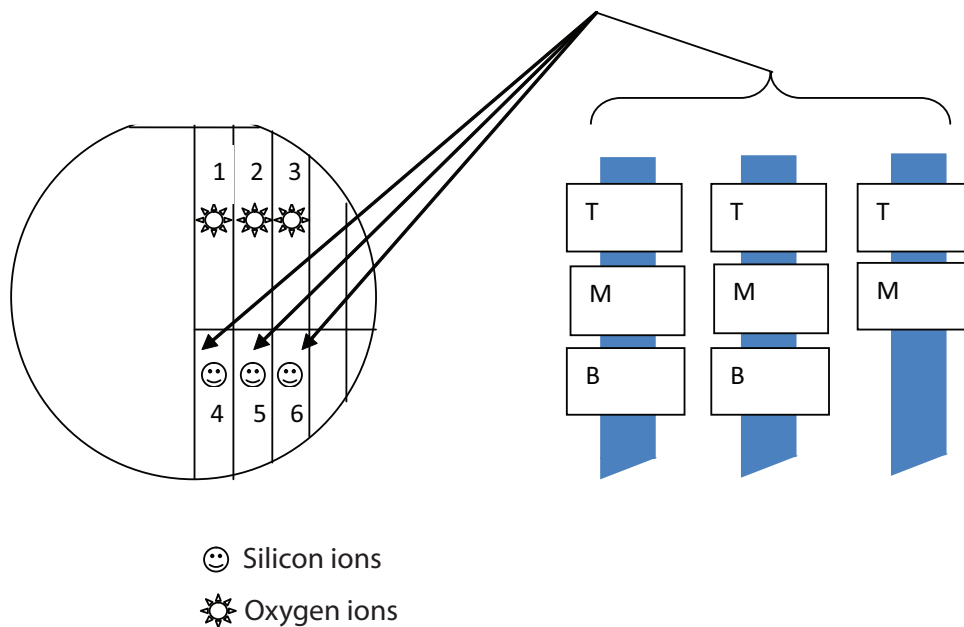


Figure B.4. Ion implantation on a test wafer. A half piece of wafer is sliced into six equally sized pieces with three of which implanted with silicon ions and other three with oxygen ions. For each ion type, a total of eight implants of various dosage levels are performed. The top, middle and bottom part of the strip is annotated as T, M and B respectively.

The implantation work are carried out at the Electronic Materials Engineering at Australian National University. Even though the dosage level has been studied with the carrier lifetime measurement (Doany *et al.* 1987), the work is relatively old and therefore a brief investigation is conducted with our collaborators. In such a work, a half of a piece of wafer is sliced into six equal sized pieces. Three of which are implanted with silicon and three with oxygen. Two of the three strips received three implants each, and one piece received two implants, making a total of eight implants for both

Table B.2. Oxygen ions implants. The oxygen ion energies computed and implantation dosage (cm^{-2}) conducted at the Electronic Materials Engineering, Australia National University are listed for each sample piece. For description of the annotations T, M, B, please refer to Figure B.4. This can be compared with the implants recipe detailed in in Doany *et al.* (1987).

Sample	Implant	270 keV	140 keV	60 keV
2	T	4.5×10^{15}	1.5×10^{15}	1.5×10^{15}
2	M	1.5×10^{15}	5.0×10^{15}	5.0×10^{15}
2	B	4.5×10^{14}	1.5×10^{14}	1.5×10^{14}
1	T	1.5×10^{14}	5.0×10^{13}	5.0×10^{13}
1	M	4.5×10^{13}	1.5×10^{13}	1.5×10^{13}
1	B	1.5×10^{13}	5.0×10^{12}	5.0×10^{12}
3	T	4.5×10^{12}	1.5×10^{12}	1.5×10^{12}
3	M	1.5×10^{12}	5.0×10^{11}	5.0×10^{11}

silicon and oxygen, as depicted in Fig. B.4. The implant details are tabulated in Table B.2 and B.3 for oxygen and silicon ions respectively. Ion implantation produces an increase in optical absorption so the implanted regions are clearly visible. The higher the implant fluence, the optically darker the sample.

The particular ion energies are selected to produce an uniform defect density throughout the sample. As demonstrated in Figure B.5, our SOS samples possess a more uniform defect density, as a function of depth, as compared to Doany *et al.* (1987).

The damaged materials also need to be thermally annealed in order to overcome the instability of the damaged materials at room temperature. A typical example for the instability is that the radiation damage is annealed away within days or weeks after implantation (Smith *et al.* 1989).

B.4 Semi-insulating gallium arsenide

Semi-Insulating Gallium Arsenide (SI-GaAs) samples are substrates for THz PCAs. These undoped high resistance ($>10 \text{ M}\Omega$) materials are supplied locally by Micro Materials & Research Consumables (MMRC). The material have an orientation of $\langle 100 \rangle$,

B.4 Semi-insulating gallium arsenide

Table B.3. Silicon ion implants. The silicon ion energies computed and implantation dosage (cm^{-2}) conducted at the Electronic Materials Engineering, Australia National University are listed for each sample piece.

Sample	Implant	450 keV	140 keV
4	T	2.4×10^{15}	9.0×10^{14}
4	M	8.0×10^{14}	3.0×10^{14}
4	B	2.4×10^{14}	9.0×10^{13}
5	T	8.0×10^{13}	3.0×10^{13}
5	M	2.4×10^{13}	9.0×10^{12}
5	B	8.0×10^{12}	3.0×10^{12}
6	T	2.4×10^{12}	9.0×10^{11}
6	M	8.0×10^{11}	3.0×10^{11}

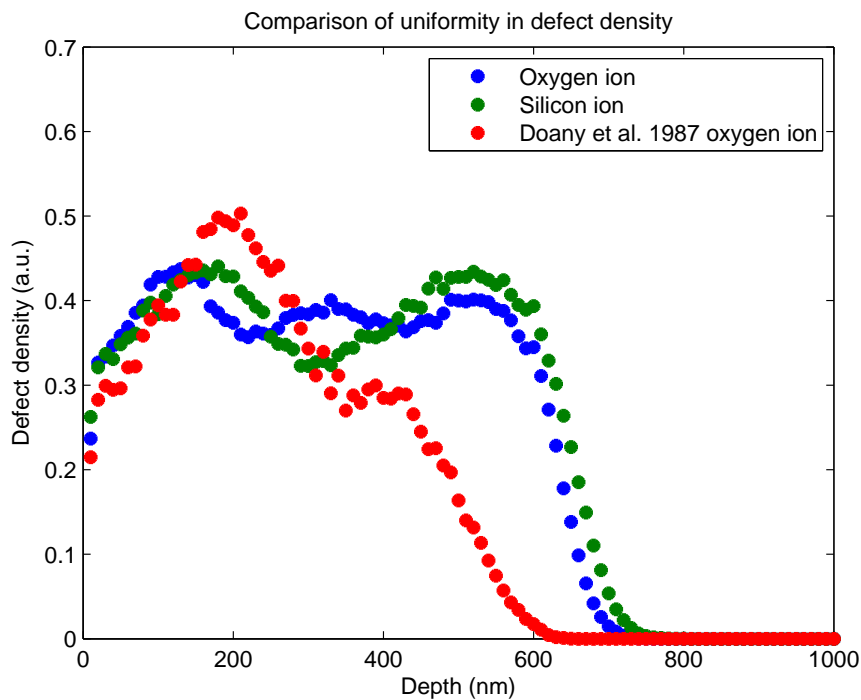


Figure B.5. Uniform ion implantation with depth of sample. A more uniform defect distribution across the depth of the substrate can be seen with our sample as opposed to the sample used in Doany *et al.* (1987).

500 μm thickness, 100 mm diameter (4 inch) and a high electron mobility greater than 5000 cm^2/Vs .

B.5 Carrier lifetime measurement

In order to estimate the trapping time τ_t for our SOS sample, we have to monitor the carrier population in the conduction band. This can be achieved by measuring the time resolved absorption changes or changes in the reflectivity. Drude model can be used for estimating the reflection changes. A full comprehensive review on carrier dynamics and measurement techniques can be found in Othonos (1998).

B.5.1 Drude model

Plasma oscillation frequency also known as Langmuir waves are rapid oscillation of the electron cloud in a conducting media such as metal. The cold plasma frequency is given by the equation

$$\omega_p = \sqrt{\frac{4\pi N_c e^2}{m^*}} \quad (\text{B.2})$$

where N_c , e and m^* are the carrier density, charge and carrier effective mass respectively. Following optical excitation, the optical reflectivity is dominated by the electron hole plasma. In order to estimate the plasma contribution to the reflectivity, Drude model is used. The Drude model was originally developed for the description of the electrical and optical properties of free carriers in simple metals. The model can also be used for doped semiconductors. The complex dielectric function in Drude model is

$$\epsilon(\omega) = \epsilon_\infty - \frac{4\pi N_c e^2}{m^*(\omega^2 + i\omega\gamma_c)} \quad (\text{B.3})$$

where γ_c is the inverse of the scattering time. Assuming no absorption, $\gamma_c = 0$, the relative transient reflectivity is derived as

$$\frac{\Delta R}{R} = \frac{4\pi N_c e^2 n}{(n^2 - 1)m^* \epsilon_\infty \omega^2} \quad (\text{B.4})$$

from which we observe a proportional relationship between transient reflectivity and carrier density (Yu and Cardona 1999).

Shank *et al.* (1983) investigates the effect of increasing the pulse intensity to an extent so that significant energy is transferred to the crystal lattice, causing it to melt. The melting starts on the surface and progresses into the bulk.

B.5 Carrier lifetime measurement

B.5.2 Experimental setup

A measurement based on optical pump and optical probe experiment commonly known as “pump probe” is carried out to measure the transient reflectivity of photoconductance in order to deduce the carrier lifetime. The principle of operation involves an optical pump beam to excite the sample of interest and photodiodes to measure the transmission or reflection of a normally incident probe beam through the excited sample.

A diagram of the initial layout of this setup is shown in Figure B.6. Mai-Tai femtosecond laser centered at 800 nm is used at a repetition rate of 80 MHz and pulsewidth of 100 fs. The setup was unsuccessful in measuring the lifetime due to limited pump power density on the sample. Moreover, having a pump probe setup operating in the transmission mode means that the detected transmitted probe is extremely weak in the presence of noise. The setup is therefore optimised to operate in reflection mode.

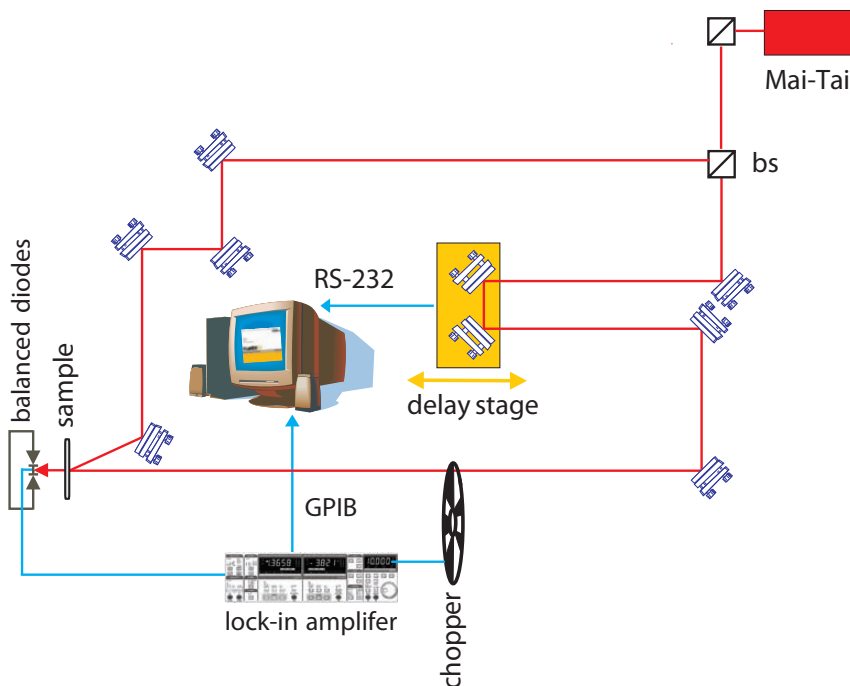


Figure B.6. Optical pump probe schematic. The schematic of the unoptimised carrier lifetime setup operating in transmission mode for measuring photoconductor carrier lifetime. The pump beam path is reflected onto the sample at a certain angle while the transmitted probe is measured by photodiodes.

A wavelength of 800 nm is slightly lower than the bandgap of GaAs (867 nm) and is within the excitation wavelength range of 780 to 805 nm where reflectivity linearly increases with pump power and is wavelength independent (Korn *et al.* 2002). Figure B.7

shows the working setup. The optical beam is split into a pump beam and probe beam by a 70% reflectance 10% transmission beam splitter. The pump beam path follows through an optical extension path to a mirror that reflects the beam onto the sample. Similarly, the probe beam goes through a delay stage and onto a mirror for reflecting to the sample. The pump is incident on the sample at 55° to the sample normal, while the probe is incident at 45° . The polarisation of the pump beam is rotated by 90° with respect to the probe beam with a half wave plate. The pump and probe beam are focused onto the sample by a pair of 200 mm focal length lens. For a 1 mm IR beam waist w , the focused Gaussian IR beam waist w_0 is estimated to be $50 \mu\text{m}$. The equation for computing Gaussian IR beam waist is

$$w_0 = \frac{f\lambda}{\pi w}. \quad (\text{B.5})$$

Since the beams are incident on the surface of the sample at an angle, the illuminated spot takes a shape of an ellipse with an area

$$A = \pi w_0^2 \sec \theta. \quad (\text{B.7})$$

The pump and probe focus area is therefore $13,700 \mu\text{m}^2$ and $11,100 \mu\text{m}^2$ respectively. The pump power is 650 mW while the probe is 3 mW. Measurement of the reflected probe beam requires a pair of auto-balanced photodiodes and a lock-in amplifier. By means of a beam sampler, a fraction of the probe beam is directed into the reference port of the photodiode to suppress the laser noise.

Coherence effects

It is well known that a coherent interaction between pump and probe pulses can alter the resulting probe signal when the two pulses overlap temporally in the sample in transient absorption or reflectivity experiments. This interaction can be described as generation of an induced grating in the sample that then scatters a fraction of the pump beam into the probe beam direction, thus affecting the recorded probe signal (Palfrey and Heinz 1985). To minimize this effect, a half wave plate is used to rotate the polarization directions of pump and probe beam to ensure orthogonality.

Debugging

The items noteworthy to check in the setup are not limited to the following:

- The pump and probe beam need to spatially overlap on the sample: Ensure this by means of operating the femtosecond laser at 710 nm, if possible, and observe using a camera with a macro lens.
- The pump power density needs to be high enough to generate a measurable signal. The controllable variables here are the incident pump power and focus size.
- The optical chopper modulates the pump beam that, in turn, modulates the overlapped probe beam for measurement.
- To accurately determine the point on probe zero delay position i.e. sample pump optical path length and probe optical length, a practical method of inserting a Second Harmonic Generation (SHG) crystal such as a Beta Barium Borate (BBO) in place of the sample is recommended. When the pulses of high power overlap, a middle beam is generated. This phenomenon is due to the phase matching criterion and is shown in the Figure B.8. By determining the probe zero delay position, one saves time from scanning for a weak signal over an entire delay stage at 10 μm step size.
- Once the feature is observed from the scans, the lock-in amplifier is autophased to obtain an accurate time representation of the signal.

The practical debugging items assist in the prompt discovery of the signal embedded in noise. These items are implemented in the following Section.

Optimisation

In an effort to optimise the setup in terms of pump power density on the sample, the setup is redesigned with the following changes under the constraint of the Mai-Tai laser power and fixed pulse repetition rate. A schematic of the optimised setup is shown in Figure B.7. This system is capable of delivering 685 times the pump power density than the previous unoptimised system. The key configurations in optimisations include the following:

- Pump beam directly incident on the sample thus creating a circular focal spot instead of an ellipse leading to smaller area.

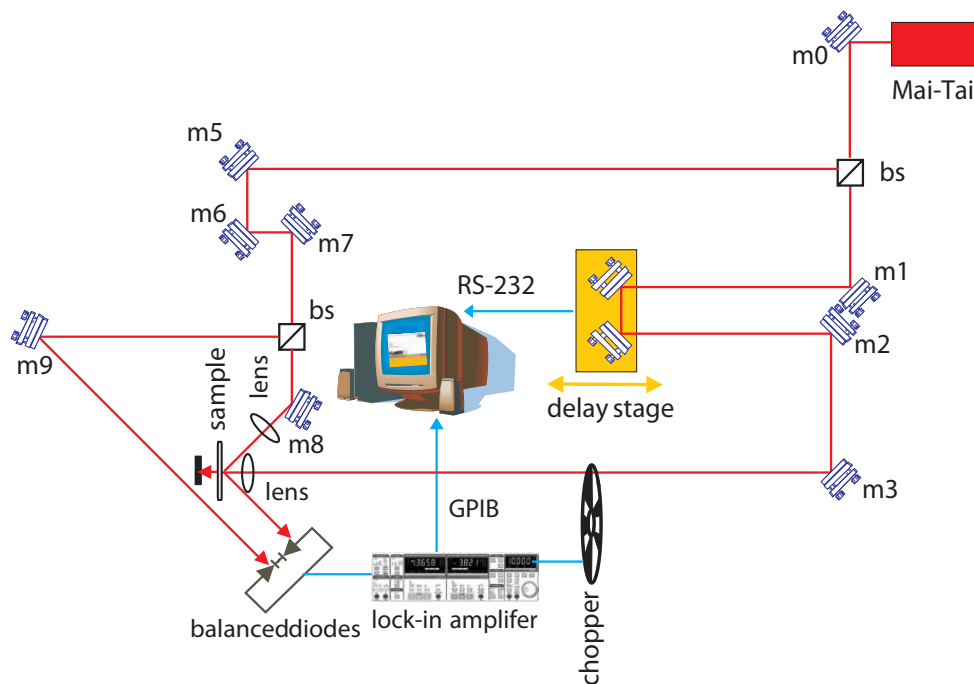


Figure B.7. Optimised optical pump probe schematic. The schematic of the optimised carrier lifetime setup operating in reflection mode. The pump beam path is directly incident onto the sample creating a circular focal spot instead of an ellipse leading to smaller optical area on the sample. A shorter focal length lens is also installed in the pump beam path to maximise the pump power density on the sample of interest.

- A 10 mm focal length lens is installed in the pump beam path to give an IR beam waist w_0 of $2.5 \mu\text{m}$. This is a reduction factor of 20 in beam waist as compared to 200 mm focal length lens.
- Installing a lens with such small focal length away from the sample affects the incoming and outgoing optical probe path. Simple trigonometry is used to determine the angle of probe incidence angle. This is calculated to be 45° after taking into account of the physical dimensions of a customised lens mount. On a side-note, the probe power density is not critical and should be of a very low power for optimised photodiodes detection.

With the system optimised, the following Section will perform photoconductor carrier lifetime measurement.



Figure B.8. Probe zero delay. To accurately determine the probe zero delay position i.e. same pump optical path length and probe optical length, a practical method of inserting a SHG crystal such as a BBO in place of the sample is attempted. When the pulses of high power overlap, a middle ultraviolet beam is generated. This phenomenon is due to the phase matching criterion. By knowing the probe zero delay position, one can save time from scanning for a weak signal over an entire delay stage at 10 μm steps.

B.6 Material characterisation

Equipped with the optimised carrier lifetime setup, various photoconductive materials are measured. The obtained measurement is curve-fitted with an exponential function to determine the carrier lifetime (Korn *et al.* 2002), expressed as

$$\exp\left(-\frac{t}{\tau}\right) \quad (\text{B.8})$$

where τ is the lifetime.

B.6.1 Low-temperature gallium arsenide

A piece of an unused LT-GaAs substrate from Freiburg University, Germany, is used as the test sample to the setup. A photo of the sample material can be found in Figure B.9. Curve-fitting of the measured change in reflectivity yields a carrier lifetime of approximately 0.35 ps in close accordance with 0.3 ps as reported by Sakai (2005) in Table B.1. Differences are attributed to sample variation and curve-fitting uncertainties. The maximum change in reflectivity from balanced photodetection measurement is 10^{-4} . The setup has a resolution down to 10^{-6} .

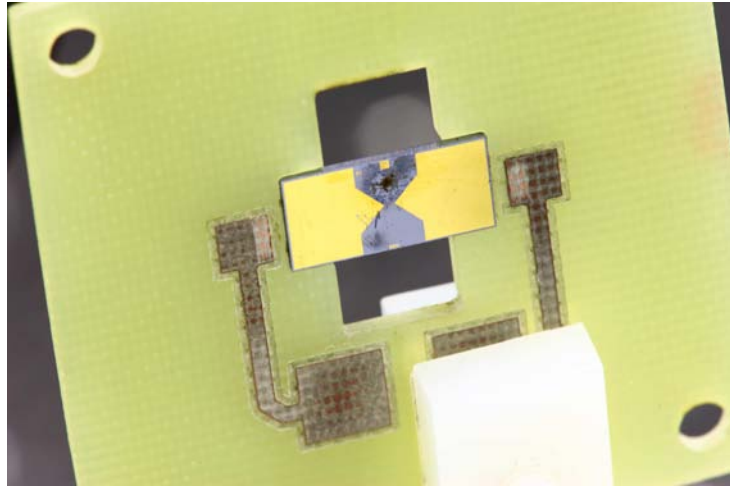


Figure B.9. Freiburg LT-GaAs test sample. An arbitrary LT-GaAs sample from the Freiburg THz group is used to validate our carrier lifetime setup. Note the black marks on the surface of the antenna are burn marks, due to excessive pump power density.

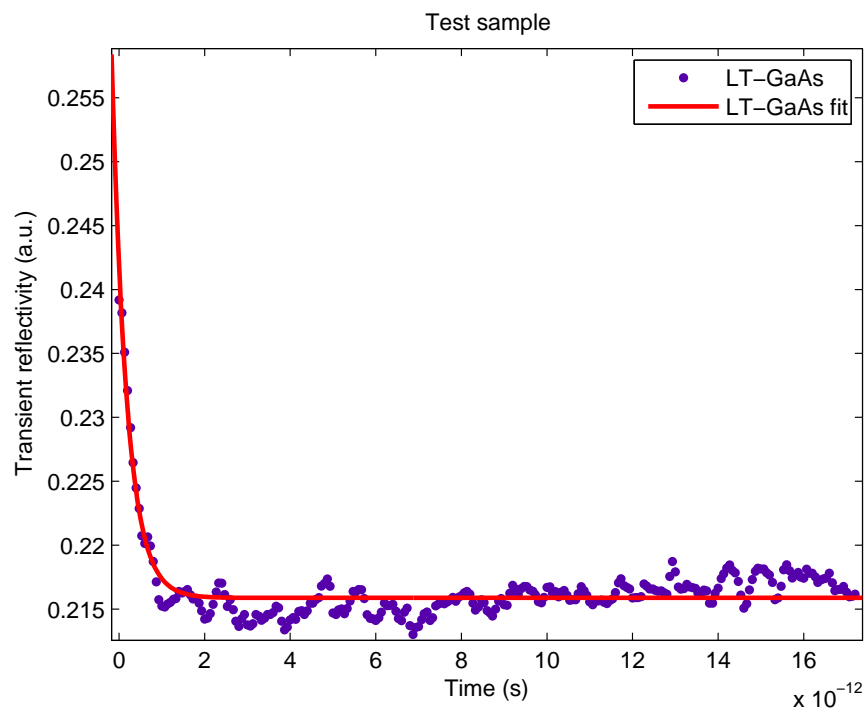


Figure B.10. Transient reflectivity measurements of LT-GaAs. The transient reflectivity measurement on a piece of LT-GaAs substrate from Freiburg Physics Group is used to validate our optical pump probe setup. The measurement is then curve-fitted to obtain to a carrier lifetime of 0.35 ps, in close agreement with the reported 0.3 ps in the literature (Sakai 2005).

B.6.2 Semi-insulating gallium arsenide

As a consistency check on our carrier lifetime measurement method, we measured the transient reflectivity signal from SI-GaAs. The result is shown in Fig. B.11. The carrier recombination time in bulk SI-GaAs is longer than the 50 ps range of our experiment and therefore it is not possible to extract the decay time constant of the conduction band by an exponential fit. Similar findings are shown in Hoffmann (2006) and therefore validates our approach. An alternative method for SI-GaAs carrier lifetimes and mobility measurement uses the optical pump-THz probe techniques in Yang *et al.* (2009).

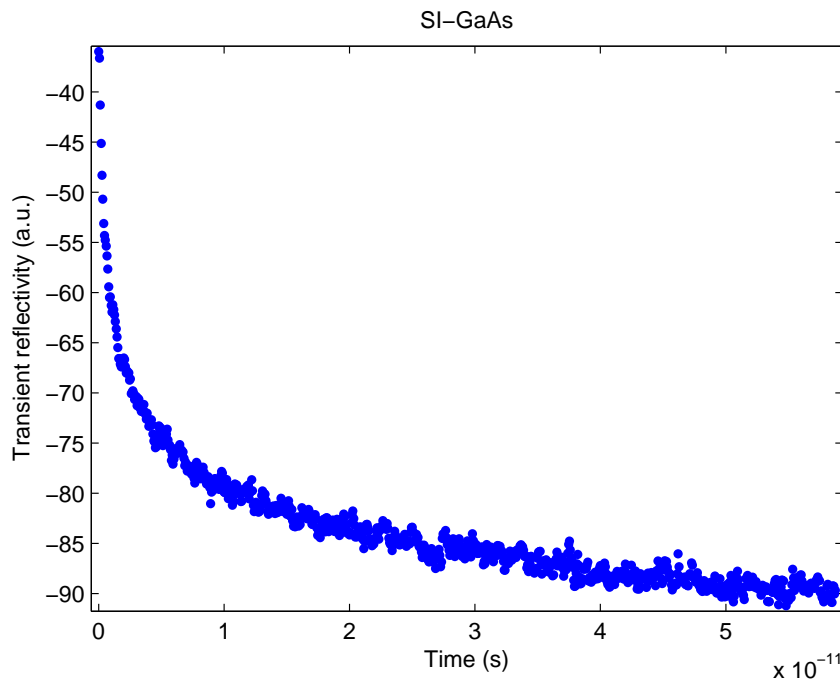


Figure B.11. Transient reflectivity measurements of SI-GaAs. The transient reflectivity measurement of a piece of SI-GaAs substrate from our research laboratory. As the carrier recombination time in SI-GaAs is longer than 50 ps measured in our experiment, it is not possible to extract the decay time constant of the conduction band by an exponential fit. This finding is in agreement with the experimental result in Hoffmann (2006).

B.6.3 Silicon-on-sapphire

Due to the fact that the direct bandgap of silicon (400 nm) is out of the wavelength range of our equipment, this measurement is carried out by our collaborator at the

Laser Spectroscopy Group, at the School of Chemistry, University of Sydney. Efforts however, were made without much success to measure the carrier lifetime with the optimised pump probe setup. This involved sweeping up the wavelength to 900 nm and half the wavelength by means of a SHG crystal, BBO. Such an attempt resulted with a limited power density on the sample. Factors attributed to the power loss include a coating on the optics that does not operate optimally at 450 nm, laser leakage through the hot mirror and poor overlap between pump and probe on the sample. The carrier lifetime of SOS substrate is measured at 625 nm by our collaborator. Unimplanted SOS substrate is measured to have a carrier lifetime slightly less than 300 ps as shown in Figure B.12 and hence is slightly better than the result reported in Doany *et al.* (1987). Figures B.13 and B.14 illustrate the measured and curve-fitted transient reflectivities of varying implants for oxygen and silicon ions respectively. The Levenberg–Marquardt algorithm (Marquardt 1963) is used to ensure the goodness of the fit to extract the carrier lifetime as tabulated in Table B.4 and B.5. Figure B.15 compares the lifetime measurements of oxygen and silicon implants. As shown, shortest carrier lifetime with oxygen ions occurs just at an implant dosage level of $3 \times 10^{13} \text{ cm}^{-2}$ giving rise to 1.3 ps carrier lifetime. This is double the 0.6 ps obtained in Doany *et al.* (1987) at $3 \times 10^{14} \text{ cm}^{-2}$. It is not known precisely why this is the case, but we suspect that the distribution of ion implants in the substrate maybe a possible reason. The silicon carrier lifetimes, however, appear to promising with 0.33 ps at $1 \times 10^{15} \text{ cm}^{-2}$. The lower carrier lifetime is achieved with a physically larger ion (silicon 110 pm atomic radii as opposed to oxygen at 60 pm) and at a higher implant dosage, leading to a greater population of recombination centers. As the study only took place over one sample for each implant, there are also experimental uncertainties that may contribute to the error in the determined carrier lifetime.

B.7 Chapter summary

This Chapter has described and characterised the material aspects of the THz photoconductive antennas suitable for THz near-field applications. This is a critical parameter because factors such as laser pulsewidth and electrodes electrical transmission line properties have negligible impact practically. In particular, radiation damaged silicon-on-sapphire is experimentally studied. Experimentally, shortest carrier lifetime is achieved with oxygen ions occurs at an implant dosage level of $3 \times 10^{13} \text{ cm}^{-2}$ giving rise to 1.3 ps as opposed to the 0.6 ps obtained in Doany *et al.* (1987) at $3 \times 10^{14} \text{ cm}^{-2}$.

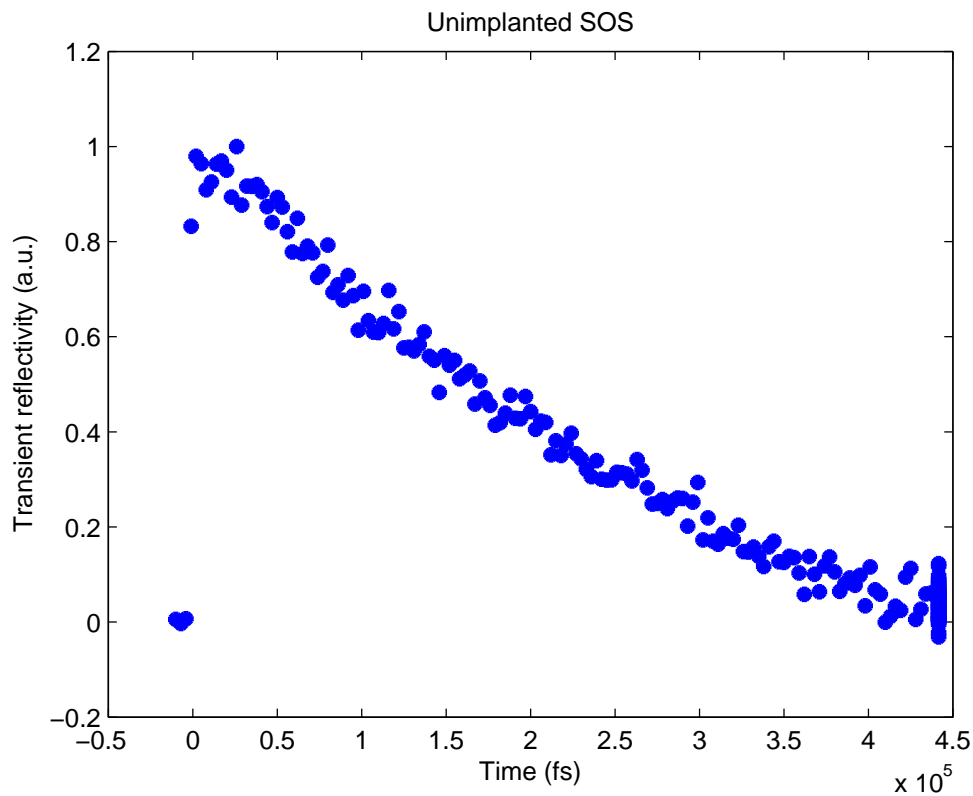


Figure B.12. Transient reflectivity measurements of unimplanted SOS. The transient reflectivity measurement of a piece of unimplanted SOS wafer with a pump probe setup and a carrier lifetime of slightly less than 300 ps is obtained in agreement with the 300 ps reported in Doany *et al.* (1987).

Table B.4. Measured oxygen ion implanted silicon-on-sapphire carrier lifetimes. The carrier lifetimes of the implants are determined through curve-fitting and is tabulated against the dosage levels annotated and described in Table B.2. The goodness of the fit is expressed by the R-squared parameter with values all exceeding 0.97.

Sample	Implant	Measured lifetime (ps)	R-squared
2	T	1.43	0.98
2	M	2.51	0.97
2	B	5.00	0.99
1	T	1.38	0.99
1	M	1.29	0.99
1	B	1.39	0.99
3	T	12.20	0.99
3	M	25.00	0.99

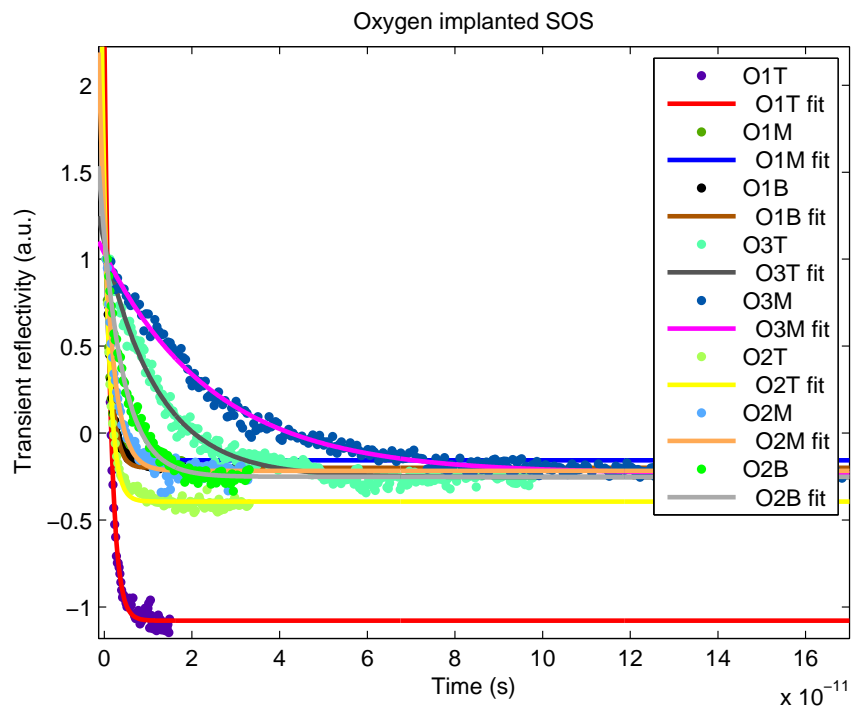


Figure B.13. Transient reflectivity measurements of radiation damaged SOS with oxygen ions. A half piece of wafer is sliced into six equal sized pieces and three of which implanted with oxygen ions. A total of eight implants of various dosage levels according to Table B.2 are performed and shown in different colours. Transient reflectivity signal, directly from the lockin amplifier, of each dosage level is obtained and curve-fitted with Levenberg–Marquardt algorithm. The goodness of the fit and the determined carrier lifetimes are tabulated in Table B.4.

The silicon implanted SOS carrier lifetimes, however, appears to be promising with 0.33 ps at $1 \times 10^{15} \text{ cm}^{-2}$. As a whole, the results are in agreement with Doany *et al.* (1987) within an order of magnitude and the variances can be explained by differences in experimental conditions, experimental uncertainties, sample variations and defect density profile. Future work on ion implantation over several samples for each ion type is definitely a must to ensure data validity.

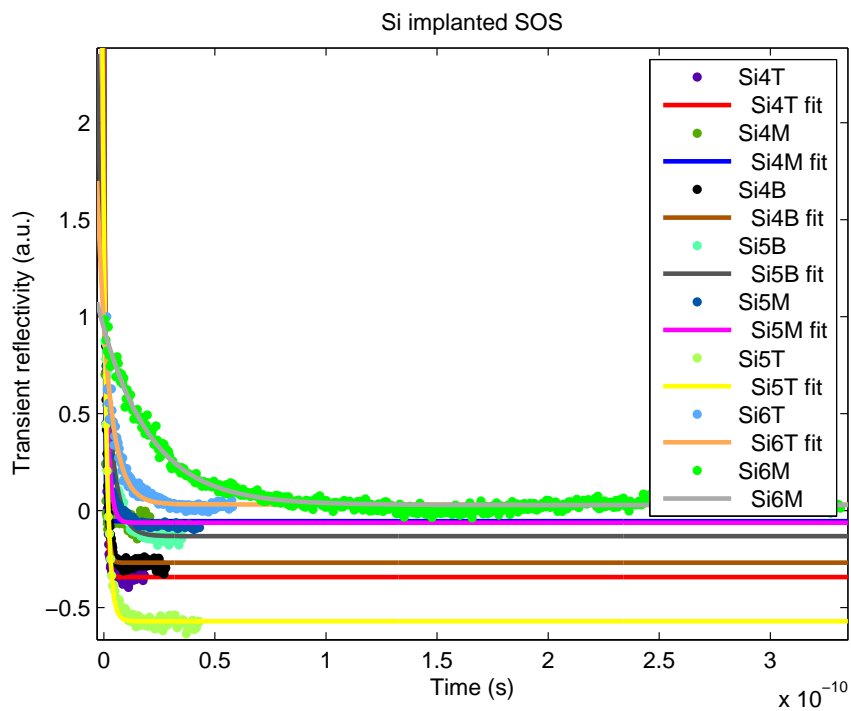


Figure B.14. Transient reflectivity measurements of the radiation damaged SOS with silicon ions. A half piece of wafer is sliced into six equal sized pieces and three of which implanted with silicon ions. A total of eight implants of various dosage levels according to Table B.3 are performed and shown in different colours. Transient reflectivity signal, directly from the lockin amplifier, of each dosage level is obtained and curve-fitted with Levenberg–Marquardt algorithm. The goodness of the fit and the determined carrier lifetimes are tabulated in Table B.5.

Table B.5. Measured silicon ion implanted silicon sapphire carrier lifetimes. The carrier lifetimes of the implants are determined through curve-fitting and is tabulated against the dosage levels annotated and described in Table B.3. The goodness of the fit is expressed by the R-squared parameter with values all exceeding 0.91.

Sample	Implant	Measured lifetime (ps)	R-squared
4	T	0.81	0.99
4	M	0.33	0.92
4	B	0.87	0.98
5	T	1.67	0.98
5	M	1.67	0.98
5	B	4.00	0.98
6	T	5.26	0.94
6	M	22.22	0.97

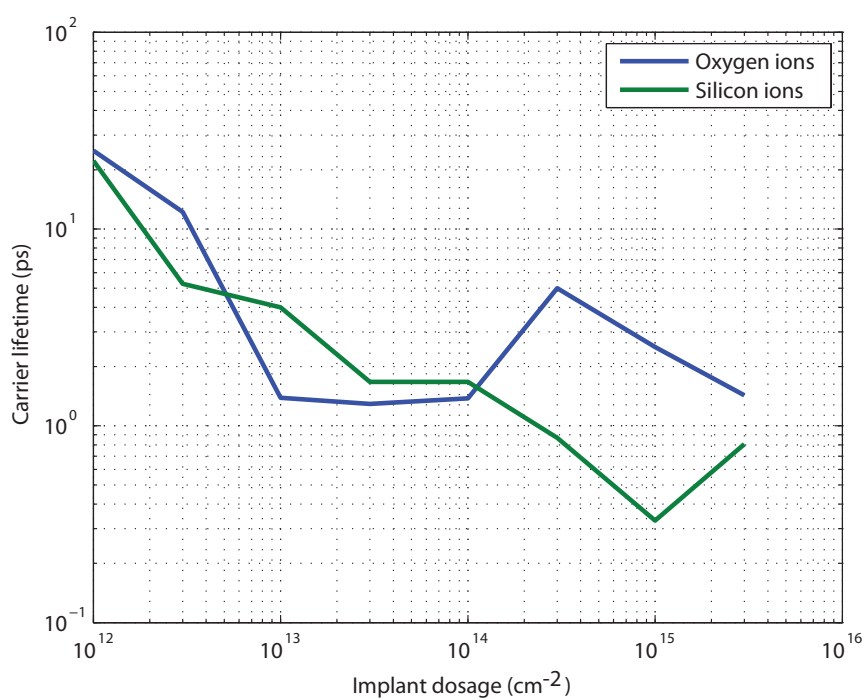


Figure B.15. Carrier lifetime of radiation damaged SOS with oxygen and silicon ions. The carrier lifetimes of the implants measured through pump probe and determined by curve-fitting as shown in Table B.4 and B.5 are illustrated against varying implant dosage levels.



Terahertz Near-Field Material Detection

TERAHERTZ near-field imaging systems offer the advantage of sub-wavelength resolution over conventional THz imaging systems. Motivated by the potential biological application, this Chapter investigates material detection with THz near-field imaging system at Tonouchi Laboratory, Osaka University .

C.1 System setup

The THz near-field system presented in Serita *et al.* (2010) employs the focused beam technique in the emission mode that is investigated throughout this Thesis. As shown in Figure C.1, the system employs a fibre coupled laser operating at a wavelength of $1.56\ \mu\text{m}$, and the optical beam is split into the pump and probe beam respectively by means of a beam splitter. The pump beam is modulated by an Acousto Optic Modulator (AOM) at a frequency in the megahertz range as opposed to the kilohertz range with conventional optical chopper system. This is advantageous in achieving a higher SNR but at the trade-off of difficult alignment, poor conversion efficiency (20 %) and pulse spreading.

Instead of moving the sample for THz image acquisition, a galvano mirror that consists of two computer controlled movable mirrors is used to raster scan the pump beam into a nonlinear crystal with a fixed sample placed directly on the crystal back surface. The change in the optical beam path therefore limits the scan range and hence the image size, and also requires the use of a large hypersemispherical silicon lens to couple the slightly misaligned THz radiation. The galvano mirror is advantageous over the mechanical actuators in terms of the response time thus allowing for fast THz image acquisitions. Furthermore, without the crystal, the reflected optical beam from the sample caters for the acquisition of the sample laser image by means of photodiodes. This is particularly useful for sample alignment and for comparing the spatial resolution between optical and THz images.

In order to improve the spatial resolution, the pump beam from the galvano mirror is optically expanded by means of a two convex lens system to further reduce the focused optical spot on the crystal. The focal length of the focusing lens is 50.6 mm to obtain a minimum optical beam waist of $25\ \mu\text{m}$ and a Rayleigh range of 1.2 mm. The achievable resolution is $50\ \mu\text{m}$. The locally generated THz radiation from nonlinear crystal, such as DAST, 4-Dimethylamino-N-methyl-4-stilbazolium p-Cholobenzene Sulfonate (DASC) and GaAs $\langle 100 \rangle$, are collimated and focused onto a PCA detector using a pair of off-axis parabolic mirrors. DASC is an organic nonlinear optical crystals with optical characteristics similar to DAST. The detector is gated with the probe beam at 780 nm obtained by SHG with a Periodically Poled Lithium Niobate (PPLN). The amplitude of the THz radiation is measured using a lock-in amplifier and recorded

C.2 Enhancement structure

using customised LabVIEW program. The THz image obtained is a plot of peak THz amplitude of the time-domain THz pulse without moving the delay stage. Image acquisition therefore takes about 47 seconds for 512 by 512 pixels and 5 seconds for 128 by 128 pixels image, but at the expense of missing frequency information. To obtain frequency information, the acquisition for a 128 by 128 pixels image, typically 40 minutes are required for up to 1.5 THz at 100 GHz frequency resolution.

C.2 Enhancement structure

With the emergence of metamaterials, structures are purposely designed for enhanced field transmission. These structures recently has attracted much interest in the literature (Bitzer and Walther 2008, Park *et al.* 2010). Motivated by potential biological application, this Section investigates the common structures through design, simulation, fabrication and test. These structures have been studied with far-field illumination, so in our study here, we will focus on near-field illumination.

C.2.1 Structure design

An initial design of the structures is conducted to gain better understanding and experience with the fabrication process and THz near-field imaging system. Among which, four different shapes of structures are investigated that are divided into four distinctive quadrants in the mask design as shown in Figure C.2. These shapes include square, triangle, octagon and bow-tie. Bow-ties are known commonly to produce power enhancement and a standard bow-tie design with 120° edge taperedness and a gap size of $20 \text{ by } 20 \mu\text{m}$ is designed. For each quadrant, the structure size decreases in order to determine the minimum sample necessary for detection i.e. system sensitivity. The minimum structure sizes, however, are constrained by the system resolution of $50 \mu\text{m}$ for THz and $20 \mu\text{m}$ for optical frequencies. The structure sizes in descending order are $75 \mu\text{m}$, $50 \mu\text{m}$, $25 \mu\text{m}$ and $10 \mu\text{m}$. Meanwhile, the separation distances between neighbouring structures are decreasing in each row to study signal interferences at small separation distances similar to Bitzer and Walther (2008). Replicated structures are also present along each row for reference measurement. As the size of structures are in tens of microns, to aid optical alignment, markers are deliberately inserted into the design as shown in Figure C.3.

C.2.2 Structure simulation

In this preliminary study, a bow-tie and a square structure is simulated in collaboration with Dr Withawat Withayachumnankul and A/Prof Christophe Fumeaux.

Bow-tie

A bow-tie structure is initially simulated with CST Microwave Studio in the free-space. Simulation measures the local THz signal strength at the gap region between the tapered edges. It assumes that the incident THz plane wave is polarised along the y -axis. The plane wave assumption is valid for a point source and a sub-wavelength structure. A local enhancement of the THz electric field in the feed region can be observed at 0.3 THz. Terahertz electric field strength is normalised to the incident field to show a clear local enhancement at 0.3 THz in Figure C.5. The far-field transmission spectra shows numerous resonances. To better investigate the reason behind this effect, a simpler shape structure is investigated using the more comprehensive Gaussian aperture modelling methodology introduced in Chapter 5. This will therefore allow for a more consistent comparison with the experimental results.

Square

Simulations are conducted using the Gaussian aperture modelling methodology as introduced in Chapter 5.

C.2.3 Structure fabrication

With the photomask design, fabrication process consists of two main distinctive steps; photomask development and device fabrication. This is shown and explained in Figure C.7 and C.8 respectively. Structures are etched out of the GaAs $\langle 100 \rangle$ crystal that is metallised with 1000 Angstroms or 0.1 μm thick gold. An extremely thin layer of titanium is used to adhere gold to GaAs. A photograph showing the fabricated structures under an optical microscope is shown in Figure C.9.

C.2.4 Experimental result

In this preliminary investigation, several fabricated structures are scanned with the THz near-field imaging system. The bow-tie and square are selected for qualitative comparison with preliminary simulation results.

Bow-tie

As an initial check, an optical and a THz time-domain image of a selected bow-tie structure is obtained from the THz near-field imaging system. This can be seen in Figure C.10. As expected, the optical image shows a higher resolution evident around the bow-tie edges as opposed to the grainier THz image. The transmission spectra is obtained by means of performing THz-TDS with a THz spot greater than the bow-tie structure. As can be observed in Figure C.11, the bow-tie becomes a high pass filter for 0.5 THz. This can be explained by the fact that THz spot becomes smaller than the etched area leading to total transmission. The result, however, is difficult to relate to simulation result in Figure C.6. The reason for the discrepancy between simulation and experiment maybe possibly due to illumination; simulation considers plane wave as opposed to a point source, i.e. Gaussian aperture in the experiment. Also, simulation considers the bow-tie structure in free space as opposed to a substrate in the experiment.

Square

To validate the Gaussian aperture model for the THz point source in the crystal, THz-TDS with two different THz beam waist ($18\ \mu\text{m}$ and $36\ \mu\text{m}$) are performed on three squares of different sizes, namely, $75\ \mu\text{m}$, $50\ \mu\text{m}$ and $25\ \mu\text{m}$. The fabricated structures can be seen in Figure C.12. It is shown in Chapter 5 that THz spot changes with frequency, and is more confined at higher frequency than lower. As can be observed in Figure C.13, for $75\ \mu\text{m}$ square, transmission with the small THz spot becomes a high pass filter at 2.25 THz as opposed to 3 THz for the big THz spot. Qualitatively, this is expected because the small THz spot would be small enough for total transmission at a lower frequency. It can also be observed that as the THz spot is very bigger than the aperture size, an increase oscillation results. This result is currently under investigation using a new distributed Gaussian aperture simulation result for validation.

C.3 Substrate structure

Alternative to enhancement structures that aims to deposit the biological sample directly on the surface, a structure with channels in the THz emitter is also investigated. The experiment design with this approach can be summarised in Figure C.14. In an effort to extract the optical constants from the samples of interest, a certain depth of GaAs is etched out, the groove is filled with biological sample deposited by means of a nano-Litre syringe and overlaid with a thin layer of high impedance silicon to reduce evaporation in the dry atmosphere and a planar sample surface. Scanning such a system under the THz near-field imaging system will be a step toward future biochip design that could be widely used in the pharmaceutical industry, where high sensitivity and high throughput are required (Kiwa *et al.* 2010).

C.3.1 Structure design

For the sake of simplicity in alignment to the GaAs $\langle 100 \rangle$ crystallographic axis, only square shapes are considered. In the first instance, in order to avoid evaporation, a depth of $200 \mu\text{m}$ is considered. Three squares for three different liquid with sizes of $300 \mu\text{m}$, $200 \mu\text{m}$, $100 \mu\text{m}$ and $75 \mu\text{m}$. The squares are separated by $300 \mu\text{m}$, $200 \mu\text{m}$, $100 \mu\text{m}$ and $75 \mu\text{m}$. The mask design is shown in Figure C.15 for the etching of the GaAs substrate.

C.3.2 Structure fabrication

The fabrication procedure is the same as described in Figure C.7 and C.8. The differences lie in that gold metallisation is no longer required and the use of a different etchant specifically for GaAs substrate. In particular, the etchant is a solution of sulfuric acid and hydrogen peroxide. The etching rate is determined by iteratively etching away a sample substrate while measuring the depth and ensuring flatness via a surface profiler. This is shown in Figure C.16 and curve fitted with a quadratic polynomial function with a R-squared value of 0.99. In order to ensure the flatness of the structure, surface profiler is iteratively used. Although this is correct on the sample substrate, the etching rate is not applicable upon GaAs square fabrication. This is perhaps due to the type of photolithography illumination used. The sample substrate used optical illumination as opposed to UV. This is the subject of current ongoing investigation.

NOTE:

This figure is included on page 162 of the print copy of the thesis held in the University of Adelaide Library.

Figure C.1. Scanning THz near-field imaging system. The system is driven by a fibre coupled laser operating at a centre wavelength of $1.56 \mu\text{m}$. The pump beam is modulated by AOM and scanned onto the nonlinear crystal, such as DASC, by means of a galvano mirror. To reduce the size of the THz source, the optical beam is first expanded by means of two convex mirrors, then focused onto the nonlinear crystal. The sample of interest is fixed onto the back surface of the crystal. Photoconductive sampling is used for detection and is gated by the optical beam at 780 nm obtained from SHG with PPLN. The spatial resolution achieved with the system is $50 \mu\text{m}$. After Serita *et al.* (2010).

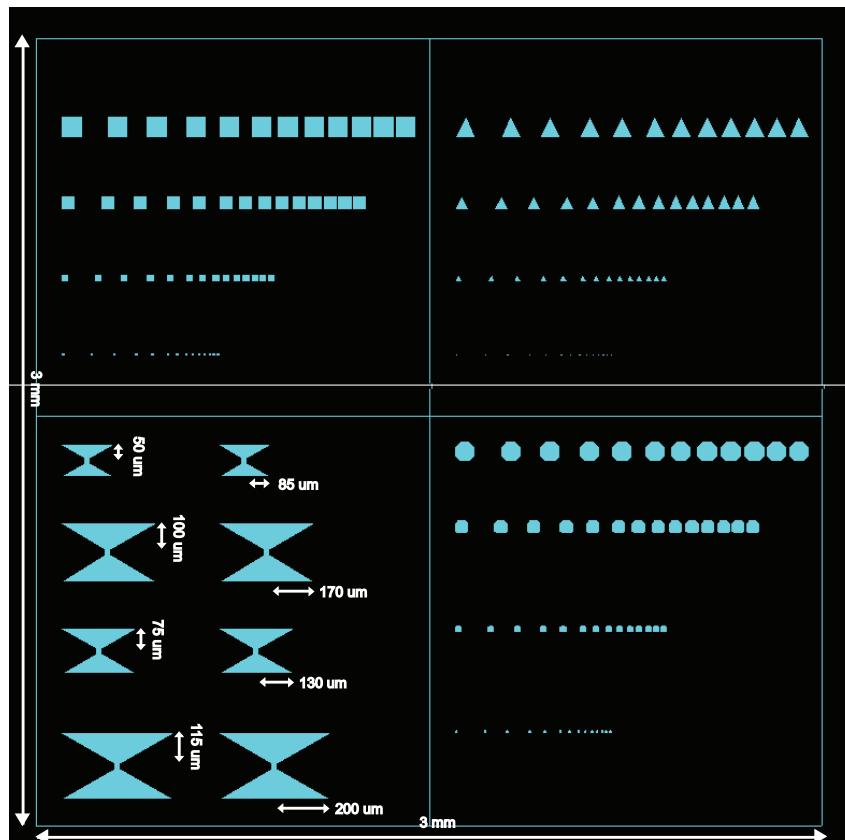


Figure C.2. Mask structures. The design of the mask comprises four quadrants, each with distinctive shape for investigation. Octagon shape is used instead of circle for fabrication simplicity. In each quadrant, the structure size decreases for determining the system sensitivity. The structure sizes in descending order are $75\ \mu\text{m}$, $50\ \mu\text{m}$, $25\ \mu\text{m}$ and $10\ \mu\text{m}$. The separation distances between neighbouring structures are decreasing in each row to study the effect of signal interferences at small separation distances. The separation distances are $100\ \mu\text{m}$, $75\ \mu\text{m}$, $50\ \mu\text{m}$ and $20\ \mu\text{m}$. Dimensions of the bow-ties are annotated. The entire design is 3 by 3 mm.

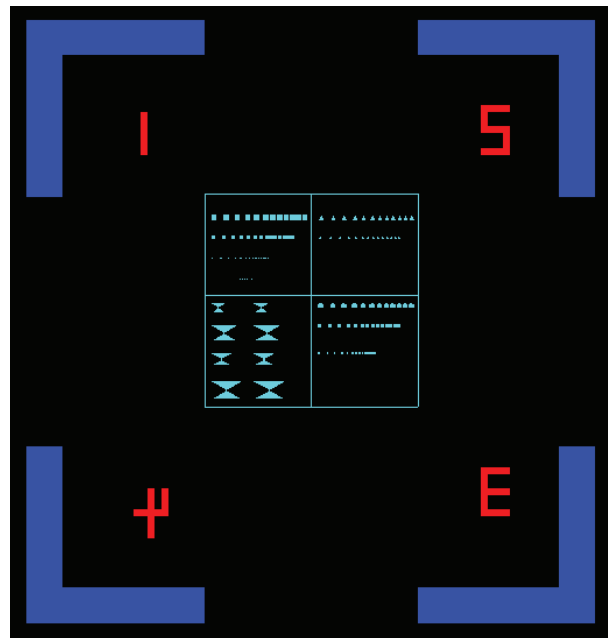
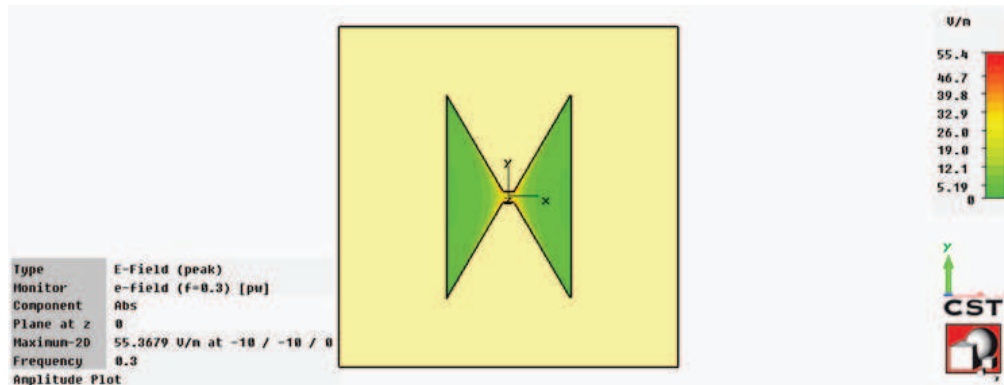
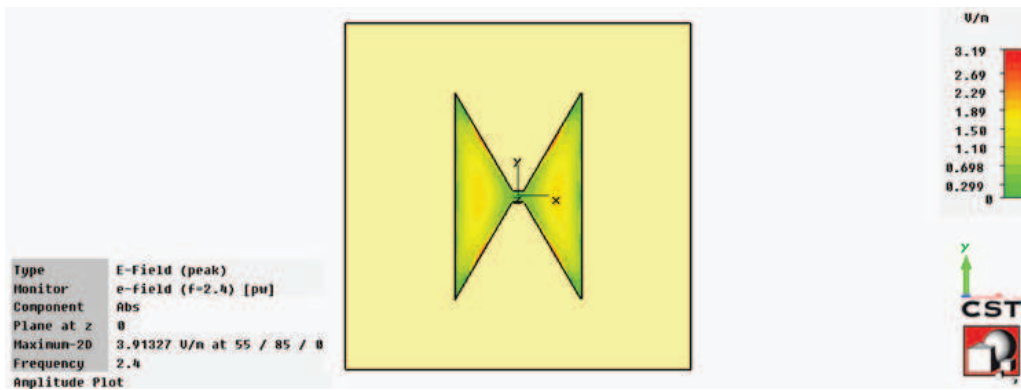


Figure C.3. Mask design. Design for the mask for fabrication including markers visible to the naked eye to aid optical alignment.



(a)



(b)

Figure C.4. Bow-tie near-field simulation in free-space. Terahertz local electric field strength at (a) 0.3 THz and (b) 2.4 THz. The simulation assumes that the incident THz plane wave is polarised along the y -axis. The colours indicate the transmitted electric field strength in V/m.

C.3 Substrate structure

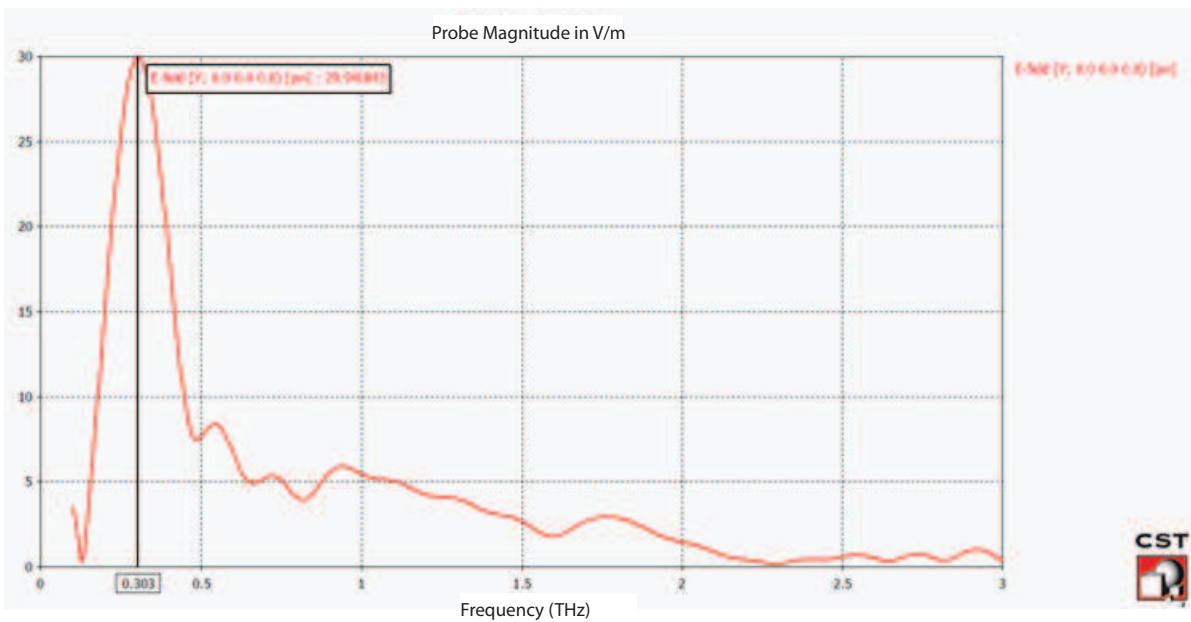


Figure C.5. Simulated bow-tie near-field frequency response. Terahertz electric field strength is normalised to the incident field to show a local enhancement at 0.3 THz in the feed region of the structure. Simulation is performed with incident plane wave and in free-space.

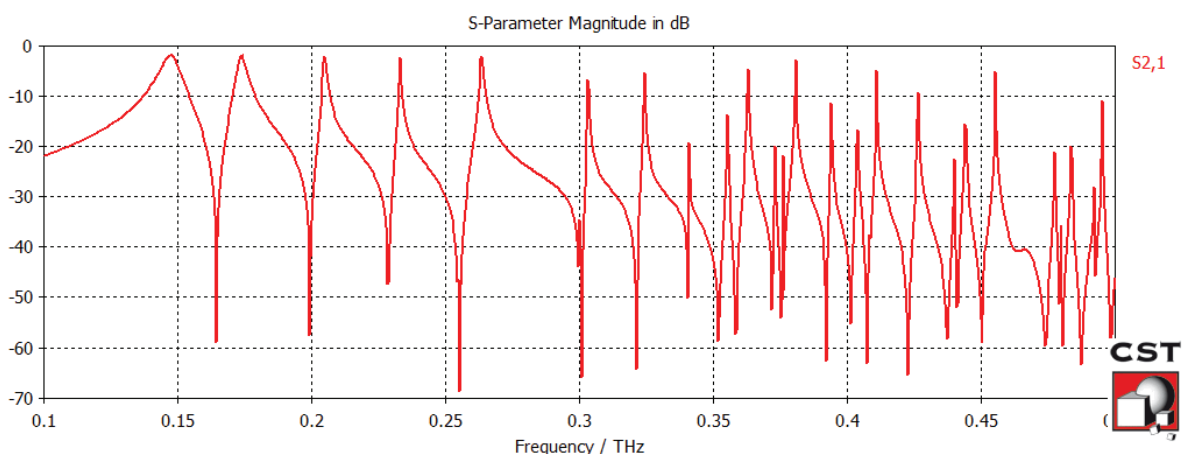


Figure C.6. Simulated bow-tie far-field transmission spectra. The far-field transmission shows numerous resonances for the bow-tie structure. The reason behind this is currently under investigation.

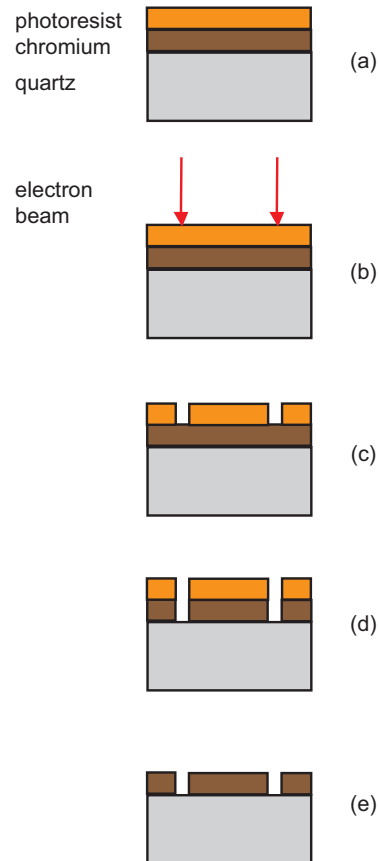


Figure C.7. Photomask development. The process flow is as follows: (a) On a quartz substrate, chromium layer is formed by sputtering followed by photoresist coating. (b) Using an electron beam, mask pattern as shown in Figure C.3 is written onto the photoresist layer. The resulting pattern is the inverse of the mask pattern. (c) A developer is applied to remove the exposed photoresist area. (d) Using either dry or wet etching, the exposed chromium layer is etched away to reveal the quartz surface. (e) Remaining photoresist is stripped away followed by clean and dry steps. The remaining area covered by chromium is opaque while the clear area transmits the incoming light source.

C.3 Substrate structure

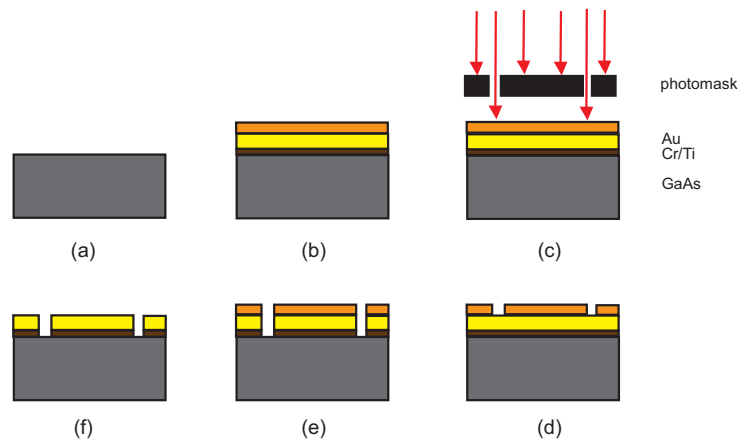


Figure C.8. Device fabrication. The process flow in clockwise is as follows: (a) Preparation of the GaAs substrate. (b) An ultra thin layer of titanium is sputtered onto the substrate followed by gold at $0.1 \mu\text{m}$ thickness. Photoresist is then applied. (c) Using the UV light and the photomask with the inverse pattern, the original photomask pattern is written onto the photoresist layer. (d) The developer is applied to remove the exposed photoresist area. (e) Using either dry or wet etching to remove the unprotected gold and titanium layer accordingly. (f) Remaining photoresist is stripped away followed by clean and dry steps.

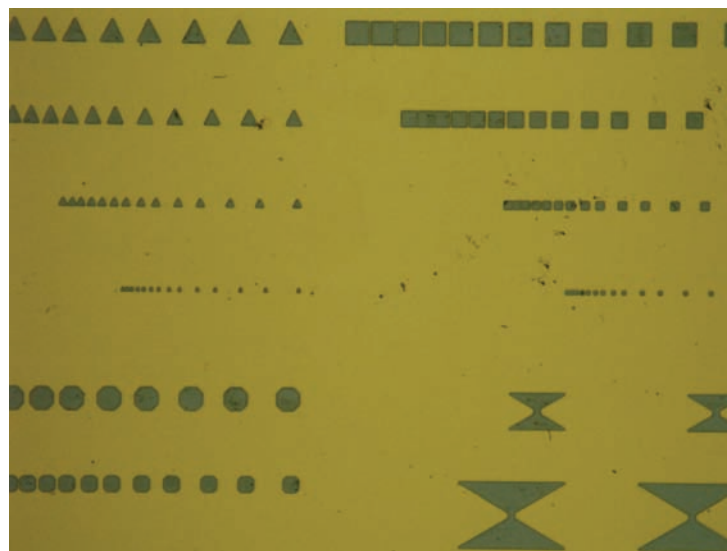


Figure C.9. Fabricated devices. This photograph shows some of the fabricated structures observed under an optical microscope. The structures are comparable to the designed mask pattern in Figure C.2

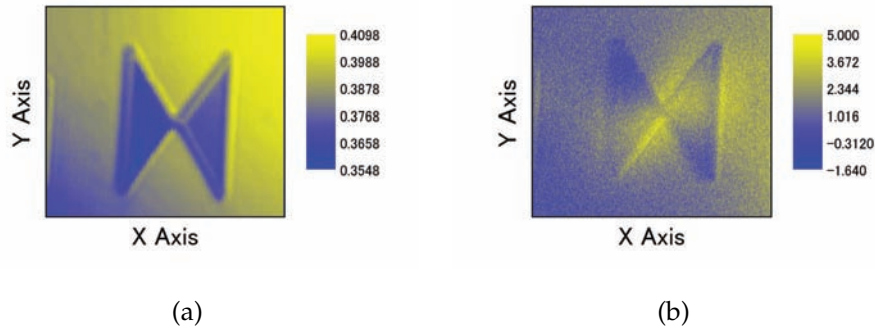


Figure C.10. Optical and THz image of bow-tie structure. Scanning a selected bow-tie structure under the THz near-field imaging system shows (a) the optical image and (b) THz time domain image. Higher resolution is expected with the optical frequencies compared to the THz image due to a beam spot size.

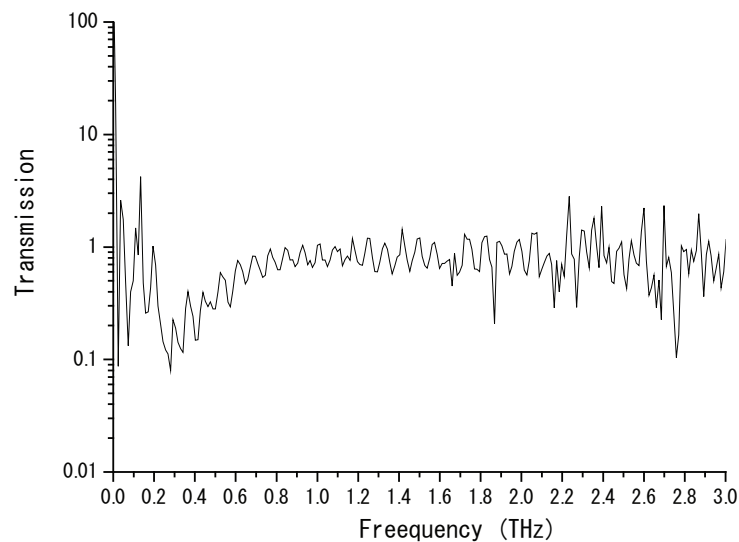


Figure C.11. Experimental bow-tie far-field transmission spectra. Transmission is unity for frequency greater than 0.5 THz. This can be explained by the fact that THz spot becomes smaller than the etched area leading to nearly complete transmission. The result, however, are presently difficult to relate to preliminary simulation in Figure C.6

C.3 Substrate structure

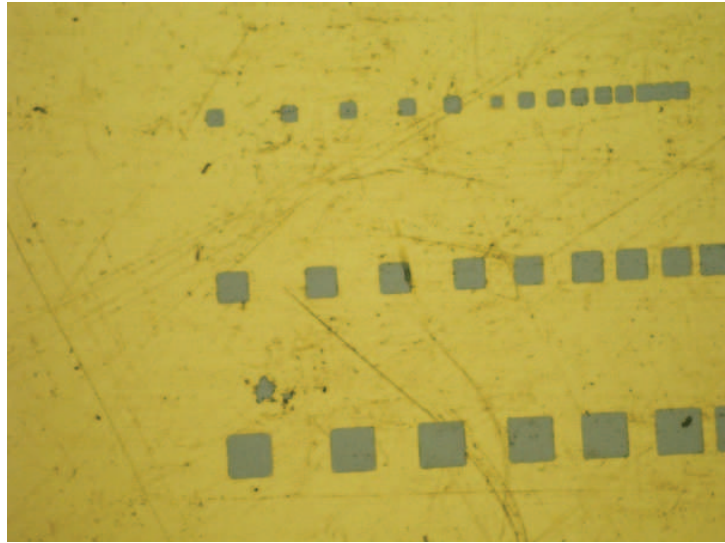


Figure C.12. Square structures. Three squares of different sizes 75 by 75 μm , 50 by 50 μm and 25 by 25 μm are used to validate the distributed Gaussian aperture model.

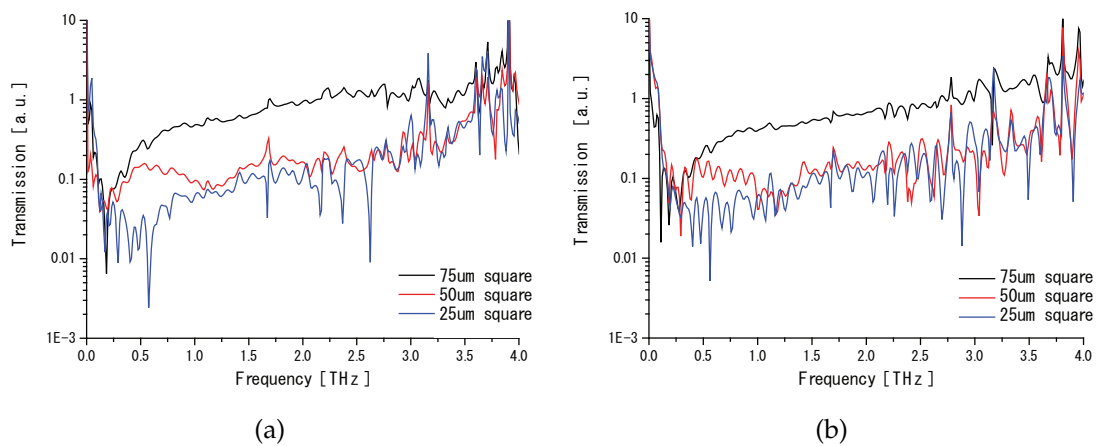


Figure C.13. Square aperture transmission spectra. Transmission spectra measured using THz-TDS for (a) small and (b) big THz spot sizes. As expected, transmission with the small THz spot becomes a high pass filter at a lower frequency i.e. 2.25 THz than the big THz spot i.e. 3 THz.

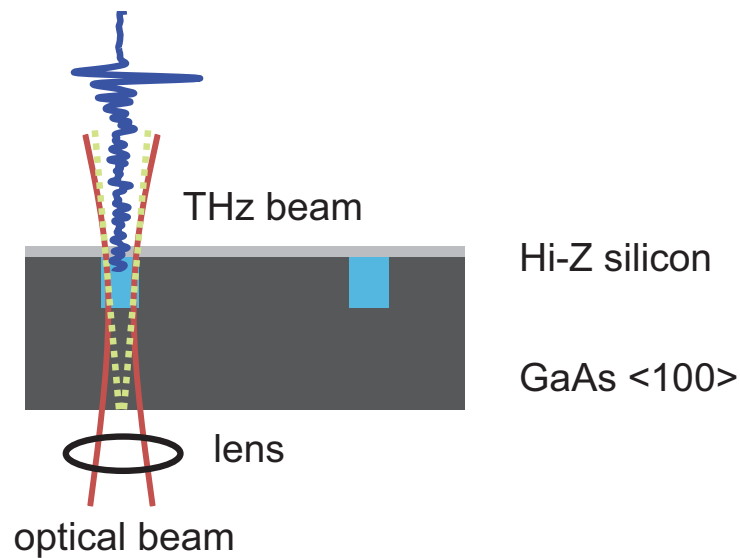


Figure C.14. Experimental design. Structure of a certain thickness are etched out from the GaAs substrate. The grooves are filled with biological sample that is overlaid with a thin layer of high impedance silicon (annotated as Hi-Z silicon) to reduce evaporation. The system is then scanned under the THz near-field imaging system.

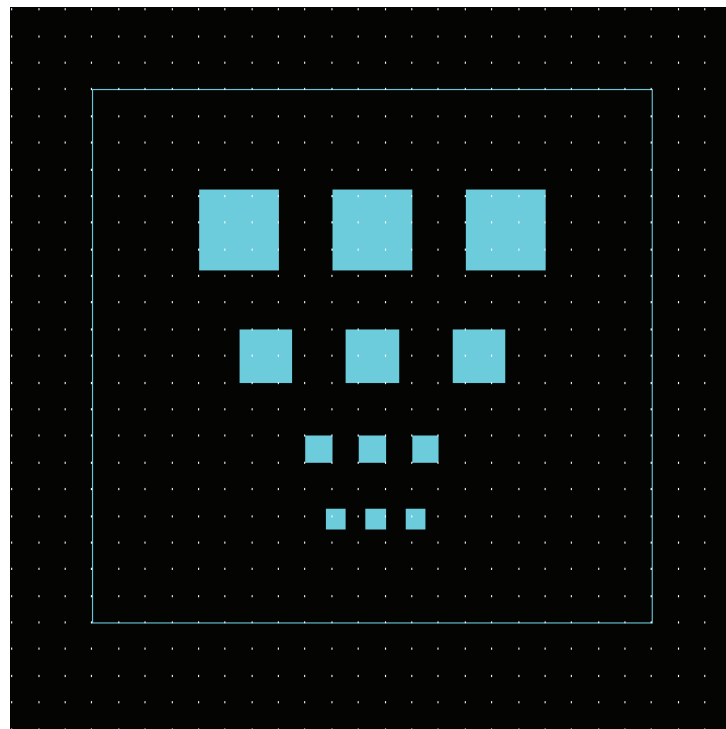


Figure C.15. Mask design. Squares with sizes of 300 μm, 200 μm, 100 μm and 75 μm are designed. The squares are separated at a distance of 300 μm, 200 μm, 100 μm and 75 μm respectively.

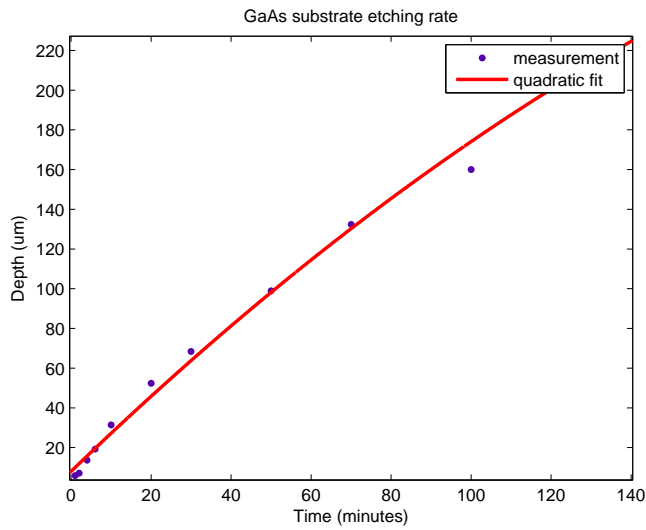


Figure C.16. GaAs etching rate. The etching rate measurement is obtained by iteratively etching away the GaAs substrate and measuring the depth of the etch by means of a surface profiler. The measurement is curve fitted with a quadratic polynomial function with a R-squared value of 0.99.

Gas Recognition with Terahertz Time Domain Spectroscopy

THE ability to detect and measure a variety of gases under certain environment conditions has a significant impact in many areas; from hazardous gas detection in the industrial domain to physical sciences in academia. Gas sensing has long received attention with microwave and infrared spectroscopy. With many molecular resonances occurring in the THz range leading to simple, unique spectral features, THz-TDS promises to be a potential technique of investigation. This chapter presents an investigation on real-time gas recognition with THz-TDS. In particular, a simple method is proposed that involves extracting line positions from gas species without the reference pulse and classifying them with the Submillimeter, Millimeter, and Microwave Spectral Line Catalog. This work is a side investigation not of direct relevance to the main theme of this Thesis, but is recorded here in an Appendix for completeness.

D.1 Introduction

D.1.1 Gas sensing technologies

Gas sensing technologies have been widely reviewed in the literature (Drafts 2001, Wilson *et al.* 2001, Lieberzeit and Dickert 2007) and can be broadly classified into four major groups; Gas Chromatography and Mass Spectrometry (GCMS), electromechanical sensors, mass sensors and optical based techniques. The typical benchmark for technology evaluation includes selectivity (the ratio of detecting the intended over the interferences), sensitivity (lowest detectable chemical concentration) and robustness (performance over various ambient conditions humidity, temperature (Wilson *et al.* 2001). Additional requirements such as power, size, electronics overhead (for decreasing size and power consumption), durability and maintenance, cost and simplicity in operation also play a decisive part for determining suitable applications (Wilson *et al.* 2001, Ho *et al.* 2001).

It is notable that GCMS is extensively used in the medical, pharmacological, environmental and law enforcement fields to analyse chemical mixtures. Even though GCMS has the best selectivity, high sensitivity, precision and reproducibility, the technology is very expensive and training maybe needed. In addition, the retention times in GCMS are typically in the order of several minutes, therefore inducing delays in the identification process (Brickhouse *et al.* 2000), thus limiting real-time applications. In contrast, electromechanical sensors are small, low cost, low power components that have short shelf-lives with performances such as sensitivity and selectivity dependent on the operating environment. Likewise, piezoelectric acoustic wave sensors are also small sized that are sensitive to various chemicals (Drafts 2001). However, they cannot discriminate across unknown mixtures and durability remains to be a concern (Ho *et al.* 2001). Fourier Transform Infrared (FTIR) spectroscopy or infrared sensing is a well established optical method that uses fingerprint absorption signatures resulting from molecular vibrations for identification. But due to the nature of molecular vibrations, only certain gas species with permanent dipole moments maybe fingerprinted and hence identified. In addition, the technology is expensive and complex in that it can be affected by water vapour and humidity. Other optical sensing methods like microwave spectroscopy (300 MHz to 300 GHz), commonly known today as Fourier Transform Microwave spectroscopy (FT-MW) (Dicke and Romer 1955), is also a highly selective method for many polar gases that exhibit unique absorption signatures of high spectral

D.1 Introduction

resolution. With the availability of highly stable microwave sources, FT-MW also has the added benefit of overall system stability and durability. In general, optical techniques can be highly selective, durable and requires less calibration than other sensing technologies (Ho *et al.* 2001), thus making it a perfect trade-off between cost, durability and performance.

D.1.2 Fundamental considerations

Fundamentally, the interaction between molecules and electromagnetic waves is in accordance with the incident energy, molecular species and substance condition. A molecule can absorb and re-emit the wave at certain frequencies, specific to the energy transitions of either the electronic, vibrational, or rotational mode. Each type of molecule absorbs the wave in a unique spectral pattern and even though the substance and surrounding environment can, to a certain extent, affect the absorption pattern, the spectrum and absorption features are generally unique to each molecules. In the gas phase, the rotational mode of transitions occurs with polar molecules, and these transitions broadly span from the microwave to IR spectra. The pure rotational transitions result in the absorption spectrum that contains Lorentzian resonances at discrete frequencies. This uniqueness enables the classification and recognition of polar gases via either microwave, THz radiation, or IR spectroscopy of a gas sample. On a fundamental level, microwaves and mid-infrared radiation have their own respective advantages and disadvantages for spectroscopy. Principally, heavy gas molecules tend to have rotational resonances in the microwave region, whereas light gas molecules have rotational resonances in the mid-infrared. The absorption resonances recorded in the mid-infrared region are generally congested and complicated from the combination of rotational and ro-vibrational modes. This therefore hinders the feature extraction process. In contrast, the rotational transition modes in the microwave region are relatively low, resulting in little features available. Terahertz radiation therefore presents a compromise for these trade-offs. In addition, the interactions between electromagnetic wave and polar molecules in the THz region are three to six orders of magnitude stronger than that in the microwave region (De Lucia 2003).

D.1.3 Real-time gas recognition

The ability to detect and measure a variety of gases under certain environmental conditions has a significant impact in many areas; from hazardous gas detection in the industrial domain to physical sciences in academia. Gas sensing has long received attention with microwave and infrared spectroscopy. With many molecular resonances occurring in the THz range leading to simple, unique spectral features, THz-TDS promises to be a potential technique of investigation.

Note that THz-TDS in general has a better resolution compared to FTIR (De Lucia 2003) and is able to collect the data almost instantaneously leading to real-time detection. In particular, the amplitude and phase information can be obtained giving rise to more features for classification purposes. Even though FTIR spectroscopy has sensitivity spanning over many frequencies (from the as low as 1 THz up to the visible spectrum), THz spectrometers are more sensitive below 3 THz (Han *et al.* 2001) where the rotational modes lie and can be improved with the use of a multipass cell (White 1942, White 1976). With many gases exhibiting absorption spectra due to molecular rotations in this region, THz-TDS promises to complement the relatively mature FTIR technology and expand the number of detectable gas species. A full description of THz-TDS can be found in Chapter 2 of this Thesis.

D.2 Feature extraction

The goal of feature extraction is to select features such that the samples from each class are in forms of clusters well separated from one another. As mentioned in Mittleman *et al.* (1998), polar gases with a sufficient concentration, exhibit an ensemble of strong and sharp resonances at discrete frequencies in THz spectrum due to quantised rotational energy transitions. As the molecules differ in structure, the resonances' position and relative strength are unique to each gas species. This uniqueness is hence used as fingerprint different gas species for recognition. A system modeling approach with linear predictive coding has been successfully employed to capture the resonant positions and strengths efficiently (Mittleman *et al.* 1998). In particular, the filter coefficients are used as classification features that are extracted from the time-domain THz waveform of specific gases. The coefficients are stored in a codebook for comparison and identification with the filter coefficients of an unknown gas. The system modelling

D.2 Feature extraction

technique, however, does not take account of the phase information leading to inability in identifying gases with many absorption lines like CH_3CN (Mittleman *et al.* 1998). Although the number of coefficients is fixed for each waveform thereby making subsequent comparisons simple, choosing the optimal number is difficult as it is dependent on the gas species. Modelling via Fourier series has also been attempted, but it was found that more coefficients were required for the sharp resonant lines that lead to only minor performance improvement (Jacobsen *et al.* 1996). Also exploiting the simplicity and uniqueness of the THz spectral signatures, we consider the absorption coefficient as the classification feature, which encompasses the resonances' position and frequency. The absorption frequency is particularly interesting because it is rarely affected by the gas pressure, gas temperature, nor system's dynamic range as is the case with absorption strength. The absorption strength on the other hand, is useful for the selection of well-defined resonances and the elimination of resonance-like spikes caused by random noise in the spectrum as well as determining the relative concentrations in mixtures. Gas spectroscopy is very established field in its own right and the use of the absorption coefficient as features allows leveraging on existing spectral catalogs instead of building a codebook from scratch. Determining the absorption from an unknown gas requires a reference pulse, which is absent in real-time gas sensing. A reference pulse estimation technique is applied to overcome this dilemma.

D.2.1 Spectroscopic catalog features

Since the development of wartime microwave radar, gas spectroscopy has received much attention starting off with microwaves and later THz. Motivated by many remote sensing applications, the spectroscopic information of virtually all of the significant atmospheric and astronomical species have been cataloged. Specifically, these catalog include Submillimeter, Millimeter, and Microwave Spectral Line Catalog and HITRAN Molecular Spectroscopic Database. The Submillimeter, Millimeter, and Microwave Spectral Line catalog covers spectral lines in the frequency range between 0 and 10,000 GHz, which covers the THz range from 0.1 to 10 THz, and therefore suitable for our purposes. This computer-accessible catalog contains a directory file, which lists all the species cataloged, number of lines recorded and additional information for intensity calculation for temperatures other than 300 K. The spectroscopic properties for each species is listed in their respective line files, which contains one line entry per spectral line. Usage to the catalog can be found in Pickett *et al.* (1998). For the sake of

feature extraction, only the frequency column and intensity column are used. The data from these columns are loaded into Matlab with the considered rotational lines to be those with an intensity greater than 1/10 of the max peak intensity in the 0.1 to 2 THz region. Preliminary study considers the frequency features in the order they appear. Computer-accessible spectroscopic information like the resonances' position, strengths and width, of many common gas species are available in many databases or catalogs, for example:

- Molecular Spectroscopy Team, at Jet Propulsion Laboratory (JPL) reports the spectral line intensity, strength, and other related parameters of 331 interstellar gas species in the submillimeter, millimeter, and microwave frequency ranges (Pickett *et al.* 1998).
- Cologne Database for Molecular Spectroscopy (CDMS) added 280 more species to its own database, with the identical data format used at JPL (Müller *et al.* 2005).
- High-resolution TRANsmision molecular absorption database (HITRAN) provided a compilation of spectroscopic parameters of 39 molecules and its isotopes, spanning the microwave and ultraviolet bands (Rothman *et al.* 2005). Apart from the line intensity and position, the list consists of the Einstein *A*-coefficients, statistical weight for upper and lower levels of the transitions, etc.
- Gestion et Etude des Informations Spectroscopiques Atmosphériques (GEISA) database contains the spectroscopic parameters of 42 molecules (96 isotopes) in the frequency range between 0 and 1076 THz (Jacquinet-Husson *et al.* 1999).

For the sake of resonant frequency extraction, only the frequency column and intensity column are used (Pickett *et al.* 1998). In this region, the absorption lines are due to the rotational and vibrational modes. Since the rotational lines are stronger than the vibrational lines in small molecules such as water, a threshold is set to filter out the rotational modes and extract their frequencies.

D.2.2 Sample spectral features

An issue arises as the gas recognition process proposed here eliminates the retrieval of a reference pulse to facilitate the measurement. This means that only the gas spectrum is available without the baseline to determine of the resonance strength. An idea to

D.2 Feature extraction

estimate the reference data from the sample data is therefore introduced. Once the reference is recovered, the full optical constants, including the absorption coefficient and the refractive index, can be reckoned. Extracting the resonances' position and strength from the absorption coefficient is then possible.

The recovery process could possibly apply with the sample data either in the time or frequency domain. In the frequency domain, the rotational resonances modify the reference only at narrow frequency bands, and the spectral shape of the reference is still preserved in general. In the time domain, the resonances cause significant distortion in the main pulse and also strong oscillations in the tail after the main pulse, leaving only small resemblance to the reference pulse. Therefore, recovery of the reference in the frequency domain is more reasonable.

Both magnitude and phase of the sample spectrum must be modified in order to recover the reference. The magnitude shape of the reference is very dependent on the system. Once interacting with a polar gas, the magnitude exhibits a number of sharp Lorentzian resonances. Filling up the resonance abysses simply regains an approximation of the reference magnitude. More specifically, the magnitude spectrum is spatially averaged to eliminate small spikes. Subsequently, the local maxima are determined. These local minima are connected linearly, resulting in the estimated reference magnitude. The process is depicted in Figure D.2 (a).

The phase of the reference is nearly linear over the whole frequency range. The existence of a polar gas in the propagation path causes small phase perturbations at resonance frequencies. Applying the least squares fitting to the sample phase could smooth out these perturbations. A comparison among reference, sample, and modified phases are shown in Figure D.2 (b).

After both the magnitude and phase of the reference are recovered, they can be used in conjunction with the sample spectrum to estimate the frequency-dependent optical constants. The absorption coefficient obtained from the measured sample and the recovered reference is plotted in Figure D.3 (a). From the estimated absorption coefficient, the resonances' position and strength can be easily determined, as shown in Figure D.3 (b). These features can be recognized by comparing against the gas spectral parameters in a spectroscopic catalog.

D.2.3 Reference-free spectral features

Recent work by Zhang *et al.* (2008) exploited the almost-linear phase spectrum to determine the resonant locations from the reference-free spectrum. This Section briefly applies the reference-free spectrum to gases to determine suitability. Figures D.4 and D.5 compare the absorption coefficient and the reference-free phase spectrum for water vapour and ammonia gas respectively. In the water vapour measurement, the resonant locations in the reference-free phase spectrum appear to coincide well with that computed from the absorption coefficient. In contrast, ammonia gas measurement from the existing Picometrix 2000 spectrometer provides a less than satisfactory result. Closer examination of the system's dynamic range (Jepsen and Fischer 2005) reveals that only resonant locations below 1.2 THz should be investigated. The reference-free phase spectrum therefore picks up the resonant peak at approximately 0.6 THz that coincides well with the absorption coefficient. Common to both measurements is the strong resonance in the frequency range below 0.2 THz in the reference-free phase spectrum. These peaks will need to be cropped out for subsequent processing.

D.2.4 Feature encoding

In order to simplify comparisons between different gas species that differ in absorption peaks, equal sized frequency bins are constructed in the frequency range of 0.1 to 2.0 THz, with the frequency resolution based on the measurement data. A typical THz-TDS system provides a frequency resolution of 37.5 GHz so this gives rise to 50 or so frequency coefficients. An absorption peak at a particular frequency marks the respective frequency bin with a Boolean one, otherwise the default value is a Boolean zero indicating no peak. This simple data encoding technique is applied to both the catalog and sample features. Figure D.7 shows a data encoding example for water spectral features recorded in the catalog and the spectral features for an arbitrary sample.

D.3 Feature selection

A typical THz-TDS system provides a frequency resolution of 37.5 GHz and a useful bandwidth of approximately 2.0 THz. This therefore leads to 50 or so frequency coefficients to be used as classification features. In practice all these coefficients will

D.4 Euclidean distance classifier

contain much redundant and irrelevant information and a classifier based on all frequency components will become computationally inefficient with poor generalisation ability called *curse of dimensionality* (Bellman 1961). The system designers are therefore required to choose a low number of coefficients from the feature space available. One approach (feature reduction) would be to reduce the dimensionality by decomposing the dataset into lower dimensions that gives rise to the greatest data variance. However, maximum variance does not always correspond to maximum discrimination between classes (Duda 2001). Another approach known as feature selection involves training a classifier with numerous sets of features and comparing the resultant classification accuracy on test data. Obviously such an approach is highly dependent on the classifier and the training and testing data. Conducting such an exhaustive search for every possible feature combination is computationally expensive. The latter approach, however, is considered here as the outputs are spectral features, as opposed to eigenvectors in principal component analysis that are more related to feature extraction.

D.4 Euclidean distance classifier

Once the spectrum is encoded, the sample gas is classified by means of minimum Euclidean distance to the gas species in the catalog. The Euclidean distance measure is a simple, fast metric that has a straightforward geometric interpretation. In general, even though the metric suffers from the drawbacks of incomparable scales of different variables and an inability to identify correlation between the variables, it nevertheless is easy to implement and computationally efficient that is sufficient for our initial purposes. By determining the Euclidean distance between an unknown gas sample and catalog gas species, the sample is considered to belong to be a particular gas that has the minimum Euclidean distance. Specifically, the distance between each respective frequency bins are computed, combined and compared. Figure D.8 shows the column plot of various Euclidean distance measures between an unknown gas sample (water vapour) and various catalog gas species including many water isotopes (HDO, D₂O) and common gases. Evidently, the unknown sample can be recognised automatically with the minimum Euclidean distance. In an effort to further minimise the Euclidean distance, the idea of zero padding was investigated, but was found to have little impact on the distance indicating the frequency resolution of the sample is sufficient. Interestingly, there is no direct correlation between the distance measure between water and its isotopes, which is due to the fact that the absorption peaks are essentially

random. Classification accuracy is largely affected by frequency resolution and the effect of noise. Frequency resolution determines the resolving power of the resonances and this is governed by the THz-TDS hardware. A typical resolution of 37.5 GHz appears to be sufficient for this work. Noise is inevitable in the THz-TDS setup and may propagate to affect the measured frequencies. Further information on the propagation of noise is provided in Withayachumnankul *et al.* (2007a). To combat the effect of noise, more measurements on the unknown sample would be necessary for subsequent averaging and comparisons.

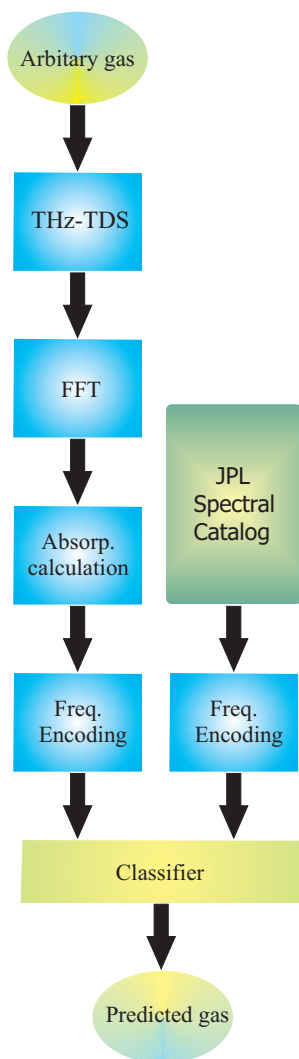


Figure D.1. The flow chart for the proposed gas recognition system. THz-TDS is performed on an arbitrary gas sample with the resonant frequencies being obtained from the spectrum and the estimated reference pulse. These frequencies are then encoded as Boolean values for classification purposes with a library of Boolean encoded cataloged gases.

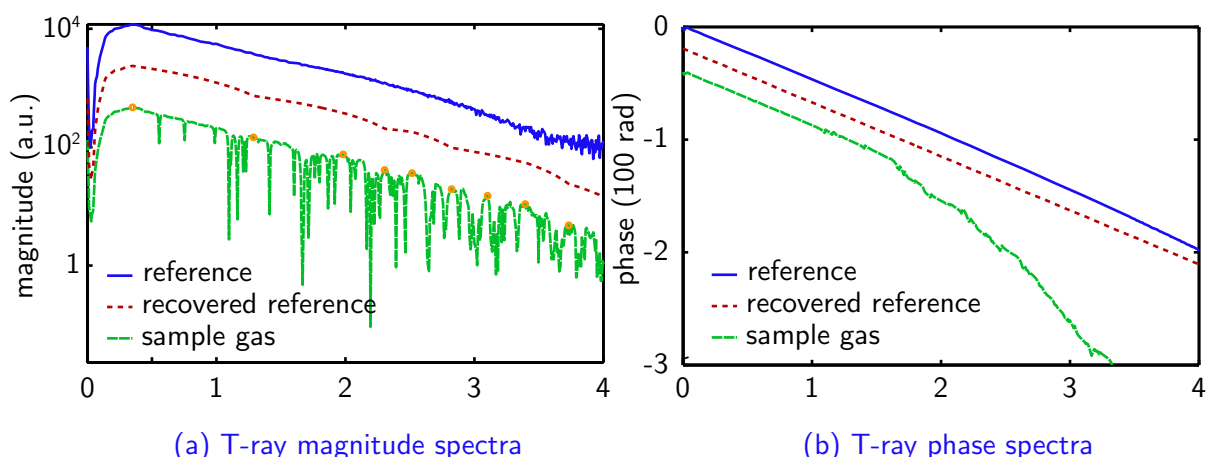


Figure D.2. Spectra for reference, recovered reference, and water vapour. (a) The water vapour or sample spectrum possesses a set of clear resonances. To determine the reference magnitude, the sample spectrum is spatially averaged and the local minima are determined, as indicated by the superimposed dotted line. Simply connecting the local minima by linear functions recovers the reference magnitude. (b) The phase spectrum of the reference also needs recovery. By fitting a linear function to the sample phase spectrum, the reference phase can be estimated.

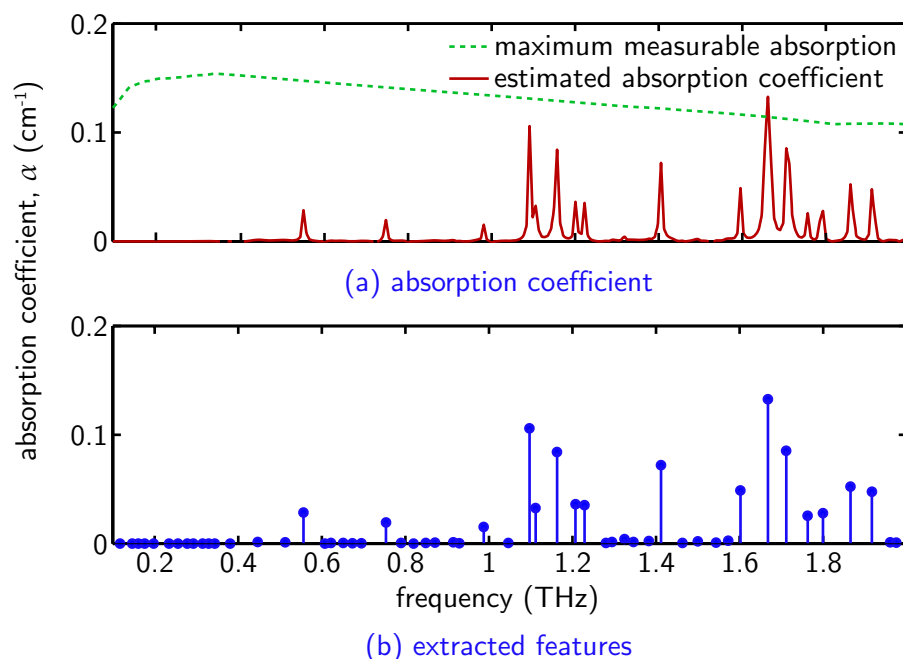


Figure D.3. Absorption coefficient and extracted features. (a) The absorption coefficient of water vapour is extracted from the measured sample spectrum and the recovered reference. (b) The coefficient in Figure (a) is determined for its local maxima, which represent the position and strength resonance features ready for gas recognition.

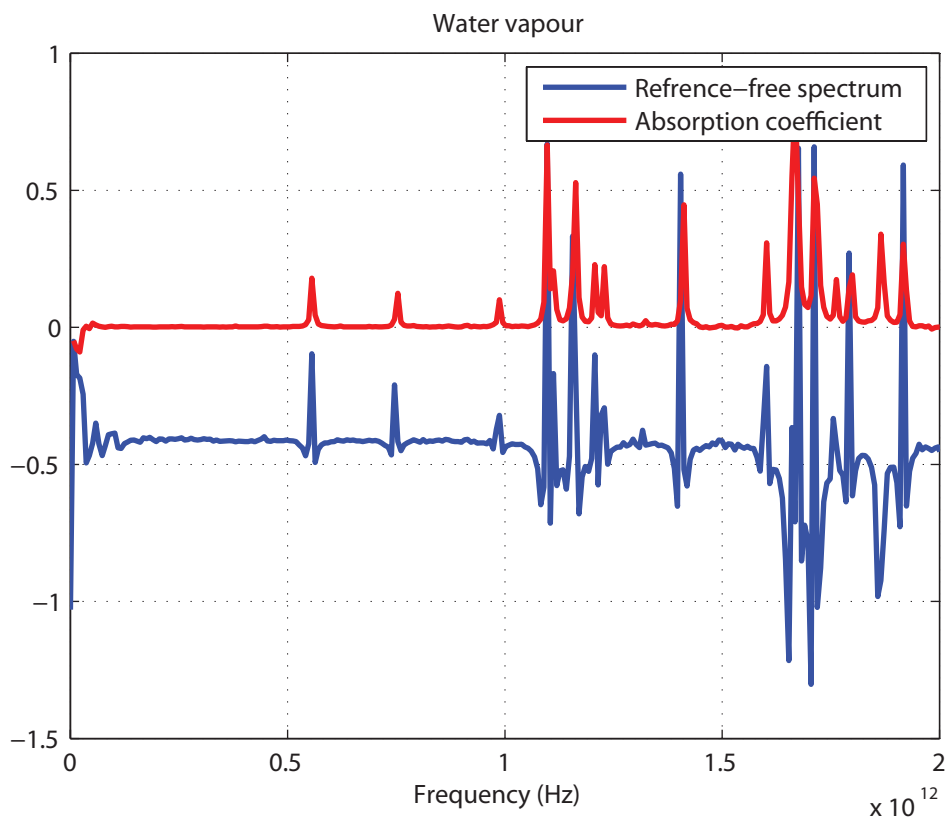


Figure D.4. Water vapour absorption coefficient and reference-free spectrum. The absorption coefficient of water vapour is compared to the reference-free spectrum for resonant location extractions.

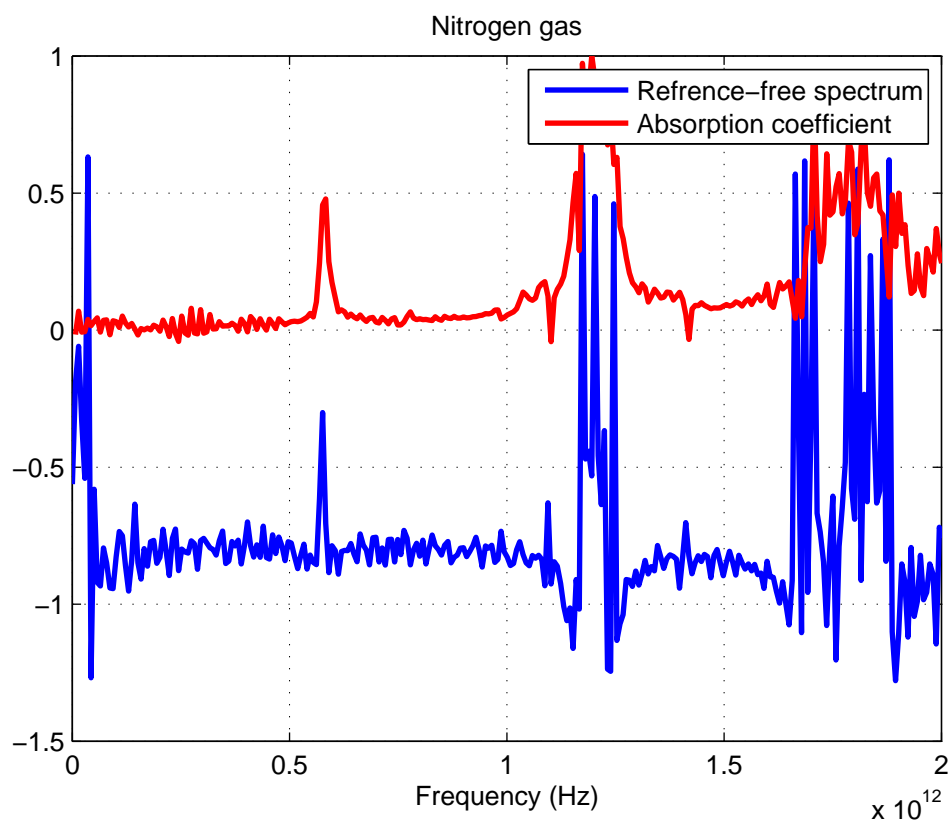


Figure D.5. Absorption coefficient and extracted features for ammonia gas. The absorption coefficient of ammonia gas is compared to the reference-free spectrum for resonant location extractions.

D.4 Euclidean distance classifier

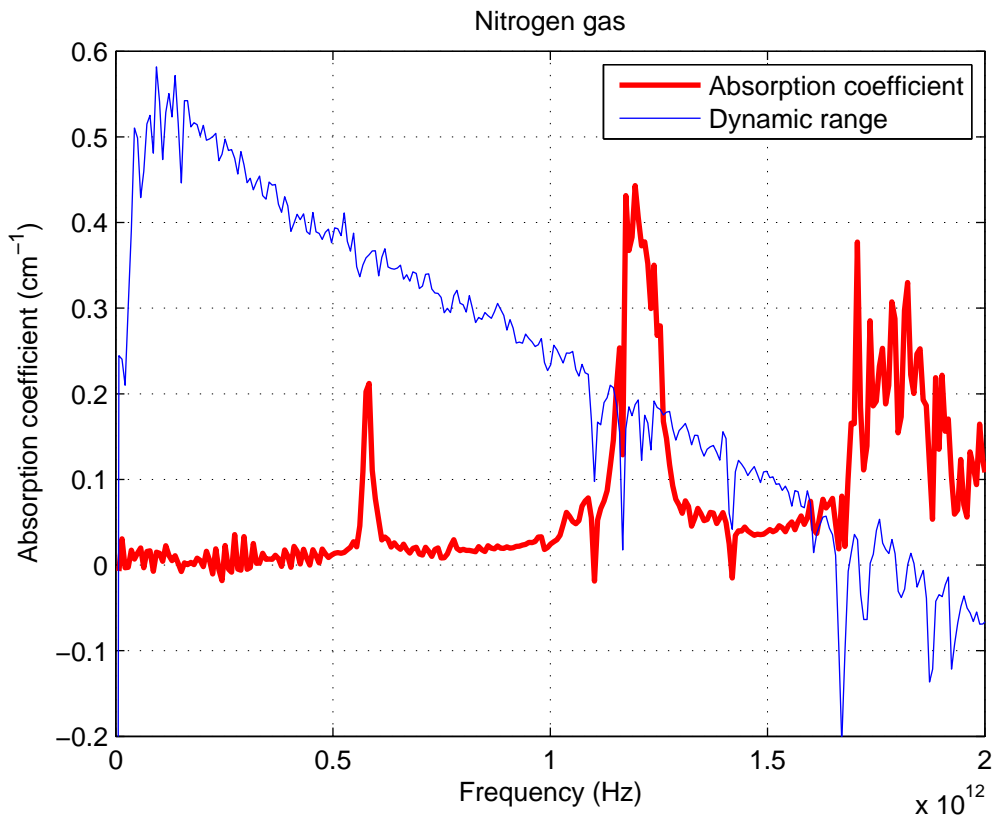


Figure D.6. Ammonia gas absorption coefficient with dynamic range. The system dynamic range reveals that only resonant locations below 1.2 THz can be used as features. The resonant peak at approximately 0.6 THz can be determined in the reference-free spectrum.

Catalog (H ₂ O)						
---	0	0	1	0	0	---
---	0.488	0.525	0.563	0.600	0.638	---
THz						
Sample (arbitrary)						
---	1	0	0	1	1	---
---	0.488	0.525	0.563	0.600	0.638	---
THz						

Figure D.7. Data encoding for the catalog and sample spectral features. The frequency resolution illustrated here is 37.5 GHz. Water has an absorption peak at 0.5569 THz and this is encoded with a boolean one in the 0.563 THz bin and zero elsewhere.

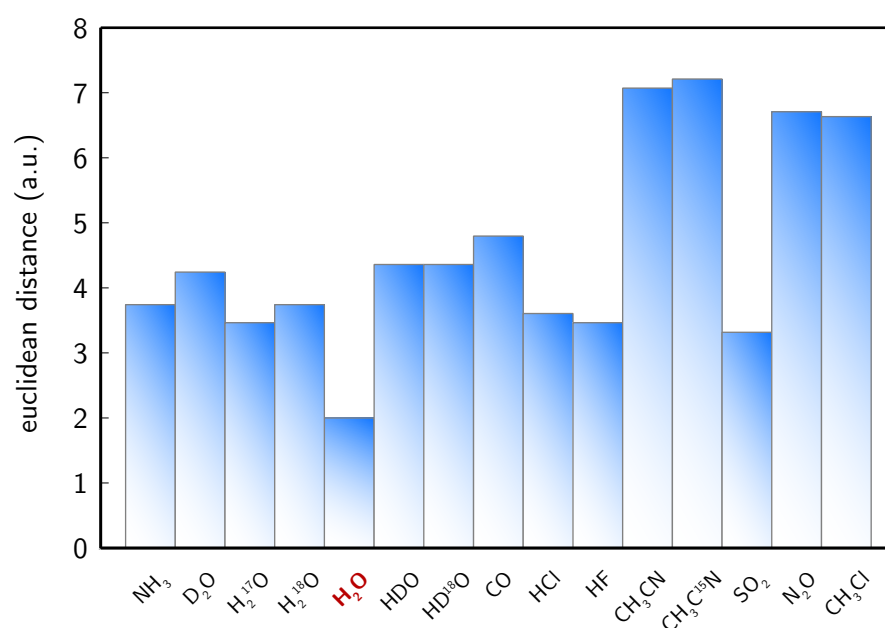


Figure D.8. Column plot of the Euclidean distance measures. The Euclidean distance measures between an unknown sample (water vapour) and various catalog gas species including water isotopes. Clearly, water can be recognised (highlighted in red) with the minimum Euclidean distance.

Appendix E



Software Implementation

A **AUTOMATED** data acquisition and processing are essential to THz systems and experiment. This Appendix outlines some of the existing and updated LabVIEW algorithms used in this Thesis for data acquisition and Matlab code listings for data processing.

E.1 Data acquisition

This section elaborates on the convergence between the motion controller of the delay stage and the lock-in amplifier. A desktop computer is connected to the motion controller via the RS-232C interface and to the lock-in via the GPIB interface. National Instruments Laboratory Virtual Instrumentation Engineering Workbench (LabVIEW) is a widely used platform and developmental environment for programming instrument hardware. LabVIEW offers the advantage of graphical abstraction for programming and provides an extensive support for many instruments.

E.1.1 THz-TDS algorithm

The intent of the LabVIEW algorithm is to coordinate the measurement of the THz voltages/current from the lock-in and the the delay stage through the motion controller. The measurement can then be processed by means of various built-in functions such as FFT and averaging. LabVIEW 8.5 is used for our purposes. The Freiburg LabVIEW algorithm for conducting THz-TDS developed by Mr Martin Schwarzer is summarised in Figure E.1.

E.1.2 Knife-edge algorithm

In order to better understand the stepping of the actuator, the control algorithm is illustrated in Figure E.2. This algorithm extends of Freiburg University's algorithm in Figure E.1.

E.1.3 Imaging algorithm

To facilitate multi-axis control capability for imaging through raster scanning, the algorithm is further extended as shown in Figure E.3. An x - y - z sample stage with computer controlled actuators installed.

E.2 Data processing

Matlab 7.6 was used to implement all the algorithms described in this Thesis. Matlab is an interpreted programming language with built in support for a large number of mathematical functions and data presentation.

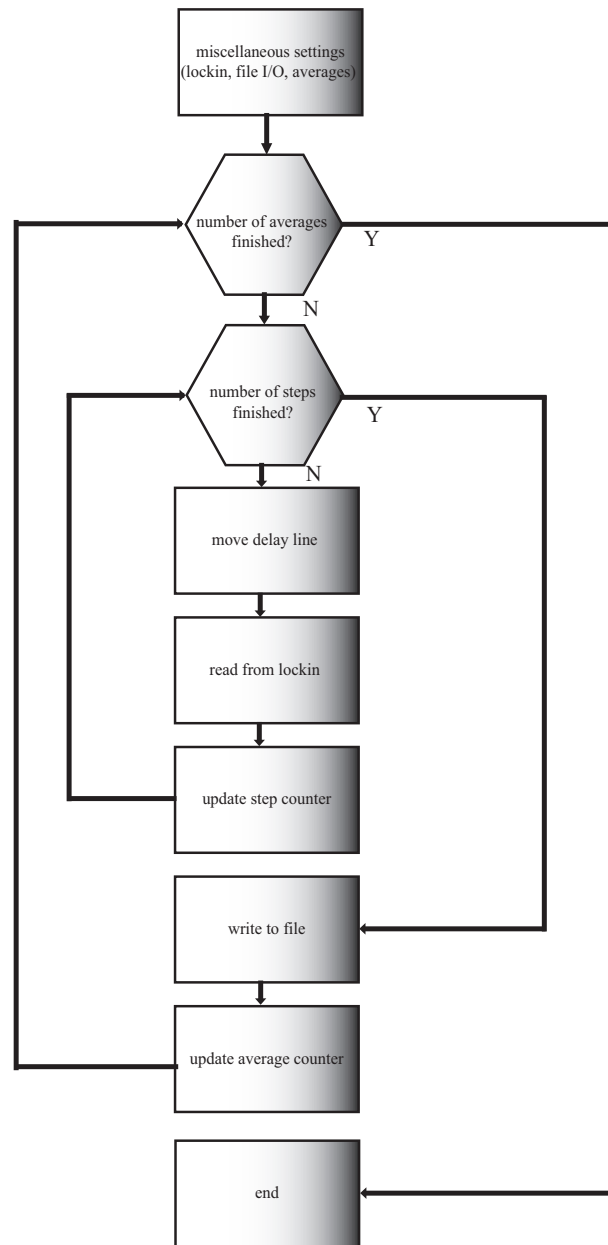


Figure E.1. THz-TDS LabVIEW algorithm. The flowchart describes the LabVIEW algorithm developed by Freiburg University, Germany, for data acquisition in a THz-TDS setup.

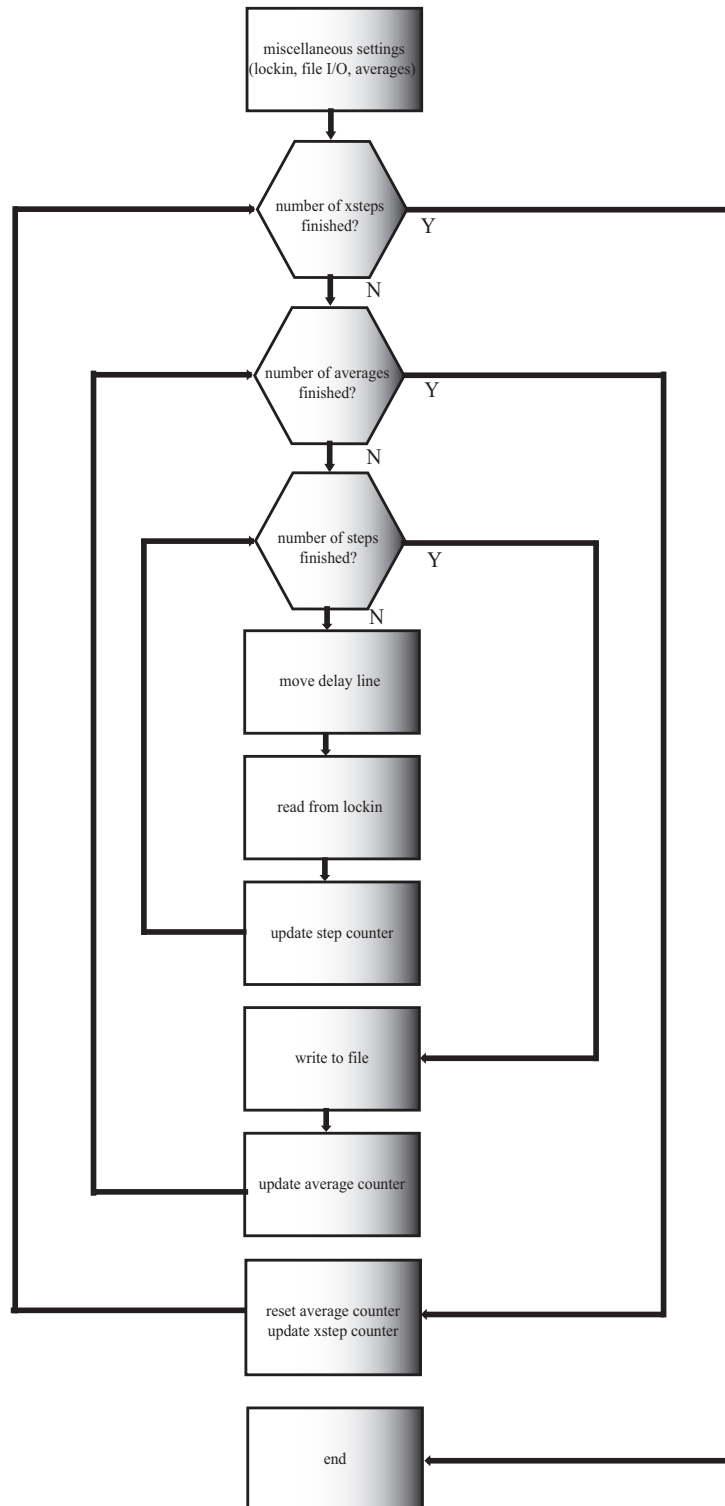


Figure E.2. LabVIEW algorithm for single axis sample scanning. The flowchart extends the THz-TDS LabVIEW algorithm developed by Freiburg University, Germany, to cater for single axis sample scanning.

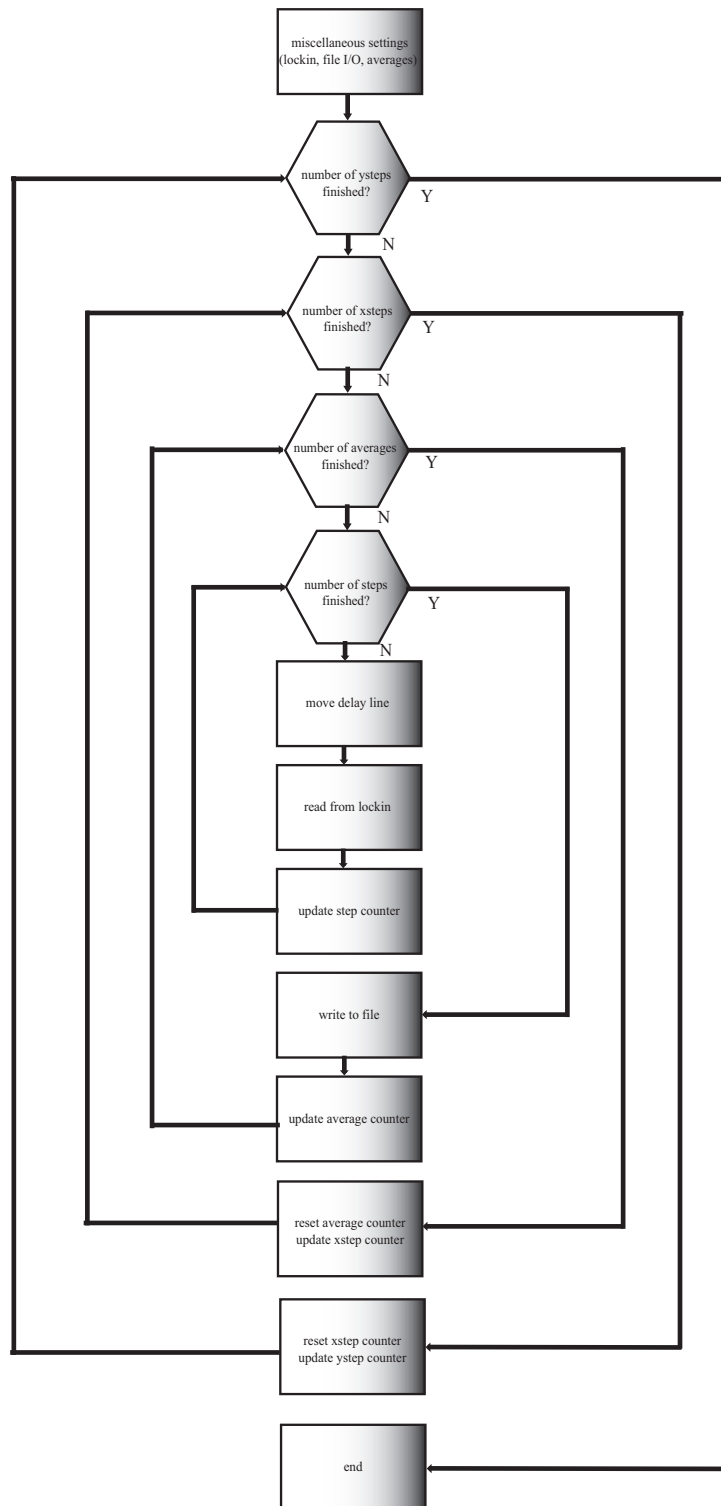


Figure E.3. LabVIEW algorithm for two axis sample scanning. The flowchart extends the THz-TDS LabVIEW algorithm developed by Freiburg University, Germany, to cater for two axis sample scanning. The raster scanning caters for THz image acquisition.

E.2.1 Code listings

The following sections provide Matlab code listings used for data processing described in this Thesis. This is only a subset of the software developed to support this research. For further information, please contact the author.

Raw THz data processing for parameter extraction

```
% Analyse the raw terahertz data pulse (ref & sample),
% plots the waveform and spectrum and phase

% By: Hungyen Lin
% Date: 18 June 2007
% =====

clear all;
close all;

% Declarations
% =====

% reference_f = 'gas_cell2.txt';
% sample_f = 'NH3_3.txt';
reference_f= '18020008.BEF'; % reference pulses
% sample_f='18020011.BEF'; % sample pulse
sample_f= '18020008.BEF';

c = 3e8;
thickness = 0.2;
fb = 0;
fe = 2e12;

% Load file
% =====

reference = load(reference_f);
sample = load(sample_f);
[m,n] = size(reference);
sam = sample(:,2)-mean(sample(:,2));
ref = reference(:,2)-mean(reference(:,2));
tscale = sample(:,1).*1e-12;

% Waveform plots
% =====

subplot(2,2,1),plot(tscale,reference(:,2),'-b','LineWidth',2);
hold all
subplot(2,2,1),plot(tscale,sample(:,2),'-r','LineWidth',2);
grid on
legend('ref','samp',1);
xlabel('Time ');
```

E.2 Data processing

```
ylabel('T-ray Intensity (a.u)');

% Spectrum
% =====

ref_fft = fft(ref);
sam_fft = fft(sam);
ref_abs = abs(ref_fft);
sam_abs = abs(sam_fft);
timestep = tscale(2) - tscale(1);
freq = [0:m-1]'/timestep/m;
omega = 2*pi*freq*1e12;

subplot(2,2,2);semilogy(freq,ref_abs,'-b','LineWidth',2);
hold all
subplot(2,2,2);semilogy(freq,sam_abs,'-r','LineWidth',2);
grid on
xlim([fb fe]);
legend('ref','sam');
xlabel('Frequency (Hz)');
ylabel('T-ray Intensity (a.u)');

% Phase
% =====

transmission = sam_fft./ref_fft;
resolution = freq(2);
transmission_abs = abs(transmission);
transmission_phase = -unwrap(angle(transmission));
% normal = -unwrap(angle(sam_fft));
normal = transmission_phase;
lower_freq = ceil(0.2/resolution);
upper_freq = floor(0.4/resolution);
phase_diff = transmission_phase(2)-transmission_phase(1);
slope = phase_diff/resolution;
yaxis = slope*freq(1:lower_freq);
j = slope*freq(lower_freq);
j2 = transmission_phase(lower_freq);
diffj = j2 - j;
diffj = diffj*-1;
a = [yaxis]';
b = [transmission_phase(lower_freq+1:m)+diffj]';
combined = [a b];

subplot(2,2,3),plot(freq(1:m/20),normal(1:m/20),'-b','LineWidth',2);
hold all
subplot(2,2,3),plot(freq(1:m/20),combined(1:m/20),'-r','LineWidth',2);
grid on
legend('original phase','extrapolated phase',1)
xlabel('Frequency (THz)');
ylabel('Phase (rad)');

subplot(2,2,4),plot(freq,transmission)
```

```

% Refractive index and absorption coefficient
% =====

% mult = c./(thickness*omega);
% coeff = mult'.*combined;
% refrac = coeff +1;
% extinction = -mult'.*log(((refrac+1).^2).*transmission_abs'./(4.*refrac));
% absorption = (2*extinction.*omega')./c;
% absorption = absorption/100;
% amax = 2/(thickness*100).*log(ref_abs);
% % subplot(2,2,3),plot(freq,refrac,'-b','LineWidth',2);
% subplot(2,2,3),plot(freq(1:end-1),-c*diff(normal/freq(end))/thickness,'-b','LineWidth',2);
% grid on
% xlabel('Frequency (Hz)');
% ylabel('Index of refraction (n)');
% xlim([fb fe]);
% subplot(2,2,4);plot(freq,absorption,'-r','LineWidth',2);
% hold all
% subplot(2,2,4);plot(freq,amax);
% grid on
% xlabel('Frequency (Hz)');
% ylabel('Absorption coefficient (cm^{-1})');
% xlim([fb fe]); ylim([-0.2 0.6]);
% % Lorentzian profile
% % =====
%
% figure(3);
% ps = -c*diff(normal/freq)/thickness;
% ps=ps/max(ps);
% plot(freq(1:end-1),ps-0.3,'-b','LineWidth',2);
% hold on;
% plot(freq,absorption/max(absorption),'-r','LineWidth',2);
% xlabel('Frequency (Hz)');
% grid on;
% xlim([fb fe]);
% legend('Refrence-free spectrum','Absorption coefficient');
% hold off;
%
% figure(2);
% plot(freq,absorption,'-r','LineWidth',2);
% hold all
% plot(freq,amax);
%
% grid on
% xlabel('Frequency (Hz)');
% ylabel('Absorption coefficient (cm^{-1})');
% xlim([fb fe]); ylim([-0.2 0.6]);
% legend('Absorption coefficient','Dynamic range');

```

Gaussian beam waist

```

% Beam waist of a focussed Gaussian beam

```

E.2 Data processing

```
% By: Hungyen Lin
% Date: 2009
% =====

f = 50e-3;           % focal length
lambda = 800e-9;    % IR centre wavelength in free space
c = 3e8;            % light speed
beam_waist = 1e-3;  % beam waist
spot_siz = (f*lambda)/(pi*beam_waist)

% Rayleigh distance
zR = (pi*spot_siz^2)/lambda

% Spot size give proppagation distance z
z = 0.2e-3;
w = spot_siz*((1+(z/zR)^2)^0.5)
```

Experimental knife-edge profile

```
% Analyse the raw terahertz data pulse (ref & sample),
% plots the waveform and spectrum and phase

% By: Hungyen Lin
% Date: 2010
% =====

clear all;
close all;
b = 1;
time_matrix = [];
fft_matrix = [];
mov_fft = [];
jj_bak = [];
numscan = 105; % testc = 97, testg = 95, testm = 110
stepsiz = 0.025; % (mm)
xstart = 8.3; % testc = 5, testg = 1, testm = 2, testh = 3
Filter=0; %
Spectro = 0;

%pathname = 'D:\Log\Hungyen\120810\';
% pathname = 'D:\Log\Hungyen\270810\'; % test
pathname = 'D:\Log\Hungyen\140910\';

if Spectro == 1 % Spectroscopy?
    reference_f= strcat(pathname,'testj_avg.dat'); % reference pulse file
    reference = load(reference_f);
    [m,n]=size(reference);
    ref = reference(:,2);
    ref_fft = fft(ref);
    ref_abs = abs(ref_fft);
end
```

```

for j = 1:numscan
    %Number of files
    zz=5;
    a=[];
%       if j == 1
%           jj = 1;
%       else
%           jj = 10*(j-1);
%       end
    jjj = int2str(j);
    jj_bak = [jj_bak,j];

    for ii = 1:zz

        % File details
        iii= int2str(ii);
        aa = '';
        b = 10^j;
%       pathname = 'D:\Log\Hungyen\290710\' ; %testa, testc

%       pathname = 'D:\Log\Hungyen\190510\' ; % testh, testk old double axis
%       pathname = 'D:\Log\Hungyen\190410\' ; % far field knife edge
%       filename_base = '\testb';
        filename_base = 'testk';
        output_filename_base = '\test';
        scan_suffix = '_';
        ending_input = '.dat';
        ending_output = '.out';

        file_input = strcat(pathname,filename_base,iii,scan_suffix,jjj,ending_input);
        fid = fopen(file_input, 'r');
        scan_ii = textscan(fid, '%f %f ', 'headerlines', 2);

        signal_ii=scan_ii{:},2};
        signal_ii(1)=0;
        signal_plot_iii=signal_ii;
        dim_file_iii=length(signal_plot_iii);
        time_iii=scan_ii{:},1}*1e-12;
        end_time=time_iii(dim_file_iii);
        if Filter==1
            F_type = 'high'; % filter type
            %Wn=[0.01,0.02,0.05];
            Wn=0.025; % 100GHZ
            F_order=200; % filter order
            b = fir1(F_order,Wn,F_type); %filter coefficients
%           figure(10)
%           freqz(b)

            BF1=conv(signal_ii,b);signal_ii=BF1((0.5*F_order+1):(length(BF1)-0.5*F_order));
            signal_ii(1:0.28*F_order+1)=zeros(size(signal_ii(1:0.28*F_order+1)));
            signal_ii((length(signal_ii)-0.45*F_order:length(signal_ii)))
            =zeros(size(signal_ii((length(signal_ii)-0.45*F_order:length(signal_ii)))));

```

E.2 Data processing

```
    end
    a=[a,signal_ii];
    fclose(fid);

end

if zz==1
    gh=a;
else
    gh=mean(a');
end
gh(1)=gh(2);
time_matrix(:,j) = gh;

% FFT
dt = 0.06667; %modify for the time step
N = length(time_iii); %modify for the number of points
% N = 525;
npads = N - length(time_iii);
fscale = [0:1/(dt*N):1/dt-1/(dt*N)]';
sam_fft = fft([gh,zeros(1,npads)]);
mov_fft(:,j) = abs(sam_fft);

if Spectro == 1

    % Transmission
    transmission = sam_fft'./ref_fft;
    resolution = fscale(2);
    transmission_abs(:,j) = abs(transmission);

    % Phase
    sam_phase = -unwrap(angle(sam_fft));
    ref_phase = -unwrap(angle(ref_fft));
    sam_phase_tmp(:,j) = sam_phase;
    ref_phase_tmp(:,j) = ref_phase;

    % Extrapolation on lower THz frequency phase
    low_freq = find(fscale<=0.35);
    hi_freq = find(fscale<=0.5);
    phase_diff_sam = sam_phase(hi_freq(end))-sam_phase(low_freq(end));
    slope_sam = phase_diff_sam/(1e12*fscale(hi_freq(end))-1e12*fscale(low_freq(end)));
    y_incpt_sam = sam_phase(low_freq(end)) - slope_sam*1e12*fscale(low_freq(end));
    sam_phase(1:low_freq(end)-1)=1e12*fscale(1:low_freq(end)-1)*slope_sam + y_incpt_sam;
    sam_phase(hi_freq(end)+1:end)=1e12*fscale(hi_freq(end)+1:end)*slope_sam + y_incpt_sam;
    sam_phase = sam_phase - y_incpt_sam;

    phase_diff_ref = ref_phase(hi_freq(end))-ref_phase(low_freq(end));
    slope_ref = phase_diff_ref/(1e12*fscale(hi_freq(end))-fscale(low_freq(end))*1e12);
    y_incpt_ref = ref_phase(low_freq(end)) - slope_ref*1e12*fscale(low_freq(end));
    ref_phase(1:low_freq(end)-1)=1e12*fscale(1:low_freq(end)-1)*slope_ref + y_incpt_ref;
    ref_phase(hi_freq(end)+1:end)=1e12*fscale(hi_freq(end)+1:end)*slope_ref + y_incpt_ref;
    ref_phase = ref_phase - y_incpt_ref;
```

```

        trans_phase(:,j) = sam_phase - ref_phase'; % transmitted phase
        sample_phase(:,j) = sam_phase;
    end

%     fft_matrix(:,j) = fft_matrix(:,j)/max(fft_matrix(2:end,j));
%     m = m(4:end);
%     plot(fscale, abs(fft(gh))/max(m),aa);hold on;
%     plot(fscale(1:length(mov_fft)), mov_fft,aa);hold on
%     plot(fscale, abs(fft(gh)),aa);hold on
%     title('Frequency');
%     grid off, set(gca, 'XLim', [0.1,5]);

%     figure(3);
%     m = m(4:end);
%     plot(fscale, abs(fft(gh))/max(m),aa);hold on;
%     grid off, set(gca, 'XLim', [0.1,5], 'YScale', 'log');
%     plot(fscale, abs(fft(gh)).^2,aa);hold on;
%     title('Spectral density');
%     grid on, set(gca, 'XLim', [0.1,10], 'YScale', 'log');
%     grid on;
end

xscale = [xstart:stepsiz:(numscan-1)*stepsiz+xstart];

if Spectro == 0

    % Spectra plot
    figure;
    mov_fft = mov_fft.^2;
    hx = plot(fscale(1:length(mov_fft)), mov_fft(:,jj_bak),aa);
    axx = gca;
    set(hx,'linewidth',2,'linestyle','-');
    legend(num2str(xscale(jj_bak)'));
    grid off, set(axx, 'XLim', [0.1,5]);
    xlabel('Frequency (THz)');
    ylabel('Fourier amplitude squared (a.u.)');

    % Logscale plot for noise floor
    figure;
    hx = plot(fscale(1:length(mov_fft)), mov_fft(:,jj_bak),aa);
    axx = gca;
    set(hx,'linewidth',2,'linestyle','-');
    legend(num2str(xscale(jj_bak)'));
    grid on, set(axx, 'XLim', [0.1,3.5], 'YScale', 'log');
    xlabel('Frequency (THz)');

    % Skip file spectra plot
    nsteps = 20;
    figure;
    hx = plot(fscale(1:length(mov_fft)), mov_fft(:, [1:nsteps:end]),aa);
    axx = gca;
    set(hx,'linewidth',2,'linestyle','-');
    legend(num2str(xscale([1:nsteps:end]')));

```

E.2 Data processing

```
grid off, set(axx, 'XLim', [0.1,5]);
xlabel('Frequency (THz)');
ylabel('Fourier amplitude squared (a.u.)');

else % Transmission & Phase plot

    % Sample plot
    % figure;
    %% transmission_abs = transmission_abs.^2;
    % hx = plot(fscale(1:length(mov_fft)), mov_fft(:,jj_bak),aa);
    % axx = gca;
    % set(hx,'linewidth',2,'linestyle','-');
    % legend(num2str(xscale(jj_bak)));
    % grid off, set(axx, 'XLim', [0.1,5]);
    % xlabel('Frequency (THz)');
    % ylabel('Fourier amplitude squared (a.u.)');
    %
    % Logscale sample plot for noise floor
    % figure;
    % hx = plot(fscale(1:length(mov_fft)), mov_fft(:,jj_bak),aa);
    % axx = gca;
    % set(hx,'linewidth',2,'linestyle','-');
    % legend(num2str(xscale(jj_bak)));
    % grid on, set(axx, 'XLim', [0.1,3.5], 'YScale', 'log');
    % xlabel('Frequency (THz)');
    %
    % Skip file sample plot
    nsteps = 20;
    figure;
    hx = plot(fscale(1:length(mov_fft)), mov_fft(:,[1:nsteps:end]),aa);
    axx = gca;
    set(hx,'linewidth',2,'linestyle','-');
    legend(num2str(xscale([1:nsteps:end])));
    grid off, set(axx, 'XLim', [0.1,5], 'YScale', 'log');
    xlabel('Frequency (THz)');
    ylabel('Transmission (a.u.)');

    % Transmission plot
    % figure;
    %% mov_fft = mov_fft.^2;
    % hx = plot(fscale(1:length(transmission_abs)), transmission_abs(:,jj_bak),aa);
    % axx = gca;
    % set(hx,'linewidth',2,'linestyle','-');
    % legend(num2str(xscale(jj_bak)));
    % grid off, set(axx, 'XLim', [0.1,5]);
    % xlabel('Frequency (THz)');
    % ylabel('Fourier amplitude squared (a.u.)');

    % Logscale plot for noise floor
    % figure;
    % hx = plot(fscale(1:length(transmission_abs)), transmission_abs(:,jj_bak),aa);
    % axx = gca;
    % set(hx,'linewidth',2,'linestyle','-');
```



```

% legend(num2str(xscale(jj_bak)'));
% grid on, set(axx, 'XLim', [0.1,3.5], 'YScale', 'log');
% xlabel('Frequency (THz)');

% Skip file spectra plot
nsteps = 20;
figure;
hx = plot(fscale(1:length(transmission_abs)), transmission_abs(:, [1:nsteps:end]), aa);
axx = gca;
set(hx, 'linewidth', 2, 'linestyle', '-');
legend(num2str(xscale([1:nsteps:end])));
grid off, set(axx, 'XLim', [0.1,5]);
xlabel('Frequency (THz)');
ylabel('Fourier amplitude squared (a.u.)');

figure;
hx = plot(fscale(1:length(sam_phase_tmp)), sam_phase_tmp(:, jj_bak), aa);
axx = gca;
set(hx, 'linewidth', 2, 'linestyle', '-');
legend(num2str(xscale(jj_bak)'));
grid off, set(axx, 'XLim', [0.1,5]);
xlabel('Frequency (THz)');
ylabel('Phase (a.u.)');

% Phase plot
figure;
hx = plot(fscale(1:length(sample_phase)), sample_phase(:, jj_bak), aa);
axx = gca;
set(hx, 'linewidth', 2, 'linestyle', '-');
legend(num2str(xscale(jj_bak)'));
grid off, set(axx, 'XLim', [0.1,5]);
xlabel('Frequency (THz)');
ylabel('Phase (a.u.)');

% Skip file phase plot
figure;
hx = plot(fscale(1:length(sample_phase)), sample_phase(:, [1:nsteps:end]), aa);
axx = gca;
set(hx, 'linewidth', 2, 'linestyle', '-');
legend(num2str(xscale([1:nsteps:end])));
grid off, set(axx, 'XLim', [0.1,5]);
xlabel('Frequency (THz)');
ylabel('Phase (a.u.)');

%

end

% freq_idnx = [11,20,37,41,52,58,68]; testc, testg
% freq_idnx = [11,21,39,43,55,61,72]; testa yslice

```

E.2 Data processing

```
% freq_idnx = [11,21,39,47,57,61,70]; testa testc
%freq_idnx = [10,17,28,39,56,66]; % NF xy axis KE
% freq_idnx = [11,21,25,28,39]; % resolving PE sample
% freq_idnx = [20,49,54,75,88]; %Lactose KE with N = 525
freq_idnx = [13,20,24,30,34,47,59];
%freq_idnx = [24,26,28,30,31,32];

% Nave = 5;
% new_fft_matrix=[];
% for i = 1:length(freq_idnx)
%     ab = mov_fft(freq_idnx(i,:),:);
%     ab = moving(ab,Nave);
%     new_fft_matrix(i,:)=ab/max(ab);
% end

% Normalise scans
% for i = 1:j
%     mov_fft(:,i)= mov_fft(:,i)/max(mov_fft(:,i));
% end
% figure;
% hx = plot(fscale(1:length(mov_fft)), mov_fft,aa);
% axx = gca;
% set(hx,'linewidth',2,'linestyle','-');
% legend(num2str(xscale(jj_bak)'));
% grid off, set(axx, 'XLim', [0.1,5]);

% Normalise frequencies
% for i = 1:length(mov_fft)
%     mov_fft(i,:)= mov_fft(i,:)/max(mov_fft(i,:));
% end
% % mov_fft = [ones(length(mov_fft),3),mov_fft]; % one pad in testh
% figure;
% hx = plot(xscale(jj_bak),mov_fft(freq_idnx,:));
% axx = gca;
% set(hx,'linewidth',2,'linestyle','-');
% legend(num2str(fscale(freq_idnx)));
% % grid off; set(axx, 'YLim', [-0.1,1.2], 'XLim', [1.4,2.5]);
% xlabel('X position (mm)');

if Spectro == 0
%     Moving average of spectra knife edge profile
    num_mov = 1;
    new_mov_fft = [];
    for i = 1:length(mov_fft)
        new_mov_fft(i,:) = moving(mov_fft(i,:),num_mov);
        new_mov_fft(i,:)= new_mov_fft(i,:)/mean(new_mov_fft(i,:));
    end
    wid = size(new_mov_fft);
    figure;
    hx = plot(xscale(jj_bak(1:length(jj_bak)-num_mov)),new_mov_fft(freq_idnx,jj_bak(1:length(jj_bak)-num_mov)));
    axx = gca;
    set(hx,'linewidth',2,'linestyle','-');
    legend(num2str(fscale(freq_idnx)));
```

```

% grid off; set(axx, 'YLim', [-0.1,2]);
xlabel('X position (mm)');
ylabel('Magnitude (a.u.)');
grid on;

else

%   f_index = find(fscale<3);
%   figure;
%   hx = plot(fscale(f_index)*1e12,sam_phase_tmp(f_index,1:40));
%   set(hx,'linewidth',2,'linestyle','-');
%   hold on;
%   hx = plot(fscale(f_index)*1e12,ref_phase_tmp(f_index,end),'r');
%   axx = gca;
%   set(hx,'linewidth',2,'linestyle','-');
%   hold off;

%   % Sample and reference plot
%   f_index = find(fscale<2.5);
%   figure;
%   hx = plot(fscale(f_index)*1e12,sam_phase(f_index));
%   set(hx,'linewidth',2,'linestyle','-');
%   hold on;
%   hx = plot(fscale(f_index)*1e12,ref_phase(f_index),'r');
%   axx = gca;
%   set(hx,'linewidth',2,'linestyle','-');
% %   hold on;
% %   hx = plot(fscale(f_index)*1e12,trans_phase(f_index,end),'k');
% %   axx = gca;
% %   set(hx,'linewidth',2,'linestyle','-');
%   hold off;
%
%   figure;
%   hx = plot(fscale(f_index),sam_phase(f_index)'./(2*pi*1e12*fscale(f_index)));
%   set(hx,'linewidth',2,'linestyle','-');
%   hold on;
%   hx = plot(fscale(f_index),ref_phase(f_index)'./(2*pi*1e12*fscale(f_index)),'r');
%   axx = gca;
%   set(hx,'linewidth',2,'linestyle','-');
%   %   grid off, set(axx, 'XLim', [0.3,1.5]);
%   hold off;

% Moving average of transmission knife edge profile
new_mov_fft =mov_fft;
num_mov = 0;
for i = 1:length(mov_fft)
    new_mov_fft(i,:)= mov_fft(i,:)/mean(mov_fft(i,:));
end
figure;
hx = plot(xscale(jj_bak(1:length(jj_bak)-num_mov)),new_mov_fft(freq_idnx,jj_bak(1:length(jj_bak)-num_mov)));
axx = gca;
set(hx,'linewidth',2,'linestyle','-');
legend(num2str(fscale(freq_idnx)));

```

E.2 Data processing

```
% grid off; set(axx, 'YLim', [-0.1,2]);
xlabel('X position (mm)');
grid on;

% Moving average of transmission knife edge profile
% num_mov = 0;
% for i = 1:length(transmission_abs)
%     transmission_abs(i,:)= transmission_abs(i,)/mean(transmission_abs(i,:));
% end
% figure;
% hx = plot(xscale(jj_bak(1:length(jj_bak)-num_mov)),transmission_abs(freq_idnx,jj_bak(1:length(jj_bak)-num_mov)));
% axx = gca;
% set(hx,'linewidth',2,'linestyle','-');
% legend(num2str(fscalescale(freq_idnx)));
%% grid off; set(axx, 'YLim', [-0.1,2]);
% xlabel('X position (mm)');
% grid on;

% Moving average of sample time delay knife edge profile
num_mov = 0;
figure;
for i = 1:length(freq_idnx)
    time_delay(i,:) = sample_phase(freq_idnx(i),jj_bak(1:length(jj_bak)-num_mov))./(2*pi*fscalescale(freq_idnx(i))*1e12);
end
hx = plot(xscale(jj_bak(1:length(jj_bak)-num_mov)),time_delay);
axx = gca;
set(hx,'linewidth',2,'linestyle','-');
legend(num2str(fscalescale(freq_idnx)));
%% grid off; set(axx, 'YLim', [-0.1,2]);
xlabel('X position (mm)');
grid on;

end
% figure(4);
% plot(fscalescale,fft_matrix(:,1:end));
% grid off, set(gca, 'XLim', [0.1,5], 'YScale', 'log');

% File output to text file for comparison (selected freq ONLY)
%file_output = strcat(filename_base,'_ke',ending_input);
%fid = fopen(file_output,'wt');
%fprintf(fid,'%12.8f %12.8f %12.8f %12.8f %12.8f %12.8f %12.8f %12.8f\n',new_mov_fft(freq_idnx,jj_bak(1:length(jj_bak)-num_mov)));
%fclose(fid);

% File output to text file for comparison (all freq)
% tmp = find(fscalescale<3); % get freq index at 3THz
% a = new_mov_fft(tmp,jj_bak(1:length(jj_bak)-num_mov));
% a = a';
% b = fscalescale(tmp);
% save yslice_ke_v3.dat a -ascii;
% save yslice_ke_v3_fscalescale.dat b -ascii;

% Contour plot (requires at least 2 rows in scanning)
```

```

% a = mov_fft(freq_idnx(3),jj_bak(1:length(jj_bak)-num_mov));
% [X,Y]=meshgrid(xscale(jj_bak(1:length(jj_bak)-num_mov)),1);

% Image plot
%
% figure;
% a = mov_fft(freq_idnx(3),jj_bak(1:length(jj_bak)-num_mov));
% imagesc(xscale(jj_bak(1:length(jj_bak)-num_mov)),1,1./a);
% colormap(gray);
% % %
% figure;
% a = mov_fft(freq_idnx(4),jj_bak(1:length(jj_bak)-num_mov));
% imagesc(xscale(jj_bak(1:length(jj_bak)-num_mov)),1,1./a);
% colormap(gray);
% % %
% figure;
% a = mov_fft(freq_idnx(5),jj_bak(1:length(jj_bak)-num_mov));
% imagesc(xscale(jj_bak(1:length(jj_bak)-num_mov)),1,1./a);
% colormap(gray);
% % %
% figure;
% a = mov_fft(freq_idnx(6),jj_bak(1:length(jj_bak)-num_mov));
% imagesc(xscale(jj_bak(1:length(jj_bak)-num_mov)),1,1./a);
% colormap(gray);
% %

```

Gas classification

```

% function nfal = bool_classifier(df)

% Compares the Euclidean distance of variables and
% selects the minimum one
%
%
% By: Hungyen Lin
% Date: July 2007
% =====

clear all;

% Declarations
% =====

% N = 10;
sample_f = 'sample.txt';
train_f = 'train.txt';
noise = 0;
% fs = 1/dt;
fe = 2e12;
% df = fs/N;          % spectral resoln
thresh = 0.1;
snr = 35;
noSet = 200;

```

E.2 Data processing

```
% Sample spectra
% =====

s = textread(sample_f,'%s');
[df,spks] = SampleData(thresh,s,noise,snr);
df = df*10;
N = round(fe/df);
sample = zeros(length(s),N);
indx = round(spks/df)+1;
if indx <= N
    sample(1,indx) = 1;
end

% Catalog spectra
% =====

c = textread(train_f,'%s');
cat = zeros(length(c),N);
for j = 1:length(c)
    cpks = TrainData(thresh,c(j),noise,snr)';
    indx = round(cpks/df)+1;
    if indx <= N
        cat(j,indx) = 1;
    end
end

% Compute Euclidean distance
% =====

sample = (sample'*ones(1,length(c)))';           % sample matrix from sample vector
diff = (sample - cat).^2;                       % Euclidean dist.
ed = sqrt(sum(diff,2));
for i = 1:length(c)                             % error percentage
    nfal(i) = nnz(diff(i,:));                   % number of false
    nfal(i) = 100*nfal(i)/sum(cat(i,:));
end

% Finds min. Euclidean distance & determines class
% =====

a = find(ed==min(ed));                          % a = index of min. dist.
class = c(a)                                    % return class based on filename

% MLP
% =====

% Training data

noise = 1;
len = length(dec2bin(length(c)));
inputTr= zeros(length(c)*noSet,N);
```

```

k = 1;
for j = 1:length(c)
    for i = 1:noSet
        pks = TrainData(thresh,c(j),noise,snr);
        indx = round(pks/df)+1;
        ii=find(indx<=N);
        inputTr(k,indx(ii)) = 1;
        k = k + 1;
    end
end

targetTr = zeros(len,length(c)*noSet);
% for j = 1:length(c)
%     for i = 1:noSet
%         dec2bin(j,len);
%         targetTr(k)=
%         k = k + 1;
%     end
% end
cs = 1;
ce = noSet;
for j = 1:length(c)
    k = 1;
    a = dec2bin(j,len);
    for i = 1:len
        targetTr(i,cs:ce)=ones(1,noSet)*bin2dec(a(i));
    end
    cs = ce + 1;
    ce = ce + noSet;
end

% Network

PR = [0 1];
PR = ones(N,1)*PR;
nhn = 2*N+1;
no = len;
net = newff(PR,[nhn no],{'tansig','logsig'});
net.trainFcn = 'trainrp';
% net.trainParam.mem_reduc = 1e3;
% net.trainParam.show = 10;
net.inputweights{1,1}.initFcn = 'rands';
net.biases{1}.initFcn = 'rands';
p = inputTr;
t = targetTr;
[trainV,valV,testV] = dividevec(p,t,0.3,0);
% net.trainParam.epochs = 1000;
% net.trainParam.show = 100;
net = train(net,trainV.P,trainV.T);
% net = init(net);
y = sim(net,sample(1,:));

% Output decoding

```

E.2 Data processing

```
y = y';
a= '';
for i = 1:no
    a=strcat(a,dec2bin(round(y(i))));
end
c(bin2dec(a))

% Generate plots
% =====

% figure(1);
% fscale = [0:df:fs-df];
% subplot(211); hx1 = stem(fscale, cat');
% set(hx1(1),'linewidth',2,'linestyle','-','color','black');
% set(hx1(2),'linewidth',2,'linestyle','-','color','green');
% xlim([0.1 2]); ylabel('magnitude (a.u.)'); xlabel('Frequency (THz)');
% legend('H2O','NH3');
% subplot(212); hx2 = stem(fscale, sample');
% set(hx2(1),'linewidth',2,'linestyle','-','color','blue');
% xlim([0.1 2]); ylabel('magnitude (a.u.)'); xlabel('Frequency (THz)');

% figure(1);
% x = [1:length(ed)];
% make a barplot
% bh= bar(x,ed,1,'b'); % barplot
%
% Use "hidden" functions to get the information you want[cax,args,nargs] = axescheck(x, data, 1,'r');
% [msg,x,y,xx,yy,linetype,plottype,barwidth,equal]=makebars(x,ed);
%
% Every bar in a bar-plot is made of a set of 5 x-y pairs.
% Create Patch indices
% ix=reshape(1:length(ed)*5,5,[]);
%
% Define RGB-triplets for every 5-set of xy-pairs
% col=rand(length(ed),3);
%
% "Patch it"
% for kk=2:length(ed)
%     p(kk)=patch(xx(ix(:,kk)),yy(ix(:,kk)),col(kk,:));
% end
%
% ylabel('Euclidean Distance (a.u.)');xlabel('Class');legend(c);
```


Bibliography

- ABBOTT-D., AND ZHANG-X.-C. (2007). Special issue on T-ray imaging, sensing, and retection, *Proceedings of the IEEE*, **95**(8), pp. 1509–1513.
- ADAM-A. J. L., BROK-J. M., SEO-M. A., AHN-K. J., KIM-D. S., KANG-J. H., PARK-Q. H., NAGEL-M., AND PLANKEN-P. C. (2008). Advanced terahertz electric near-field measurements at sub-wavelength diameter metallic apertures, *Opt. Express*, **16**(10), pp. 7407–7417.
- ASHWORTH-P. C., PICKWELL-MACPHERSON-E., PROVENZANO-E., PINDER-S. E., PURUSHOTHAM-A. D., PEPPER-M., AND WALLACE-V. P. (2009). Terahertz pulsed spectroscopy of freshly excised human breast cancer, *Opt. Express*, **17**(15), pp. 12444–12454.
- AUSTON-D. H., LAVALLARD-P., SOL-N., AND KAPLAN-D. (1980). An amorphous silicon photodetector for picosecond pulses, *Applied Physics Letters*, **36**(1), pp. 66–68.
- BAKUNOV-M., BODROV-S., AND MASLOV-A. (2007). Temporal dynamics of optical-to-terahertz conversion in electro-optic crystal, *Conference on Lasers and Electro-Optics, 2007. CLEO 2007.*, pp. 1–2.
- BALANIS-C. A. (1997). *Antenna Theory: Analysis and Design*, John Wiley & Sons.
- BASS-M., FRANKEN-P. A., WARD-J. F., AND WEINREICH-G. (1962). Optical rectification, *Phys. Rev. Lett.*, **9**(11), pp. 446–448.
- BAUMANN-D., FUMEAUX-C., HAFNER-C., AND LI-E. P. (2009). A modular implementation of dispersive materials for time-domain simulations with application to gold nanospheres at optical frequencies, *Opt. Express*, **17**(17), pp. 15186–15200.
- BELLMAN-R. E. (1961). *Adaptive Control Processes - A Guided Tour*, Princeton University Press, Princeton, New Jersey, U.S.A.
- BERTA-M., DANYLYUK-S., KADLEC-F., KUZEL-P., AND KLEIN-N. (2006). THz near-field spectroscopy based on metal dielectric antennae, *Conference Digest of the 2006 Joint 31st International Conference on Infrared and Millimeter Waves and 14th International Conference on Terahertz Electronics*, Shanghai, China, p. 373.
- BETHE-H. A. (1944). Theory of diffraction by small holes, *Phys. Rev.*, **66**, pp. 163–182.
- BITZER-A., AND WALTHER-M. (2008). Terahertz near-field imaging of metallic subwavelength holes and hole arrays, *Applied Physics Letters*. art. no. 231101.
- BITZER-A., ORTNER-A., AND WALTHER-M. (2010). Terahertz near-field microscopy with subwavelength spatial resolution based on photoconductive antennas, *Applied Optics*, **49**(19), pp. E1–E6.

Bibliography

- BONNET-P., FERRIERES-X., MICHELSEN-B. L., KLOTZ-P., AND ROUMIGUIÈRES-J. L. (1999). *Time Domain Electromagnetics*, Academic Press, chapter Finite-volume time domain method.
- BONVALET-A., JOFFRE-M., MARTIN-J., AND MIGUS-A. (1995). Generation of ultrabroadband femtosecond pulses in the mid-infrared by optical rectification of 15 fs light pulses at 100 MHz repetition rate, *Applied Physics Letters*, **67**(20), pp. 2907–2909.
- BOUWKAMP-C. J. (1950a). On Bethes theory of diffraction by small holes, *Philips Res. Rep.*, **5**, pp. 321–332.
- BOUWKAMP-C. J. (1950b). On the diffraction of electromagnetic waves by circular disks and apertures, *Philips Res. Rep.*, **5**, pp. 401–422.
- BOYD-R. W. (2003). *Nonlinear Optics*, Boston Academic Press.
- BRALY-L. B., LIU-K., BROWN-M. G., KEUTSCH-F. N., FELLERS-R. S., AND SAYKALLY-R. J. (2000). Terahertz laser spectroscopy of the water dimer intermolecular vibrations. II. (H₂O)₂, *The Journal of Chemical Physics*, **112**(23), pp. 10314–10326.
- BRANDI-H. S., LATGÉ-A., AND OLIVEIRA-L. E. (2003). Rabi oscillations, coherent properties, and model qubits in two-level donor systems under terahertz radiation, *Physical Review B*, **68**(23), pp. 233206–233209.
- BRENER-I., HUNSCHE-S., CAI-Y., NUSS-M., WYNN-J., LOPATA-J., AND PFEIFFER-L. (1998). Time resolved near field imaging with sub-wavelength far-infrared dipole sources, *Ultrafast Phenomena XI*, Vol. 63 of *Springer Series in Chemical Physics*, Springer-Verlag, Berlin, pp. 171–173.
- BRICKHOUSE-M. D., CREASY-W. R., WILLIAMS-B. R., MORRISSEY-K. M., O’CONNOR-R. J., AND DURST-H. D. (2000). Multiple-technique analytical characterization of a mixture containing chemical-weapons simulant from a munition, *Journal of Chromatography A*, **883**(1), pp. 185–198.
- BRODSCHELM-A., TAUSER-F., HUBER-R., SOHN-J., AND LEITENSTORFER-A. (2000). *Ultrafast Phenomena XII*, Springer-Verlag, chapter Amplitude and phase resolved detection of tunable femtosecond pulses with frequency components beyond 100 THz, pp. 215–217.
- CARRIG-T., RODRIGUEZ-G., SHARP CLEMENT-T., TAYLOR-A., AND STEWART-K. (1995). Scaling of terahertz radiation via optical rectification in electro-optic crystals, *Applied Physics Letters*, **66**, pp. 121–123.
- CHEN-H.-T., KERSTING-R., AND CHO-G. C. (2003). Terahertz imaging with nanometer resolution, *Applied Physics Letters*, **83**, pp. 3009–3011.
- CHEN-Q., AND ZHANG-X.-C. (1999). Polarization modulation in optoelectronic generation and detection of terahertz beams, *Applied Physics Letters*, **74**(23), pp. 3435–3437.
- CHEN-Q., AND ZHANG-X.-C. (2001). Semiconductor dynamic aperture for near-field terahertz wave imaging, *IEEE Journal of Selected Topics in Quantum Electronics*, **7**, pp. 608–614.

- CHEN-Q., JIANG-Z., XU-G., AND ZHANG-X.-C. (2000). Near-field terahertz imaging with a dynamic aperture, *Optics Letters*, **25**, pp. 1122–1124.
- COLE-B. E., WILLIAMS-J. B., KING-B. T., SHERWIN-M. S., AND STANLEY-C. R. (2001). Coherent manipulation of semiconductor quantum bits with terahertz radiation, *Nature*, **410**, pp. 60–63.
- COURJON-D., AND BAINIER-C. (1994). Near field microscopy and near field optics, *Reports on Progress in Physics*, **57**(10), pp. 989–1028.
- COWARD-P., AND APPLEBY-R. (2003). Development of an illumination chamber for indoor millimeter-wave imaging, *Proc. SPIE Passive Millimeter-Wave Imaging Technology VI and Radar Sensor Technology VII*, Vol. 5077, pp. 54–61.
- DAKOVSKI-G. L., KUBERA-B., AND SHAN-J. (2005). Localized terahertz generation via optical rectification in ZnTe, *Journal of the Optical Society of America B: Optical Physics*, **22**, pp. 1667–1670.
- DELBRIDGE-A. (2001). *The Macquarie Dictionary*, 3rd edn, The Macquarie Library, North Ryde, NSW, Australia.
- DE LUCIA-F. C. (2003). *Sensing with Terahertz Radiation*, Vol. 85 of *Springer Series in Optical Sciences*, Springer.
- DE SERIO-M., ZENOBI-R., AND DECKERT-V. (2003). Looking at the nanoscale: Scanning near-field optical microscopy, *Trends in Analytical Chemistry*, **22**, pp. 70–77.
- Dexheimer, S.. (ed.) (2007). *Terahertz Spectroscopy: Principles and Applications*, CRC Press.
- DICKE-R., AND ROMER-R. (1955). Pulse techniques in microwave spectroscopy, *Review of Scientific Instruments*, **26**(10), pp. 915–928.
- DMITRIEV-V., GURZADYAN-G., AND NIKOGOSYAN-D. (1999). *Handbook of Nonlinear Optical Crystals*, Springer.
- DOANY-F., GRISCHKOWSKY-D., AND CHI-C.-C. (1987). Carrier lifetime versus ion-implantation dose in silicon on sapphire, *Applied Physics Letters*, **50**(8), pp. 460–462.
- DRAFTS-B. (2001). Acoustic wave technology sensors, *IEEE Transactions on Microwave Theory and Techniques*, **49**(4), pp. 795–802.
- DUDA, R-O. (2001). *Pattern Classification*, John Wiley & Sons, New York.
- DUFFY-S. M., VERGHESE-S., AND MCINTOSH-K. (2004). *Sensing with Terahertz Radiation*, Springer, chapter Photomixers for continuous-wave terahertz radiation, p. 193236.
- FATTINGER-C., AND GRISCHKOWSKY-D. (1988). Point source terahertz optics, *Applied Physics Letters*, **53**(16), pp. 1480–1482.
- FERGUSON-B., WANG-S., ABBOTT-D., AND ZHANG-X.-C. (2003). Powder detection with THz imaging, *Proc. SPIE Terahertz for Military and Security Applications*, Vol. 5070, pp. 7–16.

Bibliography

- FISCHER-B. M. (2005). *Broadband THz Time-Domain Spectroscopy of Biomolecules*, PhD thesis, University of Freiburg.
- FISCHER-B. M., HOFFMANN-M., HELM-H., MODJESCH-G., AND JEPSEN-P. U. (2005). Chemical recognition in terahertz time-domain spectroscopy and imaging, *Semiconductor Science and Technology*, **20**, pp. S246–S253.
- FISCHER-B. M., WALTHER-M., AND JEPSEN-P. U. (2002). Far-infrared vibrational modes of DNA components studied by terahertz time-domain spectroscopy, *Physics in Medicine and Biology*, **47**, pp. 3807–3814.
- FITZGERALD-A., BERRY-E., ZINOV'EV-N., HOMER-VANNIASINKAM-S., MILES-R., CHAMBERLAIN-J., AND SMITH-M. (2003). Catalogue of human tissue optical properties at terahertz frequencies, *Journal of Biological Physics*, **29**, pp. 123–128.
- FUMEAUX-C., BAUMANN-D., ATAKARAMIANS-S., AND LI-E. (2009). Considerations on paraxial gaussian beam source conditions for time-domain full-wave simulations, *25th Annual Review of Progress in Applied Computational Electromagnetics*, pp. 401–406.
- FUMEAUX-C., BAUMANN-D., LEUCHTMANN-P., AND VAHLDIECK-R. (2004). A generalized local time-step scheme for efficient FDTD simulations in strongly inhomogeneous meshes, *IEEE Transactions on Microwave Theory and Techniques*, **52**(3), pp. 1067–1076.
- FUMEAUX-C., SANKARAN-K., AND VAHLDIECK-R. (2007). Spherical perfectly matched absorber for finite-volume 3-D domain truncation, *IEEE Transactions on Microwave Theory and Techniques*, **55**(12), pp. 2773–2781.
- GALLOT-G., ZHANG-J., MCGOWAN-R. W., JEON-T.-I., AND GRISCHKOWSKY-D. (1999). Measurements of the THz absorption and dispersion of ZnTe and their relevance to the electro-optic detection of THz radiation, *Applied Physics Letters*, **74**(23), pp. 3450–3452.
- GIRARD-C., JOACHIM-C., AND GAUTHIER-S. (2000). The physics of the near-field, *Reports on Progress in Physics*, **63**(6), pp. 893–938.
- GU-P., TANI-M., KONO-S., SAKAI-K., AND ZHANG-X.-C. (2002). Study of terahertz radiation from InAs and InSb, *Journal of Applied Physics*, **91**(9), pp. 5533–5537.
- HADJILOUCAS-S., KARATZAS-L. S., AND BOWEN-J. W. (1999). Measurements of leaf water content using terahertz radiation, *IEEE Transactions on Microwave Theory and Techniques*, **47**(2), pp. 142–149.
- HAN-P., CHO-G., AND ZHANG-X.-C. (2000a). Time-domain transillumination of biological tissues with terahertz pulses, *Optics Letters*, **25**, pp. 242–244.
- HAN-P., TANI-M., PAN-F., AND ZHANG-X.-C. (2000b). Use of the organic crystal DAST for terahertz beam applications, *Optics Letters*, **25**, pp. 675–677.

- HAN-P., TANI-M., USAMI-M., KONO-S., KERSTING-R., AND ZHANG-X.-C. (2001). A direct comparison between terahertz time-domain spectroscopy and far-infrared fourier transform spectroscopy, *Journal of Applied Physics*, **89**(4), pp. 2357–2359.
- HARDE-H., AND GRISCHKOWSKY-D. (1991). Coherent transients excited by subpicosecond pulses of terahertz radiation, *J. Opt. Soc. Am. B*, **8**(8), pp. 1642–1651.
- HARDE-H., CHEVILLE-R., AND GRISCHKOWSKY-D. (1997). Terahertz studies of collision-broadened rotational lines, *Journal of Physical Chemistry A*, **101**(20), pp. 3646–3660.
- HATTORI-T., TUKAMOTO-K., RUNGSAWANG-R., AND NAKATSUKA-H. (2001). Knife edge measurement of tightly focused terahertz pulses, *The 8th International Workshop on Femtosecond Technology*, p. 1.
- HEBLING-J., STEPANOV-A., ALMASI-G., BARTAL-B., AND KUHL-J. (2004). Tunable THz pulse generation by optical rectification of ultrashort laser pulses with tilted pulse fronts, *Applied Physics B: Lasers and Optics*, **78**(5), pp. 593–599.
- HERRMANN-M., TANI-M., SAKAI-K., AND FUKASAWA-R. (2002). Terahertz imaging of silicon wafers, *Journal of Applied Physics*, **91**(3), pp. 1247–1250.
- HILLENBRAND-R., AND KEILMANN-F. (2002). Material-specific mapping of metal semiconductor dielectric nanosystems at 10 nm resolution by backscattering near-field optical microscopy, *Applied Physics Letters*, **80**, pp. 25–27.
- HILLENBRAND-R., TAUBNER-T., AND KEILMANN-F. (2002). Phonon-enhanced light-matter interaction at the nanometre scale, *Nature*, **417**, pp. 159–162.
- HO-C. K., ITAMURA-M. T., KELLEY-M., AND HUGHES-R. C. (2001). Review of chemical sensors for in-situ monitoring of volatile contaminants, *Technical Report SAND2001-0643*, Sandia National Laboratories.
- HOFFMANN-M. (2006). *Novel Techniques in THz-Time-Domain-Spectroscopy - A Comprehensive Study of Technical Improvements to THz-TDS*, PhD thesis, Freiburg University.
- HUBER-A. J., KEILMANN-F., WITTBORN-J., AIZPURUA-J., AND HILLENBRAND-R. (2008). Terahertz near-field nanoscopy of mobile carriers in single semiconductor nanodevices, *Nano Letters*, **8**(11), pp. 3766–3770.
- HUBER-R., BRODSCHELM-A., TAUSER-F., AND LEITENSTORFER-A. (2000). Generation and field-resolved detection of femtosecond electromagnetic pulses tunable up to 41 THz, *Applied Physics Letters*, **76**, pp. 3191–3193.
- HUNSCHE-S., KOCH-M., BRENER-I., AND NUSS-M. (1998). THz near-field imaging, *Optics Communications*, **150**, pp. 22–26.
- JACOBSEN-R., MITTLEMAN-D., AND NUSS-M. (1996). Chemical recognition of gases and gas mixtures with terahertz waves, *Optics Letters*, **21**(24), pp. 2011–2013.

- JACQUINET-HUSSON-N., ARIÉ-E., BALLARD-J., BARBE-A., BJORAKER-G., BONNET-B., BROWN-L. R., CAMY-PEYRET-C., CHAMPION-J. P., CHÉDIN-A., CHURSIN-A., CLERBAUX-C., DUXBURY-G., FLAUD-J.-M., FOURRIÉ-N., FAYT-A., GRANER-G., GAMACHE-R., GOLDMAN-A., GOLOVKO-V., GUELACHVILI-G., HARTMANN-J. M., HILICO-J. C., HILLMAN-J., LEFÈVRE-G., LELLOUCH-E., MIKHAÏLENKO-S. N., NAUMENKO-O. V., NEMTCHINOV-V., NEWNHAM-D. A., NIKITIN-A., ORPHAL-J., PERRIN-A., REUTER-D. C., RINSLAND-C. P., ROSENMAN-L., ROTHMAN-L. S., SCOTT-N. A., SELBY-J., SINITSIA-L. N., SIROTA-J. M., SMITH-A. M., SMITH-K. M., TYUTEREV-V. G., TIPPING-R. H., URBAN-S., VARANASI-P., AND WEBER-M. (1999). The 1997 spectroscopic GEISA databank, *Journal of Quantitative Spectroscopy and Radiative Transfer*, **62**(2), pp. 205–254.
- JEON-T.-I., AND GRISCHKOWSKY-D. (1998). Observation of a Cole-Davidson type complex conductivity in the limit of very low carrier densities in doped silicon, *Applied Physics Letters*, **72**(18), pp. 2259–2261.
- JEPSEN-P. U., AND FISCHER-B. (2005). Dynamic range in terahertz time-domain transmission and reflectionspectroscopy, *Opt. Lett.*, **30**(1), pp. 29–31.
- JEPSEN-P. U., JACOBSEN-R. H., AND KEIDING-S. R. (1996). Generation and detection of terahertz pulses from biased semiconductor antennas, *J. Opt. Soc. Am. B*, **13**(11), pp. 2424–2436.
- KAINDL-R., SMITH-D., JOSCHKO-M., HASSELBECK-M., WOERNER-M., AND ELSAESSER-T. (1998). Femtosecond infrared pulses tunable from 9 to 18 mm at an 88-MHz repetition rate, *Optics Letters*, **23**, pp. 861–863.
- KAPPERT-H., SIXT-G., AND SCHWUTTKE-G. (1979). Minority carrier lifetime in silicon after Ar⁺ and Si⁺ implantation., *Physica Status Solidi (A) Applied Research*, **52**(2), pp. 463 – 474.
- KATZENELLENBOGEN-N., AND GRISCHKOWSKY-D. (1991). Efficient generation of 380 fs pulses of THz radiation by ultrafast laser pulse excitation of a biased metal?semiconductor interface, *Applied Physics Letters*, **58**(3), pp. 222–224.
- KAWANO-Y., AND ISHIBASHI-K. (2008). An on-chip near-field terahertz probe and detector, *Nature Photonics*, **2**, pp. 618–621.
- KAWASE-K., OGAWA-Y., WATANABE-Y., AND INOUE-H. (2003). Non-destructive terahertz imaging of illicit drugs using spectral fingerprints, *Opt. Express*, **11**(20), pp. 2549–2554.
- KEILMANN-F. (1995). FIR microscopy, *Infrared Physics & Technology*, **36**(1), pp. 217–224.
- KERSTING-R., BUERSGENS-F., ACUNA-G., AND CHO-G. (2008). Terahertz near-field microscopy, in R. Haug. (ed.), *Advances in Solid State Physics*, Vol. 47 of *Advances in Solid State Physics*, Springer Berlin / Heidelberg, pp. 203–222.
- KIM-S., MURAKAMI-H., AND TONOUCHE-M. (2008). Transmission-type laser THz emission microscope using a solid immersion lens, *IEEE Journal of Selected Topics in Quantum Electronics*, **14**(2), pp. 498–504.

- KIWA-T., KONDO-Y., MINAMI-Y., KAWAYAMA-I., TONOUCHI-M., AND TSUKADA-K. (2010). Terahertz chemical microscope for label-free detection of protein complex, *Applied Physics Letters*, **96**(21), pp. 211114–211116.
- KIWA-T., TONOUCHI-M., YAMASHITA-M., AND KAWASE-K. (2003). Laser terahertz-emission microscope for inspecting electrical faults in integrated circuits, *Optics Letters*, **28**, pp. 2058–2060.
- KLEIN-N., LAHL-P., POPPE-U., KADLEC-F., AND KUZEL-P. (2005). A metal-dielectric antenna for terahertz near-field imaging, *Journal of Applied Physics*, **98**(1), p. 14910.
- KNAB-J. R., ADAM-A. J. L., NAGEL-M., SHANER-E., SEO-M. A., KIM-D. S., AND PLANKEN-P. C. M. (2009). Terahertz near-field vectorial imaging of subwavelength apertures and aperture arrays, *Opt. Express*, **17**(17), pp. 15072–15086.
- KNOBLOCH-P., SCHILDKNECHT-C., KLEINE-OSTMANN-T., KOCH-M., HOFFMANN-S., HOFMANN-M., REHBERG-E., SPERLING-M., DONHUIJSEN-K., HEIN-G., AND PIERZ-K. (2002). Medical THz imaging: an investigation of histo-pathological samples, *Physics in Medicine and Biology*, **47**(21), pp. 3875–3884.
- KNOLL-B., AND KEILMANN-F. (1999). Near-field probing of vibrational absorption for chemical microscopy, *Nature*, **399**(6732), pp. 134–137.
- KORN-T., FRANKE-WIEKHORST-A., SCHNULL-S., AND WILKE-I. (2002). Characterization of nanometer as-clusters in low-temperature grown gaas by transient reflectivity measurements, *Journal of Applied Physics*, **91**(4), pp. 2333–2333.
- KRISTENSEN-T. T. L., WITHAYACHUMNANKUL-W., JEPSEN-P. U., AND ABBOTT-D. (2010). Modeling terahertz heating effects on water, *Opt. Express*, **18**(5), pp. 4727–4739.
- KUBLER-C., HUBER-R., AND LEITENSTORFER-A. (2005). Ultrabroadband terahertz pulses: generation and field-resolved detection, *Semiconductor Science and Technology*, **20**, pp. 128–133.
- LAMPRECHT-K. F., JUEN-S., PALMETSHOFER-L., AND HÖPFEL-R. A. (1991). Ultrashort carrier lifetimes in h⁺ bombarded inp, *Applied Physics Letters*, **59**(8), pp. 926–928.
- LECAQUE-R., GRÉSILLON-S., AND BOCCARA-C. (2008). THz emission microscopy with sub-wavelength broadband source, *Opt. Express*, **16**(7), pp. 4731–4738.
- LECAQUE-R., GRESILLON-S., BARBEY-N., PERETTI-R., RIVOAL-J.-C., AND BOCCARA-C. (2006). THz near-field optical imaging by a local source, *Optics Communications*, **262**(1), pp. 125–128.
- LEE-C. H., ANTONETTI-A., AND MOUROU-G. (1977). Measurements on the photoconductive lifetime of carriers in gaas by optoelectronic gating technique, *Optics Communications*, **21**(1), pp. 158–161.
- LEE-J. W., PARK-T. H., NORDLANDER-P., AND MITTLEMAN-D. M. (2009). Terahertz transmission properties of an individual slit in a thin metallic plate, *Opt. Express*, **17**(15), pp. 12660–12667.

Bibliography

- LEE-K., KIM-J., PARK-H., HAN-H., PARK-I., AND LIM-H. (2007). Numerical simulation of apertureless terahertz near-field microscopes, *CLEO/Pacific Rim 2007 Conference on Lasers and Electro-Optics - Pacific Rim, 2007*, pp. 1–2.
- LEE-K., YUN-S., CHO-M., PARK-H., KIM-J., HAN-H., AND PARK-I. (2006). Ftd simulation of terahertz near-field microscopes, *Joint 31st International Conference on Infrared Millimeter Waves and 14th International Conference on Terahertz Electronics, 2006. IRMMW-THz 2006.*, p. 435.
- LEE-Y. S. (2008). *Principles of Terahertz Science and Technology*, Springer.
- LEE-Y.-S., MEADE-T., PERLIN-V., WINFUL-H., NORRIS-T., AND GALVANAUSKAS-A. (2000). Generation of narrow-band terahertz radiation via optical rectification of femtosecond pulses in periodically poled lithium niobate, *Applied Physics Letters*, **76**(18), pp. 2505–2507.
- LEITENSTORFER-A., HUNSCHE-S., SHAH-J., NUSS-M. C., AND KNOX-W. H. (2000). Femtosecond high-field transport in compound semiconductors, *Phys. Rev. B*, **61**(24), pp. 16642–16652.
- LEVINE-H., AND SCHWINGER-J. (1948). On the theory of diffraction by an aperture in an infinite plane screen, *Phys. Rev.*, **74**(8), pp. 958–974.
- LIEBERZEIT-P. A., AND DICKERT-F. L. (2007). Sensor technology and its application in environmental analysis, *Analytical and Bioanalytical Chemistry*, **387**(1), pp. 237–247.
- LIN-H., FISCHER-B. M., AND ABBOTT-D. (2010a). Comparative simulation study of ZnTe heating effects in focused THz radiation generation, *35th International Conference on Infrared, Millimeter, and Terahertz Waves*, pp. 63–64.
- LIN-H., FUMEAUX-C., FISCHER-B. M., AND ABBOTT-D. (2010b). Modelling of sub-wavelength THz sources as gaussian apertures, *Opt. Express*, **18**(17), pp. 17672–17683.
- LIN-H., FUMEAUX-C., UNG-B. S. Y., AND ABBOTT-D. (2011). Comprehensive modeling of THz microscope with a sub-wavelength source, *Opt. Express*, **19**(6), pp. 5327–5338.
- LIN-H., UNG-B. S. Y., FISCHER-B. M., MICKAN-S. P., AND ABBOTT-D. (2009). Effect of crystal thickness in localized terahertz generation via optical rectification in ZnTe - preliminary investigation, *34th International Conference on Infrared and Millimeter Waves and Terahertz Waves*. doi:10.1109/ICIMW.2009.5325560.
- LIN-H., WITHAYACHUMNANKUL-W., FISCHER-B., MICKAN-S., AND ABBOTT-D. (2008). Gas recognition with terahertz time-domain spectroscopy and reference-free spectrum: A preliminary study, pp. 1–2.
- LIN-H., WITHAYACHUMNANKUL-W., FISCHER-B. M., MICKAN-S. P., AND ABBOTT-D. (2007). Gas recognition with terahertz time-domain spectroscopy and spectral catalog: a preliminary study, in C. Zhang., and X.-C. Zhang. (eds.), *Proc. SPIE*, Vol. 6840. doi:10.1117/12.760558.
- LIU-H.-B., CHEN-Y., BASTIAANS-G. J., AND ZHANG-X.-C. (2006). Detection and identification of explosive RDX by THz diffuse reflection spectroscopy, *Opt. Express*, **14**(1), pp. 415–423.

- LIU-H.-B., PLOPPER-G., EARLEY-S., CHEN-Y., FERGUSON-B., AND ZHANG-X.-C. (2007a). Sensing minute changes in biological cell monolayers with THz differential time-domain spectroscopy, *Biosensors and Bioelectronics*, **22**(6), pp. 1075–1080.
- LIU-H.-B., ZHONG-H., KARPOWICZ-N., CHEN-Y., AND ZHANG-X.-C. (2007b). Terahertz spectroscopy and imaging for defense and security applications, *Proceedings of the IEEE*, **95**(8), pp. 1514–1527.
- LIU-K., XU-J., AND ZHANG-X.-C. (2004). GaSe crystals for broadband terahertz wave detection, *Applied Physics Letters*, **85**, pp. 863–865.
- LU-Z. G., CAMPBELL-P., AND ZHANG-X.-C. (1997). Free-space electro-optic sampling with a high-repetition-rate regenerative amplified laser, *Applied Physics Letters*, **71**(5), pp. 593–595.
- MAIR-S., GOMPF-B., AND DRESSEL-M. (2004). Spatial and spectral behavior of the optical near field studied by a terahertz near-field spectrometer, *Applied Physics Letters*, **84**(7), pp. 1219–1221.
- MARKELZ-A. (2008). Terahertz dielectric sensitivity to biomolecular structure and function, *IEEE Journal of Selected Topics in Quantum Electronics*, **14**(1), pp. 180–190.
- MARQUARDT-D. W. (1963). An algorithm for least-squares estimation of nonlinear parameters, *Journal of the Society for Industrial and Applied Mathematics*, **11**(2), pp. pp. 431–441.
- MATSUURA-S., AND ITO-H. (2005). *Terahertz Optoelectronics, Vol. 97 of Topics in Applied Physics*, Springer-Verlag, chapter Generation of CW terahertz radiation with photomixing, pp. 157–204.
- MICKAN-S. P. (2002). *T-ray Biosensing*, PhD thesis, The University of Adelaide.
- MITROFANOV-O., BRENER-I., HAREL-R., WYNN-J., PFEIFFER-L., WEST-K., AND FEDERICI-J. (2000a). Terahertz near-field microscopy based on a collection mode detector, *Applied Physics Letters*, **77**(22), pp. 3496–3498.
- MITROFANOV-O., BRENER-I., WANKE-M., RUEL-R., WYNN-J., BRUCE-A., AND FEDERICI-J. (2000b). Near-field microscope probe for far infrared time domain measurements, *Applied Physics Letters*, **77**(4), pp. 591–593.
- MITROFANOV-O., LEE-M., HSU-J., BRENER-I., HAREL-R., FEDERICI-J., WYNN-J., PFEIFFER-L., AND WEST-K. (2001a). Collection-mode near-field imaging with 0.5-THz pulses, *IEEE Journal of Selected Topics in Quantum Electronics*, **7**, pp. 600–607.
- MITROFANOV-O., LEE-M., HSU-J., PFEIFFER-L., WEST-K., WYNN-J., AND FEDERICI-J. (2001b). Terahertz pulse propagation through small apertures, *Applied Physics Letters*, **79**(7), pp. 907–909.
- MITTLEMAN-D., JACOBSEN-R., NEELAMANI-R., BARANIUK-R., AND NUSS-M. (1998). Gas sensing using terahertz time-domain spectroscopy, *Applied Physics B (Lasers and Optics)*, **67**, pp. 379–390.
- MITTLEMAN-D. M., CUNNINGHAM-J., NUSS-M. C., AND GEVA-M. (1997). Noncontact semiconductor wafer characterization with the terahertz hall effect, *Applied Physics Letters*, **71**(1), pp. 16–18.

Bibliography

- MOHR-P. J., AND TAYLOR-B. N. (2005). Codata recommended values of the fundamental physical constants: 2002, *Reviews of Modern Physics*, **77**(1), pp. 1–107.
- MOUROU-G., STANCAMPIANO-C. V., ANTONETTI-A., AND ORSZAG-A. (1981). Picosecond microwave pulses generated with a subpicosecond laser-driven semiconductor switch, *Applied Physics Letters*, **39**(4), pp. 295–296.
- MÜLLER-H. S. P., SCHLÖDER-F., STUTZKI-J., AND WINNEWISSER-G. (2005). The Cologne Database for Molecular Spectroscopy, CDMS: A useful tool for astronomers and spectroscopists, *Journal of Molecular Structure*, **742**, pp. 215–227.
- MURAKAMI-H., AND TONOUCHE-M. (2008). Laser terahertz emission microscopy, *Comptes Rendus Physique*, **9**(2), pp. 169–183.
- NAFTALY-M., AND MILES-R. (2007). Terahertz time-domain spectroscopy for material characterization, *Proceedings of the IEEE*, **95**(8), pp. 1658–1665.
- NAHATA-A., AUSTON-D., WU-C., AND YARDLEY-J. (1995). Generation of terahertz radiation from a poled polymer, *Applied Physics Letters*, **67**, pp. 1358–1360.
- NAHATA-A., WELING-A., AND HEINZ-T. (1996). A wideband coherent terahertz spectroscopy system using optical rectification and electro-optic sampling, *Applied Physics Letters*, **69**, pp. 2321–2323.
- NOVOTNY-L., AND HECHT-B. (2006). *Principles of Nano-Optics*, Cambridge University Press.
- NUSS-M. C., KISKER-D. W., SMITH-P. R., AND HARVEY-T. E. (1989). Efficient generation of 480 fs electrical pulses on transmission lines by photoconductive switching in metalorganic chemical vapor deposited cdte, *Applied Physics Letters*, **54**(1), pp. 57–59.
- ORFANIDIS-S. J. (2008). *Electromagnetic Waves and Antennas*, <http://www.ece.rutgers.edu/orfanidi/ewa/ch17.pdf>.
- OTHONOS-A. (1998). Probing ultrafast carrier and phonon dynamics in semiconductors, *Journal of Applied Physics*, **83**(4), pp. 1789–1830.
- PALANKER-D., KNIPPES-G., SMITH-T., AND SCHWETTMAN-H. (1998). IR microscopy with a transient photo-induced near-field probe (tipless near-field microscopy), *Optics Communications*, **148**, pp. 215–220.
- PALFREY-S., AND HEINZ-T. (1985). Coherent interactions in pump-probe absorption measurements: the effect of phase gratings, *Journal of the Optical Society of America B (Optical Physics)*, **2**(4), pp. 674–679.
- Palik, E. D.. (ed.) (1998). *Handbook of Optical Constants of Solids*, Orlando, FL, USA.
- PARK-D. J., CHOI-S. B., AHN-Y. H., ROTERMUND-F., SOHN-I. B., KANG-C., JEONG-M. S., AND KIM-D. S. (2009). Terahertz near-field enhancement in narrow rectangular apertures on metal film, *Opt. Express*, **17**(15), pp. 12493–12501.

- PARK-H., KIM-J., KIM-M., AND HANL-H. (2006). Terahertz near-field microscope, *Conference Digest of the 2006 Joint 31st International Conference on Infrared and Millimeter Waves and 14th International Conference on Terahertz Electronics*, Shanghai, China, p. 13.
- PARK-H. R., KOO-S. M., SUWAL-O. K., PARK-Y. M., KYOUNG-J. S., SEO-M. A., CHOI-S. S., PARK-N. K., KIM-D. S., AND AHN-K. J. (2010). Resonance behavior of single ultrathin slot antennas on finite dielectric substrates in terahertz regime, *Applied Physics Letters*. doi:10.1063/1.3437091.
- PARK-S.-G., MELLOCH-M., AND WEINER-A. (1998). Comparison of terahertz waveforms measured by electro-optic and photoconductive sampling, *Applied Physics Letters*, **73**(22), pp. 3184–3186.
- PICKETT-H., POYNTER-R., COHEN-E., DELITSKY-M., PEARSON-J., AND MULLER-H. (1998). Submillimeter, millimeter, and microwave spectral line catalog, *Journal of Quantitative Spectroscopy and Radiative Transfer*, **60**(5), pp. 883–890.
- PICKWELL-E., AND WALLACE-V. P. (2006). Biomedical applications of terahertz technology, *Journal of Physics D: Applied Physics*, **39**(17), pp. R301–R310.
- PICKWELL-E., COLE-B., FITZGERALD-A., PEPPER-M., AND WALLACE-V. (2004). In vivo study of human skin using pulsed terahertz radiation, *Physics in Medicine and Biology*, **49**, pp. 1595–1607.
- PLANKEN-P. C., NIENHUY-S.-H.-K., BAKKER-H. J., AND WENCKEBACH-T. (2001). Measurement and calculation of the orientation dependence of terahertz pulse detection in ZnTe, *Journal of the Optical Society of America B: Optical Physics*, **18**(3), pp. 313–317.
- RICE-A., JIN-Y., MA-X., ZHANG-X.-C., BLISS-D., LARKIN-J., AND ALEXANDER-M. (1994). Terahertz optical rectification from $\langle 110 \rangle$ zinc-blende crystals, *Applied Physics Letters*, **64**(11), pp. 1324–1326.
- ROSKOS-H. G., NUSS-M. C., SHAH-J., LEO-K., MILLER-D. A. B., FOX-A. M., SCHMITT-RINK-S., AND KÖHLER-K. (1992). Coherent submillimeter-wave emission from charge oscillations in a double-well potential, *Phys. Rev. Lett.*, **68**(14), pp. 2216–2219.
- ROTHMAN-L. S., JACQUEMART-D., BARBE-A., BENNER-D. C., BIRK-M., BROWN-L. R., CARLEER-M. R., CHACKERIAN-C., CHANCE-K., COUDERT-L. H., DANA-V., DEVI-V. M., FLAUD-J. M., GAMACHE-R. R., GOLDMAN-A., HARTMANN-J. M., JUCCS-K. W., MAKI-A. G., MANDIN-J. Y., MASSIE-S. T., ORPHAL-J., PERRIN-A., RINSLAND-C. P., SMITH-M. A. H., TENNYSON-J., TOLCHENOV-R. N., TOTH-R. A., VANDER AUWERA-J., VARANASI-P., AND WAGNER-G. (2005). The HITRAN 2004 molecular spectroscopic database, *Journal of Quantitative Spectroscopy and Radiative Transfer*, **96**, pp. 139–204.
- RUDD-J. V., AND MITTLEMAN-D. M. (2002). Influence of substrate-lens design in terahertz time-domain spectroscopy, *J. Opt. Soc. Am. B*, **19**(2), pp. 319–329.
- Sakai, K. (ed.) (2005). *Terahertz Optoelectronics (Topics in Applied Physics Vol.97)*, Berlin, Germany.
- SALEH-B. E. A., AND TEICH-M. (1991). *Fundamentals of Photonics*, John Wiley & Sons.

- SCHNEIDER-A., NEIS-M., STILLHART-M., RUIZ-B., KHAN-R., AND GUNTER-P. (2006). Generation of terahertz pulses through optical rectification in organic DAST crystals: Theory and experiment, *Journal of the Optical Society of America B*, **23**, pp. 1822–1835.
- SERITA-K., MIZUNO-S., MURAKAMI-H., KAWAYAMA-I., TONOUCHE-M., TAKAHASHI-Y., YOSHIMURA-M., KITAOKA-Y., AND MORI-Y. (2010). Development of laser scanning terahertz imaging system using organic nonlinear optical crystal, *35th International Conference on Infrared, Millimeter, and Terahertz Waves*. doi:10.1109/ICIMW.2010.5612990,.
- SHANK-C., YEN-R., AND HIRLIMANN-C. (1983). Time-resolved reflectivity measurements of femtosecond-optical-pulse-induced phase transitions in silicon, *Physical Review Letters*, **50**(6), pp. 454–457.
- SHEN-Y. (1976). Far-infrared generation by optical mixing, *Progress in Quantum Electronics*, **4**, pp. 207–238.
- SHEN-Y. C., UPADHYA-P. C., LINFIELD-E. H., BEERE-H. E., AND DAVIES-A. G. (2003). Ultrabroadband terahertz radiation from low-temperature-grown GaAs photoconductive emitters, *Applied Physics Letters*, **83**(15), pp. 3117–3119.
- SHEN-Y. R. (1984). *The Principles of Nonlinear Optics*, Wiley.
- SIEGEL-P. (2004). Terahertz technology in biology and medicine, *IEEE Transactions on Microwave Theory and Techniques*, **52**(10), pp. 2438–2447.
- SINYUKOV-A. M., AND HAYDEN-L. M. (2002). Generation and detection of terahertz radiation with multilayered electro-optic polymer films, *Optics Letters*, **27**, pp. 55–57.
- SMITH-F., LE-H., DIADIUK-V., HOLLIS-M., CALAWA-A., GUPTA-S., FRANKEL-M., DYKAAR-D., MOUROU-G., AND HSIANG-T. (1989). Picosecond gaas-based photoconductive optoelectronic detectors, *Applied Physics Letters*, **54**(10), pp. 890–892.
- SMITH-P., AUSTON-D., JOHNSON-A., AND AUGUSTYNIAK-W. (1981). Picosecond photoconductivity in radiation-damaged silicon-on-sapphire films, *Applied Physics Letters*, **38**(1), pp. 47–50.
- STANDARDS AUSTRALIA COMMITTEE ME/71, QUANTITIES, UNITS, AND CONVERSION. (1998). ASISO 10001998: The international system of units (SI) and its application, *Australian Standard*.
- STEPANOV-A., AND HEBLING-J. (2005). THz generation via optical rectification with ultrashort laser pulse focused to a line, *Applied Physics B (Lasers and Optics)*, **B81**, pp. 23–26.
- STONE-M. R., NAFTALY-M., MILES-R. E., MAYORGA-I. C., MALCOCI-A., AND MIKULICS-M. (2005). Generation of continuous-wave terahertz radiation using a two-mode titanium sapphire laser containing an intracavity Fabry-Perot etalon, *Journal of Applied Physics*. doi:10.1063/1.1904724.
- STRACHAN-C. J., RADES-T., NEWNHAM-D. A., GORDON-K. C., PEPPER-M., AND TADAY-P. F. (2004). Using terahertz pulsed spectroscopy to study crystallinity of pharmaceutical materials, *Chemical Physics Letters*, **390**(1-3), pp. 20–24.

- STRACHAN-C. J., TADAY-P. F., NEWNHAM-D. A., GORDON-K. C., ZEITLER-J. A., PEPPER-M., AND RADES-T. (2005). Using terahertz pulsed spectroscopy to quantify pharmaceutical polymorphism and crystallinity, *Journal of Pharmaceutical Sciences*, **94**(4), pp. 837–846.
- TADAY-P. F. (2004). Applications of terahertz spectroscopy to pharmaceutical sciences, *Philosophical Transactions of the Royal Society of London. Series A: Mathematical, Physical and Engineering Sciences*, **362**(1815), pp. 351–364.
- TAFLOVE-A., AND HAGNESS-S. C. (2005). *Computational Electrodynamics: The Finite-Difference Time-Domain Method*, Artech House.
- TANI-M., MATSUURA-S., SAKAI-K., AND ICHI NAKASHIMA-S. (1997). Emission characteristics of photoconductive antennas based on low-temperature-grown GaAs and semi-insulating GaAs, *Appl. Opt.*, **36**(30), pp. 7853–7859.
- TONOUCHI-M. (2007). Cutting-edge terahertz technology, *Nature Photonics*, **1**, pp. 97–105.
- TONOUCHI-M., KIM-S., KAWAYAMA-I., AND MURAKAMI-H. (2011). Laser terahertz emission microscope, *Proc. SPIE Terahertz Physics, Devices, and Systems V: Advance Applications in Industry and Defense*, Vol. 8023. doi:10.1117/12.887937.
- VANDER-A. J., SHERMAN-J. H., AND LUCIANO-D. S. (1990). *Human Physiology: The Mechanisms of Body Function*, McGraw-Hill Publishing Company.
- VAN DER VALK-N., AND PLANKEN-P. (2002). Electro-optic detection of subwavelength terahertz spot sizes in the near field of a metal tip, *Applied Physics Letters*, **81**(9), pp. 1558–1560.
- VAN DER VALK-N., PLANKEN-P., BUIJSERD-A., AND BAKKER-H. (2005). Influence of pump wavelength and crystal length on the phase matching of optical rectification, *Journal of the Optical Society of America B (Optical Physics)*, **22**, pp. 1714–1718.
- VAN EXTER-M., AND GRISCHKOWSKY-D. (1990a). Characterization of an optoelectronic terahertz beam system, *IEEE Transactions on Microwave Theory and Techniques*, **38**(11), pp. 1684–1691.
- VAN EXTER-M., AND GRISCHKOWSKY-D. (1990b). Optical and electronic properties of doped silicon from 0.1 to 2 THz, *Applied Physics Letters*, **56**(17), pp. 1694–1696.
- VAN EXTER-M., FATTINGER-C., AND GRISCHKOWSKY-D. (1989). High-brightness terahertz beams characterized with an ultrafast detector, *Applied Physics Letters*, **55**(4), pp. 337–339.
- VON RIBBECK-H.-G., BREHM-M., VAN DER WEIDE-D. W., WINNERL-S., DRACHENKO-O., HELM-M., AND KEILMANN-F. (2008). Spectroscopic THz near-field microscope, *Opt. Express*, **16**(5), pp. 3430–3438.
- WÄCHTER-M., NAGEL-M., AND KURZ-H. (2009). Tapered photoconductive terahertz field probe tip with subwavelength spatial resolution, *Applied Physics Letters*. doi:10.1063/1.3189702.

Bibliography

- WALLACE-V. P., FITZGERALD-A. J., PICKWELL-E., PYE-R. J., TADAY-P. F., FLANAGAN-N., AND HAT. (2006). Terahertz pulsed spectroscopy of human basal cell carcinoma, *Applied Spectroscopy*, **60**(10), pp. 1127–1133.
- WALTHER-M. (2003). *Modern Spectroscopy on Biological Molecules Structure and Bonding Investigated by THz Time-Domain and Transient Phase-Grating Spectroscopy*, PhD thesis, University of Freiburg.
- WALTHER-M., FISCHER-B. M., AND JEPSEN-P. U. (2003). Noncovalent intermolecular forces in polycrystalline and amorphous saccharides in the far infrared, *Chemical Physics*, **288**, pp. 261–268.
- WANG-H., AND CHU-W. (2009). Thermal conductivity of ZnTe investigated by molecular dynamics, *Journal of Alloys and Compounds*, **485**(1-2), pp. 488–492.
- WANG-K., AND MITTLEMAN-D. M. (2004). Metal wires for terahertz wave guiding, *Nature*, **432**(7015), pp. 376–379.
- WANG-K., BARKAN-A., AND MITTLEMAN-D. (2003). Sub-wavelength resolution using apertureless terahertz near-field microscopy, *Conference on Lasers and Electro-Optics (CLEO)*, Baltimore, MD, USA, p. 2.
- WANG-K., BARKAN-A., AND MITTLEMAN-D. (2004a). Propagation effects in apertureless near-field optical antennas, *Applied Physics Letters*, **84**(2), pp. 305–307.
- WANG-K., MITTLEMAN-D. M., VAN DER VALK-N. C., AND PLANCKEN-P. C. (2004b). Antenna effects in terahertz apertureless near-field optical microscopy, *Applied Physics Letters*, **85**(14), pp. 2715–2717.
- WARD-J. F. (1966). Absolute measurement of an optical-rectification coefficient in ammonium dihydrogen phosphate, *Phys. Rev.*, **143**, pp. 569–574.
- WARREN-A. C., KATZENELLENBOGEN-N., GRISCHKOWSKY-D., WOODALL-J. M., MELLOCH-M. R., AND OTSUKA-N. (1991). Subpicosecond, freely propagating electromagnetic pulse generation and detection using gaas:as epilayers, *Applied Physics Letters*, **58**(14), pp. 1512–1514.
- WATANABE-Y., KAWASE-K., IKARI-T., ITO-H., ISHIKAWA-Y., AND MINAMIDE-H. (2003). Component spatial pattern analysis of chemicals using terahertz spectroscopic imaging, *Applied Physics Letters*, **83**(4), pp. 800–802.
- WHITE-J. U. (1942). Long optical paths of large aperture, *Journal of the Optical Society of America*, **32**, pp. 285–288.
- WHITE-J. U. (1976). Very long optical paths in air, *Journal of the Optical Society of America*, **66**(5), pp. 411–416.
- WILLIAMS-B. S. (2007). Terahertz quantum-cascade lasers, *Nature Photonics*, **1**, p. 517525.
- WILSON-D., HOYT-S., JANATA-J., BOOKSH-K., AND OBANDO-L. (2001). Chemical sensors for portable, handheld field instruments, *IEEE Sensors Journal*, **1**(4), pp. 256–274.

- WITHAYACHUMNANKUL-W., LIN-H., MICKAN-S. P., FISCHER-B. M., AND ABBOTT-D. (2007a). Analysis of measurement uncertainty in THz-TDS, in A. Serpenguzel., G. Badenes., and G. C. Righini. (eds.), *Proc. SPIE*, Vol. 6593. art. no. 659326L.
- WITHAYACHUMNANKUL-W., PNG-G., YIN-X., ATAKARAMIANS-S., JONES-I., LIN-H., UNG-S. Y., BALAKRISHNAN-J., NG-B.-H., FERGUSON-B., MICKAN-S., FISCHER-B., AND ABBOTT-D. (2007b). T-ray sensing and imaging, *Proceedings of the IEEE*, **95**(8), pp. 1528–1558.
- WOLF-E., AND NIETO-VESPERINAS-M. (1985). Analyticity of the angular spectrum amplitude of scattered fields and some of its consequences, *J. Opt. Soc. Am. A*, **2**(6), pp. 886–889.
- WOODWARD-R. M., COLE-B. E., WALLACE-V. P., PYE-R. J., ARNONE-D. D., LINFIELD-E. H., AND PEPPER-M. (2002). Terahertz pulse imaging in reflection geometry of human skin cancer and skin tissue, *Physics in Medicine and Biology*, **47**(21), pp. 3853–3863.
- WOODWARD-R., WALLACE-V., ARNONE-D., LINFIELD-E., AND PEPPER-M. (2003a). Terahertz pulsed imaging of skin cancer in the time and frequency domain, *Journal of Biological Physics*, **29**, pp. 257–259.
- WOODWARD-R., WALLACE-V., PYE-R., COLE-B., ARNONE-D., LINFIELD-E., AND PEPPER-M. (2003b). Terahertz pulse imaging of ex vivo basal cell carcinoma., *The Journal of investigative dermatology*, **120**(1), pp. 72–78.
- WU-Q., AND ZHANG-X.-C. (1996a). Design and characterization of traveling-wave electrooptic terahertz sensors, *IEEE Journal of Selected Topics in Quantum Electronics*, **2**, pp. 693–700.
- WU-Q., AND ZHANG-X.-C. (1996b). Ultrafast electro-optic field sensors, *Applied Physics Letters*, **68**, pp. 1604–1606.
- WYNNE-K., AND JAROSZYNSKI-D. (1999). Superluminal terahertz pulses, *Optics Letters*, **24**(1), pp. 25–27.
- XIE-X., XU-J., DAI-J., AND ZHANG-X.-C. (2007). Enhancement of terahertz wave generation from laser induced plasma, *Applied Physics Letters*. doi:10.1063/1.2719165.
- XING-Q., LANG-L., TIAN-Z., ZHANG-N., LI-S., WANG-K., CHAI-L., AND WANG-Q. (2006). The effect of two-photon absorption and optical excitation area on the generation of THz radiation, *Optics Communications*, **267**(2), pp. 422–426.
- XU-J., AND ZHANG-X.-C. (2002). Optical rectification in an area with a diameter comparable to or smaller than the center wavelength of terahertz radiation, *Optics Letters*, **27**, pp. 1067–1069.
- XU-L., ZHANG-X.-C., AND AUSTON-D. (1992). Terahertz beam generation by femtosecond optical pulses in electro-optic materials, *Applied Physics Letters*, **61**(15), pp. 1784–1786.
- YAMAMOTO-K., YAMAGUCHI-M., MIYAMARU-F., TANI-M., HANGYO-M., IKEDA-T., MATSUSHITA-A., KOIDE-K., TATSUNO-M., AND MINAMI-Y. (2004). Noninvasive inspection of c-4 explosive

in mails by terahertz time-domain spectroscopy, *Japanese Journal of Applied Physics*, **43**(3B), pp. L414–L417.

YAMASHITA-M., KAWASE-K., OTANI-C., KIWA-T., AND TONOUCHE-M. (2005). Imaging of large-scale integrated circuits using laser-terahertz emission microscopy, *Opt. Express*, **13**(1), pp. 115–120.

YAMASHITA-M., KIWA-T., TONOUCHE-M., NIKAWA-K., OTANI-C., AND KAWASE-K. (2004). Laser terahertz emission microscope for inspecting electrical failures in integrated circuits, Kyoto, Japan, pp. 29–30.

YANG-H. Y., SHI-Y., ZHOU-Q., ZHAO-D., LI-L., AND ZHANG-C. (2009). Ultrafast carrier transport in GaAs measured by optical pump-terahertz probe spectroscopy, in C. Zhang., and T. Liu. (eds.), *Proc. SPIE*, Vol. 7512. doi:10.1117/12.838020.

YUAN-T., MICKAN-S., XU-J., ABBOTT-D., AND ZHANG-X.-C. (2002). Towards an apertureless electro-optic T-ray microscope, *Conference on Lasers and Electro-Optics*, Long Beach, CA, United States, pp. 637–638.

YUAN-T., PARK-H., XU-J., HAN-H., AND ZHANG-X.-C. (2005). Field induced THz wave emission with nanometer resolution, Vol. 5649, Sydney, Australia, pp. 1–8.

YUAN-T., XU-J., AND ZHANG-X.-C. (2004). Development of terahertz wave microscopes, *Infrared Physics and Technology*, **45**, pp. 417–425.

YU-P., AND CARDONA-M. (1999). *Fundamentals of Semiconductors*, Berlin, Germany.

ZANDONELLA-C. (2003). T-ray specs, *Nature*, **424**, pp. 721–722.

ZENHAUSERN-F., MARTIN-Y., AND WICKRAMASINGHE-H. (1995). Scanning interferometric apertureless microscopy: optical imaging at 10 Angstrom resolution, *Science*, **269**(5227), pp. 1083–1085.

ZHANG-L., ZHONG-H., DENG-C., ZHANG-C., AND ZHAO-Y. (2008). Terahertz wave reference-free phase imaging for identification of explosives, *Applied Physics Letters*. doi:10.1063/1.2891082.

ZHANG-X.-C. (2002). Terahertz wave imaging: horizons and hurdles, *Physics in Medicine and Biology*, **47**(21), pp. 3667–3677.

ZHANG-X.-C., JIN-Y., AND MA-X. (1992). Coherent measurement of THz optical rectification from electro-optic crystals, *Applied Physics Letters*, **61**, pp. 2764–2766.

ZHAO-G., SCHOUTEN-R., VAN DER VALK-N., WENCKEBACH-W., AND PLANKEN-P. (2002). Design and performance of a THz emission and detection setup based on a semi-insulating GaAs emitter, *Review of Scientific Instruments*, **73**(4), pp. 1715–1719.

Glossary

The physical constants used in this thesis are in accordance with a recommendation of the Committee on Data for Science and Technology (Mohr and Taylor 2005).

Quantity	Symbol	Value
Avogadro constant	N_A	$6.022\,1415(10) \times 10^{23} \text{ mol}^{-1}$
Boltzmann constant	k_B	$1.380\,6505(24) \times 10^{-23} \text{ J/K}$ $8.617\,343(15) \times 10^{-5} \text{ eV/K}$
electron volt	eV	$1.602\,176\,53(14) \times 10^{-19} \text{ J}$
Planck constant	h	$6.626\,0693(11) \times 10^{-34} \text{ J}\cdot\text{s}$ $4.135\,667\,43(35) \times 10^{-15} \text{ eV}\cdot\text{s}$
speed of light in vacuum	c, c_0	299 792 458 m/s
vacuum permeability (magnetic constant)	μ_0	$4\pi \times 10^{-7} \text{ N/A}^2$
vacuum permittivity (electric constant)	ϵ_0	$8.854\,187\,817 \dots \times 10^{-12} \text{ F/m}$

Acronyms

AOM	acousto optic modulator, 157
BWO	backward wave oscillators, 4
CCD	charge coupled device, 63
CDMS	Cologne database for molecular spectroscopy, 179
CW	continuous-wave, 4
DASC	4-dimethylamino-N-methyl-4-stilbazolium p-cholobenzene sulfonate, 157
DAST	dimethylamino-N-methylstilbazolium tosylate, 21
DFG	difference frequency generation, 4
FDTD	finite-difference time-domain, 100
FEL	free electron lasers, 4
FIR	far-infrared, 3
FT-MW	Fourier transform-microwave spectroscopy, 175
FTIR	Fourier transform infrared spectroscopy, 175
FVTD	finite-volume time-domain, 100
GCMS	gas chromatography and mass spectrometry, 175
GEISA	Gestion et Etude des Informations Spectroscopiques Atmosphériques, 179
HFSS	High Frequency Structural Simulator, 67
HITRAN	high-resolution transmission molecular absorption database, 178
IR	infrared, 3

Acronyms

JPL	Jet Propulsion Laboratory, 178
LT-GaAs	low-temperature grown gallium arsenide, 4
LTEM	laser THz emission microscope, 47
MMRC	Micro Materials & Research Consumables , 139
OR	optical rectification, 15
PCA	photoconductive antenna, 10
PEC	perfect electric conductor, 101
PMC	perfect magnetic conductor, 101
PPLN	periodically poled lithium niobate, 157
QCL	quantum cascade lasers, 5
SI-GaAs	semi-insulating gallium arsenide, 134
SNR	signal-to-noise ratio, 9
SOS	silicon on sapphire, 10
THz	terahertz, 3
THz-TDS	terahertz time-domain spectroscopy, 3
TOPAS	cyclic-olefin copolymer, 110
UV	ultraviolet, 133

Index

- aberration, 102
- acceptance angle, 60, 72, 75, 102–104
- amorphous, 137
- angle tuning, 19
- annealing, 139
- azimuthal angle, 17

- backward wave oscillators (BWO), 4
- balanced photodiodes, 145
- beta barium borate (BBO), 149
- biochip, 161
- biotin avidin, 52
- Bose-Einstein statistics, 136
- boundary conditions, 104
- bow-tie, 158–160

- carrier dynamics, 141
- carrier lifetime, 10, 133, 136, 142, 146, 149, 151
- carrier mobility, 133, 134
- chromium, 167
- coherence effects, 143
- coherence length, 62
- Complementary metal-oxide-semiconductor, 137
- convolution, 109
- coplanar transmission lines, 27
- covalent bond crystals, 19
- crystal heating, 9, 11, 17, 75, 81
- crystal-parabolic distance, 72, 104
- CST Microwave Studio, 159
- curve fitting criterion, 73, 80
- cyclic-olefin copolymer (TOPAS), 110, 129

- damage threshold, 19
- DASC, 157
- DAST, 21, 157
- dc bias, 133, 134
- detection path, 90, 102
- difference frequency generation (DFG), 4, 15
- diffraction, 73, 102, 104, 105, 110

- dipole moment, 21
- direct bandgap, 133, 134, 142, 148
- doping, 136
- Drude model, 141

- electro-optical coefficient, 17, 19, 20
- electro-optical polymers, 20
- electro-optical sampling, 18, 23, 29, 42, 44, 45
- electrodes separation distance, 22
- electron beam, 167
- electron mobility, 141
- enhancement, 50, 54
- epoxy, 91
- etch, 161
- etching, 168
- etching rate, 161
- evanescent waves, 37, 38, 89

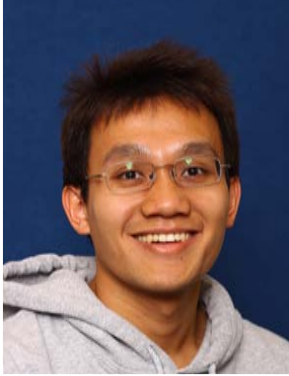
- finite difference time domain, 52
- finite integration technique, 46
- finite-volume time-domain, 100
- Fraunhofer distance, 133
- free electron lasers (FEL), 4

- GaAs, 4, 10, 17, 19, 29, 60, 90, 133, 139, 146, 148, 157, 159, 161
- gallium selenide (GaSe), 19
- galvano mirror, 157
- gas recognition, 8, 10
- Gaussian aperture, 55, 68, 71, 72, 90, 111
- Gaussian beam, 57, 75, 91
 - beam waist, 57, 62, 72, 75, 77, 80, 104
 - divergence angle, 58, 75
 - Rayleigh range, 57, 60
- Gaussian intensity distribution, *see* Gaussian beam,
see Gaussian beam, *see* Gaussian beam
- goodness of fit, 73, 80, 151
- grating, 143
- groove function, 109

- high pass filter, 160
- Huygens' surface, 102
- implant fluence, 139
- implantation dosage, 138
- index matching, 20, 91
- inorganic crystals, 19
- intensity distribution, 60
- ion implantation, 137, 151
- ionic crystals, 19
- ions
 - argon, 138
 - oxygen, 138, 139, 149, 151
 - silicon, 138–140, 149
- Kirchhoff's heating equation, 76
- knife-edge, 60, 61, 72, 95, 103, 105, 106, 111
- LabVIEW, 60
- lens-crystal distance, 91
- Levenberg Marquardt, 149
- lithium niobate, 20
- micro-fabrication, 90
- microscopy, 8, 37, 38, 42
- near-field, 90, 94, 96, 109, 110, 112, 133
- nonlinear crystal, 16, 31, 48, 60, 61, 90
- nonlinear susceptibility, 19
- numerical model, 59
- obliquity factor pattern, 59, 62, 74, 80, 106
- optical constants, 5, 76, 110
- optical phonons, 5
- optical pump probe, 142, 149
- optical pump THz probe, 148
- optical rectification (OR), 5, 9, 15, 17, 48, 90, 91
- paraxial approximation, 57, 62, 74, 75
- penetration depth, 81
- perfectly matched absorber, 101
- phase matching, 18, 19, 146
- phase matching criterion, 144
- photoconductive antenna (PCA), 5, 10, 15, 21, 25, 28, 29, 31, 40, 44, 47, 52, 60, 80, 133, 139
- photocurrent, 5, 22, 25, 134
- photodamage, *see* crystal heating, 75
- photomask, 158, 159
- photomixing, *see* difference frequency generation (DFG)
- photoresist, 167
- pinhole, 60
- plasma frequency, 141
- plasma generation, 80
- Pockels effect, 23
- polarisation transients, 16
- power enhancement, 90, 92
- probe zero delay, 144
- projection distance, 72
- propagation loss, 102
- quantum cascade lasers (QCL), 5
- quantum well structures, 5
- radiating aperture, 59, 111
- radiation damage, 133, 136, 137, 149
- radiation pattern, 9, 10, 59, 73, 102
- Rayleigh's criterion, 89
- recombination centres, 136, 138, 149
- relaxation times, 138
- resistivity, 22, 133, 134
- running average, 72, 104
- sapphire, 134
- Shockley-Read-Hall statistics, 136
- silicon on insulator, 137
- SOS, 10, 29, 54, 133, 134, 136, 137, 149
- spatial resolution, 89
- standing-wave pattern, 101
- sub-wavelength resolution, 90, 110
- superconductor, 5
- susceptibility tensor, 16
- T-rays, *see* terahertz (THz)
- terahertz (THz), 3
 - beam profile, 90, 94, 109
 - continuous-wave (CW) generation, 4
 - image, 7, 37, 89

- pulsed
 - detection, 15, 23, 25
 - generation, 5, 15, 23
 - localised generation, 11, 18, 47, 50, 57
- terahertz gap, 3
- terahertz time-domain spectroscopy (THz-TDS),
 - 5, 7, 8, 10, 28, 31, 90
- equipment, 10
 - balanced photodiodes, 143
 - beam splitter, 143
 - delay line, 26, 144
 - half wave plate, 143
 - PCA, *see* photoconductive antenna (PCA)
 - pellicle, 26
 - photodetector, 25
 - quarter-wave plate, 25
 - silicon lens, 22
 - wollaston prism, 25
 - zinc telluride, *see* ZnTe
- thermal conductivity, 76
- thermal equilibrium, 136
- thick crystals, 18, 50, 90
- thin crystals, 10, 18, 19, 50, 54, 90–92, 111
- THz near-field imaging, 8, 9, 37, 89, 110, 111, 133, 157
 - aperture, 39, 40, 89
 - focused beam, 47, 54, 89, 112, 157
 - tip, 42, 44, 89
 - waveguide, 44
- tilted pulse front, 20
- time resolution, 26
- transient current, *see* photocurrent
- transient reflectivity, 141–143, 146, 148–150
- trap density, 138
- trapping time, 136, 141
- true Gaussian beam, *see* Gaussian beam
- two photon absorption, 20, 50, 59, 91
- ultraviolet, 146, 168
- unimplanted, 149
- velocity matching, 18–20
- water vapour absorption, 72, 104
- waveguide effects, 89
- ZnTe, 19, 29, 31, 48, 60, 90, 95, 111

Biography



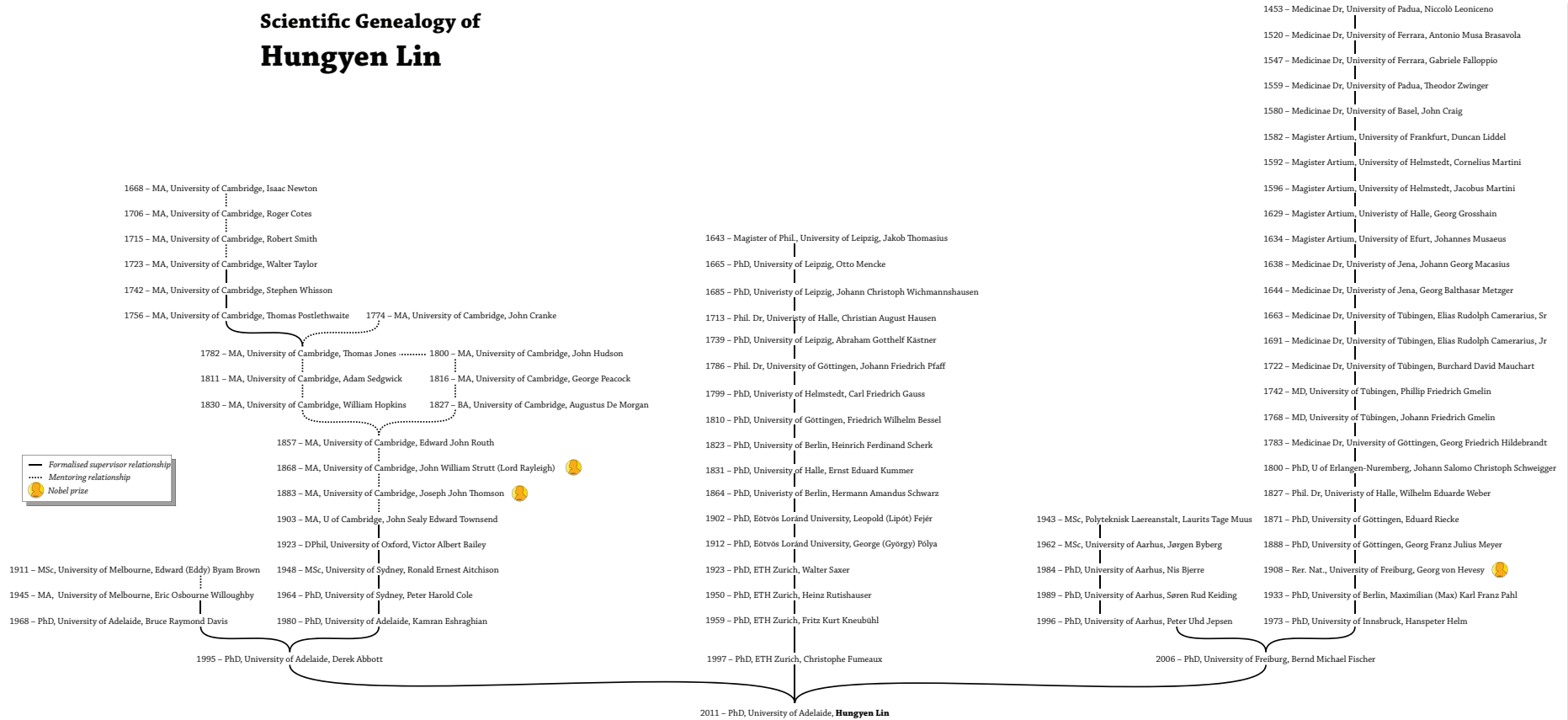
Hungyen Lin was born in Kaohsiung City, Taiwan in 1982. From 2000 to 2003, he was educated at The University of Adelaide, Australia, where he obtained a Bachelor's Degree in Computer Systems Engineering with first class honours. He was subsequently offered an Australian Postgraduate Award (Industry) to conduct a Masters by Research at University of South Australia. During his time there, he performed industrial research involving modelling degradation data using artificial neural networks. In 2006, following the completion of Masters, he was awarded an Australian Postgraduate Award to study toward his PhD under Prof Derek Abbott, Dr Bernd Fischer, and A/Prof Christophe Fumeaux, within the Adelaide T-ray group, the School of Electrical & Electronic Engineering, The University of Adelaide. Mid-way through candidature, he took a six months leave of absence to pursue a software engineering internship at Fujitsu Siemens Computers GmbH, Germany. He received a company patent encouragement award for his work there.

During his PhD candidature, Mr Hungyen Lin has received a IEEE Photonics Society Graduate Student Fellowship, DR Stranks Postgraduate Travelling Fellowship, Barbara Crase Bursary from the AFUW, IEEE South Australia Section Travel Assistance Fund and The University of Adelaide Research Abroad Scholarship. He was the reserved candidate for the 2009 Fulbright Postgraduate Scholarship in three categories; Technology & Communication, Science & Engineering and General Award. In 2010, he won a prestigious Australian Prime Minister's Asia Endeavour Award to conduct research with Prof Masayoshi Tonouchi at Tonouchi Laboratory, Institute of Laser Engineering, Osaka University, Japan.

Hungyen Lin was on the executive committee of IEEE affiliated Electrical and Electronic Engineering Society of Adelaide University (2006-2009) and is a member of IEEE, SPIE and the OSA.

Hungyen Lin
hlin@eleceng.adelaide.edu.au

Scientific Genealogy of Hungyen Lin



Note: to view an expanded version, please zoom in using the PDF electronic copy